5-3-2012 12:00 AM

A Study on the Turbulent Characteristics within the Hurricane Boundary Layer

Sunwei Li
The University of Western Ontario

Supervisor
Dr. Craig Miller
The University of Western Ontario

Graduate Program in Civil and Environmental Engineering
A thesis submitted in partial fulfillment of the requirements for the degree in Doctor of Philosophy

Recommended Citation

Li, Sunwei, "A Study on the Turbulent Characteristics within the Hurricane Boundary Layer" (2012). *Electronic Thesis and Dissertation Repository*. 529.
https://ir.lib.uwo.ca/etd/529

A Study on the Turbulent Characteristics within the Hurricane Boundary Layer

(Thesis format: Monograph)

by

Li Sunwei

Graduate Program in Department of Civil and Environmental Engineering

Submitted in partial fulfillment
of the requirements for the degree of
Doctor of Philosophy

The School of Graduate and Postdoctoral Studies
The University of Western Ontario
London, Ontario, Canada

THE UNIVERSITY OF WESTERN ONTARIO
School of Graduate and Postdoctoral Studies

CERTIFICATE OF EXAMINATION

Supervisor:

. . . .
Dr. Craig Miller

Co-Supervisor:

. . . .
Dr. Gregory Kopp

Supervisory Committee:

. . . .
Dr. Horia Hangan

. . . .
Dr. Ralph Baddour

Examiners:

. . . .
Dr. Gregory Kopp

. . . .
Dr. Girma Bitsuamlak

. . . .
Dr. Wayne Hocking

. . . .
Dr. Peter Taylor

The thesis by

Sunwei Li

entitled:

A Study on the Turbulent Characteristics within the Hurricane Boundary Layer

is accepted in partial fulfillment of the
requirements for the degree of
Doctor of Philosophy

. . . .
Date

. . . .
Chair of the Thesis Examination Board

Abstract

As the medium between the sea surface and the upper atmosphere in a hurricane, the Hurricane Boundary Layer (HBL) plays a key role in the overall dynamics of a tropical cyclone, and therefore turbulence exchanges within the HBL deserve a thorough investigation. However, since it is dangerous and difficult to take direct measurements within the HBL, studies of the HBL turbulence processes based on direct observations are rare. Thanks to the newly developed dropwindsonde equipped with a Global Position System (GPS) receiver, it is now possible to measure wind velocities and other meteorological variables with an unprecedented accuracy and resolution in the HBL.

To fully utilize dropwindsonde measurements, it is necessary to thoroughly understand its motion characteristics in the measured wind field since its horizontal motions are usually reported as wind measurements. For that reason, the dropwindsonde motion in a pseudo-stochastic wind field with known statistics is simulated. The simulation results illustrate the importance of the wind finding equations introduced by Hock and Franklin (1999) which calculate local winds from dropwindsonde motions. The simulation results show that they are important in reproducing both mean and turbulent wind structures in the HBL. One of its basic assumptions that the dropwindsonde drag coefficient is a constant regardless of the angle of attack is, however, invalidated by the wind tunnel tests conducted in this study. Given that this assumption is essential in both deriving the wind finding equations and in conducting the numerical dropwindsonde motion simulation described above, it is necessary to adapt the dropwindsonde motion model and to repeat the motion simulation to recheck the validity of the wind finding equations demonstrated in the previous simulation. The results validates the wind finding equations although it is derived based on a false assumption that the dropwindsonde drag coefficient is a constant regardless of angles of attack. Moreover, through analyzing the adapted dropwindsonde motion model, a new approach to estimate the vertical wind is proposed which is shown to increase the accuracy in vertical wind estimation by nearly 70%.

Based on the findings derived in the dropwindsonde motion simulations, an in-house software package is designed to process the actual dropwindsonde measurements gathered from 1997 to 2010. The in-house software package, showing an effectiveness equivalent to other widely used processing systems, gives users more control over the processing and compositing procedures used to derive the desired statistics of the measured wind field. With the help of this software package, dropwindsonde measurements are processed and composited to produce the mean, turbulence intensity, and turbulent length scale profiles of the HBL. While the mean wind structure confirms the findings made by several previous studies, the turbulence structure reveals that the turbulence diffusivity formulation currently used by the Yonsei University planetary boundary layer scheme, or the YSU scheme, in Weather Research and Forecasting Model(WRF), a widely used hurricane wind simulation package, correctly simulate turbulent mixing in the HBL up to $200m$ from the sea surface. In a theoretical discussion of the validity of the YSU scheme, it is found that both the velocity scale and height scale used in its turbulence diffusivity formulation should be revised to take into consideration the special turbulence characteristics in the HBL.

For the purpose of checking the turbulence diffusivity formulation used in the YSU scheme, high resolution numerical simulations of an idealized tropical cyclone are conducted using WRF. The simulation results show that only revising the HBL height calculation is not adequate to improve the numerical simulation of hurricanes. Therefore, a deeper investigation of the YSU scheme in simulating the HBL turbulence is required.

Keywords: Turbulence characteristics; GPS dropwindsonde; Hurricane boundary layer; Direct observation; Numerical simulation; Turbulence model

Acknowledgements

First, I would like acknowledge the generous support made by China Scholarship Council and the University of Western Ontario who provide the financial support for me to pursue my PhD degree here. The scholarship from the State Scholarship Fund of China and Western Engineering Scholarship made it possible for me to chase my childhood dream.

The greatest thanks to my supervisor, Dr. Craig Miller for his countless hours of guidance and help, no matter it is academic or personal. His help got me through the difficult time of settling down in Canada, and his support is very important in the process of pursuing my PhD degree. The wisdom and knowledge passed on will help me in the future career.

I also want acknowledge the Hurricane Research Division (HRD) in the National Oceanic and Atmospheric Administration (NOAA) who collects and maintains the Global Positioning System (GPS) dropwindsonde data. Without such an effort, my research would be impossible. Also, I want to acknowledge the great computational facility, SHARCNET, made available by Compute Canada. Its world-leading capacity made the numerical simulation part in this study possible.

Thanks to the crew and members of the Alan G. Davenport Wind Engineering Group. It is such an honour to complete my PhD here in one of the top research facilities in the field of Wind Engineering. Your kindness and friendship would accompany me for the rest of my life.

Finally, I would like thank my wife, Yu yuanyuan, for her endless love and support. It is her love got me through this tough time. This work is dedicated to my family, my parents, my wife, and my child. Although we do not have the name yet, I wish he, or she, can be pride of me one day.

Contents

Nomenclature

β	The angle between the orientation of the dropwindsonde body and one reference direction
δ	The boundary layer height scale, m
ϕ	The Monin-Obukhov function evaluated at the top of the surface layer
ρ	The air density, kg/m^3
τ	The turbulent shear stress, m^2/s^2
θ	The virtual potential temperature, K
A	The area of the cross-section of the dropwindsonde body, m^2
a	The shape parameter used by Vickery et al(2009) in HBL mean wind profile model
C_D	The drag coefficient
C_L	The list coefficient
C_T	The torque coefficient
f	The Coriolis parameter, s^{-1}
F_D	The drag force, N
F_L	The lift force, N
G	The gravitational force, N
g	The gravity acceleration, m/s^2
h	The boundary layer height, m
H^*	The HBL height scale used by Vickery et al(2009) in HBL mean wind profile model, m
I	The moment of inertia of the dropwindsonde body rotating around its center, kgm^2
I	The tropical cyclone inertial stability, s^{-1}

k	The von-Karman constant
K_m	The turbulence diffusivity for the momentum, m^2/s
L	The Monin-Obukhov length, m
l	The mixing length, m
M	The magnitude of the relative motion vector describing motion of the dropwindsonde relative to the flow, m/s
m	The angular momentum, s^{-1}
n	The shape parameter used by Vickery et al(2009) in HBL mean wind profile model
p	$p = p_x, p_y, p_z$ is the dropwindsonde body orientation vector
p	The shape parameter used by the YSU scheme to describe the turbulence diffusivity in the PBL
Ri	The bulk Richardson number
T	The torque, Nm
U	The mean wind velocity of the HBL, m/s
u	The longitudinal wind component, m/s
u_{*0}	The surface value of the shear velocity, m/s
u_*	The shear velocity, could be a function of height, m/s
V	The tropical cyclone gradient wind velocity, m/s
v	The lateral wind component, m/s
w	The vertical wind component, m/s
x	The longitudinal coordinate in the Cartesian coordinates system
y	the lateral coordinate in the Cartesian coordinates system
z	The vertical coordinate in the Cartesian coordinates system, the distance from sea surface
z_0	The surface aerodynamic roughness length, m
z_i	The boundary layer height, m

List of Tables

List of Figures

Chapter 1

Introduction

The tropical cyclone is one of the extreme weather conditions experienced by human beings. It produces powerful winds, torrential rains, high waves, damaging storm surges and, in some cases, inland tornadoes. All these phenomena greatly influence both human lives over land in hurricane-prone regions and shipping over the sea. Most of its influence is devastating and destructive. Over the past two centuries, tropical cyclones are responsible for deaths of about 1.9 million people worldwide, and Hurricane Katrina (2005) alone cost the U.S. more than 80 billion dollars for recovery and reconstruction.[1] It even impacts nature sources by reshaping the geology near coasts and causing landslides in some area due to the heavy rain. Thus, a thorough understanding on dynamics of tropical cyclones can be beneficial not only because it helps avoid negative effects but also because it helps explore possible, positive effects.

The boundary layer of tropical cyclone atmosphere is responsible for integrating the sea surface with the upper level wind field, and to then form the tropical cyclone dynamic system. Since the warm sea surface temperature is the ultimate energy source in the ”hurricane engine” (Wang and Wu, 2004), the importance of understanding exchange processes within the Hurricane Boundary Layer (HBL) is obvious. As one major transportation mechanism in the HBL, turbulence exchanges need to be investigated for one to fully comprehend the transportation of both momentum and energy between the sea

---

[1] http://en.wikipedia.org/wik/Tropical cyclone

and the atmosphere, and then to make a more accurate and reliable estimate of tropical cyclones' impact.

1.1 Background and Motivation

Although the HBL plays a significant role in overall hurricane dynamics, the characteristics of its wind field, however, are still far from being clear. As indicated by Braun and Tao (2000), an accurate and reliable description of turbulent mixing within the HBL is still not fully established despite its importance in numerical simulations of hurricane winds. In the contrast to the hurricane track numerical prediction which has been improved significantly in the last decade (Hill and Lackmann, 2009), the hurricane intensity numerical prediction does not provide an estimate more reliable than a simple empirical model (Hill and Lackmann, 2009). As one important parameter in Numerical Weather Prediction (NWP) models, the model of turbulent mixing within the Atmospheric Boundary Layer (ABL) determines descriptions of a "local" meteorological phenomenon, such as the intensity of tropical cyclones as indicated by Kepert and Wang (2001).

As noted by many previous studies (Powell et al., 2003; Vickery et al., 2009; Yu et al., 2008; Schroeder and Smith, 2003; Schroeder et al., 2009), wind characteristics in the HBL is appreciably different from wind characteristics in standard ABL. In standard ABL, which can be defined as the ABL over land or over water in neutral stability under low wind speed conditions (under $20m/s$ measured by averaging wind velocity in the lowest $500m$ in the ABL), the mean wind profile can be described by a logarithmic function and wind velocities above the gradient height is taken as a constant throughout the entire ABL. In contrast, the mean wind profile found in the HBL shows a super-gradient phenomenon under the gradient height, and therefore only a logarithmic is inadequate to describe the mean wind velocity variation with height. Moreover, the studies focusing on the turbulent characteristics in the HBL indicated that the turbulence in hurricane winds is spatially better correlated and the turbulent kinetic energy is concentrated at a frequency lower than that found in the standard ABL. These studies substantiated the need to thoroughly investigate the wind characteristics in the HBL, especially the turbulent characteristics, focusing on its difference from wind characteristics in the standard ABL.

Although endeavours of taking direct measurements of turbulence variables within the HBL has been made as early as the 1970's, as described by Moss (1978) and Sethraman (1979), few studies have been performed to derive a reliable model of turbulent mixing because of the rarity of measurements, which is due to the difficulty and danger of taking measurements at a sufficiently low altitude in the HBL. Until very recently, the invention of research aircraft at a sufficiently low altitude while maintaining safe and operational, like the ones used in the Coupled Boundary Layer Air-Sea Transfer Experiment, make it possible to take direct measurements of turbulence variables, like wind velocity variances and turbulent momentum fluxes, within the HBL. An other currently available technique of analyzing the HBL turbulence is remote sensing techniques. As described by Lorsolo et al. (2010), remote sensing techniques are able to reveal a crude structure of the HBL turbulent kinetic energy. In addition to studies based on direct observations over water, measurements taken over land are also used to analyze turbulence characteristics within the HBL, as in the study of Yu et al. (2008). Although research aircraft measurements provide, so far, the most reliable observations of the HBL turbulence, the scarcity of its measurement data hampers retrieving a comprehensive wind structure of the HBL. Limitations of the remote sensing observations and over land tower observations are crude resolutions and restrictions in measurement height respectively. Without a reliable direct observation, numerical models describing turbulent mixing in the standard ABL are used extensively to model the HBL turbulence for engineering applications.

Thoroughly described by Hock and Franklin (1999), the Global Position System (GPS) dropwindsonde, or dropwindsonde for simplicity, has been regularly used since the early 1990's to take measurements of the wind and other meteorological variables when it falls through the HBL, and therefore a considerable database of dropwindsonde measurements has been built up. A picture of the dropwindsonde is shown in Fig. 1.1. Although many studies were conducted to analyze the mean wind profile of the HBL based on this database, there is no attempt, as far to my knowledge, has been made to derive turbulence characteristics of the HBL from dropwindsonde observations. The abundance of dropwindsonde measurements overcomes the scarcity of research aircraft observations and gives a more comprehensive description of the HBL, and its relatively high resolution, measuring winds every $0.5s$, overcomes the shortage of remote sensing techniques. In addition, its capacity to measure the entire HBL overcomes the shortage of tower observations over land. In conclusion, the dropwindsonde provides us an unprecedented opportunity to analyze turbulence characteristics within the HBL.

Figure 1.1: A photo of the GPS dropwindsonde falling with a parachute attached.

As indicated by several previous studies (Powell et al., 2003; Franklin et al., 2003; Vickery et al., 2009), the composition technique is unavoidable to calculate more useful wind statistics from raw dropwindsonde measurements. Since this approach is followed in finding turbulent characteristics in the HBL through dropwindsonde measurements and the discussion on the turbulent characteristics in the HBL is the main part of this thesis, the composition approach is briefly introduced here. When a dropwindsonde is released by reconnaissance flights when they are penetrating tropical cyclones, it reports wind velocity in its fall till it reaches the sea surface. Because one dropwindsonde drop only produces a single profile describing instantaneous wind velocity variation with height, it is necessary to composite many dropwindsonde profile together to derive the variation of wind statistics with height. In the composition process, many individual dropwindsonde profiles are actually averaged to calculate a "representative" profile. When these individual profiles contains the raw wind measurements, the calculation results represent the mean wind velocity variation with height. Meanwhile, when these individual profiles contains turbulent components of measured wind velocities, or contains other turbulence instantaneous measurements, the calculation results represent the variation of various turbulent characteristics with height. Using the dropwindsonde observations as a validation criteria, the turbulence model currently used in numerical simulations of hurricanes can be investigated and improved.

1.2 Objective and Scope

As mentioned above, this study is mainly aimed to provide a better numerical model of the HBL turbulence, which helps improve the Planetary Boundary Layer Scheme (PBL) scheme used by various numerical simulation packages, which is responsible for simulating the PBL turbulence, using the ample measurements taken by the dropwindsonde. Thus, the scope of this study is defined by the HBL turbulence information derived from dropwindsonde measurements. In other words, besides the vertical profile of turbulence variables, other useful values are also derived from dropwindsonde observations, like the mean wind profile. However, we focus on the turbulence characteristics, like the vertical stricture of the turbulent wind velocity and turbulent integral length scale. Moreover, the HBL height is also a topic due to its importance in numerical simulations of hurricanes, especially ones using "non-local" PBL schemes. Furthermore, to investigate the findings made by analyzing the composited dropwindsonde measurements more closely, numerical simulations of an idealized tropical cyclones, are also carried out.

The major objective of this study is to gain a better understanding of turbulence exchange processes in the HBL. It is useful since it has many applications. For example, the NWP of a tropical cyclone, especially the hurricane intensity prediction, relies heavily on accurately modelling turbulent mixing within the HBL. In addition, dynamic responses of man-made structures subjecting to hurricane winds are also partially determined by the turbulence characteristics within the HBL. Although this study only explores one of its potential applications, improving numerical simulations of hurricanes, it should be noted that the turbulence characteristics in the HBL found by the dropwindsonde have extensive applications.

To be more illustrative, the major objective is broken down. It is helpful to list the objectives of each step taken toward the final goal, since they are also outcomes of this study.

- Understand the dropwindsonde motion, and then give a better interpretation of its measurement by numerically simulating its fall in a pseudo-stochastic wind field with statistics close to those found in natural winds.
- Estimate the mean wind profile of the HBL using the actual dropwindsonde measurements, reveal the dynamical structure of the HBL in a more detailed and comprehensive way.
- Derive the vertical turbulence structure of the HBL, including the turbulence intensity, turbulence length scale and HBL height, from dropwindsonde measurements, and propose adaption to the turbulence numerical model to take into account special HBL turbulence characteristics.
- Numerically simulate an idealized tropical cyclone to investigate the adapted HBL turbulence model more closely by comparing the numerical simulation results to the composited dropwindsonde measurements.

Following the introduction, literature concerning turbulence within the HBL and the use of dropwindsonde are reviewed in chapter 2. Chapter 3 presents the numerical simulations of the dropwindsonde motion in a pseudo-stochastic wind field and an investigation of various aspects of post-processing and compositing dropwindsonde measurements. Chapter 4 details the procedures used to process and composite the actual dropwindsonde measurements and presents the mean and turbulent structure of the HBL derived from the dropwindsonde composition. Chapter 5 analyzes the turbulence characteristics derived from dropwindsonde measurements and possible adaption to the PBL scheme currently used in numerically simulating hurricanes. The main content of the chapter 5 is to describe numerical simulations of an idealized tropical cyclone and to discuss the alternations upon the originally used turbulence model. Chapter 6 gives conclusions of, and possible future works can be performed to extend, this work.

Chapter 2

Literature Review

To systematically summarize previous studies relevant to the work of this thesis, the literature review given in this chapter is organized as following. Section 2.1 reviews observational studies focusing on the wind field of tropical cyclones, including observations over the sea made by reconnaissance flights, remote sensing techniques and in-situ observations over land made by towers and masts. Since the dropwindsonde is one significant observation data source used to get wind characteristics within the HBL and it is the major data source for this thesis work, literature concerning the use of the dropwindsonde is reviewed exclusively in an individual section, section 2.2. Section 2.3 gives the summary of modelling studies on the HBL wind field, including ones using the analytical modelling approach and numerical simulations.

2.1 Observational Study

The observational study contributes significantly to advance our understanding on the wind field of tropical cyclones, and serves as the only validation criteria for either numerical simulations or analytical modelling since experimental studies are still not feasible.

Because it is difficult and dangerous to take direct measurements of the wind in hurricanes by other instruments, measurements taken by reconnaissance flights at high altitudes are the primary data source for observational studies of the hurricane wind field. However, reconnaissance flights contribute little to enhance the description of the wind field within the HBL because few research airplanes have the capacity to fly low enough to take measurements in the HBL where extreme weather conditions may cause it to fail. The Coupled Boundary Layer Air-Sea Transfer Experiment (CBLAST) data is one of a few data sources came from reconnaissance flights concerning the HBL at this stage.

The observation of winds within the HBL can also be established by remote sensing techniques. Although the remote sensing has merely been devoted to study the wind field within the HBL, and are mainly used to get the ”bigger picture” of a hurricane, several previous studies revealed some features of the wind field within the HBL.

Besides the observations taken over the sea, in-situ measurements taken by towers and masts over land are also one data source for observational studies of the hurricane wind field. Unlike observations made by reconnaissance flights and remote sensing techniques, the measurements taken by towers and masts over land when a tropical cyclone is passing are limited to the surface layer, i.e. in the lowest $\sim 10m$, due to the limitation of its measuring equipments.

2.1.1 Reconnaissance Flight

Although instrumented aircraft have been sent out to make observations of the wind field in tropical cyclones as early as the late 1950’s (Dorst, 2007), systematical investigations of the wind field in tropical cyclones based on compositing the reconnaissance flight data actually began at 1970’s. One important study is that of Shea and Gray (1973). Winds and other meteorological information from 533 flight legs for over 13 years were collected and analyzed. Data were composited with respect to individual Radius of the Maximum Wind (RMW)s of hurricanes to give a general description of relative horizontal hurricane wind structures. The idealized, steady-state schematic model presented in that study has showed several significant features:

- storm inflows are limited in the lowest layer of storms and they mainly occur outside the RMW

- outflows, on the other hand, occur within the RMW
- coincident with inflows, largest convergences occur in the lowest layer at the RMW.

The relative wind field, when storm movements are subtracted, shows that the inner core of a storm experiences a natural asymmetry beyond that introduced by storm movements. Due to safety restrictions, most of their data were taken above $900mb$, which is approximately $1km$. Thus, this study revealed little information about the HBL.

Since reconnaissance flight data from an individual flight leg can only cover a small portion of the total wind field of hurricanes, composition is necessary to derive the "global picture" of the measured wind field. However, besides studies like that of Shea and Gray (1973), which depicts some common features of all hurricanes, several studies tried to derive the wind field of a specific hurricane by compositing reconnaissance flight measurements taken in a single hurricane, such as that described by Frank (1984). In the study, data measured in the mature stage of Hurricane Frederic (1979) were processed and analyzed. A total number of 40 flight legs were used. The inflow layer height analysis suggested that the drag coefficient does not increase with the increasing wind speed. Moreover, the asymmetry analysis suggested that the movement of storm is not the only reason for an asymmetric pattern of the hurricane wind field. In fact, this study supported the asymmetric drag coefficient theory described by Sharpiro (1980). The uniqueness of this study is that the surface data for the same hurricane were also available as it is described by the study of Powell (1982). By integrating the surface data, fields of wind divergence and vertical wind in the inner core region of Hurricane Frederic (1979) were investigated. It is worth mentioning that these vertical estimates agreed well with observed cloud water patterns and radar echo composites. Again, the reconnaissance flight data used in this study were taken at a height which is above the HBL. In addition, the reconnaissance flight was only operated at two distinct heights which mean that the vertical structure of the wind field in the HBL can not be calculated based on flight observations alone.

Due to safety concerns, few studies have tried to find wind characteristics of the HBL using the reconnaissance flight data. One exception is the CBLAST experiment. As described by Black et al. (2007), in this unprecedented experiment, specially instrumented aircraft, with an ability to fly as low as $40m$ above the sea surface, were used to obtain direct measurements within the HBL. Since this project has been carried out for several years, data accumulated in the CBLAST experiment were sufficient to calculate the vertical structure of not only the mean wind but also some turbulence parameters, such as turbulent momentum fluxes and heat fluxes, i.e. $\overline{u'w'}, \overline{v'w'}$ and $\overline{\theta'w'}, \overline{q'w'}$. As illustrated in the studies of French et al. (2007) and Drennan et al. (2007), the CBLAST data were used to calculate momentum and latent heat fluxes within the HBL. In a qualitative agreement with Powell et al. (2003), which gave the sea surface drag coefficient behaviour under high wind speed conditions based on the mean HBL wind profile measured by the dropwindsonde, momentum fluxes measured in the CBLAST experiment also showed that the drag coefficient rolls-off at high wind speeds. However, the roll-off amount and the wind speed at which the drag coefficient begins to roll-off are still uncertain. Unlike the drag coefficient which can be inferred otherwise, latent fluxes measured inthe CBLAST experiment was the first attempt to derive the humidity structure in the high wind speed region. When compared to the data collected in the Humidity Exchange of the Sea Project (HEXOS) project, Drennan et al. (2007) found that the Dalton Number in high wind speed region is not significantly different from one found in the low wind speed region. In addition, the CBLAST data were also used to derive the vertical turbulence structure of the HBL between the outer rain bands of hurricanes, as described by Zhang et al. (2009). For the first time, the vertical profile of normalized momentum fluxes, sensible heat fluxes, latent heat fluxes, and variances of three-dimensional winds were calculated with the surface wind speed in the region of $20m/s - 30m/s$. Momentum fluxes, i.e. $\overline{u'w'}, \overline{v'w'}$, calculated in the study of Zhang et al. (2009) are reproduced here for the purpose of illustration (Fig. 2.1). In addition, they analyzed the turbulent kinetic energy budget, and they found that the shear production and dissipation of turbulent kinetic energy are the major source and sink terms. Another finding of the study of Zhang et al. (2009) concerned the boundary layer height. When comparing the thermodynamic structure to the mechanical structure of the HBL, they concluded that the boundary layer height determined thermodynamically is just half of that determined by momentum fluxes. Due to the safety and instrument operation restrictions, the CBLAST experiment was mainly carried out in a heavy-rain free area outside eye-wall regions to avoid the extreme conditions under which the instruments equipped in aircraft may fail to take reliable measurements.

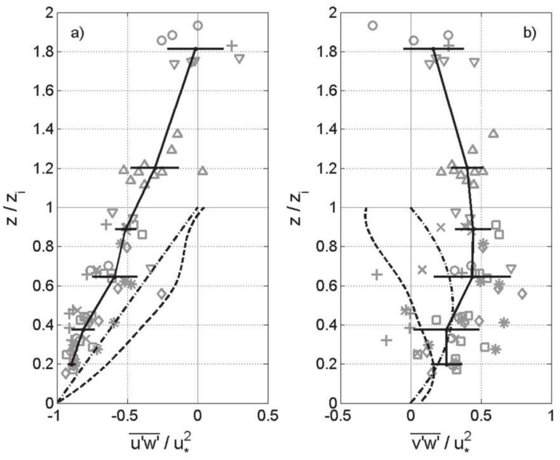

Figure 2.1: The momentum flux calculated from the CBLAST experiment in between outer rain bands of a hurricane, reproducing Fig. 4 in the study of Zhang et al. (2009). ©American Meteorological Society. Reprinted with permission.

As seen in these reviewed works, the most obvious advantage of using reconnaissance flight data in studying the wind field in the HBL is that the measurements are taken directly. Thus, it provides one of the most reliable data sources for analyzing the hurricane wind field. Moreover, the ample data accumulated for years give an opportunity to reveal the wind structure in detail. The most significant disadvantage of using such measurements is that little information about the HBL wind could be retrieved until the invention of the CBLAST experiment. Even in the CBLAST experiment, and several other low-level unmaned flight experiments currently carried out, the data gathered were still relatively scare and confined to rain-free environments.

2.1.2 Remote Sensing

As mentioned in the previous section, the major obstacles blocking observations of the wind field within the HBL are the safety considerations and instrument limitations. Remote sensing techniques provide an alternative solution. The most popular remote sensing technique presently used to get the information about the hurricane wind field is Doppler radars. Usually equipped in research aircraft, this kind of radar, like the Imaging Wind and Rain Airborne Profiler (IWRAP), is able to take high-resolution measurements of the volume backscatter reflectivity and Doppler velocity. Although this technique is essential in capturing "general" characteristics of the hurricane wind field, it does not give the hurricane wind structure in great detail.

One important study revealing the turbulence structure within hurricanes by analyzing Airborne Doppler Radar measurements was conducted by Lorsolo et al. (2010). Using the ample data collected by National Oceanic and Atmospheric Administration (NOAA) WP-3D TA radars for decades, the turbulent kinetic energy was calculated. Thanks to a relatively small radar composition beam size, $< 8km$, it is possible to estimate the sub-kilometre turbulence processes using this data. Due to the aircraft flight pattern, only two-dimensional, in the radial and vertical direction, turbulent kinetic energy profile is calculated. The reconstructed profile revealed that strongest turbulence is generally located in convective regions, such as the eye-wall, and often exceeds $15m^2/s^2$. Within the HBL, the turbulent kinetic energy is in the region of $5 - 10m^2/s^2$. Beyond the HBL, the turbulent kinetic energy sharply decreases and levels off to a small value outside the RMW. Also, a correlation study showed that the strong turbulence is generally associated with strong wind shears. Since the smallest radar data composition size is in the order of $\sim 1km$, it can be seen that the Doppler radar data used in this study was not able to describe the turbulence within a spatial scale of $\sim 1km$, and it should be considered as an relatively coarse resolution if the turbulence within the HBL is of interest.

To reevaluate some commonly held beliefs regarding the vertical structure of tropical cyclones, Stern and Nolan (2009) used a database of three-dimensional wind information measured by airborne Doppler Radars. As the storm center determined by the operational flight observations, three-dimensional velocity measured by the airborne Doppler Radar is decomposed into radial and tangential components. Based on the tangential winds retrieved, the RMW slope and M, or the angular momentum, were objectively determined. It should be noted that the RMW and M are not only functions of the radial distance from the storm center r, but also functions of the height. In detail, it is commonly believed that the RMW increase with height which forms a outwards RMW slope. In this study, the outwards slope of RMW was found to increase with radius which agrees with the commonly held belief. However, there was no evidence to support the belief that the RMW slope is related to the storm intensity. The result showed the RMW is indeed approximated by the M surface, but there is a systematical difference decreasing upwards along the RMW. Utilizing an analytical model and using results of numerical simulations, a new equation depicting the RMW slope was derived, which ideally explained why the RMW slope depends on the size of the storm but not on the intensity of the storm.

It is obvious that the most significant advantage of using remote sensing techniques, i.e. to cover a relatively large area at one "scan", also leads to its disadvantage, i.e. a relatively crude resolution in measurements. Taking into the consideration that the boundary layer height is in the order of $1km$, the wind field within the HBL is currently not resolvable based on remote sensing observations. Thus, if the wind field within HBL is of interest, remote sensing techniques are not an ideal choice.

2.1.3 In-situ Observation Over Land

In addition to observations made over the sea, observations of hurricane winds taken over land are also an important data source of direct measurements used in studying the wind field of the HBL. Unlike measurements taken above the sea by reconnaissance aircraft or by Doppler Radars, the in-situ measurement taken over land can only capture wind dynamics at several discrete points where the observational tower or mast stands. Thus, studies using the in-situ observation data concentrated on "local" HBL wind features.

As early as 1979, Sethraman (1979) tried to analyze characteristics of hurricane winds using the wind measurements taken by observational towers along the coast at the moment a hurricane passes by. By investigating the mean and fluctuating wind in the surface layer at three locations in the Long Island, N.Y. during the landfall of Hurricane Belle (1976), he found some basic wind characteristics of hurricanes making landfall, such as the significant increase of wind shears, the rough range of the friction velocity and turbulent energy dissipation rate. Besides, this study also revealed that the wind speed measured at the beach is $3-5$ times of that measured in land indicating a sharp decrease of the surface wind speed due to land friction.

In a series of studies conducted by Schroeder et al. (1998), Schroeder and Smith (2003) and Schroeder et al. (2009), meteorological data gathered when hurricanes making landfall by many mobile towers and masts deployed by several different institutes were analyzed in order to obtain hurricane wind characteristics. They focused on "local" turbulence features, such as the point gust factor, turbulence intensity and turbulent integral length scale. By analyzing these "local" features in different measuring environments, they studied the variation of such turbulence characteristics with surface roughness, with mean wind speeds, and with relative positions where the measurement is taken. The major finding of these studies is that the turbulence of the HBL is noticeably different from the turbulence in the standard ABL. More specifically, a considerable amount of turbulent energy of hurricane winds is concentrated in the region with a frequency lower than that found in ordinary ABL winds. Moreover, they concluded such turbulence characteristics strongly depend on the surface roughness, or the surface exposure, although some secondary dependencies were also presented.

Yu et al. (2008) followed the trend of using in-situ observations over land to derive turbulence characteristics of the HBL. The analysis was conducted based on the calculated wind spectra S_{uu}, co-spectra S_{uw} and turbulent integral length scale from data measured in the Florida Coastal Monitoring Program (FCMP). Different from the study of Sethraman (1979), this study utilized data from five towers during four hurricane passages. In an agreement with Schroeder and Smith (2003), they concluded that the energy at lower frequency is considerably higher in the hurricane winds than that in non-hurricane winds. The wind spectra, co-spectra and length scale derived can be used as a validation criteria in designing the novel wind tunnel facility in which the hurricane wind needs to be reproduced.

Using the data from the same measurement project, i.e. the FCMP, Yu and Chowdhury (2009) and Masters et al. (2010) extended the study of Yu et al. (2008). In addition to the spectral representation of hurricane winds, Yu and Chowdhury (2009) discussed the gust factor. Based on the FCMP data, they found that the current model is inadequate to predict the gust factor of hurricane winds over land with the surface exposure categorized as open flat terrain according to the American Society of Civil Engineers (ASCE) 7 Standard Commentary, and it is $10\% - 15\%$ higher than the gust factor found in extratropical winds. Using nine mobile observation towers in the FCMP project, Masters et al. (2010) focused on mean and turbulence characteristics of hurricane winds for three hurricanes in 2005, i.e. Hurricane Katrina, Hurricane Rita and Hurricane Wilma. Since the purpose of the study of Masters et al. (2010) was to provide inputs for structural wind tunnel tests or full-scale assessments for wind loads on structures, it contained turbulence characteristics in addition to those summarized by Yu et al. (2008), which are the friction velocity, u_*, aerodynamic roughness length z_0 and the $3-s$ gust wind velocity. Using wind statistics summarized by Masters et al. (2010), it is possible to reproduce a wind field statistically close to natural hurricane winds in a experimental environment.

It can be seen that all studies using data from in-situ observations over land are confined to analyze wind characteristics within the surface layer for only a few discrete points. It is impossible to derive the vertical structure of wind characteristics in the entire HBL from such observations. Taking into consideration that observations over land follow the conventional methodology and give sufficient measurements to derive turbulence characteristics, its result should be used to find the conventional turbulence statistics of the hurricane winds at isolated points, but not the vertical structure of the entire HBL.

2.2 Dropwindsonde Measurements

Since the dropwindsonde measurement is the major data source used in this work, this section is exclusively devoted to review studies concerning the use of the dropwindsonde. Considering that the horizontal motion of the dropwindsonde is often taken as the horizontal wind, it is necessary to gain a better understanding of th edropwindsonde motion to thoroughly understand, and then to better interpret, measurements taken by the dropwindsonde. Therefore, a series of studies analyzing the motion of objects similar to the dropwindsonde, including their responses to external wind excitations, are also reviewed. Generally speaking, studies concerning the motion and response characteristics of dropwindsonde-like objects take two branches: one is modelling the object as a point and the other is modelling the payload and parachute separately. As the basis of the dropwindsonde motion simulation which will be presented in chapter 3, both branches are reviewed in this section.

2.2.1 The GPS Dropwindsonde

Until very recently, low level flights through hurricanes have not been practicable. Therefore, research on the HBL is mainly based on other kinds of observations as summarized in section 2.1. The dropwindsonde is one commonly used technique to measure the vertical profiles of winds and other meteorological variables in a hurricane. Although the Omega dropwindsonde was used as early as the 1970's in meteorological measurement projects, only the dropwindsonde with GPS capacity is able to give measurements of the vertical profile in detail. As indicated by Franklin et al. (1996), the omega dropwindsonde is able to report its measurement at a $50mb$ interval, which is roughly $\sim 400m$ in the vertical direction, down to a height of $50mb$ above the sea surface, whereas the GPS dropwindsonde is able to report its measurement every $0.5s$, or $\sim 6m$, giving the falling speed is $12m/s$, down to the very surface of the sea.

Hock and Franklin (1999) gave a fairly comprehensive description of the National Center of Atmospheric Research (NCAR) GPS dropwindsonde, and briefly discussed the dropwindsonde motion characteristics by linearizing its motion governing equations. One useful finding in this study is that they introduced the wind finding equations which retrieve horizontal wind velocities from raw dropwindsonde measurements. A study following Hock and Franklin (1999) is that of Franklin et al. (2003), in which 620 profiles measured by dropwindsonde during 1997-1999 were composited and analyzed. This study reported that the maximum wind occurs around $500m$ above the sea surface in the eye-wall region, and the wind speed decreases above this maximum wind height. The wind velocity under this height is governed by a log-law profile. The $10m$ height wind speed found by the dropwindsonde, comparing with the reconnaissance flight measured wind speed, substantiated that the $10m$ wind reduction factor adopted by the National Hurricane Center (NHC), which on average is 0.9. The reduction factor is a empirical parameter used in the slab HBL model to calculate the $10m$ wind speed over water from the gradient wind measured by reconnaissance flight. In this study, the wind reduction factor was found differ from, and is considerably higher when compared to, that derived from previous studies which is only $0.6 - 0.8$.

Using dropwindsonde measurements, Powell et al. (2003) for the first time explored the sea surface drag coefficient behaviour in the high wind speed region. In this study, 331 wind profiles measured by the dropwindsonde for more than 2 years are processed and composited. Composition was conducted based on the mean of the measured wind speeds within the lowest $500m$. Various individual dropwindsonde wind profiles under $3000m$ are composited. The result showed that the mean wind speed logarithmically increases with height in the lower part of the HBL which indicates the log-law profile may be a good approximation of the mean wind variation in the HBL. After fitting the composited dropwindsonde measured profile to the logarithmic function, the surface stress, the roughness length and the neutral stability drag coefficient are found. This study also provided an direct evidence of the drag coefficient behaviour under high wind speed conditions. More specifically, it found that the drag coefficient levels off when wind speed exceeds $40m/s$.

Another comprehensive study based on the composition of dropwindsonde measurements was done by Vickery et al. (2009). Following the same analysis technique used by Powell et al. (2003), 896 profiles from various hurricanes from 1997 to 2003 were gathered and composited. Besides the grouping indicator used in the study of Powell et al. (2003), which is the mean of the measured wind speeds within the lowest $500m$, the radial distance of the dropwindsonde splash down location was also taken into consideration. The results showed that the wind maximum height decreases with the increasing inertial stability approaching the tropical cyclone eye. Based on this abundant data, the level-off behaviour of the drag coefficient was also examined, which substantiated the finding made by Powell et al. (2003). In addition, they found that the wind speed at which the drag coefficient starts to level off depends on the storm size. A empirical profile function was proposed from analyzing the composited dropwindsonde measurements, which have two independent model parameters controlling the profile shape. This function is repeated as,

$$U(z) = \frac{u_*}{k}\left[\ln\frac{z}{z_0} + a\left(\frac{z}{H^*}\right)\right] \tag{2.1}$$

and the comparison of the empirical profile function to the dropwindsonde observed mean wind profile is reproduced as in Fig. 2.2. Together with a land-sea transition model, this empirical profile function is able to depict the mean wind profile in the HBL under various conditions.

One recent study done based on dropwindsonde measurements is that of Zhang et al. (2011). Using the composition scheme different from that used in previous studies, such as that of Powell et al. (2003) and Vickery et al. (2009), they analyzed the characteristic height scale of the HBL by compositing dropwindsonde measurement based on the dropwindsonde splash down location relative to the storm center. Comparisons between dynamical and thermodynamical definitions of the HBL height have been conducted to reveal that the HBL height defined by the maximum wind and inflow layer depth are

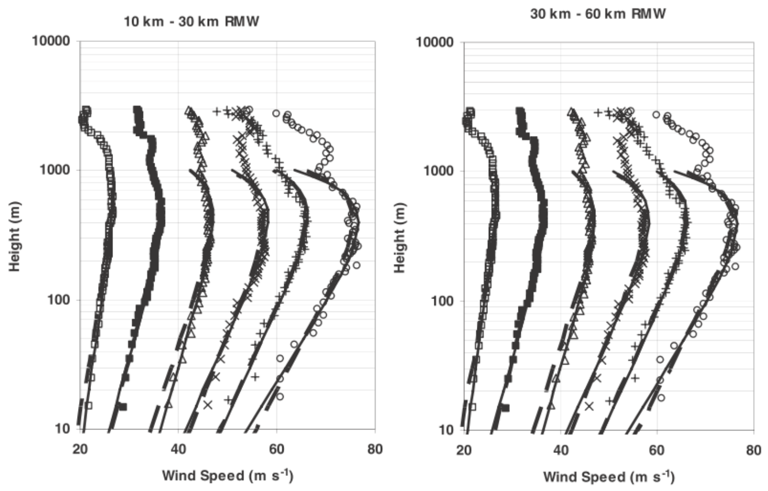

Figure 2.2: Measured wind velocity profile and the best fit result based on the profile function given, reproducing Fig. 6 in Vickery et al. (2009). ©American Meteorological Society. Reprinted with permission.

nearly twice that defined by the virtual potential temperature. However, they show the same variation shape with radius from the storm center. Unlike other definitions, the HBL height calculated using the critical Richardson number showed a different trend which may indicate the use of the bulk Richardson number to calculate the HBL height as conducted by many numerical simulation packages is questionable in simulating hurricane winds.

Besides compositing dropwindsonde measurements to get a "general" picture of the HBL wind field, researchers also use dropwindsonde measurements to reproduce the HBL wind field for particular hurricanes, like the study of Kepert (2006a) and Kepert (2006b). In these companion studies, dropwindsonde data were used to reconstruct the wind field of Hurricane George (1998) and Hurricane Mitch (1998). The main purpose of these studies is to validate the HBL wind field model proposed by Kepert (2001), which will be reviewed in the next section. In general, the dropwindsonde data demonstrated that the model gives a reasonable description of the HBL wind field. For Hurricane George, the model successfully predicted the wind-reduction factor, i.e. the ratio of the surface wind speed to the wind speed above the boundary layer, increasing inwards to the RMW, and to be larger to the left of the track than to the right. However, the super-gradient wind at upper boundary layer, which is the main feature of the model was not found in Hurricane George. It may be due to a special radial structure of Hurricane George, i.e. it has a comparably slow-decreasing wind speed with radius outside the RMW. In contrast, the strong super-gradient wind in the middle to upper boundary layer was found in Hurricane Mitch. The wind speed in Hurricane Mitch outside the RMW is decreasing much faster than that in Hurricane George, and this leads to a strong angular momentum near the RMW. Because the model proposed in Kepert (2001) gives significant super-gradient winds under this condition, the agreement actually showed that the model of Kepert (2001) is valid to depict the wind field within the HBL.

2.2.2 Motion of the GPS dropwindsonde and Similar Objects

As introduced by Hock and Franklin (1999), measurements taken by the dropwindsonde when it falls through the atmosphere are neither in a Eulerian framework nor in a perfect Lagrangian framework, therefore a proper post-processing of such measurement is needed, and such post-processing should be based on a theoretical analysis of the difference between the dropwindsonde motion, which is reported as the wind velocity, and the driving wind, which is the ”real” wind velocity. Thus, the dropwindsonde motion should be analyzed first to make a theoretical foundation for properly post-processing dropwindsonde measurements. Hock and Franklin (1999) introduced wind finding equations which are used to derive horizontal winds from measurable motion quantities of the dropwindsonde. The derivation is based on an assumption that the dropwindsonde motion can be modelled as a point translating in a Cartesian coordinate system. This assumption is widely used in analyzing the motion of vertically moving sensors. For example, the study of Scoggins (1965) discussed the response characteristics of spheres freely rising in the atmosphere based on such assumption. In this study, data measured by the balloon up to $120m$ at Huntsville, Alabama and up to $12km$ at Cape, Kennedy were reported. Although the accuracy and resolution, $\sim 600m$, of the measurement is pretty crude from present point of view, this study validated the use of such equipment to measure winds. What is useful from this study in understanding dropwindsonde measurements is its discussion of the wind measurement capacity of vertically moving sensors. Through investigating spectral characteristics of a vertical moving sensor under horizontal wind perturbations, the study concluded that a response function needs to be determined for translating "apparent" measurements to actual wind speeds. For the measurement taken by the freely rising sensor, high frequency information is not picked up and some smooth filter needs to be applied according to their analysis.

Adopting the same assumption, a systematical investigation of responsive behaviours of a rising, or falling, sphere based on its motion governing equations has been conducted by Fichtl (1971). In this study, linearized equations governing a sensor's motion subjecting to aerodynamic drags were developed. After processing the wind environment and sensor velocity through the Fourier-Stieltjes integral, the response function and phase lag were derived. The results showed that both the response function and phase lag depend on the external wind perturbation frequency and the sensor's aerodynamic properties. As expected, the sensor is capable of measuring low frequency wind perturbations while is not that responsive to high frequency wind perturbations. Moreover, the "apparent" mass, which is the mass of the ambient air affected by the sensor's motion, made the sensor responsive. At last, the analysis of the response function revealed that the sensor is more sensitive to vertical wind perturbations than to horizontal wind perturbation. Since this linearization and analysis framework is capable of thoroughly investigating responsive behaviours of a rising, or falling, object in the atmosphere, they are used to analyze the dropwindsonde behaviour as described in chapter 3.

Besides assuming the vertically moving sensors as point objects with a constant mass, an alternative way to model the motion of vertically moving parachute systems is to separate the payload from the parachute. As indicated by Cockrell (1987), which thoroughly discussed the parachute aerodynamics, two types of models can generally be formulated in analyzing a parachute system's motion. One, the parachute and payload are modelled as one rigid body; two, the parachute and payload are modelled as two separate rigid bodies with interactions. In the case of the dropwindsonde, the mass of the parachute is far less than the mass of the dropwindsonde body, and therefore can be modelled as an external force. In other words, a revised two rigid bodies model can be used to describe the motion of the dropwindsonde where the parachute is modelled as an external passive load acting on the dropwindsonde body whose direction is opposite to the relative dropwindsonde motion. It is worth mentioning that although the drag coefficient of the dropwindsonde derived from its terminal velocity given by Hock and Franklin (1999) is widely used in post-processing its wind measurement, no experiment has been conducted, as far to my knowledge, to obtain a reliable estimate of its aerodynamics under a controlled condition.

From the studies reviewed above, it can be seen that the parachute's aerodynamics are an important and challenging component of a reliable dropwindsonde motion model. Thus, aerodynamics measured in a wind tunnel test are necessary for a model to realistically depict the dropwindsonde motion. Consulting a summary of wind tunnel test methods on the parachute given by Croll et al. (1981), a wind tunnel test is conducted to measure reliable aerodynamics of the dropwindsonde. Details of the motion derivation and the wind tunnel test are given in chapter 3

Having motion characteristics similar to those of the dropwindsonde, investigations on heavy particle motions in the atmosphere sheds some lights on the motion analysis of the dropwindsonde. A series of studies by Pinsky and Khain (1996) and Khain and Pinsky (1995) described the motion simulation of heavy particles in a field with some natural turbulence features. Using motion governing equations similar to those in Pinsky and Khain (1996), chapter 3 presents a numerical simulation of the dropwindsonde motion, and their simulation methodology is followed in this simulation of the dropwindsonde motion. More specifically, they investigated the heavy particle motion through analytically analyzing and numerically integrating the motion governing equations, and this investigation approach is repeated in chapter 3 to understand the dropwindsonde motion in a wind field. Same as that in dropwindsonde motion studies, such as that of Hock and

Franklin (1999) and Fichtl (1971), their result showed that the turbulence has a great impact on the motion of heavy particles.

2.3 Modelling Study of Hurricane Wind Field

Since the modelling study of the wind field in hurricanes is critically important in not only the numerical prediction of the development of a tropical cyclone but also in the probability model for hurricane damage, it has attracted attention from researchers for decades. As the understanding of the wind field structure within the HBL progresses, its model becomes more and more realistic and accurate. In this process, it becomes clear that the turbulence model within the HBL largely determines the wind fields produced by the models. Both analytical models and numerical simulations include a turbulence parametrization since it is essential in the governing equations and is not fully solvable presently. An accurate and reliable turbulence model within the HBL is important in both modelling approaches. The influence of the turbulence model within the HBL on the overall model output seen in the previous studies is reviewed in this section, which illustrates the motivation of this work, providing suggestions for improving the turbulence model used in numerical simulations of hurricanes.

2.3.1 Analytical Model of HBL Wind Field

Companion papers by Kepert (2001) and Kepert and Wang (2001) proposed a linear analytical model, and its nonlinear numerical enhancement, to described the wind field under a symmetric gradient wind field found in tropical cyclones. In the linear theory part (Kepert, 2001), the three-dimensional governing equation were analytically solved after the equations were linearized. The solution successfully reproduced the low-level jet observed in the HBL which is absent from the slab boundary layer model. It is worth mentioning that the spectral formulation truncation, introduced by Sharpiro (1980), was also employed in this study, and only the wave number 0 and 1 are considered, which means all nonlinear interactions between wave numbers were neglected. One drawback of this linear theory is the low-level jet reproduced is weaker than observed. The results of Kepert and Wang (2001), solving the more complicated nonlinear equations using numerical techniques, showed that this may be due to the neglect of vertical advections in the linear model. The turbulence diffusivity, appeared in the governing equations, was modelled differently in the linear model and in its nonlinear numerical enhancement. The improvement of the nonlinear numerical solution seen in the Kepert and Wang (2001) has the contribution of a more realistic boundary layer turbulence diffusivity model, although the authors argued that the inclusion of vertical advections may have greater influence on the wind field produced.

Based on the work done by Kepert (2001), the study of Foster (2009) tried to extend the model to include nonlinear momentum advections and curvature terms. Using a similarity approach, this study solved the simplified Navier-Stokes equation under an axisymmetric gradient wind field. Unlike the study of Kepert (2001), which took the turbulent diffusivity as a constant throughout the entire boundary layer to linearize the model, this study tested various formulations of the turbulent diffusivity, including a polynomial and an exponential formulation. The result showed that the near surface wind characteristics, like the inflow angle, surface wind reduction factor, diffusive transportation of the kinetic energy into the surface layer and dissipational heat are sensitive to the choice of the turbulence parametrization.

2.3.2 Numerical Simulation

Another important application that the turbulence model in the HBL has great influence on is numerical simulations of hurricanes. As illustrated in the analytical model studies, the turbulence diffusivity plays a key role in the vertical mixing term that appears in the governing equations. It is also true when numerical simulations are in the play. More specifically, the turbulence model within the HBL, referred as the PBL scheme in various numerical simulation software, partially determines the vertical transportation of both the sensible heat and latent heat, and therefore determines the intensity of simulated tropical cyclones sine the warm, moist air at low altitudes is the energy source for the whole hurricane.

Many studies revealed the importance of correctly modelling the turbulence within the HBL, such as that of Bryan and Rotunno (2009). By conducting a sensitivity analysis of the hurricane intensity numerical prediction to different turbulence parametrization schemes, this study showed that it is critical to find an appropriate boundary layer turbulence model. In addition, it found that the radial turbulence weakens the radial gradient of angular momentum and entropy, which prevents the hurricane intensity from increasing. As argued by Bryan and Rotunno (2009), the simulated tropical cyclone is sensitive to the turbulence intensity in the HBL, which is, unfortunately, the most uncertain part in a numerical simulation. This study also discovered that one important factor in predicting hurricane intensity is a correct model of surface exchange processes, including momentum exchanges and moist exchanges between the atmosphere and the sea. However, it seems that the hurricane intensity is less sensitive to surface exchanges in an intense tropical cyclone than several previous studies have suggested.

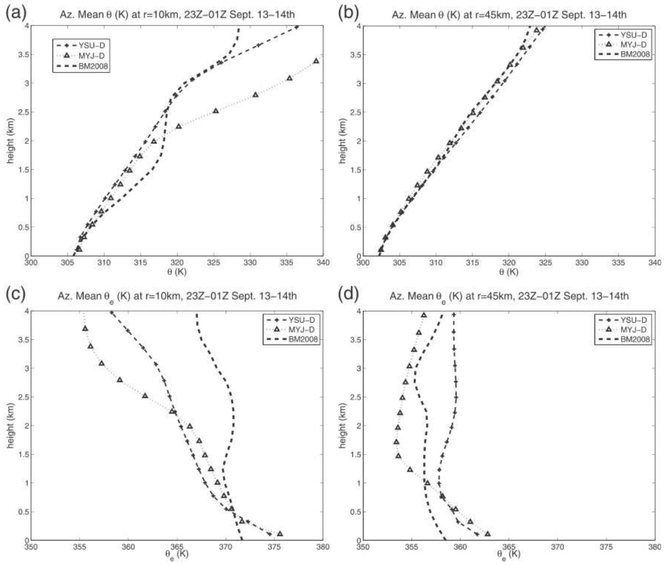

Figure 2.3: The potential temperature profile from the observation and numerical simulations with different PBL schemes, reproducing Fig.5 in Nolan et al. (2009a). ©American Meteorological Society. Reprinted with permission.

A high resolution numerical simulation of Hurricane Bob (1991) conducted by Braun and Tao (2000) also analyzed the sensitivity of the simulated hurricane wind field to the boundary layer turbulence parametrization. In this study, four different parametrization schemes are tested, and the sensitivity is seen. The pressure drop difference among different parametrization schemes is up to $16mb$ and the difference among the maximum wind velocity is up to $15m/s$. Besides the difference seen in the simulated wind fields, the precipitation distributions generated from different parametrization schemes also contained a substantial difference. By isolating the effect of vertical mixing, which is the major job of the turbulence parametrization in a numerical simulation software, from the surface flux parametrization, this study found that the simulated hurricane is more sensitive to surface fluxes than to vertical mixing, except for the Medium Range Forecast Model (MRF) model. This "non-local" turbulent mixing which transport humidity more rapidly gives a drier lower boundary layer which reduces the intensity of simulated hurricanes. Using the CBLAST data as a validation criteria, Nolan et al. (2009b) and Nolan et al. (2009a) simulated Hurricane Isabel (2003) using a series of "local" and "non-local" turbulence mixing schemes. Although neither turbulent mixing scheme is designed specially for simulating the HBL turbulence, they both produced reasonable result. "Local" schemes consistently produce larger frictional tendencies in the boundary layer than the "non-local" schemes, leading to a stronger low-level inflow and a stronger azimuthal wind maximum at the top of the boundary layer. The vertical profile of the potential temperature produced by the numerical simulations with different boundary layer turbulence schemes are repeated here for the purpose of illustration, as in Fig. 2.3.

The study of Davis and Bostart (2002) also analyzed the sensitivity of a hurricane simulation to the boundary layer turbulence modelling, but it focused on the genesis of a tropical cyclone rather than the simulation of its wind field. The sensitivity analysis is done by doing numerous numerical simulations using different cumulus parametrization, boundary layer treatments, sea surface temperatures and grid spacing. In the discussion, they came to the same conclusion as in the study of Braun and Tao (2000), which is that the "non-local" model gives a too dry and too deep boundary layer as the simulated hurricane is intensifying. Although this study did not favour the use of "non-local" schemes in simulating the genesis of hurricanes, it focused primarily on the hurricane development rate rather than the hurricane wind field, and therefore did not preclude the use of "non-local" schemes in simulating a hurricane which is already in the mature stage.

Due to the importance of the turbulence parametrization on tropical cyclone simulations, endeavours are continuously being made to propose a more accurate and realistic turbulence model. One recent study of Zhu (2008) enlightened the thought of modelling the turbulence transportation based on large eddies. Using the Large Eddy Simulation (LES) within the framework of Weather Research and Forecast Model (WRF), this study is able to derive some coherent structure of large eddies within the HBL. The simulation results supported the idea that large eddies exist in the stable environment and is able to be represented by large scale up-drafts and down-drafts. It is found that the organized up-drafts and down-drafts, or large eddies, interact with the sea surface and the entrainment at the boundary layer top, which makes the main vortex more intense than that produced by the current turbulence parametrization. This finding illustrated the need to devise a new parametrization taking into account the large eddy effect. As a beginning, it proposed a conceptual model, using statistical distribution of organized up-drafts and down-drafts revealed by the LES, which can be potentially implemented in any widely used numerical simulation package. Another pioneer study using the LES to simulate the hurricane wind is that of Rotunno et al. (2009). It described a LES simulation of an idealized tropical cyclone in a favourable environment. They discovered that the resolved turbulence exchanges with a length scale of $\sim 100m$ has a great impact on the simulated hurricane wind field. It increases the simulated turbulence gust while decreasing the mean maximum wind. Furthermore, this simulation showed noticeable differences between the resolved and parametrized turbulence, and therefore called for a further study on the small scale turbulence characteristics of the hurricane wind. It should be noted that this simulation focused on the horizontal turbulence diffusion rather than turbulent vertical mixing in the HBL, but the finding should be equally applicable in describing turbulent mixing in the HBL due to the similarity of small scale turbulence processes.

Chapter 3

Simulations of GPS Dropwindsonde Motions

Since the dropwindsonde is only able to report its own velocity, rather than the real local wind velocity, in its fall through the measured wind field, the measurement is taken in neither a conventional Eulerian framework, which requires that the measurement is taken at a fixed point, nor a perfect Lagrangian framework, which requires that the measurement is taken smoothly following the flow. The dropwindsonde motion is close to the local wind velocity, but they are not the same since the dropwindsonde is not instantaneously responsive due to its mass.

Thus, it is necessary to introduce the wind finding equations to derive wind velocities from dropwindsonde motions. Hock and Franklin (1999) introduced the currently used wind finding equations based on a brief analysis of the equations governing the dropwindsonde motion. Their equations have been widely adopted in processing dropwindsonde measurements as it is embedded in one standard processing software package named EDITSONDE. Their validity, however, has not been thoroughly evaluated. In addition, Hock and Franklin (1999) only briefly discussed the performance of their wind finding equations in reproducing the mean wind profile, but no follow-up studies have been conducted to evaluate their performance in reproducing a turbulent variable profile, such as the turbulent flux profile.

Based on a simulation of the dropwindsonde motion in a pseudo-stochastic wind field with known statistics, this study analyzed dropwindsonde motion characteristics. We focus on evaluating the wind finding equations introduced by Hock and Franklin (1999) in reproducing the vertical structure of both the mean and turbulence variables in the measured wind field. From the simulation and following analyses, the currently used wind finding equations are validated in a more thorough and systematical way. In addition, the numerical simulation also provided an opportunity to investigate various aspects of post-processing and compositing dropwindsonde measurements, which lays the foundation for revising the post-processing and composition techniques currently used to improve the interpretation of actual dropwindsonde measurements.

In order to conduct the numerical simulation described above, the dropwindsonde motion governing equations and their numerical discretization need to be analyzed. Moreover, the methodology of generating a pseudo-stochastic wind field based on given statistics also needs to be reviewed for preparing the driving wind field in the simulation. These two topics are discussed in sections 3.1 and 3.2. With these prerequisites formulated properly, the dropwindsonde motion simulation is conducted and its results are presented and discussed in section 3.3. At this point, the simulation is based on a unvalidated assumption that the dropwindsonde can be treated as a point object with a constant drag coefficient regardless of the angle of attack. To improve the dropwindsonde motion model, wind tunnel tests are then conducted to measure dropwindsonde aerodynamics and their variation with angles of attack. The wind tunnel test results, along with their configurations, are presented and discussed in section 3.4. Using the wind tunnel test results, an alternative motion model which separates the parachute from the dropwindsonde body and explicitly includes the dropwindsonde body orientation is presented in section 3.5. A numerical simulation of the dropwindsonde motion in the same pseudo-stochastic wind field, using the alternative model, is then carried out to further validate the wind finding equations and to investigate the calculation of the vertical wind from raw dropwindsonde measurements. The simulation results and a discussion on both the horizontal and vertical wind retrieval from raw dropwindsonde measurements are presented in section 3.6.

3.1 Simple Motion Model

To fully utilize its measurements, it is necessary to gain a better understanding of dropwindsonde motion characteristics which helps improve post-processing techniques used to retrieve wind velocities from raw dropwindsonde measurements. Naturally, an analysis of the dropwindsonde motion governing equations is the starting point, like in the study of Hock and Franklin (1999). Methodologies used in studies analyzing motion characteristics and measurement interpretations of rising, or falling, wind sensors are followed here. Fichtl (1971) derived a set of differential equations governing the motion of vertically moving sensors. Using a set of equations similar to those used by Fichtl (1971), Nastrom and Vanzandt (1982) investigated the rising process of a wind sensor in the atmosphere by seeking the analytical solution to the governing equations. The advanced part of this study is that the analytical solution discussed includes nonlinear responses. Although the aerodynamics of wind sensors are different from those of the dropwindsonde, their derivation and analysis shed lights on the analysis of dropwindsonde motion characteristics.

As described in the beginning of this chapter, this section covers the analysis of the dropwindsonde motion governing equations and its numerical discretization based on which a numerical integration approach can be employed to solve for dropwindsonde motion variables. Therefore, this section is divided into two subsections, the first shows the derivation of the dropwindsonde motion governing equation and the second shows the numerical approach simulating dropwindsonde motions and measurements.

3.1.1 Governing Equation of the Motion of the Dropwindsonde

When the dropwindsonde is treated as a point object falling through the atmosphere, its motions are driven by the combination of the weight force and aerodynamic forces. Furthermore, aerodynamic forces are reduced to pure drag in the point object motion model. If the drag coefficient can be modelled as a constant regardless of angles of attack, as indicated by Hock and Franklin (1999) in their derivation of the wind finding equations, the aerodynamic drag has a simple expression. Following the derivation of the motion governing equations of vertically moving wind sensors presented by Nastrom and Vanzandt (1982), this simple expression of the aerodynamic drag, when the vertical variation of the air density is neglected, is

$$\begin{aligned} F_{Dx} &= \frac{1}{2}\rho A C_D (u-\dot{x})(\sqrt{(u-\dot{x})^2+(v-\dot{y})^2+(w-\dot{z})^2}) \\ F_{Dy} &= \frac{1}{2}\rho A C_D (v-\dot{y})(\sqrt{(u-\dot{x})^2+(v-\dot{y})^2+(w-\dot{z})^2}) \\ F_{Dz} &= \frac{1}{2}\rho A C_D (w-\dot{z})(\sqrt{(u-\dot{x})^2+(v-\dot{y})^2+(w-\dot{z})^2}) \qquad (3.1) \end{aligned}$$

where F_D is the drag force in which subscripts stand for the force direction, C_D is the drag coefficient, A gives the equivalent cross-section area, and ρ gives the air density. If (x, y, z), as a vector, is used to represent the dropwindsonde position, $(\dot{x}, \dot{y}, \dot{z})$ indicates its velocity at the position (x, y, z). The vertical velocity of the dropwindsonde $\dot{z}$ is positive when the dropwindsonde goes upwards. Similarly to $(\dot{x}, \dot{y}, \dot{z})$, (u, v, w) is employed as the wind velocity vector. This point object model and its driving forces are illustrated in Fig. 3.1.

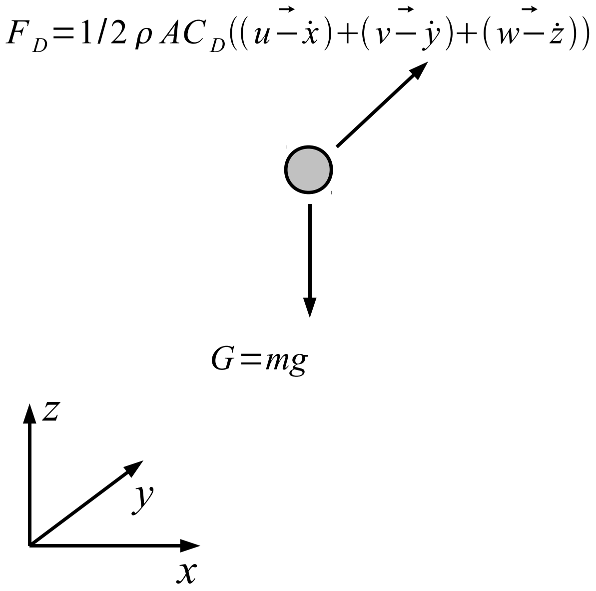

Figure 3.1: Sketch illustrating the point object model simulating the dropsonde motion and driving forces, including the weight force G and the aerodynamic drag F_D.

If the dropwindsonde weight force is modelled as $G = mg$, where m is the mass of the dropwindsonde system and g is the gravity, motions of the dropwindsonde are driven by the combination of the aerodynamic drag expressed in equation (3.1) and the weight force as,

$$m\vec{a} = \sum \vec{F} \tag{3.2}$$

Substituting the explicit expression of the aerodynamic drag and weight force into equation (3.2) gives the dropwindsonde motion governing equations, which show,

$$\begin{aligned}
m\ddot{x} &= \frac{1}{2}\rho A C_D (u - \dot{x})(\sqrt{(u-\dot{x})^2 + (v-\dot{y})^2 + (w-\dot{z})^2}) \\
m\ddot{y} &= \frac{1}{2}\rho A C_D (v - \dot{y})(\sqrt{(u-\dot{x})^2 + (v-\dot{y})^2 + (w-\dot{z})^2}) \\
m\ddot{z} &= \frac{1}{2}\rho A C_D (w - \dot{z})(\sqrt{(u-\dot{x})^2 + (v-\dot{y})^2 + (w-\dot{z})^2}) + mg
\end{aligned} \tag{3.3}$$

where $(\ddot{x}, \ddot{y}, \ddot{z})$ indicates the dropwindsonde accelerations.

Equation (3.3) is a set of nonlinear Ordinary Differential Equation (ODE)s, mainly because they contain a nonlinear term $\sqrt{(u-\dot{x})^2 + (v-\dot{y})^2 + (w-\dot{z})^2}$. If the horizontal velocity difference between the wind and dropwindsonde is far smaller than the vertical velocity difference, i.e. $(\dot{z} - w) >> (\dot{x} - u)$ and $(\dot{z} - w) >> (\dot{y} - v)$, and therefore is neglected in the square root expression, equation (3.3) can be simplified as,

$$\begin{aligned}
m\ddot{x} &= \frac{1}{2}\rho A C_D |\dot{z} - w|(u - \dot{x}) \\
m\ddot{y} &= \frac{1}{2}\rho A C_D |\dot{z} - w|(v - \dot{y}) \\
m\ddot{z} &= \frac{1}{2}\rho A C_D |\dot{z} - w|(w - \dot{z}) + mg
\end{aligned} \tag{3.4}$$

Furthermore, when the assumption is taken that the vertical wind velocity is much smaller than the dropwindsonde falling speed and is then neglected in the term $|\dot{z} - w|$, this simplified equation, equation (3.4), can be further simplified as,

$$
\begin{aligned}
m\ddot{x} &= \frac{1}{2}\rho A C_D |-\dot{z}|(u-\dot{x}) && (3.5)\\
m\ddot{y} &= \frac{1}{2}\rho A C_D |-\dot{z}|(v-\dot{y}) && (3.6)\\
m\ddot{z} &= \frac{1}{2}\rho A C_D |-\dot{z}|(w-\dot{z}) + mg && (3.7)
\end{aligned}
$$

Equations (3.5), (3.6) and (3.7) are the simplified equations governing the dropwindsonde motion which are equivalent to the wind finding equations introduced by Hock and Franklin (1999). Their apparent difference is due to that the wind finding equations include the drag coefficient implicitly in the falling rate term rather than explicitly as in equations (3.5), (3.6) and (3.7). To eliminate this explicit expression of the drag coefficient, the equation governing the dropwindsonde vertical motion is solved. More specifically, if the vertical wind is neglected in equation (3.7), the dropwindsonde falling speed is related to the drag coefficient as,

$$\dot{z}^2 = \frac{2m(g-\ddot{z})}{\rho A C_D} \tag{3.8}$$

Noticing that the quantity $(g-\ddot{z})$ should be positive for expression (3.8) to be valid, this suggests that the dropwindsonde vertical acceleration, $\ddot{z}$, should be less than the gravity acceleration, g. In the case $\ddot{z} > g$, the instantaneous dropwindsonde vertical moving speed would be expressed as,

$$\dot{z}^2 = \frac{2m(\ddot{z}-g)}{\rho A C_D} \tag{3.9}$$

which is considered very unlikely.

In addition, if the vertical motion of the dropwindsonde is assumed in equilibrium state, which indicates a steady fall of the dropwindsonde, its vertical acceleration is zero. In this case, equation (3.8) is reduced to

$$\dot{z} = -\sqrt{\frac{2mg}{\rho A C_D}} \tag{3.10}$$

Using the drag coefficient expressed in equation (3.10), the equations governing horizontal dropwindsonde motions, equations (3.5) and (3.6), can be further reduced to,

$$\ddot{x} = -\frac{g}{\dot{z}}(u - \dot{x}) \tag{3.11}$$

$$\ddot{y} = -\frac{g}{\dot{z}}(v - \dot{y}) \tag{3.12}$$

Equations (3.11) and (3.12), depicting the dropwindsonde motion in a partially linearized and simplified manner, are essentially the wind finding equations introduced by Hock and Franklin (1999) when some terms are rearranged,

$$u = -\frac{\dot{z}}{g}\ddot{x} + \dot{x} \tag{3.13}$$

$$v = -\frac{\dot{z}}{g}\ddot{y} + \dot{y} \tag{3.14}$$

In summary, the dropwindsonde motion governing equations can be partially linearized and simplified, which is also a derivation of the wind finding equations currently used, under the following conditions,

- The velocity difference between the dropwindsonde and wind in the vertical direction is much larger than that in other directions, i.e. $(\dot{z} - w) >> (\dot{x} - u)$ and $(\dot{z} - w) >> (\dot{y} - v)$.
- The vertical wind is much smaller than the dropwindsonde falling rate and can be neglected, i.e. $\dot{z} >> w$.
- The dropwindsonde vertical motion is stable and its vertical acceleration is zero.
- The drag coefficient can be modelled as a constant, independent from the dropwindsonde body orientation, and the variation of the air density can be neglected

in dropwindsonde falls.

In addition, for equations (3.13) and (3.14), it is possible to derive analytical solutions since they are linear ODEs. Appendix A (page 206) details the derivation of these analytical solutions and discusses dropwindsonde response characteristics based on these analytical solutions.

From the simplification shown above, it is obvious that equations (3.11) and (3.12) can only depict the dropwindsonde motion in a steady fall. Thus, they will not be valid when the local wind driving the dropwindsonde dramatically changes its magnitude or direction. In other words, the simplified equations, and therefore the wind finding equations, may not be valid if the dropwindsonde reports dramatic vertical wind velocity changes. As indicated by Aberson et al. (2006), the dropwindsonde may encounter local extreme winds when it is released around an eye-wall. In this case, the dropwindsonde may be suspended, or even ascend, due to vertical winds pointing upwards, which means the vertical wind is not negligible in equation (3.7). The horizontal velocity difference, however, still remains small due to the strong driving force of local extreme winds. In this case, the simplified equations are not valid, but the conditions for the partial linearization are still satisfied. Moreover, the drag force equation, equation (3.8), which is derived from the partially linearized motion equation in the vertical direction, is also valid with some minor changes and can be rewritten as,

$$(w - \dot{z})^2 = \frac{2m(g - \ddot{z})}{\rho A C_D} \tag{3.15}$$

When the vertical dropwindsonde acceleration in equation (3.15) is neglected, which indicates the vertical motion of the dropwindsonde is in an equilibrium state, moving either upwards or downwards, equation (3.15) can be simplified as,

$$|w - \dot{z}| = \sqrt{\frac{2mg}{\rho A C_D}} \tag{3.16}$$

Substituting equation (3.16) into the linearized motion equations, equation (3.4), and rearranging gives,

$$u = -\frac{w}{g}\ddot{x} + \frac{\dot{z}}{g}\ddot{x} + \dot{x} \tag{3.17}$$

$$v = -\frac{w}{g}\ddot{y} + \frac{\dot{z}}{g}\ddot{y} + \dot{y} \tag{3.18}$$

for the case $\dot{z} > w$, in which the dropwindsonde moves upwards in an updraft, or

$$u = \frac{w}{g}\ddot{x} - \frac{\dot{z}}{g}\ddot{x} + \dot{x} \tag{3.19}$$

$$v = \frac{w}{g}\ddot{y} - \frac{\dot{z}}{g}\ddot{y} + \dot{y} \tag{3.20}$$

for the case $w > \dot{z}$, in which the dropwindsonde moves downwards with non-negligible vertical winds.

When compared to the simplified motion governing equations (3.13) and (3.14), equations (3.19) and (3.20) have one additional term, w/g, to account for the vertical wind influence on dropwindsonde motions.

3.1.2 Simulation and Post-processing Methodology

As discussed above, the dropwindsonde motion is governed by equation (3.3), and its motion is fully described by solutions to this equation. Obviously, the understanding of dropwindsonde motion characteristics should include knowledge gained from an analysis of these solutions. The theoretical analysis based on the analytical solutions to the linearized governing equations, which is presented in appendix A in detail (see page 206), shows that the dropwindsonde hardly responds to high frequency horizontal wind perturbations and its lag increases with frequency. Although this finding reveals one fairly important dropwindsonde motion characteristic, which influences its turbulence measurement significantly, it is found by analyzing the linearized motion governing equations. Therefore, it is necessary to analyze the solutions to the full nonlinear equations in order to validate these findings. However, equation (3.3) is not analytically solvable, and a numerical approach needs to be taken to find its solution. In addition, considering that the numerical solutions describing the dropwindsonde velocities are essentially raw wind measurements from the dropwindsonde, finding the numerical solutions under the condition that the driving wind is statistically close to natural winds gives a chance to investigate dropwindsonde measurements processing and composition techniques realistically. Although the wind field simulation will be detailed in section 3.2, the following description assumes the required pseudo-stochastic wind field is generated beforehand.

Since equation (3.3) is a set of typical ODEs, the fourth-order Runge-Kutta method is appropriate to numerically integrate it. Since the actual dropwindsonde sampling interval is $0.5s$, the time step used in numerical simulation takes the value of $0.05s$ to ensure an adequate sampling database for post-processing dropwindsonde simulation results. As indicated by the analytical solution to linearized dropwindsonde motion governing equation as detailed in appendix A, the dropwindsonde velocity captures the driving wind velocity quickly, as an exponential function of time, after it is released. Therefore, the initial condition affects simulated dropwindsonde motion for only a few seconds. In this simulation, the initial condition assumes that the dropwindsonde is immobile at the releasing moment. Although the total height of the pseudo-stochastic wind field is $600m$, the dropwindsonde is assumed to be released at $580m$, which gives the dropwindsonde a stable fall since it may occasionally move upwards at the very beginning of the simulation. Other parameters needed in the simulation are the constants that appears in equation (3.3), such as the drag coefficient and air density. These constants are calculated such that the terminal falling speed of the dropwindsonde is $-12m/s$ in steady air. As for the driving wind velocity that appears in the motion governing equations, (u, v, w), it is calculated based on the generated pseudo-stochastic wind field. After the numerical integration configuration and parameters are determined, the dropwindsonde motion is simulated by numerically solving the governing equations. Both dropwindsonde accelerations and velocities are directly solved until the simulated dropwindsonde reaches the bottom of the pseudo-stochastic wind field. The dropwindsonde position, however, is not directly generated in the simulation, and the solved dropwindsonde velocities are numerically integrated to recover it. After the motion variables of the dropwindsonde are directly solved, pseudo measurements are sampled from the solved dropwindsonde heights, velocities and accelerations at a frequency of $2Hz$. Figure 3.2 shows one simulated dropwindsonde drop including the directly solved dropwindsonde velocity, the "correct" wind velocity calculated using the wind finding equations introduced by Hock and Franklin (1999) and the driving wind velocity interpolated from the known pseudo-stochastic wind field.

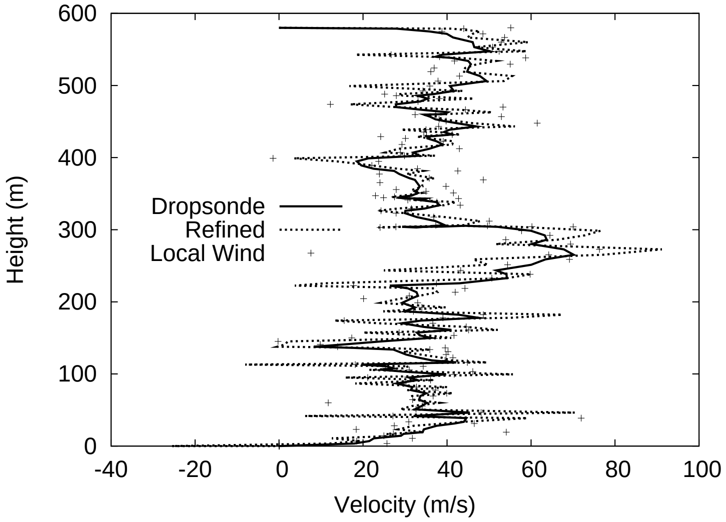

Figure 3.2: Velocity profile from one simulated dropwindsonde drop, where "Dropsonde" equals the velocity solved in the simulation, "Refined" equals the velocity dynamically corrected using the wind finding equation and "Local wind" equals the wind velocity interpolated from the known pseudo-stochastic wind field.

To simulate the measurement error buried in raw dropwindsonde measurements, a series of independent random variables are added to the solved velocities. Since they are independent, they act like a background white noise. In the raw dropwindsonde document kept by the Hurricane Research Division (HRD), there is a wind error column indicate the magnitude of the measurement error buried in the actual dropwindsonde wind measurements. After statistically analyzing this wind error record using various random variable distribution models, it has been found that the amplitude of the wind error record follows a log-normal distribution. The parameters determining the log-normal distribution shape are calculated from a statistical distribution model fit as shown in

Fig. 3.3. The sampling database for this model fit is the wind error records taken for hurricanes occurred in 2009, including Hurricane Danny, Hurricane Erika and Hurricane Ida. The model fit results show the log-normal distribution parameters are $\mu = -1.00934$ and $\sigma = 0.76032$. Since the wind error record kept in raw dropwindsonde measurement documentation only indicates the magnitude of the measurement error and no information is available to indicate whether the dropwindsonde measurement overestimates or underestimates the true wind velocity, one uniformly distributed random variable, in a range $[-1, 1]$, is used to determine if the log-normally distributed random variable is enhancing or reducing pseudo raw dropwindsonde measurements of the absolute wind velocity.

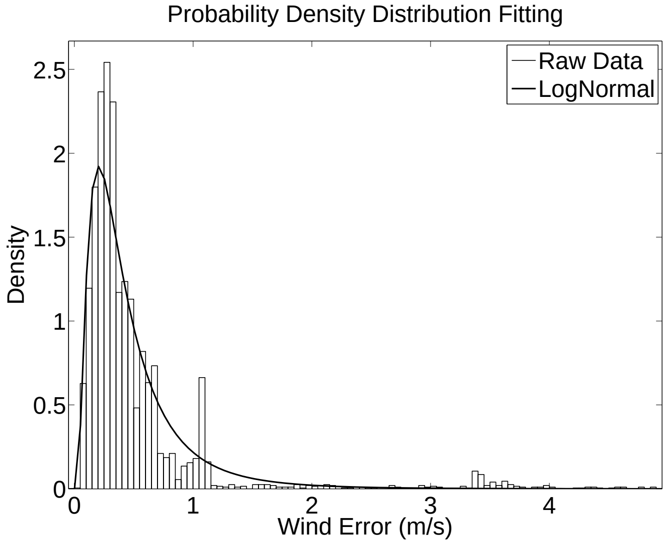

Figure 3.3: Random error distribution fitting, where the "raw data" displayed in bars are the wind error binned, the line represents the fitting curve for the log-normal distribution.

After the pseudo measurements are sampled from the numerical solutions and the simulated measurement errors are added, they are ready to be post-processed and composited to derive statistics of the measured wind field. The post-processing is done in two steps and the composition is done in three steps. Since the post-processing and composition are the subjects of the following investigation, they are articulated in detail in the following paragraphs.

First, the pseudo measurements are dynamically corrected through the wind finding equations introduced by Hock and Franklin (1999). The correction requires the acceleration and falling rate of the dropwindsonde. Currently, the acceleration is not directly reported by the instrument but must be calculated by differentiating the dropwindsonde velocity. In some cases, the falling rate directly measured by the dropwindsonde is considered unreliable and therefore is calculated indirectly by differentiating dropwindsonde height measurements. In these cases, the differentiation scheme used to calculate the acceleration and falling rate of the dropwindsonde determines, to some extent, outcomes of the wind finding equations. According to the EDITSONDE source code (J. L. Franklin 2011, Personal communication), the first-order backwards difference is currently employed without any further validations. Given the importance of the finite difference scheme in retrieving horizontal winds from raw dropwindsonde measurements using the wind finding equations, it is worth evaluating various finite difference schemes other than the first-order backwards difference. In this study, the first- and second-order, backwards, forwards and central finite difference schemes are employed in calculating the required dropwindsonde accelerations. The composition results, calculated based on different differentiation schemes evaluated, are then compared to the statistics calculated from the known pseudo-stochastic wind field. Provided that the statistics calculated directly from the pseudo-stochastic wind field represent the "true" values, the influence of differentiation schemes can be reliably evaluated.

After dropwindsonde measurements are corrected using the wind finding equations, pseudo dropwindsonde profiles, made up by the pseudo dropwindsonde measurements from one simulated dropwindsonde drop, are smoothed using a low-pass filter. When compared to differentiation schemes, low-pass filter designs attract even less attentions from researchers. Since there are unavoidable measurement errors buried in dropwindsonde measurements, such as those introduced by the dropwindsonde body oscillation due to its interaction with the parachute through the rope connecting the dropwindsonde body and the parachute. In previous studies, a low-pass filter with a $5-s$ cut-off time scale has been employed without any further specifications (Franklin et al., 2003;

Vickery et al., 2009). It is obvious that the filter characteristics impact the composition results of dropwindsonde measurements, especially when the turbulence information is of interest. To understand the influence of the low-pass filter design on statistics derived from dropwindsonde measurements, simple moving average filters and Butterworth filters with different cut-off time scales are used in post-processing pseudo dropwindsonde measurements.

After filtering, pseudo dropwindsonde profiles are composited to produce statistics of the measured wind field. More specifically about the composition, it is an "average process" that calculates a representative profile out of numerous wind velocity profile measured by different simulated dropwindsonde drops. Therefore, numerous pseudo dropwindsonde wind profiles need to be generated first by assuming the dropwindsonde is released at different moments. In order to evenly reflect statistical characteristics of the measured wind field, the releasing moments are generated by a uniformly distributed random variable in the range of the time length of the pseudo-stochastic wind field. Once the composition database, containing numerous pseudo dropwindsonde profiles, is set up, the composition is done in three steps following the methodology provided by Powell et al. (2003). First, the pseudo-stochastic wind field is discretized vertically with equal space into 100 height bins. Second, an individual pseudo dropwindsonde profile is segmented into these height bins according to single pseudo measurement heights. Third, all pseudo measurements within one height bin from numerous pseudo dropwindsonde profiles are weighted-averaged to produce the result, which can be recognized as the desired statistic at the center of the height bin. The weight of each pseudo measurement point is assigned according to the distance from the measurement height to the center of the height bin, varying linearly from 1, at the center of the bin, to 0, at the boundary of the bin. The composited mean wind profile is calculated as the weighted mean of raw pseudo measurements, and the turbulent wind velocity is calculated after the mean profile is subtracted. In an attempt to quantify the data size sufficient to produce statistically meaningful results, composition is conducted based on databases containing different number of pseudo dropwindsonde profiles.

3.2 Wind Field Simulation

As introduced in section 3.1, simulating dropwindsonde motions in a pseudo-stochastic wind field statistically close to natural winds is essential to ensure that the motion simulation results are applicable to understand actual dropwindsonde motions and measurements. The generation of such a pseudo-stochastic wind field is presented in this section. As it is widely used in the wind engineering field, various numerical techniques have been developed to generate such a field. For example, as summarized by Solari et al. (2007) and Carassale et al. (2007), the Proper Orthogonal Decomposition (POD) technique can be used, which requires a conventional spectrum matrix to describe all second-order spectral statistics of the target stochastic wind field. Besides, procedures described by Mann (1998) are also available to transform a spectral tensor into a pseudo-stochastic field with required statistics. The spectral tensor, which describes the spectral representation of the target stochastic field uniformly in three spatial directions, gives the chance to explore the possibility of extracting spectral information of the measured wind field from dropwindsonde measurements.

3.2.1 POD simulation

In this stimulation, statistical characteristics of the target pseudo-stochastic wind field rely only on the formulation of the spectrum matrix which contains expressions of wind spectra S_{uu}, S_{vv}, S_{ww} and co-spectra S_{uw}, S_{vw}, S_{uv} for all points in the target pseudo-stochastic wind field. In detail, the spectrum matrix is formulated based on three spectral descriptions, point wind spectra S_{uu}, S_{vv}, S_{ww}, spatial correlation coefficients used to calculate co-spectra of wind velocities at two points and point cohesion coefficients used to calculated point co-spectra S_{uw}, S_{vw}, S_{uv}. In this study, the spectrum matrix is formulated based on point wind spectra described by Von Karman (1948), which is also known as the "Karman spectrum", an exponential decay model of the spatial correlation coefficients following Solari and Piccardo (2001), which is an extension of the model provided by Davenport (1967), and a point cohesion coefficient model given by Solari and Piccardo (2001). Since these models are commonly used to describe spectral statistics of a natural wind field, the generated pseudo-stochastic field can be recognized as a good numerical, stochastic replica of the natural wind field. In calculating the spatial correlation coefficients, the simple model which relates the decay of the spatial correlation directly to the distance between two given points is used and the constants governing the decay rate are taken from the study of Davenport (1967), which are 10 for the longitudinal wind, 6.5 for the lateral wind and 3 for the vertical wind. Although this formulation is not entirely correct, especially for the spatial correlation decay of lateral and vertical winds, it is good enough to provide a driving force in the dropwindsonde motion simulation.

More specially in formulating the spectrum matrix used in the POD simulation, a 3×3 matrix is used to summarize the spectral statistics of a single point in the target pseudo-stochastic wind field. The matrix is shown as,

$$S_{ii} = \begin{bmatrix} s_{uu'}(\omega), s_{uv'}(\omega), s_{uw'}(\omega) \\ s_{vu'}(\omega), s_{vv'}(\omega), s_{vw'}(\omega) \\ s_{wu'}(\omega), s_{wv'}(\omega), s_{ww'}(\omega) \end{bmatrix} \tag{3.21}$$

In expression (3.21), $S_{uu'}(\omega), S_{vv'}\omega, S_{ww'}(\omega)$ are power spectral density expressions of longitudinal, lateral and vertical winds and ω is the frequency in the unit of $radians$, while $S_{uw'}(\omega), S_{vw'}(\omega), S_{uv'}(\omega)$ are co-spectra of the three wind components. Using expression (3.21) to calculate spectral wind characteristics at a single point, the spatial co-spectra between given two given point i and j can be expressed as,

$$S_{ij} = S_{ii} \times S_{jj} \times \Lambda_{i,j}(\omega) \tag{3.22}$$

In expression (3.22), S_{ii} and S_{jj} are calculated according to the definition shown in expression (3.21) and $\Lambda_{i,j}(\omega)$ is the spatial correlation correlation calculated according to the exponential decay model using the distance between point i and j. After matrices S_{ii} and S_{ij} are formulated, the whole spectrum matrix describing the spectral wind characteristics of the target pseudo-stochastic wind field can be expressed as,

$$S(\omega) = \begin{bmatrix} S_{11} & \cdots & S_{iN} \\ \vdots & \ddots & \vdots \\ S_{N1} & \cdots & S_{NN} \end{bmatrix} \tag{3.23}$$

in the case that the target pseudo-stochastic wind field contains N single points. It should be noted that in expression (3.21), S is a matrix containing $3N \times 3N$ elements, and every element is a function of the frequency ω.

In the POD simulation, the target pseudo-stochastic wind field is generated by decomposing the spectrum matrix, as shown in equation (3.23), and modulating the decomposed matrix with random phases. This is done in three steps. Firstly, the spectrum matrix is decomposed. Secondly, since elements in the decomposed matrix, as functions of frequency, depict the magnitude of periodic variations constituting the target pseudo-stochastic field, they can be multiplied by a set of independent random processes with unit magnitude to form the basis which define a vector space in frequency domain. Thirdly, the linear space basis formulated in frequency domain are transformed by the Discrete Fourier Transformation to generate the target stochastic field.

To simplify the pseudo-stochastic field generation without sacrificing its validity, the target stochastic field is assumed to be uniform in both longitudinal and lateral directions, and Taylor's hypothesis is invoked to transfer wind velocity time histories to longitudinal wind variations. As for the configuration of the numerical generation, 120 points are formulated in the vertical direction and wind velocity time histories are generated for every point. The time step in the wind velocity time history generated is 0.1 second and the height step is 5 meters, giving the a time length of 1.8 hours and a total height of 600 meters. In addition, the logarithmic profile is used to describe the mean wind structure and the generated pseudo-stochastic field, representing the turbulence, is superimposed onto the mean wind structure.

To validate that the generated pseudo-stochastic wind field has the required statistics, it is necessary to compare the statistics calculated directly from the generated field with

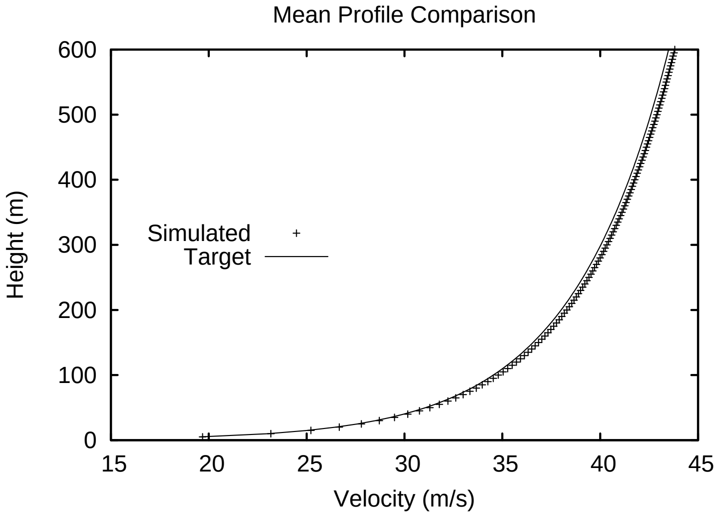

Figure 3.4: Mean velocity profile comparison, where target means the preset value and simulate means statistical profile averaged by velocities sampled in the simulated wind field.

those preset in the spectrum matrix. The mean profile comparison is shown in Fig. 3.4 while the turbulence intensity and turbulent shear stress profile comparisons are shown in Fig. 3.5. Longitudinal wind spectra and point cohesion coefficients, calculated using longitudinal and vertical winds, are compared in Fig. 3.6. It is obvious that the spectral information calculated from the generated pseudo-stochastic wind field is in reasonable agreement with their preset values. In summary, the pseudo-stochastic wind field generated using the POD technique is a good stochastic realization of the preset statistics, in terms of both the overall vertical turbulence structure and point spectral statistics.

3.2.2 Spectral tensor model

As for simulating the wind field using the spectral tensor model, both the model itself and simulation procedures are described by Mann (1998). A more comprehensive study on the spectral model is presented by Mann (1994). Unlike the spectrum matrix, the spectral tensor is essentially a 3 × 3 matrix, which shows,

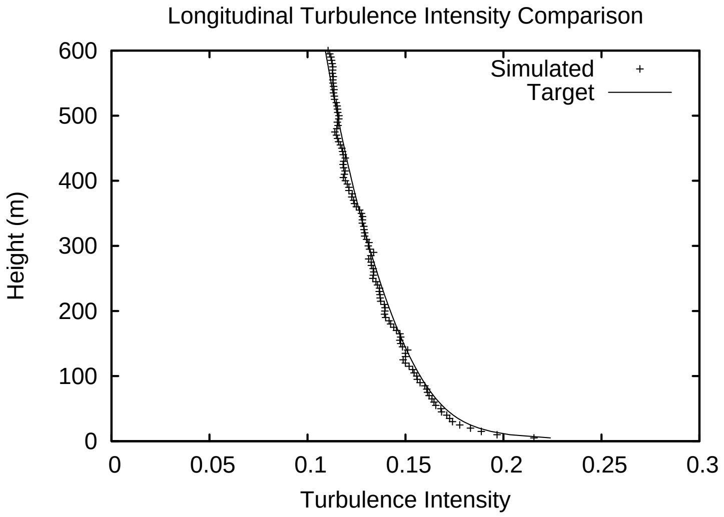

(a) Turbulence Intensity Profile

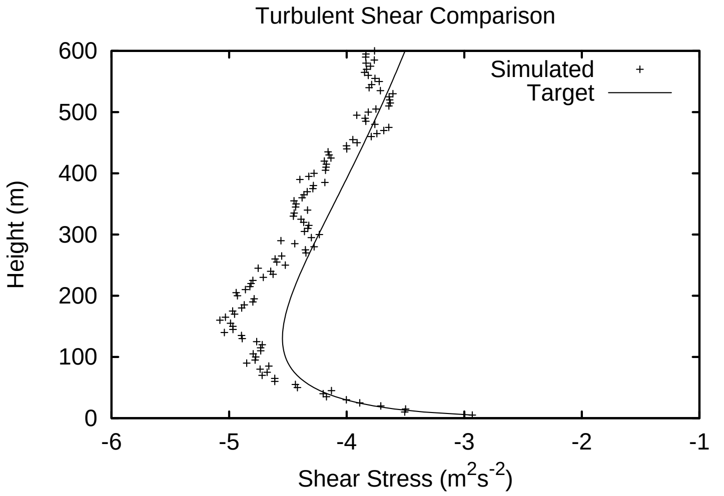

(b) Turbulent Shear Profile

Figure 3.5: Longitudinal turbulence intensity, UW turbulent shear profile comparison, where target means preset value while simulated means statistical profile calculated by averaging values sampled from the simulated wind field.

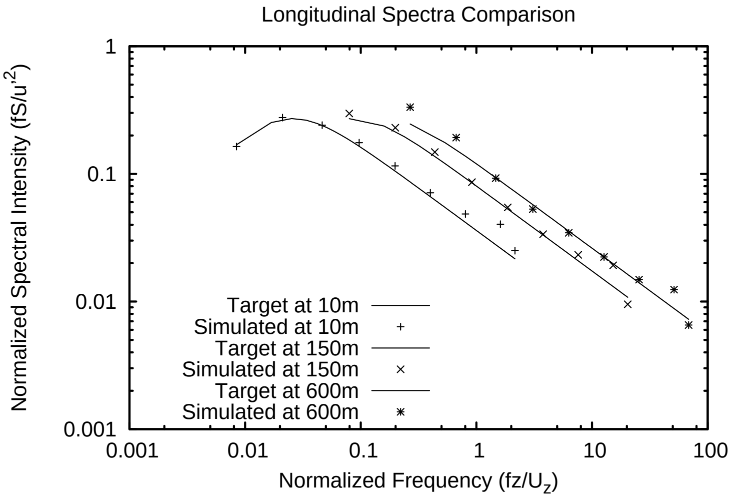

(a) Spectral Density

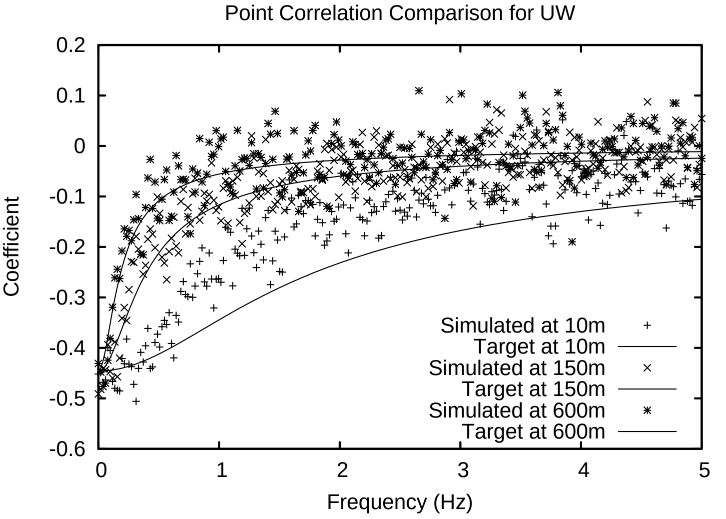

(b) Point Correlation Coefficient

Figure 3.6: Spectral density for longitudinal wind and cross spectral density for longitudinal and vertical winds comparison, where target means preset value while simulated means spectrum calculated by values sampled from simulated wind field.

$$T(k_1,k_2,k_3) = \begin{bmatrix} t_{uu}(k_1,k_2,k_3) & t_{uv}(k_1,k_2,k_3) & t_{uw}(k_1,k_2,k_3) \\ t_{uv}(k_1,k_2,k_3) & t_{vv}(k_1,k_2,k_3) & t_{vw}(k_1,k_2,k_3) \\ t_{uw}(k_1,k_2,k_3) & t_{vw}(k_1,k_2,k_3) & t_{ww}(k_1,k_2,k_3) \end{bmatrix} \tag{3.24}$$

Each element in matrix (3.24) is a function of the wave number vector $\vec{k} = (k_1, k_2, k_3)$, and therefore describes either the power spectral density, for elements t_{uu}, t_{vv} and t_{ww}, or the co-spectra, for elements t_{uv}, t_{vw} and t_{uw}, of the target stochastic field. It should be noted that physical meanings of the power spectral density and co-spectra are slightly different from their conventional definitions. In expression (3.24), t_{uu}, t_{vv}, t_{ww} describes the turbulent kinetic energy distribution in three wave number space directions k_1, k_2, k_3, and co-spectra t_{uv}, t_{uw}, t_{vw} describes the spectral correlations of three wind components in three wave number space directions k_1, k_2, k_3. In a comparison with the spectrum matrix formulation, calculations of the spectral tensor are relatively easy since only one calculation is needed for each of the six independent elements in matrix (3.24) to depict the entire pseudo-stochastic field. Details of calculations can be found in the study of Mann (1998), and a brief summary is given here. Each of elements used in equation (3.24) is derived from its counterpart appeared in the Von Karman isotropic turbulence model (Von Karman, 1948) and calculated based on the Von Karman turbulence kinetic energy expression,

$$E(k) = \alpha\epsilon^{2/3} L^{5/3} \frac{(Lk)^4}{(1+(Lk)^2)^{\frac{17}{6}}} \tag{3.25}$$

In expression (3.25), $E(k)$ depicts the turbulent kinetic energy distribution, α is an empirical constant which takes the value of 1.7, ϵ is the viscous dissipation of the turbulent kinetic energy and L gives a turbulence length scale. In the spectral tensor model based wind field simulation, L is calculated as $L = 0.87z$ following Mann (1998) where z takes the value of the midpoint height in the target pseudo-stochastic wind field. Using the turbulent kinetic energy expressed in equation (3.25), the spectral tensor shows,

$$\begin{aligned}
t_{uu} &= \frac{E(k_0)}{4\pi k_0^4}[k_0^2 - k_1^2 - 2k_1k_{30}\zeta_1 + (k_1^2 + k_2^2)\zeta_1^2] \\
t_{vv} &= \frac{E(k_0)}{4\pi k_0^4}[k_0^2 - k_2^2 - 2k_2k_{30}\zeta_2 + (k_1^2 + k_2^2)\zeta_2^2] \\
t_{ww} &= \frac{E(k_0)}{4\pi k^4}(k_1^2 + k_2^2) \\
t_{uv} &= \frac{E(k_0)}{4\pi k_0^4}[-k_1k_2 - k_1k_{30}\zeta_2 - k_2k_{30}\zeta_1 + (k_1^2 + k_2^2)\zeta_1\zeta_2] \\
t_{uw} &= \frac{E(k_0)}{4\pi k_0^2 k^2}(-k_1k_{30} + (k_1^2 + k_2^2)\zeta_1) \\
t_{vw} &= \frac{E(k_0)}{4\pi k_0^2 k^2}(-k_2k_{30} + (k_1^2 + k_2^2)\zeta_2) \qquad (3.26)
\end{aligned}$$

In expression (3.26), the calculation at the wave number vector $\vec{k} = (k_1, k_2, k_3)$ is based on its counterpart in the isotropic tensor model $\vec{k_0} = (k_1, k_2, k_{30})$, and their relationship is calculated as,

$$\begin{aligned}
k_3 &= k_{30} - k_1\beta \\
\beta &= \Gamma dU/dz(kL)^{-3/5} \qquad (3.27)
\end{aligned}$$

in which Γ is a model parameter which takes the value of 3.2 and dU/dz is the mean wind profile derivative. In expression (3.26), there are two parameters need to be determined, ζ_1 and ζ_2. In the model proposed by Mann (1994), they are expressed as,

$$\begin{aligned}
\zeta_1 &= \left[C_1 - \frac{k_2}{k_1}C_2\right] \\
\zeta_2 &= \left[\frac{k_2}{k_1}C_1 + C_2\right] \qquad (3.28)
\end{aligned}$$

in which parameters C_1 and C_2 are determined as,

$$\begin{aligned} C_1 &= \frac{\beta k_1^2(k_0^2 - 2k_{30}^2 + \beta k_1 k_{30})}{k^2(k_1^2 + k_2^2)} \\ C_2 &= \frac{k_2 k_0^2}{(k_1^2 + k_2^2)^{3/2}} \arctan\left[\frac{\beta k_1(k_1^2 + k_2^2)^{1/2}}{k_0^2 - k_{30}k_1\beta}\right] \end{aligned} \tag{3.29}$$

In expressions shown above, k stands for the magnitude of the wave number vector and is calculated as $k = \sqrt{k_1^2 + k_2^2 + k_3^2}$ while k_0 stands for the magnitude of corresponding wave number vector in isotropic turbulence model which is calculated as $k_0 = \sqrt{k_1^2 + k_2^2 + k_{30}^2}$.

After the spectral tensor is formulated as described above, the target pseudo-stochastic wind field is generated following the same methodology employed in the POD simulation. The only noticeable difference is that the Discrete Fourier Transformation used in this case is three dimensional since elements in the spectral tensor matrix, expression (3.24), are all three-dimensional functions, which leads to their decomposed results being also three-dimensional functions. In this field, measuring the wind velocity in the vertical direction is not fundamentally different from measuring it in the longitudinal direction, which means the velocity series documented by the dropwindsonde is capable to derive spectral information of the measured wind field.

As for the configuration of the pseudo-stochastic field generation, since the spectral tensor is formulated in the wave number space and no frequency is involved, the generated pseudo-stochastic field contains only spatial information. As a result, only a "snapshot", without any time evolution, of the target pseudo-stochastic field can be generated based on the spectral tensor. As in the POD simulated wind field, Taylor's hypothesis is invoked to transfer longitudinal wind velocity series back to time histories when the wind velocity at a moment other than the "freeze" moment is required in the dropwindsonde motion simulation. In addition, as in the the POD simulated wind field, the lateral wind speed variation is neglected. 128 points in the vertical direction 65536 points in the longitudinal direction are used to generated the discrete pseudo-stochastic wind field. Given that the longitudinal spatial step and the vertical spatial step is 0.1 meters and 4.6875 meters respectively, the total length of the pseudo-stochastic wind field is 6.5 km while the total height remains the same, which is 600 m.

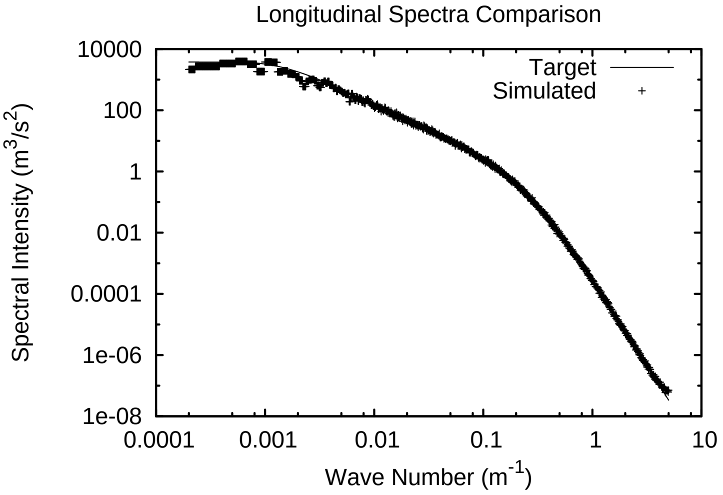

(a) Spectral Density

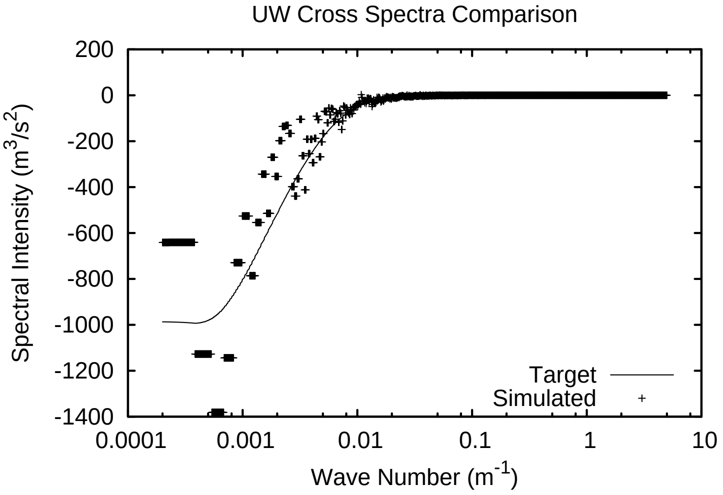

(b) Cross Spectral Density

Figure 3.7: Spectral density comparison for longitudinal wind, where target means preset value while simulated means spectrum measured from simulated wind field.

As in the wind field simulation using the POD simulation, to ensure that the pseudo-stochastic wind field has the required statistics, it is necessary to compare the statistics calculated directly from the generated pseudo-stochastic wind field to their preset values used to formulate the spectral tensor. However, comparisons in this simulation are concentrated on the spectral statistics of the pseudo-stochastic field since it is the main reason to use the spectral tensor model. The comparisons of the longitudinal wind spectrum and cross spectrum of the longitudinal and vertical wind are shown in Fig. 3.7. Obvious in these figures, although there is a pronounced difference in the very low wave number region in the comparison shown in Fig. 3.7(b), the calculated and preset spectra are in reasonable agreement in a large portion of comparisons, and the difference can be explained by the scarcity of pseudo wind velocities in the region where generated and preset spectra show different values. Besides, wind velocities separated by such a distance, $\sim 1000m$, are usually assumed to be uncorrelated. In conclusion, the pseudo-stochastic wind field simulated through the spectral tensor approach is suitable in exploring the possibility of extracting spectral information of the measured wind field from raw dropwindsonde measurements.

3.3 Simple Model Simulation Results and Discussions

Adopting the simulation procedures and numerically generated pseudo-stochastic wind fields, which are detailed in sections 3.1 and 3.2 respectively, the dropwindsonde motion is simulated by numerically solving the motion governing equations, and then the pseudo measurements are sampled from numerically solved dropwindsonde motion variables. Afterwards, these pseudo measurements are post-processed and composited to produce statistics of the measured wind field as if they were actual dropwindsonde measurements. Considering that the statistics are also derived from the generated pseudo-stochastic wind fields, comparisons of statistics derived differently provide a unique opportunity to investigate various aspects of post-processing and compositing dropwindsonde measurements, which include the validity of the wind finding equations, the finite difference schemes used to calculate the dropwindsonde acceleration required by the wind finding equations, the low-pass filter to smooth individual dropwindsonde profiles, the composition data size sufficient to derive statistically meaningful results, the gust time scale of the dropwindsonde wind measurement and the wind spectrum derived from dropwindsonde documented wind velocity series. Discussions based on the simulation results are presented in the following subsections in the order described above. It should be noted that except for the analysis of the composition data size, statistics of the measured wind field are derived by compositing 1000 pseudo dropwindsonde profiles.

3.3.1 Validity of The Wind Finding Equation

As shown in Fig. 3.2, the wind finding equations make the "corrected" wind velocity closer to the "true" wind velocity interpolated from the pseudo-stochastic wind field than the estimates made using the dropwindsonde velocity alone, especially in the area where the wind velocity varies significantly with height. In addition to individual dropwindsonde profiles, the wind finding equations also influence composition results. Its influence on reconstructing the mean profile is shown in Fig. 3.8. Obviously, the dynamic correction term in the wind finding equations is essential to reduce the difference between the profile measured by the dropwindsonde and the "true" wind in a sheared wind field. This substantiates the finding made by Hock and Franklin (1999) in their discussion on the effectiveness of the wind finding equations in which they argued that the lag effect of fast falling objects would account for such a difference and the dropwindsonde acceleration helps to correct this lag effect. Due to the vertical resolution of the composition, the residual error discussed by Hock and Franklin (1999) is not entirely resolvable in the comparison, and therefore is not shown in Fig. 3.8. Besides, the residual error, which is theoretically left over by the wind finding equation, is only pronounced in the lowest $\sim 5m$ of the boundary layer as indicated by Hock and Franklin (1999) (see their Fig. 9). Thus, this unresolved residual error is not important since the wind behaviour in that region is not expected to be found by dropwindsonde measurements currently.

In addition to correcting the lag effect in the mean wind profile composition, the wind finding equations are also essential in reconstructing the turbulence intensity profile of the measured wind field, as shown in Fig. 3.9. In this figure, the comparison of the turbulent

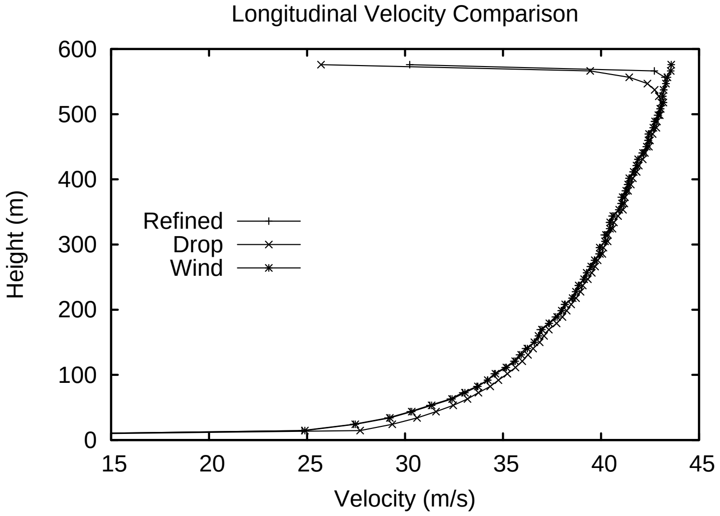

Figure 3.8: Mean velocity profile comparison, where "Refined" equals the velocity calculated using the wind finding equation, "Drop" equals the dropwindsonde velocity alone and "Wind" equals the wind velocity interpolated from the pseudo-stochastic wind field.

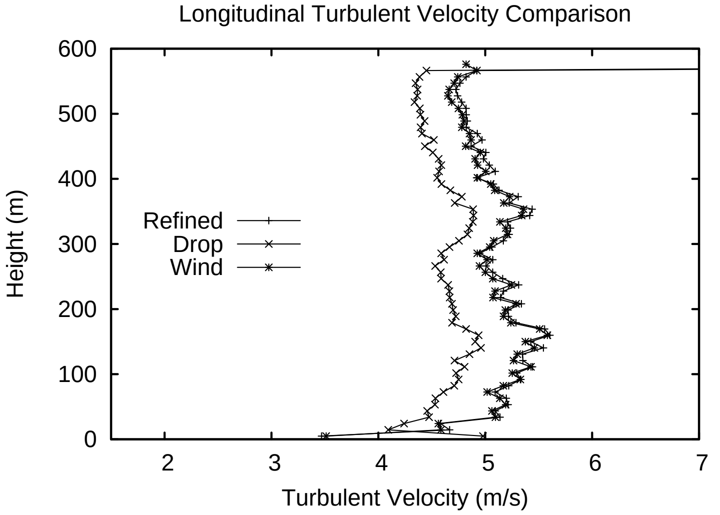

Figure 3.9: Turbulent velocity comparison, where "Refined" equals the velocity dynamically corrected by the wind finding equation, "Drop" equals the dropwindsonde velocity alone and "Wind" equals the wind velocity interpolated from the pseudo-stochastic wind field.

wind velocity, which is defined as the square root of the wind velocity variance about the mean wind calculated above, indicates the wind finding equations offset a part of the turbulence energy missed by the raw dropwindsonde measurement. More specifically, while the turbulent velocity profile composited from raw pseudo dropwindsonde measurements is constantly lower, by a value close to $1m/s$, than the "true" profile calculated from the known pseudo-stochastic wind field, this difference is significantly reduced by the wind finding equations. This feature implies that raw dropwindsonde measurements underestimates the true turbulence intensity of the measured wind field due to its deficiency in capturing high frequency turbulence information as discussed in analyzing the analytical solutions to the linearized dropwindsonde motion governing equations presented in appendix A (see page 206). However, the acceleration of the dropwindsonde, which is more sensitive to high frequency excitations, returns the turbulent energy missed by the dropwindsonde velocity alone.

3.3.2 Finite Difference Scheme to Calculate the Dropwindsonde Acceleration

As discussed above, the dropwindsonde acceleration is essential in reconstructing both the mean and turbulent wind profiles of the measured wind field. The value of the acceleration is, however, not directly reported by the dropwindsonde instrumentation but must be calculated by differentiating the dropwindsonde velocity. As a result, it is obvious the finite difference scheme used to calculate the dropwindsonde acceleration influences outcomes of the wind finding equations. A first-order backwards finite difference based on the velocity at the present time step and last observed time step is used currently without any further justifications. To quantify the influence of the finite difference scheme, pseudo dropwindsonde measurements are post-processed with different finite difference scheme to calculate the acceleration. One reasonable assumption is that a higher order central difference would produce a more accurate acceleration to be used in the wind finding equations. For that reason, the first- and second-order, forwards, backwards and central schemes are evaluated in processing the pseudo dropwindsonde measurement.

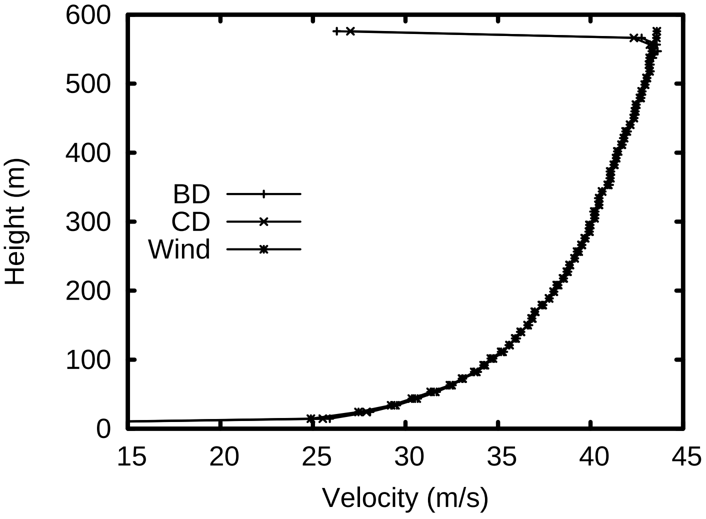

(a) Differentiation Comparison

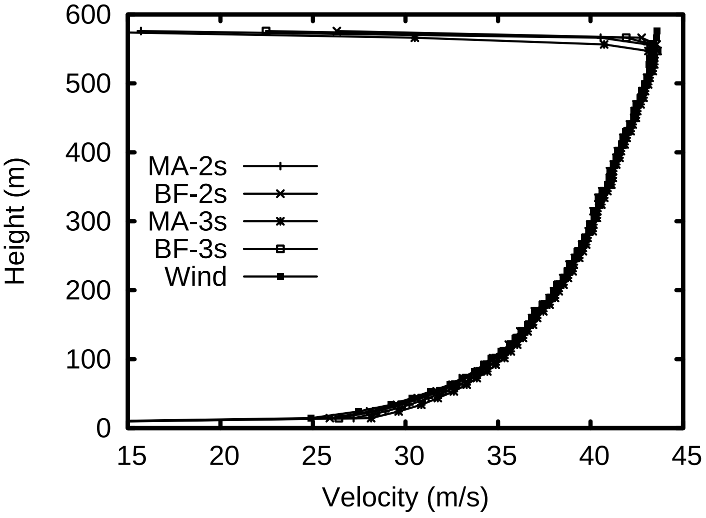

(b) Filter Comparison

Figure 3.10: Mean velocity profile comparison showing the impact of various differentiation schemes and filter designs, where "BD" stands for the 1^{st} order backwards differentiation, "CD" stands for the 2^{nd} order central differentiation, "MA" stands for the moving average, "BF" stands for the 1^{st} order Butterworth filter (the cut-off time scale is specified after these symbols), "Wind" equals the "true" wind velocity interpolated from the pseudo-stochastic wind field.

As shown in Fig. 3.10(a), the finite difference scheme used to calculate the dropwindsonde acceleration has negligible impact on the mean profile composition which is demonstrated by the fact that different curves in Fig. 3.10(a) are distinguishable. The turbulent velocity profile comparison, on the other hand, clearly shows the influence of finite difference scheme (see Fig. 3.11(a)) where there is noticeable difference between the profiles calculated using different schemes. It should be noted that the apparent difference between the "true" mean wind profile preset in the wind field simulation and profile measured by simulated dropwindsonde is because the simulated dropwindsonde requires some distance in its fall to capture the mean wind profile of the pseudo-stochastic wind field. Thus, the mean profiles derived pseudo dropwindsonde measurements contain values smaller than the true mean wind velocity interpolated from the pseudo-stochastic wind field.

To gain a more direct understanding of the influence of finite difference schemes, the error is calculated, which is defined as the composited squared difference between the "reported" wind velocity calculated based on pseudo dropwindsonde motions and the "true" wind velocity interpolated from the known pseudo-stochastic wind field at the height where the measurement is taken. As shown in Fig. 3.12(a), the second-order central difference yields the best estimate of turbulent wind velocities, although the error is still appreciable, i.e. in the order of $8m^2/s^2$ for the squared velocity difference. Also shown in Fig. 3.12(a) is the vertical variation of the error. As expected, the error monotonically decreases with height for all schemes evaluated since both the lag effect and turbulence intensity, which are the reasons inducing the difference between the "true" and "measured" wind velocity, are pronounced in the lower portion of the pseudo-stochastic wind field.

3.3.3 Low-pass Filtering of Dropwindsonde Profiles

As introduced above, low-pass filters are commonly employed to smooth dropwindsonde profiles. Although their characteristics obviously impact the statistics, especially the turbulence intensity, of the measured wind field derived by compositing dropwind-

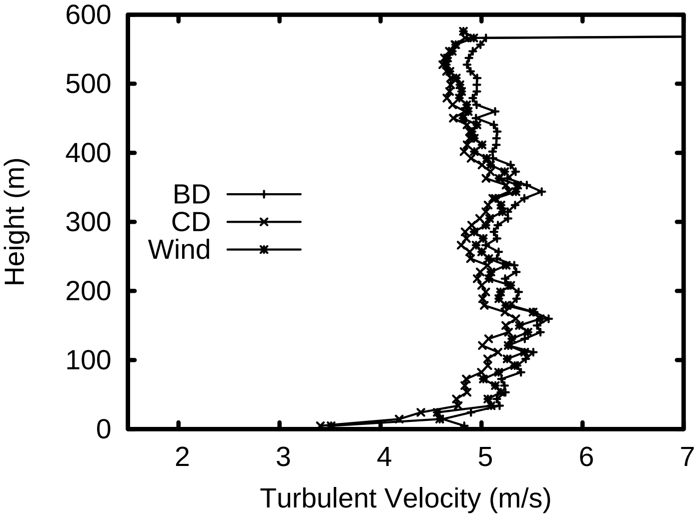

(a) Differentiation Comparison

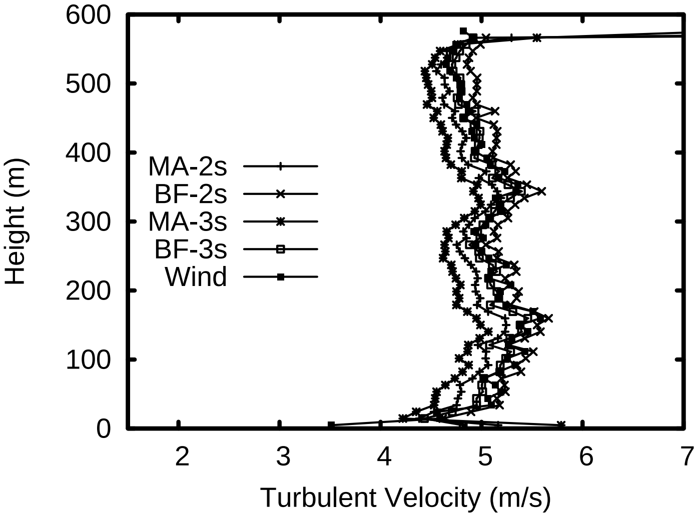

(b) Filter Comparison

Figure 3.11: Turbulent velocity profile comparison showing the impact of various differentiation schemes and filter designs, where "BD" stands for the 1^{st} order backward differentiation, "CD" stands for the 2^{nd} order central differentiation,"MA" stands for the moving average, "BF" stands for the 1^{st} order Butterworth filter (the cut-off time scale is specified after these symbols), "Wind" equals the "true" wind velocity interpolated from the pseudo-stochastic wind field.

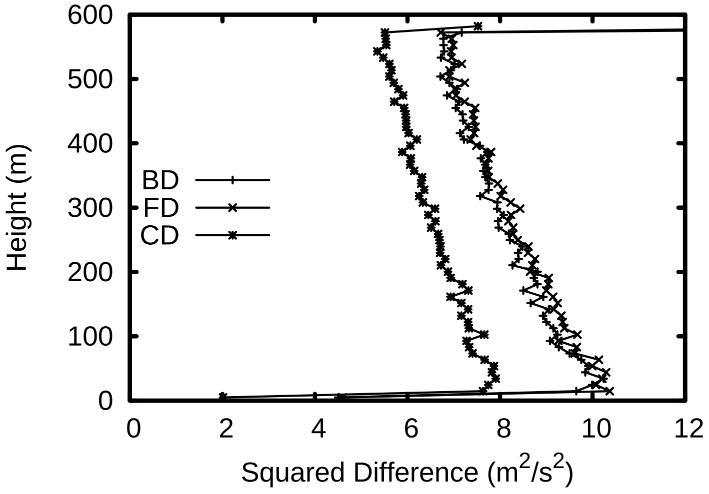

(a) Differentiation Error Comparison

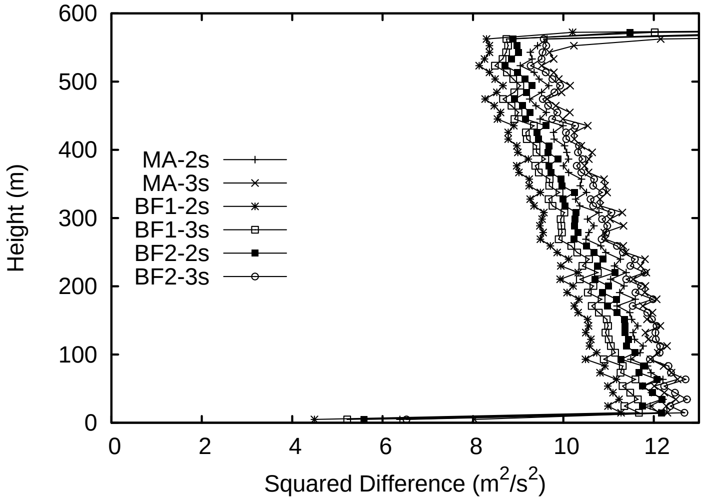

(b) Filter Error Comparison

Figure 3.12: Error profile comparisons showing the impact of various differentiation schemes and filter designs, where "BD" stands for the 1^{st} order backward differentiation, "CD" stands for the 2^{nd} order central differentiation, "FD" stands for the 1^{st} order forward differentiation, "MA" stands for the moving average, "BF" stands for the Butterworth filter (the filter order and the cut-off time scale are specified after the filter symbol.

sonde measurements, a $5-s$ filter, without any further specifications, is used in previous studies with no theoretical or experimental justification (Franklin et al., 2003; Vickery et al., 2009), and its influence on the composition result has not been thoroughly discussed. To explore the influence of low-pass filters on dropwindsonde profiles, individual pseudo dropwindsonde profiles filtered by two types of filters, a moving average filter and a Butterworth filter, with 2 seconds and 3 seconds taken as cut-off time scales, were used to derive the mean and turbulent wind velocity profiles of the measured pseudo-stochastic wind field. Due to the limitation of the pseudo-stochastic wind field height, $600m$, the widely adopted cut-off time scale, 5 seconds, is considered too large since it produces a $60m$ smoothing scale given that the falling rate of the dropwindsonde is $12m/s$. However, the influence of using a larger cut-off time scale, such as 5 second, is predictable based on the trends found here. Since the frequency response of the filters clearly impacts the fluctuations remaining in the filtered measurements, this aspect should be investigated. Because the frequency response of the Butterworth filter performs better, in a comparison with the moving average filter, in filtering out high frequency fluctuations, it is expected to see that it produces improvements in reconstructing the turbulent wind velocity profile of the measured wind field.

Similar to the comparison for evaluating finite difference schemes, Fig. 3.10(b) shows that the mean wind profiles composited from pseudo measurements processed using different filter designs are indistinguishable. This indicates that the influence of the low-pass filter characteristics, including the cut-off time scale and the type of the filter, on the mean wind structure found by the dropwindsonde is negligible, and therefore the design of the filter is not important when only the mean wind profile is of interest. In contrast, the influence of filter characteristics on the turbulent velocity profile composition is obvious. Figure 3.11(b) shows the difference of the turbulent wind velocity profiles calculated using different filter designs can go up to $0.6m/s$, or 12% in the relative sense.

The comparison of the error, defined exactly as in the discussion of the influence of the differentiation scheme, is shown in Fig. 3.12(b). The comparison indicates the first-order

Butterworth with the cut-off scale of $2 - s$ gives the best estimate, in general, of the instantaneous wind speed of the measured wind field. This implies that the currently used $5 - s$ cut-off time scale is too large. In addition, the moving average generally gives larger errors, as expected, comparing to the results smoothed by the Butterworth filter, although the improvement of using Butterworth filter is not significant. It should be noted that this finding is made based on the assumption that the dropwindsonde measurement error can be described by a series of independent, log-normally distributed random variables. This error assumption is rather crude and unvalidated, and therefore the conclusion presented should be used with caution. A further investigation, taking various causes of the measurement error into account, is needed to yield a more sound suggestion on the filter design in processing dropwindsonde measurements.

Since the filter is commonly used in post-processing dropwindsonde measurements, the influences of filter characteristics and finite difference scheme are combined when the measurement needs to be dynamically corrected by the wind finding equations. Since there is no evidence so far indicating that their influences can be superimposed, their combination should be examined in addition to individual investigations. In Figs. 3.10 and 3.11, the profiles showing the influence of the finite difference schemes investigated are calculated using the Butterworth filter with 2 second cut-off scale while those showing the influence of low-pass filter characteristics are calculated using the first-order backwards scheme. Since the influences of both finite difference schemes and filter characteristics on the mean wind profile composition are negligible, discussions in following paragraphs are concentrated on their combined influence on the turbulent wind velocity profile composition and the turbulent wind velocity definition can be found in the discussion of the wind finding equations' validity.

Seen in Fig. 3.11(a), the second-order central difference yields an overall better estimate when pseudo measured profiles are smoothed by the best available filter, which follows the trend found in the analysis of the error introduced solely by finite difference schemes, as shown in Fig. 3.12(a). The improvement, however, is not as obvious as in Fig.

3.12(a). This implies that higher order difference schemes, which are better in capturing the trend of high order variations within a finite step, does not outperform the lower order differentiation scheme. The reason for this is that the variation of a pseudo dropwindsonde measured profile, including the trend resolved by a high order finite difference, is filtered out by a low-pass filter. Therefore, the selection of the differentiation scheme is not as important as indicated by Fig. 3.11(a). Consistent with the findings made in analyzing filter characteristics individually, the Butterworth filter with cut-off scale of 2 second produces the turbulent wind velocity profile close to the one calculated from the pseudo-stochastic wind field, as shown in Fig. 3.11(b). However, the Butterworth filter with cut-off scale of $3s$ also produces a profile approximating the "true" profile. This indicates the importance of time scales used in the filter design may not be as significant as indicated by the individual examination articulated above. This is because extra small scale variations introduced by the dropwindsonde acceleration compensate the smoothing given by the filter with a larger cut-off scale.

3.3.4 Composition data size

Apparently, a small database of dropwindsonde measurements would make the composited statistics unreliable, especially when the turbulence information is of interest. However, there is no systematical investigation, as far to my knowledge, that quantifies the composition data size which can be taken as sufficient to produce statistically meaningful wind turbulence statistics. To investigate this matter, the influence of the composition data size is analyzed based on the numerical simulation results. As shown in Fig. 3.13(a), the composited, dropwindsonde measured mean profile converges to the "true" mean profile calculated from the pseudo-stochastic wind field as the number of pseudo dropwindsonde profiles used in composition increases. When the number of pseudo dropwindsonde profiles exceeds 100, the difference between the composited profile and "true" mean profile reaches the order of $\sim 0.1m/s$. Thus, a composition database with 100 dropwindsonde profiles would be enough to derive the mean wind structure. The turbulent wind velocity profile composition, on the other hand, needs a larger database to get converged results. As shown in Fig.3.13(b), a database containing 500 dropwindsonde profiles is necessary to get a reasonable estimate of the turbulent wind velocity profile. The definition of turbulent wind velocity can be found in the discussion of the wind finding equations' validity.

If the difference between the composited value, calculated based on pseudo dropwindsonde measurements, and the "true" statistics, calculated from the pseudo-stochastic wind field, for each height bin is treated as a random variable, the standard deviation of this random variable, showing the deviation of the composition result from "true" wind statistics, can be calculated for compositions using different number of pseudo dropwindsonde profiles. Defining this standard deviation as an error, the influence of the composition data size is quantified. Apparently, another factor influencing this error is the turbulence intensity of the pseudo-stochastic wind field, which conventionally defined the square root of the turbulence variance normalized by the mean wind velocity at the same height. If the turbulence intensity of the whole pseudo-stochastic wind field is defined as the mean of the turbulence intensities calculated at all discrete heights in the pseudo-stochastic wind field, fields with intensities 4.5%, 9%, 15%, 18%, 24%, 28.5% are generated numerically for the purpose of identifying the influence of the turbulence intensity. Based on the methodology articulated above, the influence of the composition data size is systematically investigated. As shown in Fig. 3.14, the error, following the expectation, decreases with the increase of data sizes, and increases with the turbulence intensity. Furthermore, as indicated in Fig. 3.14(a), to reduce the error to the level of $1m/s$ in the mean profile composition, which is roughly 3% in a relative sense, the database should contain 100 dropwindsonde profiles in fields with the turbulence intensity under 20%. When the composition contains 500 profiles, errors in all fields tested go under the $1m/s$ level. Similar data size is needed to make the composited turbulent wind velocity profile reach the error level of $1m/s$. However, the $1m/s$ error in the turbulent wind velocity profile composition is roughly 20% in a relative sense. When 200 profiles are used in the composition, only the wind fields with turbulence intensities under 20% produce errors under $0.5m/s$, or 10% in a relative sense, and when 500 profiles are composited, only the wind fields with turbulence intensities under 10% produce errors under

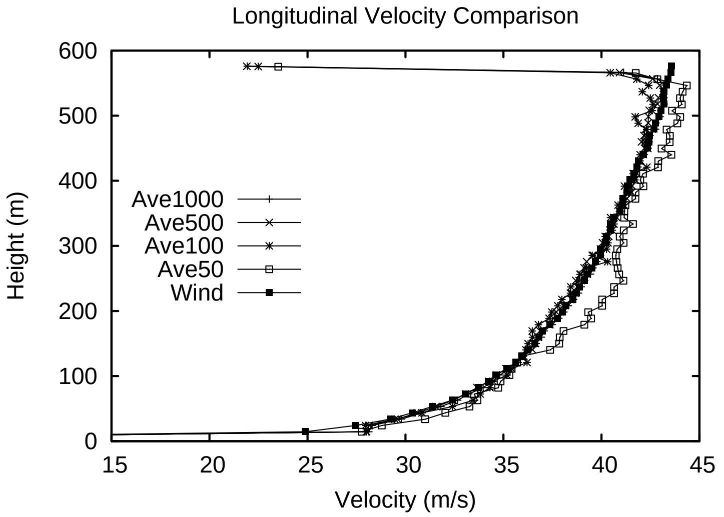

(a) Mean Profile

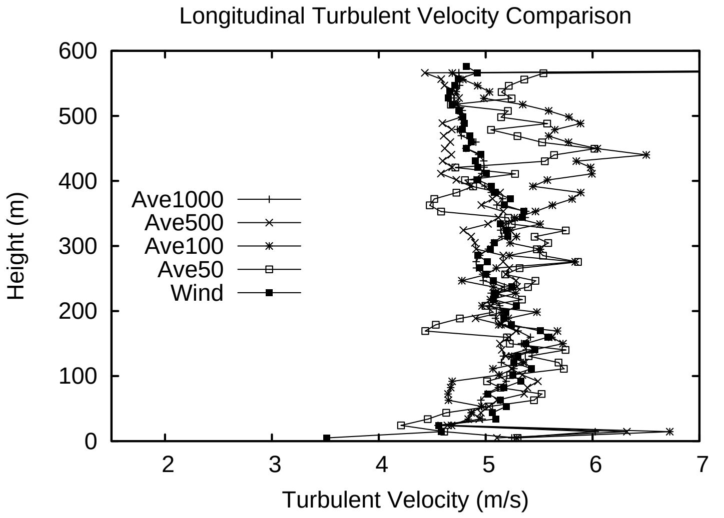

(b) Turbulent Profile

Figure 3.13: Mean and turbulent velocity profile comparisons showing the imapct of composition data size, where the size is indicated by the legend. "Wind" equals the "true" wind statistic calculated from the pseudo-stochastic wind field.

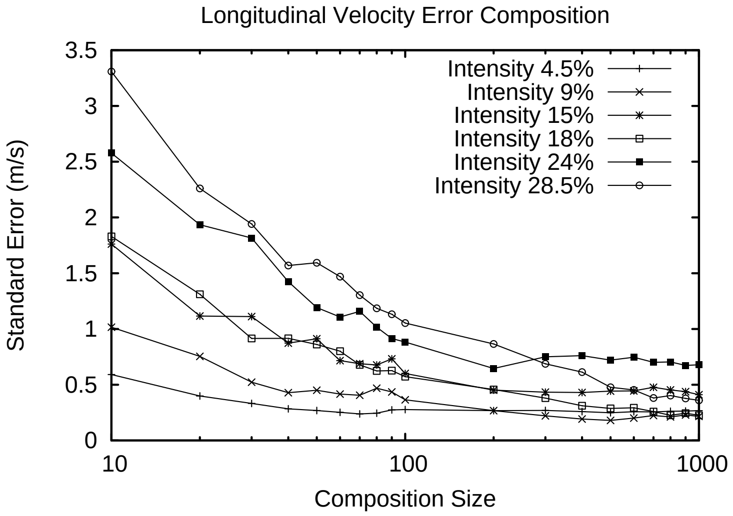

(a) Mean Profile Error

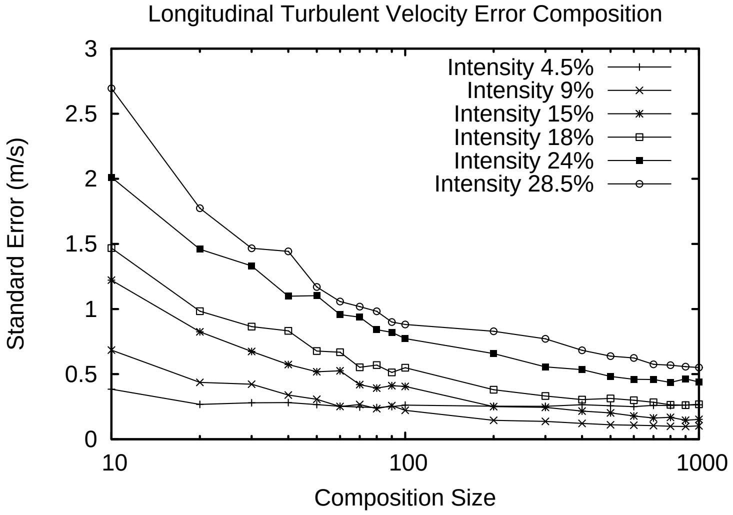

(b) Turbulent Velocity Profile Error

Figure 3.14: Error of the composited mean and turbulent wind velocity profile versus the composition data size.

$0.25 m/s$.

3.3.5 Gust time scale

In addition to investigating post-processing techniques, the known pseudo-stochastic wind field also provides an opportunity to discover the gust time scale of dropwindsonde wind measurements. Although it is one important piece of information in understanding the dropwindsonde measurement, little is known about the dropwindsonde measurement gust time scale.

Given that wind velocity time histories for every point in the pseudo-stochastic wind field are known, the gust time scale of the dropwindsonde wind measurement can be crudely found as following. First, the pseudo-stochastic wind field is filtered using different time scales. Then, the dropwindsonde "reported" wind velocity, calculated from pseudo measurements, is compared with the filtered wind velocity at the height where the measurement is taken to find a time scale making the filtered wind velocity closest to the "reported" wind velocity. Such scales calculated for numerous pseudo dropwindsonde profiles are then averaged to produce the time scale for the entire measurement database. In the filtering, moving average filters, with cut-off time scales varying from $0.5s$ to $5s$, are used. In finding the time scale described above, the mean of absolute differences between the "reported" and filtered wind velocities are used as an indicator. More specifically, the time scale used to filter the pseudo-stochastic wind field which makes this mean minimal is taken as the gust time scale for an individual pseudo dropwindsonde profile.

Averaging time scales found for 1000 pseudo dropwindsonde profiles produces the gust time scale for the entire database, which is $2.24s$ if the "reported" wind velocity is the raw dropwindsonde velocity and is $0.5s$ if the "reported" wind velocity is calculated by the wind finding equations. This indicates the dropwindsonde is quite sensitive, after dynamically corrected by the wind finding equations, to the driving wind, and therefore it nearly instantaneously reflects gusts in the measured wind field.

3.3.6 Wind spectrum

The velocity series documented by the dropwindsonde can derive a wind spectrum, but the interpretation of this spectrum is not thoroughly investigated. Since the wind velocity is not measured in a conventional way by the dropwindsonde, this spectrum can not be interpreted as a usual wind spectrum, e.g. one derived from tower measurements. Meanwhile, the spectral tensor describes the spectral information of the wind field uniformly in three spatial directions, and therefore is one of appropriate interpretations of this wind spectrum. To explore the possibility of extracting spectral information of the measured wind field from dropwindsonde measurements, the pseudo-stochastic wind field generated based on the spectral tensor, instead of that based on the POD simulation, is used as the driving wind in numerically simulating the dropwindsonde motion. Comparing the wind spectrum derived from pseudo dropwindsonde measurements to the one calculated using spectral tensor will shed some lights on the interpretation of the spectral information revealed by the dropwindsonde.

The "true" wind spectrum should be calculated, in theory, by integrating the tensor along two directions perpendicular to the falling track of the dropwindsonde. However, it is extremely difficult to define a calculable falling track since the dropwindsonde changes directions substantially during its fall and different dropwindsondes give significantly different directions. Moreover, when Taylor's hypothesis is invoked, all dropwindsonde falling tracks can be approximated by the vertical axis. Therefore, the "true" wind spectrum, used to compare the spectrum calculated based on pseudo dropwindsonde measurements, is calculated by integrating the spectral tensor along k_1 and k_2 axis which represent two horizontal directions, x and y, in the physical space.

A general agreement shown in Fig. 3.15(a) indicates that the wind spectrum derived from dropwindsonde measurements can reflect the spectral energy distribution of the measured wind field. It is obvious that the spectrum derived from the dropwindsonde velocity alone deviates from that calculated based on the "corrected" wind velocity produced by the wind finding equations, around the wave number of $0.05m^{-1}$. Given that the "corrected" wind spectrum is closer to the "true" wind spectrum, the dropwindsonde velocity alone keeps underestimating the spectral intensity of the measured wind field in the region where it deviates from the "corrected" wind spectrum. This feature directly substantiates the finding made in the theoretical analysis detailed in appendix A (see page 206). Through analytically analyzing the linearized dropwindsonde motion equation in the appendix, it has been found that the dropwindsonde hardly responds to high frequency excitations while the acceleration terms in the wind finding equations, i.e. $(\dot{z}/g)\ddot{x}$ and $(\dot{z}/g)\ddot{y}$, are sensitive to high frequency excitations. The significant difference between the measured and "true" wind spectrum in really low wave number region may be due to the combination of the lack of pseudo measurements in that region and the impact of integrating the spectral tensor along two horizontal directions rather than following the track of simulated dropwindsonde motions. It is worth mentioning that the wind spectrum calculated following the same composition methodology but using the "true" wind velocity interpolated from the known pseudo-stochastic wind field is in reasonable agreement with the wind spectrum derived from pseudo measurements in both the low wave number region, under $0.05m^{-1}$, and high wave number region, above $0.2m^{-1}$, despite that the "true" wind spectrum calculated by integrating the spectral tensor gives different spectral intensity estimates in these two regions. This implies although the dropwindsonde is able to reveal the spectral information of the measured wind field with a satisfactory accuracy in the whole calculable wave number region, only a relatively small portion of the dropwindsonde measured line spectrum should be used to derive the governing spectral tensor.

Shown in Fig. 3.15(b) is a similar comparison of the cross spectrum of the longitudinal and vertical wind. The agreement is not as good as that shown in Fig. 3.15(a), especially in the low wave number region. The major reason for this may be that the cross spectrum of u and w are more sensitive to the integration direction since the u, w interaction is the main mechanism, according to the spectral tensor model currently employed (Mann, 1994), distorting the spectral tensor from the isotropic state to the sheared state. Nevertheless, the spectrum derived from pseudo measurements starts to

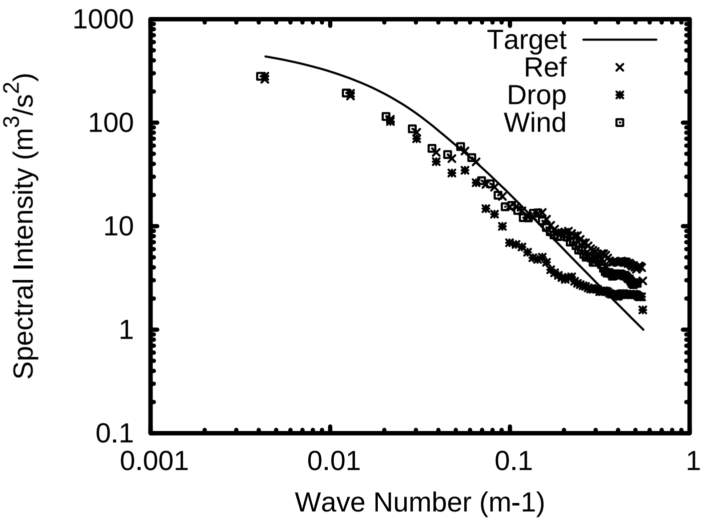

(a) Spectral Density Comparison

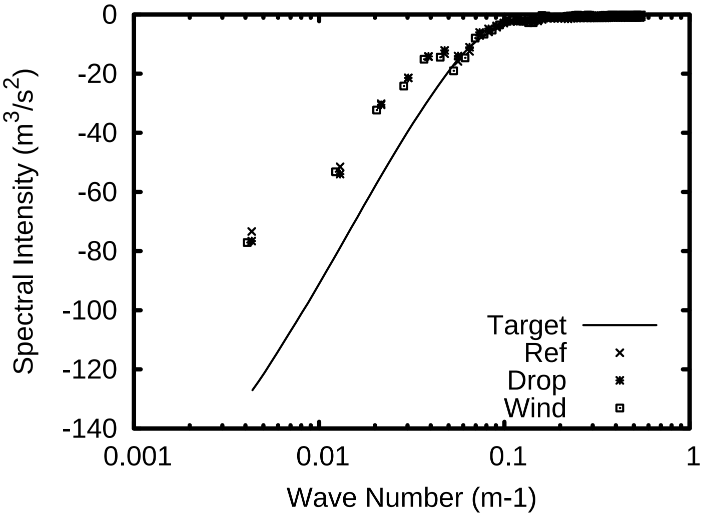

(b) Cross Spectral Density Comparison

Figure 3.15: Comparisons of the longitudinal wind spectral density and cross spectral density for the longitudinal and the vertical wind, in which "Target" equals to the spectrum integrated from the spectral tensor, "Ref" equals the spectrum calculated using the wind finding equation, "Drop" equals to the spectrum derived based on the dropsonde velocity alone, and "Wind" refers to the "true" wind spectrum calculated from the pseudo-stochastic wind field.

give good estimates of the spectral intensity, comparing with the "true" spectrum, in the high wave number region (above $0.05m^{-1}$). This supports the use of dropwindsonde measurements to get cross turbulence statistics, at least for local turbulence correlations.

3.3.7 Conclusions

Since the measurement taken by the dropwindsonde contributes significantly in improving our understanding on wind structures in tropical cyclones, it deserves a thorough and systematical study. In addition, when the dropwindsonde falls, the measurement is taken in neither a conventional Eulerian framework nor a perfect Lagrangian framework, and a proper processing and composition approach should be taken to retrieve conventional Eulerian wind statistics of the measured wind field from raw dropwindsonde measurements. As one widely used post-processing technique, the wind finding equations provided by Hock and Franklin (1999) have been found important to correct the mean wind profile measured by the dropwindsonde. Moreover, the analytical solutions to the linearized dropwindsonde motion governing equations reveal that the dropwindsonde hardly responds to high frequency horizontal wind perturbations while the acceleration terms in the wind finding equations are sensitive to high frequency excitations. This indicates that the wind finding equations are not only important in recovering the mean wind profile from dropwindsonde measurements, but also in returning high frequency turbulence information missed by raw dropwindsonde measurements.

For the purpose of validating the wind finding equations more thoroughly and systematically and investigating several unchecked aspects in processing and compositing dropwindsonde measurements, a numerical simulation of the dropwindsonde motion in a pseudo-stochastic wind field has been conducted. In the numerical simulation, the solved dropwindsonde motion variables are taken as pseudo dropwindsonde measurements to be processed and composited to produce statistics of the measured wind field. Given that the statistics can also be calculated directly from the pseudo-stochastic wind field, comparisons between the statistics composited from numerical simulation results and calculated from pseudo-stochastic wind field provides a unique opportunity to investigate unchecked aspects in processing and compositing dropwindsonde measurements. Findings can be summarized as

- The wind finding equations are essential in reducing the dropwindsonde deficiency in reproducing the mean profile of the measured wind field with strong shear.
- The acceleration term in the wind finding equation, $\dot{z}\ddot{x}/g$ and $\dot{z}\ddot{y}/g$, returns the high frequency turbulence information missed by the dropwindsonde velocity alone.
- The finite difference scheme works with the filter design to determine the turbulence profile measured by the dropwindsonde and they have little impact on the mean profile composition.
- The accuracy of the resulting profile depends on the composition data size, and the calculation of turbulence statistics needs a larger data size.
- The gust time scale of the dropwindsonde measurement for the raw measurement is about $2.24s$ and for the velocity dynamically corrected by the wind finding equations is about $0.5s$.
- The wind spectrum derived from velocity series measured by the dropwindsonde are able to depict the spectral distribution of turbulence energy, provided a spectral tensor is capable of describing the wind spectra in the entire wind field.

3.4 Aerodynamics of the Dropwindsonde

Aerodynamic parameters of the dropwindsonde, such as the drag coefficient C_D, strongly influence its motion due to their roles in the motion governing equations. However, no estimates of their values have been made by an experiment in controlled environments. Moreover, Hock and Franklin (1999) derived the wind finding equations under an assumption that the dropwindsonde drag coefficient is a constant independent from angles of attack. This assumption lacks any theoretical or experimental foundations. Since the wind finding equations are essential in reconstructing not only the mean but also turbulent wind structure in the measured wind field, a systematical measurement of the dropwindsonde aerodynamics not only improves the description of the dropwindsonde motion but also validates the wind finding equations. Wind tunnel tests conducted as a part of this thesis work are reported in this section which measures the dropwindsonde aerodynamics, and their variations with angles of attack. In addition, based on the measurements gathered in the wind tunnel test, it is feasible to model the dropwindsonde motion more realistically. The theoretical derivation of such a model is presented in section 3.5.

3.4.1 Tunnel test configuration

The wind tunnel test is conducted in the BLWTL-2 wind tunnel in the Boundary Layer Wind Tunnel Laboratory of the University of Western Ontario. The dropwindsonde model is placed and tested in the high speed section of BLWTL-2, which has dimensions $39m \times 3.4m \times 2.5m$ ($length \times width \times height$) and its maximum wind speed allowed is $28m/s$.

The dropwindsonde model is a full scale replica of the real dropwindsonde body made by the University Machine Shop of the University of Western Ontario using plastic, which is roughly a cylinder with a diameter of $6.86cm$ and a height of $40.89cm$. The parachute used in this test is the real one used in the dropwindsonde system, which is the NCAR's (National Center for Atmospheric Research) unique square-cone parachute. A more comprehensive technical description of the dropwindsonde system and parachute can be found on the dropwindsonde website. [1]

The model is installed close to the flow inlet. The forces in two perpendicular directions and the torque experienced by the model are measured by wind tunnel balances. A steel bar is used to support the model between two balances. The contribution of the bar to the measured aerodynamics is subtracted based on forces measured in a separate test where only the bar is installed. The general setting of the wind tunnel test is shown in

---

[1] http://www.eol.ucar.edu/isf/facilities/dropsonde/gpsDropsonde.html

Fig. 3.16.

Figure 3.16: The setting of the dropwindsonde wind tunnel test.

The angle of attack is defined as the angle of the model orientation relative to the horizontal flow, as shown in Fig. 3.17. It increases at a 5° step. The range of angles of attack tested is from $-75°$ to $75°$, while the wind speed used is from $6.1m/s$ to $21.3m/s$ with increments of $3.05m/s$. Although this wind speed is much less than hurricane wind speeds found in a real dropwindsonde fall, the velocity influencing dropwindsonde aerodynamics is the relative wind velocity calculated by subtracting the dropwindsonde motion from surrounding winds. Since the dropwindsonde horizontal motion is close to the surrounding horizontal wind and the vertical relative wind velocity is close to the dropwindsonde falling rate ($12m/s$), the total relative wind speed can be reasonably assumed in the range of the wind speeds used in the test. Moreover, as seen in the following discussions, the dropwindsonde aerodynamics are Reynolds number independent when the relative wind velocity exceeds some critical value. This substantiates that aerodynamics measured under low wind speed conditions are valid under high wind speed conditions. As for the flow condition, the test is conducted in a smooth flow, in which the flow is only confined by tunnel walls, and in a turbulent flow, in which the flow is passing a grid shield to generate small scale turbulence. This configuration gives a opportunity to investigate the influence of small scale turbulence on the dropwindsonde aerodynamics. To simplify the test, the range of angles of attack tested in the turbulent flow is only from −15° to 75°, and the symmetry of the dropwindsonde aerodynamic behaviour in the turbulent flow is assumed.

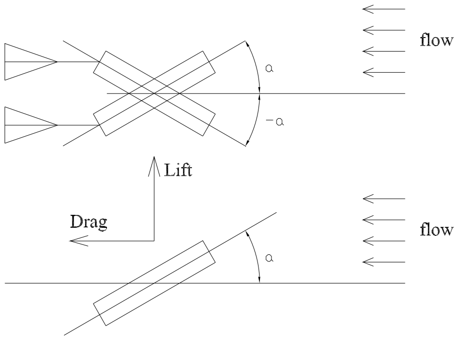

Figure 3.17: The sketch showing the definition of the angle of attack.

To identify contributions of the parachute, the test is conducted for both the whole system with the parachute attached and for the dropwindsonde body alone. Aerodynamics of the parachute itself can then be estimated by taking away the test results of the dropwindsonde body from the results of the whole system with the parachute.

3.4.2 Results and Discussions

The most useful results from the wind tunnel tests are the drag, lift and torque coefficient of the dropwindsonde system with the parachute attached and of the dropwindsonde body alone. The drag and lift are defined as the force along and perpendicular to the horizontal flow, as shown in Fig. 3.17. This is equivalent to defining the drag and lift according to the relative dropwindsonde movement direction. The variation of the drag, lift and torque coefficient with angles of attack, including for the whole system with the parachute and for the dropwindsonde body alone, are shown in Figs. 3.18(a), 3.18(b) and 3.18(c) respectively. These coefficients are calculated by normalizing the measured force, i.e. drag, lift and torque, by the wind speed, the dropwindsonde sectional area and the air density, such as,

$$\begin{aligned} C_D &= \frac{F_D}{\rho A V_r^2} \\ C_L &= \frac{F_L}{\rho A V_r^2} \\ C_T &= \frac{T}{\rho A l V_r^2} \end{aligned} \tag{3.30}$$

In expression (3.30), C indicates the aerodynamic coefficient while the subscript gives the kind of the coefficient, D represents the drag, L represents the lift and T is the torque. V_r represents the tunnel test wind speed. A is the sectional area. Following the EDITSONDE source code (J. L. Franklin 2011, Personal communication), this parameter takes the value of $0.0676m^2$ to make the wind tunnel measurements comparable to the drag coefficient implied by Hock and Franklin (1999). In addition, ρ is the air density, which takes the value of $1.235kgm^{-3}$ in the test, and l is half of the dropwindsonde body length, which is $20.45cm$.

It is obvious that the behaviour of aerodynamics of both the dropwindsonde body and whole system with the parachute attached is roughly symmetric, as expected. Although the weight force of the parachute violates this symmetry since it points downwards in both positive and negative angle of attack region, its influence becomes negligible under high wind speed conditions as revealed by Fig. 3.19(a). There is a slight asymmetry seen in Fig. 3.18(a), which can be explained by the wake effect of the dropwindsonde body. When the angle of attack is negative, the parachute is strongly influenced by the wake of the dropwindsonde body since the parachute's own weight makes it stay in a position lower than the horizontal plane. When the angle of attack is positive, the parachute is less affected by the wake. Since this asymmetry is minimal and is not seen in the variation of the lift coefficient, its influence is negligible.

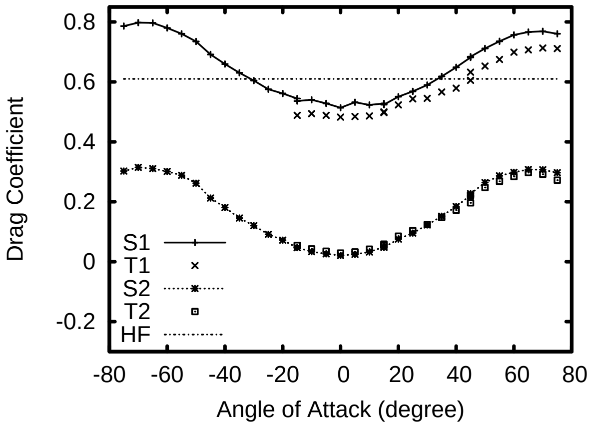

(a) Drag Coefficient

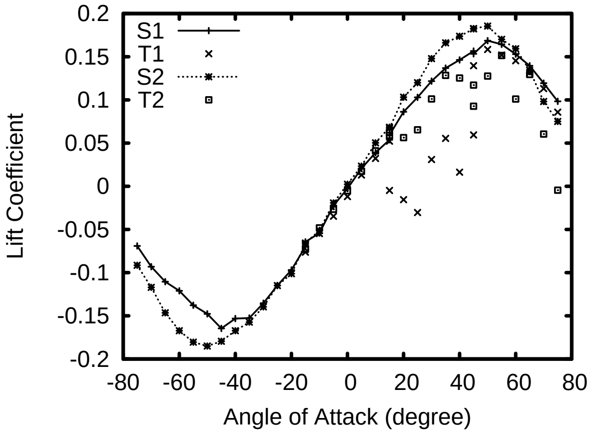

(b) Lift Coefficient

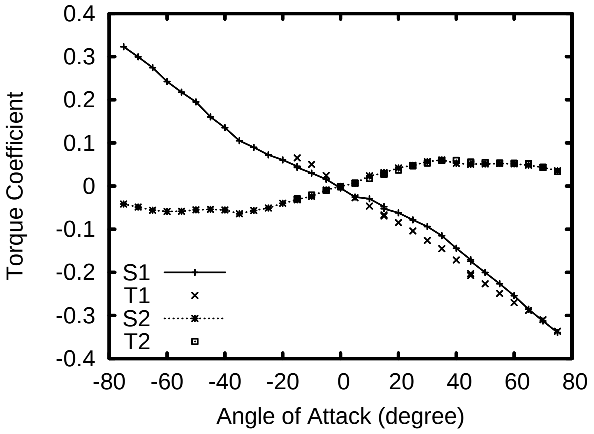

(c) Torque Coefficient

Figure 3.18: Variation of the drag, lift and torque coefficient with angle of attack, "T" refers to the measurement in the turbulent flow, while "S" refers to the measurement in the smooth flow, and "1" means the measurement is for the whole system with parachute while "2" means the measurement is for the dropsonde body alone. "HF" refers to the drag coefficient implied by Hock and Franklin (1999).

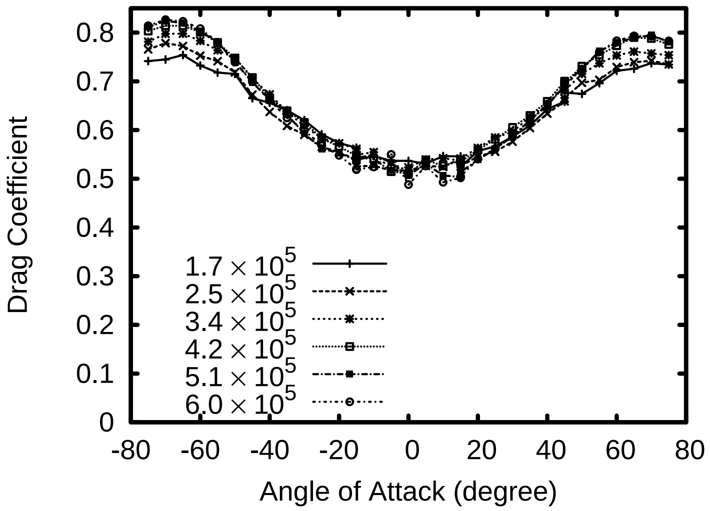

(a) Drag Coefficient with parachute

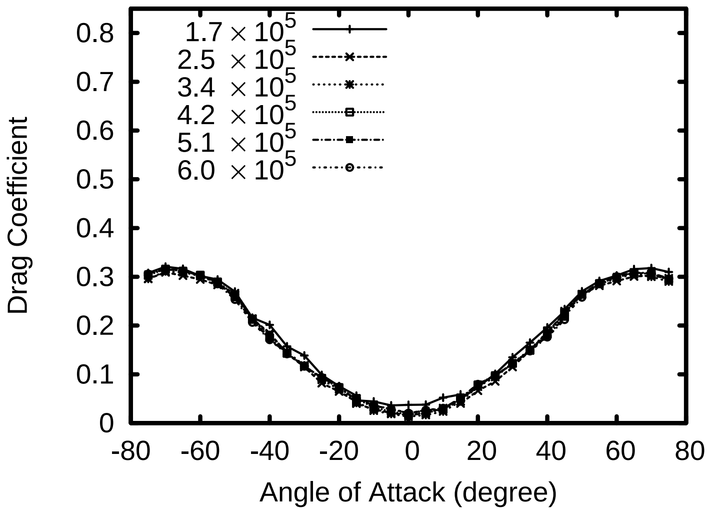

(b) Drag Coefficient without parachute

Figure 3.19: Variation of the drag coefficient with angle of attack under different testing wind speeds, Reynolds numbers are indicated by the legend.

Figures 3.19(a) and 3.19(b) show the drag coefficient of the dropwindsonde body and of the whole system with the parachute attached under different testing wind speeds. In both cases, measurements collapse into a single curve when the wind speed exceeds $10m/s$. In addition to demonstrating the influence of the parachute weight force is negligible under high wind speed conditions, this also substantiates that the drag coefficient of both the dropwindsonde body and parachute is Reynolds number independent. The Reynolds number independence is shared by other dropwindsonde aerodynamics, which can be seen in Figs. 3.20(a), 3.20(b), 3.21(a) and 3.21(b). In the above discussions, the Reynolds number is defined as,

$$Re = \frac{V_r L}{\upsilon} \tag{3.31}$$

in which V_r is the wind tunnel testing wind speed, L is the length of the dropwindsonde model and υ gives the kinetic viscosity. Considering the testing wind speeds adopted in the wind tunnel test is in the range of $(6m/s, 12m/s)$, Reynolds numbers evaluated is in the range of $(1.7 \times 10^5, 6.0 \times 10^5)$

The variation of aerodynamics with angles of attack is appreciable as seen in the figures. The standard deviation of the drag coefficient of the whole system with the parachute in a smooth flow is 0.099, or 15.3% in a relative sense. Thus, assuming that the dropwindsonde drag coefficient is constant throughout the measuring process regardless of the angle of attack is not supported by the wind tunnel test results. As for the drag coefficient value, the one calculated implicitly using the terminal falling rate of the dropwindsonde (Hock and Franklin, 1999) is also shown in Fig. 3.18(a). On average, the drag coefficient measured in this test is close to the value implied by Hock and Franklin (1999), but their value deviates considerably from the measured drag coefficient when the absolute angle of attack is too high (larger than $60°$ or smaller than $-60°$) or too low (within the range $(-30°, 30°)$).

Small scale turbulence introduced by the grid installed in front of the dropwindsonde model has little impact on the aerodynamics measured, expect for the drag and lift

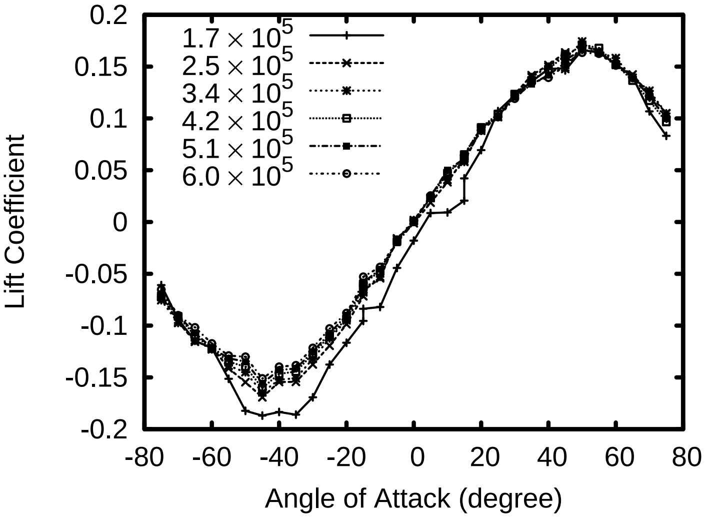

(a) Lift Coefficient with parachute

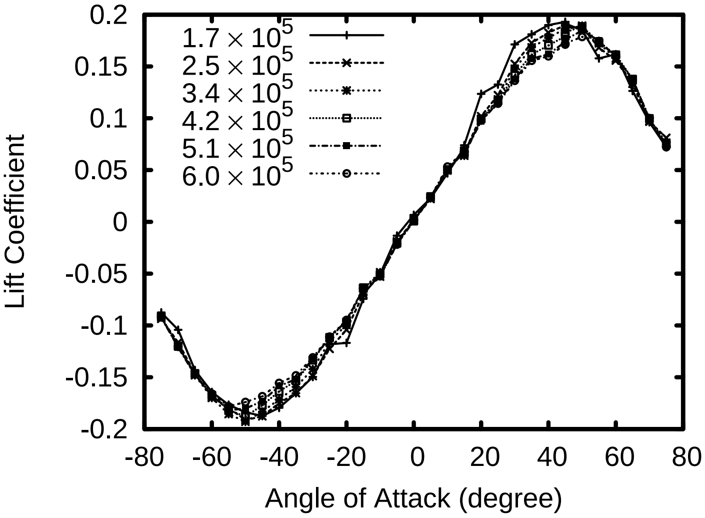

(b) Lift Coefficient without parachute

Figure 3.20: Variation of the lift coefficient with angle of attack under different testing wind speeds, Reynolds numbers are indicated by the legend.

coefficient of the whole system with the parachute. This can be explained by the random vibration of the parachute. When the parachute randomly vibrates in the small-scale turbulent flow, with an amplitude larger than that found in the smooth flow, the "added mass" of the parachute increases. According to Cockrell (1987), the "added mass", which can be roughly defined as the mass of the air strongly perturbed by the parachute, acts as the additional mass associated with the parachute. Therefore, the increase of the "added mass", due to larger amplitudes of random vibrations, produces a higher "apparent" weight force experienced by the parachute. This higher "apparent" weight force then leads to a negative contribution to the lift force measured by the balances, since the lift is always defined positive when it points upwards. As a result, the lift coefficient measured in the small scale turbulent flow is smaller than in the smooth flow, as indicated by the comparison shown in Fig. 3.18(b). The parachute vibration also makes a part of the drag acting on the parachute turn into the lift, since the total aerodynamic force acting on the parachute has a lift component when the parachute is not in the exact horizontal position. This explains why the drag coefficient measured in the turbulent flow is constantly lower than that measured in the smooth flow, as shown in Fig. 3.18(a). The added lift, however, is then swallowed in the averaging process in calculating the lift coefficient since the parachute vibration is about the angle of attack of 0. This explains that the lift coefficient measured in the turbulent flow does not increase, as shown in Fig. 3.18(b), even it contains the contribution made by the random vibration of the parachute to transfer a part of its drag into the lift. In conclusion, small scale turbulence does not fundamentally influence aerodynamics of the dropwindsonde and its effect can be neglected in a engineering application.

As shown in Figs. 3.22(a) and 3.22(b), the drag provided by the parachute alone is nearly constant regardless of angles of attack, while the lift coefficient of the parachute fluctuates around 0 at all angles of attack tested. This feature substantiates that the parachute is able to adjust its orientation to provide a relatively constant drag coefficient. As for the torque of the parachute, shown in Fig. 3.22(c), it ensures that the dropwindsonde body keeps the right vertical position during the falling process, since the

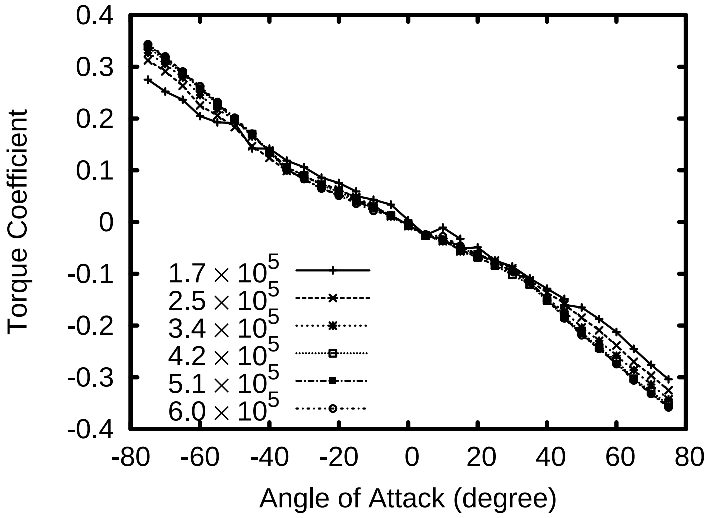

(a) Torque Coefficient with parachute

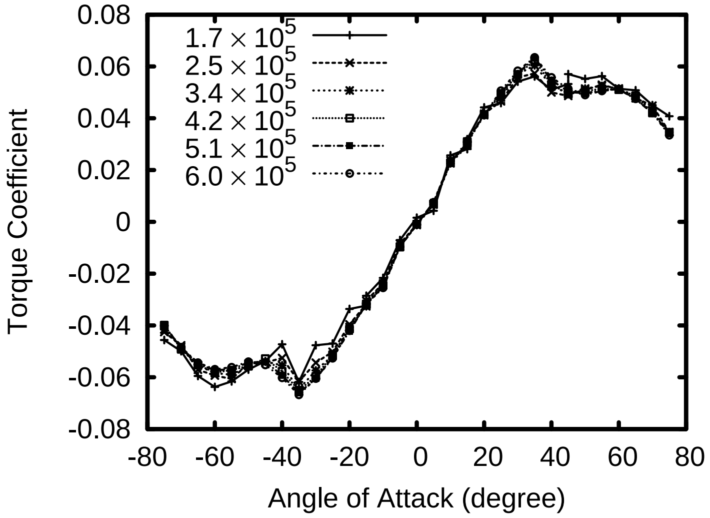

(b) Torque Coefficient without parachute

Figure 3.21: Variation of the torque coefficient with angle of attack under different testing wind speed. Reynolds numbers are indicated by the legend.

it has a sign opposite to the angle of attack. In other words, the parachute provides a recovery torque to reduce the dropwindsonde angle of attack back to 0.

General speaking, the mean of the drag coefficient of the whole dropwindsonde system with the parachute in the smooth flow is 0.65, while the maximum, 0.80, takes place at the angle of attack of 70° and the minimum, 0.51, takes place at the angle of attack of 0°. The coefficient derived implicitly from the terminal falling rate of the dropwindsonde (Hock and Franklin, 1999) is 0.61, as shown in Fig. 3.18(a). The averaged lift coefficient is 0.0011 and the averaged torque coefficient is -0.0033. The drag coefficient for the parachute alone, which can be modelled as a constant, is 0.48.

3.4.3 Conclusions

In conclusion, a wind tunnel test has been conducted to examine the dropwindsonde aerodynamics and their variation with angle of attack to provide reliable estimates of the dropwindsonde aerodynamics and to check the assumption that the variation of the drag coefficient with angle of attack is negligible. The range of angles of attack examined is from -75^o to 75^o, and the range of wind speeds is from $6.1m/s$ to $21.3m/s$. The test results confirm that dropwindsonde aerodynamics are Reynolds number independent. Although the variation of the drag coefficient of the parachute alone can be modelled as a constant, the variation of the drag coefficient of the whole system with the angle of attack is appreciable. This finding invalidates one assumption used in deriving the wind finding equations. Moreover, this feature allows us to model the parachute as a deceleration force applied on the dropwindsonde body which can adjust its orientation to provide a constant drag coefficient. Based on that, the dropwindsonde motion can be described using a motion model different from the one based on the point object assumption shown in section 3.1. In this alternative motion model, the parachute, modelled as a deceleration force, and the dropwindsonde body are described separately.

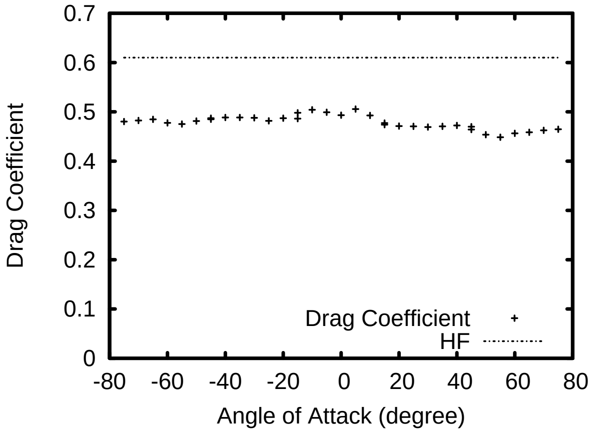

(a) Drag Coefficient

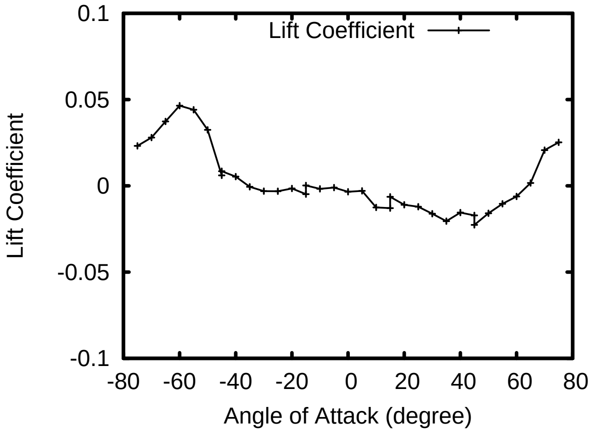

(b) Lift Coefficient

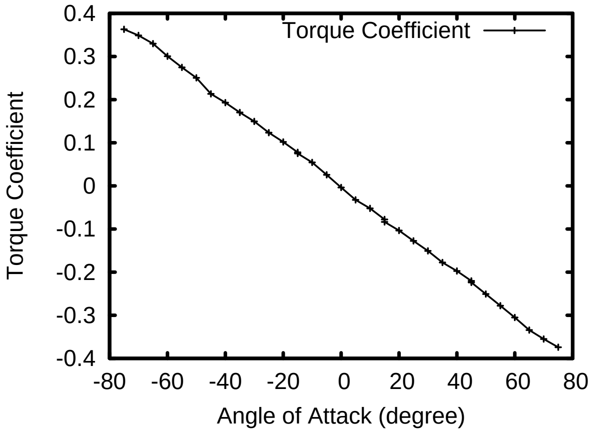

(c) Torque Coefficient

Figure 3.22: Variation of the drag, lift and torque coefficient of the parachute alone with angle of attack. "HF" refers the drag coefficient implied by Hock and Franklin (1999).

3.5 Alternative Motion Model

Adopting findings made in the wind tunnel tests, it is possible to analyze motion characteristics of the dropwindsonde in a more sophisticated way in which the variation of its aerodynamics with angles of attack is included in the model. As opposed to treating the dropwindsonde as a point object with a constant drag coefficient, this model is based on a separation of the dropwindsonde body from the parachute which allows an explicit expression for the variation of the dropwindsonde aerodynamics with angles of attack. This section is devoted to describing this alternative dropwindsonde motion model, including a discussion on its necessity and the model's theoretical derivation.

As introduced in section 3.4, the wind finding equations introduced by Hock and Franklin (1999) are based on the assumption that the dropwindsonde drag coefficient is independent the angle of attack. Due to its importance in reconstructing both the mean and turbulent wind structure of the measured wind field, it is necessary to recheck the validity of the wind finding equations since the wind tunnel test indicates that the constant drag coefficient assumption is invalid. Because the angle of attack is not calculable from dropwindsonde measurements currently, the reinvestigation can only be based on theoretical analyses and numerical simulations. Cockrell (1987) gave a fairly comprehensive description of ways of modelling the motion of a parachute system, in which he suggested that the parachute and its payload (the dropwindsonde body in our case) can be modelled separately to taken into account the difference between the aerodynamics of the parachute and of its payload. Adopting this alternative dropwindsonde motion model, dropwindsonde motion characteristics can be analyzed theoretically and numerically to evaluate the influence of the findings made in the wind tunnel tests. In the evaluation, the winding finding equations, which are derived based on the invalid constant drag coefficient assumption, can be rechecked since the alternative motion model allows the dropwindsonde aerodynamics to vary with angles of attack.

Analyzing dropwindsonde motion characteristics based on the alternative model also improves the calculation retrieving the vertical wind from raw dropwindsonde measurements. The vertical turbulent wind, as one important component in the hurricane wind, determines turbulent fluxes, and correctly estimating vertical turbulent fluxes is critical in hurricane intensity predictions (French et al., 2007; Drennan et al., 2007). Direct observations on the vertical wind, however, are rather rare. Although French et al. (2007), Drennan et al. (2007) and Zhang et al. (2009) revealed some important aspects of turbulent fluxes within the HBL, they did not provide a comprehensive picture of turbulent fluxes in the entire HBL due to their instrument limitations. The dropwindsonde, on the other hand, provides an unprecedented opportunity to measure the vertical wind, and then to calculate turbulent vertical fluxes, in the entire HBL. The conventional way of calculating the vertical wind, as the measured falling speed subtracted from the theoretical falling speed, is crude. Furthermore, the accuracy of this method has yet to be evaluated. The alternative motion model described above, which takes into account the variation of the drag coefficient with angles of attack, leads to a theoretically better estimation of the vertical wind. Based on the dropwindsonde motion simulation, the improvement of using this vertical wind estimation can be evaluated in the comparison with the crude calculation since the "true" vertical wind is known in the pseudo-stochastic wind field.

3.5.1 Description of the Alternative Model

As introduced above, the alternative motion model which separates the parachute and dropwindsonde body is expected to be more appropriate in describing the dropwindsonde motion since the wind tunnel tests showed that the variation of the drag coefficient with angle of attack is not negligible. According to Cockrell (1987), in this alternative model, the parachute and its payload are modelled as two rigid bodies. However, the wind tunnel test results showed that the parachute is able to adjust its orientation to provide a constant drag coefficient. As a result, it is not necessary to model the parachute as a rigid body but it can be simplified as an external deceleration force. Moreover, Cockrell (1987) described both two degrees of freedom motion, i.e. translations in a plane, and three degrees of freedom motion, i.e. adding the rotation to the planar motion. Using the three degrees of freedom motion model, the variation of the dropwindsonde aerodynamics with angle of attack can be taken into account since the rotation explicitly produces the orientation of the dropwindsonde body. The sketch of this alternative motion model is shown in Fig. 3.23.

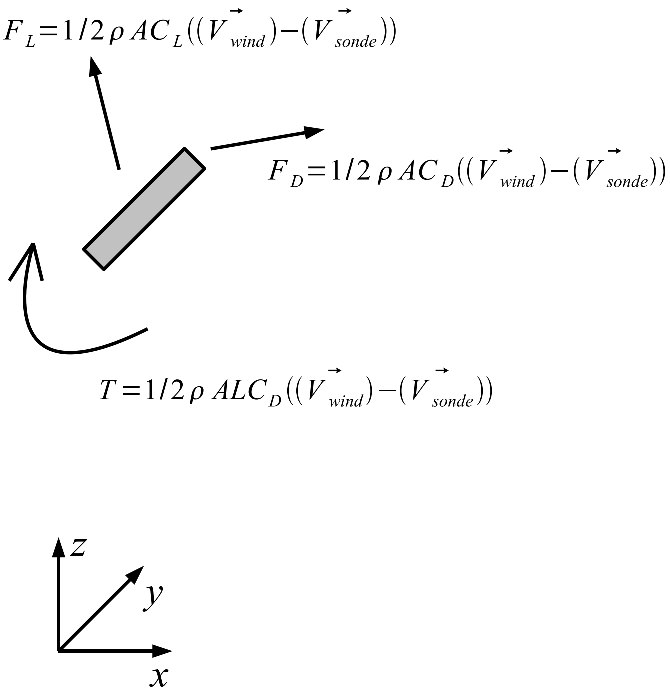

Figure 3.23: Sketch of the alternative model and forces acting on the model.

In this alternative motion model, the dropwindsonde body drag needs to be calculated based on the angle of attack, and can be expressed as,

$$\begin{aligned}
F_{Dx} &= \frac{1}{2}\rho AC_D(\alpha)M(u-\dot{x}) \\
F_{Dy} &= \frac{1}{2}\rho AC_D(\alpha)M(v-\dot{y}) \\
F_{Dz} &= \frac{1}{2}\rho AC_D(\alpha)M(w-\dot{z})+mg
\end{aligned} \tag{3.32}$$

where M is the magnitude of the relative wind vector, $(u-\dot{x}, v-\dot{y}, w-\dot{z})$, and can be expressed as

$$M = \sqrt{(u-\dot{x})^2 + (v-\dot{y})^2 + (w-\dot{z})^2} \tag{3.33}$$

In expressions (3.32) and (3.33), the drag coefficient $C_D(\alpha)$ is consists of two parts: one is provided by the dropwindsonde body $C_{Dbody}(\alpha)$ which depends on angles of attack, α, and the other is provided by the parachute $C_{Dparachute}$ and is constant regardless of angle of attack. F_D represents the drag force while the subscript indicates the force direction. A is the area of dropwindsonde body cross section. $(\dot{x}, \dot{y}, \dot{z})$ is a vector giving the velocity of the dropwindsonde at the position (x, y, z) while the vector (u, v, w) gives the velocity of the driving wind. Moreover, the upward direction is defined as positive in all equations, and therefore the gravity should take the value of $-9.8m/s^2$.

In contrast to treating the dropwindsonde as a point object experiencing only drag, the alternative motion model allows an explicit expression for the lift, such as

$$\begin{aligned}
F_{Lx} &= \frac{1}{2}\rho A C_{Lbody}(\alpha) M (c(v-\dot{y}) - b(w-\dot{z})) \\
F_{Ly} &= \frac{1}{2}\rho A C_{Lbody}(\alpha) M (-c(u-\dot{x}) + a(w-\dot{z})) \\
F_{Lz} &= \frac{1}{2}\rho A C_{Lbody}(\alpha) M (b(u-\dot{x}) - a(v-\dot{y})) + mg
\end{aligned} \tag{3.34}$$

All symbols have similar meanings as in expression (3.32) except the lift coefficient C_L reflects only the contribution made by the dropwindsonde body. $\vec{q} = (a, b, c)$ is a parametric vector with unit magnitude, i.e. $a^2+b^2+c^2 = 1$. This parametric vector is used to determine the direction of the lift. In reality, the total aerodynamic force experienced by the dropwindsonde is decomposed into three spatial components. However, if the force is described in the coordinate system defined by the dropwindsonde relative motion and the coordinate system follows the change of the dropwindsonde body orientation, the lift force calculated according to the lift coefficient measured in the wind tunnel test is actually a combined force whose components are perpendicular to the relative motion vector of the dropwindsonde in two orthogonal directions. As a result, the aerodynamic force experienced by the dropwindsonde needs only be decomposed into the drag and lift, and the parametric vector q, giving the direction of this combined lift force, is calculated as the cross product of the dropwindsonde relative motion vector, $\vec{m} = (u - \dot{x}, v - \dot{y}, z - \dot{z})$, and the orientation vector of the dropwindsonde body, $\vec{p} = (p_x, p_y, p_z)$, as

$$\begin{aligned} \vec{q} &= \vec{m} \times \vec{p} \\ &= (u - \dot{x}, v - \dot{y}, w - \dot{z}) \times (p_x, p_y, p_z) \end{aligned} \tag{3.35}$$

In a component fashion, the parametric vector q reads,

$$\begin{aligned} a &= p_z(v - \dot{y}) - p_y(w - \dot{z}) \\ b &= p_x(w - \dot{z}) - p_z(u - \dot{x}) \\ c &= p_x(u - \dot{x}) - p_y(v - \dot{y}) \end{aligned} \tag{3.36}$$

Considering the rigid body motion of the dropwindsonde body is driven by a combination of aerodynamic forces and the weight force as $m\vec{a} = vecF_D + \vec{F_L}$, it is determined as,

$$\begin{aligned} m\ddot{x} &= \frac{1}{2}\rho AM(C_D(\alpha)(u - \dot{x}) + C_{Lbody}(\alpha)[c(v - \dot{y}) - b(w - \dot{z})]) \\ m\ddot{y} &= \frac{1}{2}\rho AM(C_D(\alpha)(v - \dot{y}) + C_{Lbody}(\alpha)[-c(u - \dot{x}) + a(w - \dot{z})]) \\ m\ddot{z} &= \frac{1}{2}\rho AM(C_D(\alpha)(w - \dot{z}) + C_{Lbody}(\alpha)[b(u - \dot{x}) - a(v - \dot{z})]) + mg \end{aligned} \tag{3.37}$$

Equation (3.37) governs the translation of the dropwindsonde.

Considering that the rotation is driven by the torque, its governing equation can be expressed as,

$$I\ddot{\beta} = T(\alpha) \tag{3.38}$$

where I is the moment of inertia of the dropwindsonde body for rotating around its center, β is the angle between the dropwindsonde body orientation and a reference direction, and $\ddot{\beta}$ represents the angular acceleration. One uncertainty in equation (3.38) is the moment of inertia value, I. Since the exact calculation of I is extremely difficult, a sensitivity analysis of the I value on the dropwindsonde motion simulation is performed. In this sensitivity analysis, a single dropwindsonde drop is simulated based on different moment of inertia values, including $I1$, which is calculated assuming the mass is evenly distributed in the cylinder defined by the outer geometry of the dropwindsonde body, $I2$, which is calculated assuming the mass is concentrated in a slender cylinder with a diameter only 10% of the value found in a real dropwindsonde body and $I3$, which is calculated assuming the mass is concentrated in a tube with an outer diameter the same as the cylinder describing the real dropwindsonde body and a thickness of 10% of that diameter. Figure 3.24 shows the simulation results. It is obvious that the influence of using different values of the moment of inertia is negligible, and therefore the value $I1$ is used in the following simulations and discussions.

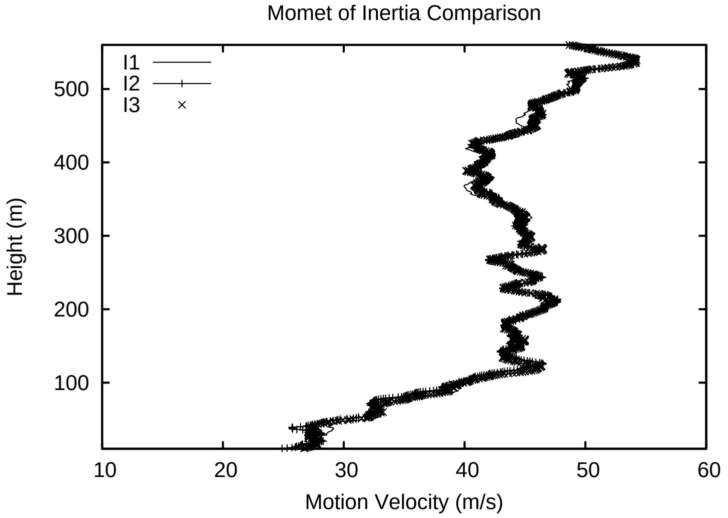

Figure 3.24: Comparison of the velocity profiles from different dropsonde drops simulated based on different momentum of inertia values, the meanings of $I1, I2, I3$ can be found in the text.

In summary, equations (3.37) and (3.38) govern the motion of the dropwindsonde, as a rigid body, and formulate the alternative dropwindsonde motion model.

3.5.2 Numerical Simulation of the Dropwindsonde Motion

Based on the alternative motion model described above, it is feasible to analyze the dropwindsonde motion more realistically. In the simulation, equation (3.37), which is a nonlinear ODE, can be solved numerically to give the dropwindsonde translation in three spatial directions. In addition to translations, since equation (3.38) governs the dropwindsonde rotation, integrating its solution gives the dropwindsonde body orientation. In a word, the dropwindsonde motion can be fully described by these solutions, and the simulation is essentially a proceses seeking these solutions numerically.

One precondition of the motion simulation is the driving wind that appears in the equations, (u, v, w). As for the case of the motion simulation based on the simple model, the pseudo-stochastic wind field with required statistics generated previously serves as the driving wind in this motion simulation. Since the purpose of the simulation presented in this section is to recheck the wind finding equations and to improve the vertical wind calculation, only the pseudo-stochastic wind field generated through the POD approach is used, since there is no need to derive the spectral information out of dropwindsonde measurements now. Details of the pseudo-stochastic wind field generation can be found in section 3.2.

Aerodynamics required in solving the governing equation, such as $C_D(\alpha)$, are given by the wind tunnel test results described in section 3.4. In the simulation, the angle of attack is calculated based on the relative motion vector, $(u-\dot{x}, v-\dot{y}, w-\dot{z})$, and position vector of the dropwindsonde body, (p_x, p_y, p_z), which is derived by integrating the angular accelerations solved for equation (3.38) beforehand, and then the aerodynamic parameters are found by linearly interpolating from wind tunnel measurements.

Under the condition that both the driving wind and real-time aerodynamics are found, the dropwindsonde body motion, including its orientation, can be numerically solved based on equations (3.37) and (3.38). In this process, the fourth-order Runge-Kutta method is adopted to do the numerical integration using a $0.05s$ time step. Both the dropwindsonde body accelerations and velocities are solved directly from the simulation while the positions and orientations are found by integrating direct solutions.

After falling processes of numerous dropwindsondes are simulated, each simulation run makes up an individual pseudo dropwindsonde profile. All pseudo dropwindsonde profiles are then composited to calculate the desired statistics of the measured wind field, as in the case of the motion simulation based on the simple model, which is presented in detail in section 3.1. Both the mean profile, calculated based on pseudo raw measurements, and turbulent variables, calculated based on residuals of pseudo measurements produced by eliminating the mean wind profile, are composited and compared with the "true" statistics calculated from the pseudo-stochastic wind field.

3.6 Alternative Model Simulation Results and Discussions

As the alternative motion model describes the dropwindsonde motion in the measured wind field more realistically, the motion simulation of the dropwindsonde using this alternative model gives the possibility to recheck the validity of the wind finding equations introduced by Hock and Franklin (1999) and to explore a more sophisticated way to calculate the vertical wind. This section is structured into three parts: first, a theoretical analysis of the wind finding equations and a new approach to calculate the vertical wind; second, validations of the wind finding equations based on the dropwindsonde motion numerical simulation and third, an evaluation of the new approach to calculate the vertical wind, also based on the numerical simulation.

3.6.1 Theoretical Analysis

The necessity of re-validating the wind finding equations relies on the difference between the dropwindsonde motion based on the alternative model and the simple motion model, since the analysis would be redundant if there is no obvious difference detected. For that reason, the simple model is also employed to simulate the dropwindsonde motion in the same pseudo-stochastic wind field. Shown in Fig. 3.25 are the dropwindsonde velocities from simulations based on the two different motion models. It can be seen that the velocity series produced are noticeably different in some areas. For example, there is velocity difference up to $3m/s$ in the height region $(250m, 300m)$. However, the dropwindsonde velocity profiles produced by the two motion models does different from each other by a value of $5m/s$ or higher. The feature discussed above substantiates the need to investigate motions and measurements of the dropwindsonde using the alternative model.

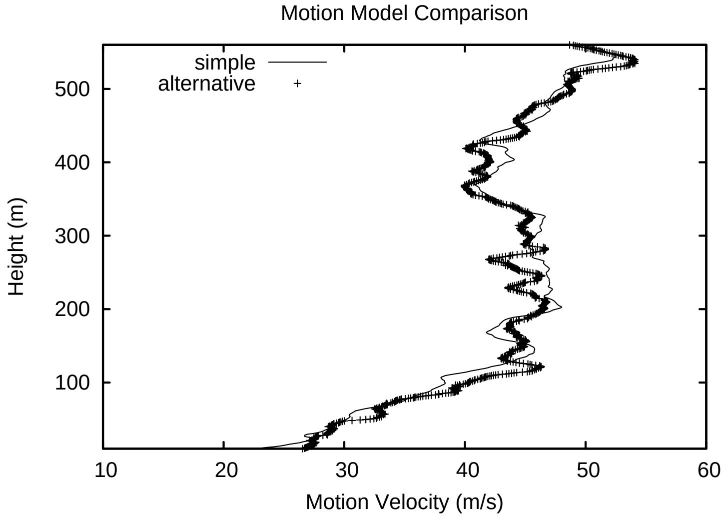

Figure 3.25: Comparison of the velocity profile from a single dropwindsonde drop simulated based on both the simple and alternative motion model.

Substantiated by the comparison seen in Fig. 3.25, the dropwindsonde motion described by the alternative model is close to, but different from, the dropwindsonde motion described by the simple model. Therefore, it is necessary to re-investigate the wind finding equations theoretically using the alternative motion model. In equation (3.32), if the lift force is neglected and the vertical motion equation is linearized under the assumption that $|u - \dot{x}| << |w - \dot{z}|$ and $|v - \dot{y}| << |w - \dot{z}|$, which means the nonlinear term

$$M = \sqrt{(u - \dot{x})^2 + (v - \dot{y})^2 + (w - \dot{z})^2} \tag{3.39}$$

can be linearized as $|w - \dot{z}|$, the equation expressing the drag force in the vertical direction can be solved for the drag coefficient as,

$$C_D(\alpha) = \frac{2m(\ddot{z} - g)}{\rho A |w - \dot{z}|(w - \dot{z})} \tag{3.40}$$

Furthermore, under the assumption that the vertical wind $|w|$ is far less than the dropwindsonde falling rate, $|\dot{z}|$, this expression is simplified as,

$$C_D(\alpha) = -\frac{2m(\ddot{z} - g)}{\rho A \dot{z}^2} \tag{3.41}$$

Substituting equation (3.41) back into equation (3.37) and simplifying under both the linearization assumption and the assumption that $|w| << |\dot{z}|$ gives,

$$\begin{aligned} \ddot{x} &= -\frac{\ddot{z} - g}{\dot{z}}(u - \dot{x}) \\ \ddot{y} &= -\frac{\ddot{z} - g}{\dot{z}}(v - \dot{y}) \end{aligned}$$

Rearranging equation (3.42) produces a set of wind finding equations similar to that found by Hock and Franklin (1999),

$$\begin{aligned} u &= \dot{x} - \frac{\dot{z}}{\ddot{z} - g}\ddot{x} \\ v &= \dot{y} - \frac{\dot{z}}{\ddot{z} - g}\ddot{y} \end{aligned} \tag{3.42}$$

When the dropwindsonde is in a steady fall, in which the absolute value of dropwindsonde vertical acceleration $|\ddot{z}|$ is far less than $|g|$, the term $\ddot{z} - g$ can be replaced by $-g$, and equation (3.42) can be further reduced to

$$\begin{aligned} u &= \dot{x} + \frac{\dot{z}}{g}\ddot{x} \\ v &= \dot{y} + \frac{\dot{z}}{g}\ddot{y} \end{aligned} \tag{3.43}$$

which are exactly the wind finding equations introduced by Hock and Franklin (1999) (see equations (3.13) and (3.14)).

The derivation shown above indicates, although the assumption that the drag coefficient is constant regardless of angles of attack is not valid as revealed by the wind tunnel tests, the wind finding equations are still reliable. This is theoretically understandable since from equation (3.41) it can be seen that the influence of the drag coefficient variation is implicitly reflected by the variation of the measured dropwindsonde falling rate. As a result, it is not necessary to introduce any further corrections about the false constant drag coefficient assumption. From equation (3.42), it is found that the vertical dropwindsonde acceleration should be taken into account when the dropwindsonde motion variables are used to retrieve horizontal winds.

In addition to validating the use of the wind finding equations, the alternative motion model is also able to produce a more sophisticated way to calculate the vertical wind from raw dropwindsonde measurements. The calculation is also derived based on equation (3.37) under the same linearization assumption, which leads to the equation governing the vertical dropwindsonde motion reduces to

$$m\ddot{z} = \frac{1}{2}\rho A|w - \dot{z}|(w - \dot{z})C_D(\alpha) + mg \tag{3.44}$$

Then, the vertical wind can be solved as,

$$w = \sqrt{\frac{2m(\ddot{z} - g)}{\rho A C_D(\alpha)}} + \dot{z} \tag{3.45}$$

under the assumption that the vertical wind, w, is always larger than the falling rate $\dot{z}$, which is around $-12m/s$. Since the vertical wind should fluctuate around $0m/s$ in theory, it is smaller than $-12m/s$ is considered very unlikely even under hurricane wind conditions. Comparing with the conventional way to calculate the vertical wind using the measured dropwindsonde falling speed subtracting the theoretical falling rate, which can be expressed as,

$$w = \dot{z}_{theoretical} + \dot{z} \tag{3.46}$$

where the theoretical dropwindsonde falling speed is

$$\dot{z}_{theoretical} = \sqrt{\frac{2mg}{\rho A C_D}} \tag{3.47}$$

Equation (3.45) takes two additional factors into consideration, the vertical dropwindsonde acceleration and variation of the drag coefficient with angle of attack.

3.6.2 Validation of the Wind Finding Equation

In addition to validating the wind finding equations theoretically, numerical simulation results are employed in the re-investigation process. Simulations are conducted in the same pseudo-stochastic wind field based on both the simple model, in which the dropwindsonde is treated as a point object with a constant drag coefficient regardless of angles of attack, and on the alternative model. Once the improvement of using the wind finding equations in deriving desired wind statistics from pseudo measurements simulated using the alternative motion model is found similar to that using the simple motion model, the conclusion can be drawn that the wind finding equations are still valid even through the variation of the drag coefficient with angle of attack is not negligible.

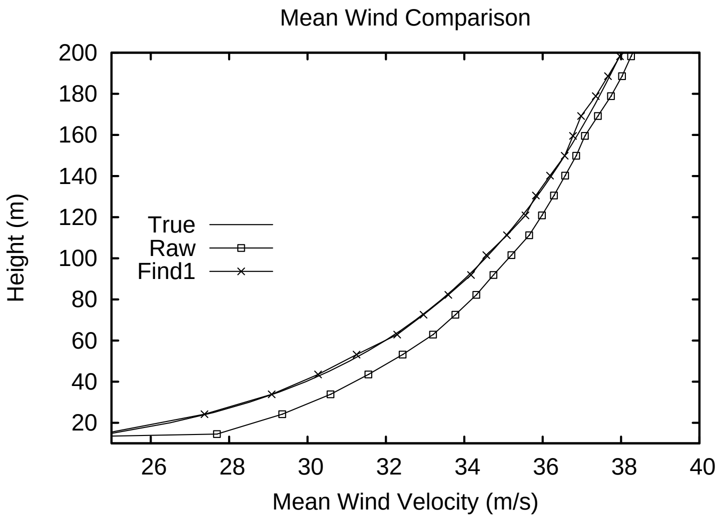

(a) Simple Model

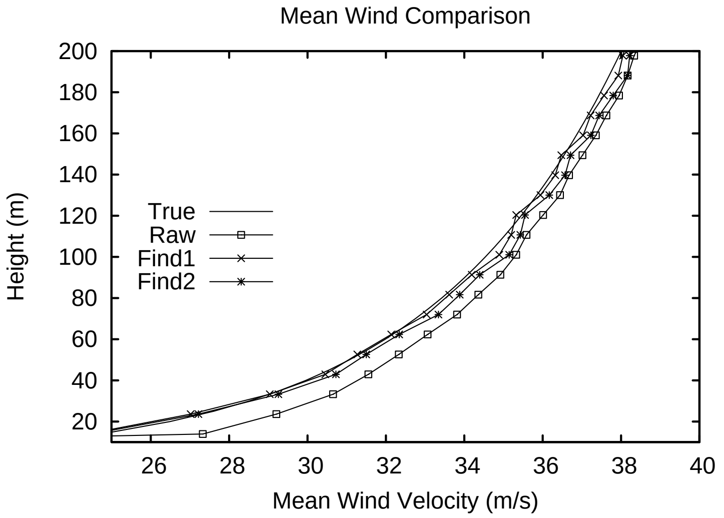

(b) Alternative Model

Figure 3.26: Comparison of the mean wind velocity profiles, "Raw" refers to the composition results based on raw dropwindsonde measurements, "Find1" refers to the wind retrieved by the wind finding equations, "Find2" refers to the calculation results of equation (3.42) and "True" refers to the preset value of the pseudo-stochastic wind field.

Shown in Fig. 3.26 is the comparison of the mean wind profile composited from pseudo dropwindsonde measurements generated based on two different motion models. Comparing Fig. 3.26(a) to Fig. 3.26(b), it is obvious that the wind finding equations are still valid to correct the dropwindsonde deficiency in reproducing the mean profile in a sheared wind field. The similar improvement seen in these two figures substantiates that the variation of the drag coefficient with angle of attack does not invalidate the use of the wind finding equations to find the correct mean wind profile. In addition, a similar improvement is also seen in Fig. 3.27 which compares the turbulent wind velocity profile. This demonstrates the wind finding equations are still valid to recover the turbulence intensity profile of the measured wind field, which was underestimated by raw dropwindsonde measurements.

In the theoretical discussion of the validity of the wind finding equation detailed in the previous subsection, there is an additional correction appeared, comparing with the conventional wind finding equation, to take into account the influence of the dropwindsonde vertical acceleration (see equation (3.43 and equations (3.13), (3.14)). The effect of using the term $\ddot{z} - g$ to replace $-g$ in the wind finding equations is illustrated in Figs. 3.26(b) and 3.27(b). It is found that the improvement is insignificant. Moreover, since the dropwindsonde acceleration is not directly reported by the dropwindsonde but must be calculated by differentiating the dropwindsonde falling rate, the improvement of this additional correction will be easily buried by extra errors introduced by the differentiation. Besides, since the dropwindsonde acceleration is relatively small comparing with the gravity acceleration, g, its influence is expected to be minimal in the term $\ddot{z} - g$. As evidence of this statement, the vertical acceleration solved directly from simulations concentrates in the range of $(-1m/s^2, 1m/s^2)$ (more than 70%), as shown in Fig. 3.28. In conclusion, this additional correction is not recommended in processing actual dropwindsonde measurements.

It can be noticed that pseudo measurements produced by the alternative motion model, after dynamically corrected using the wind finding equations, overestimate the turbulence

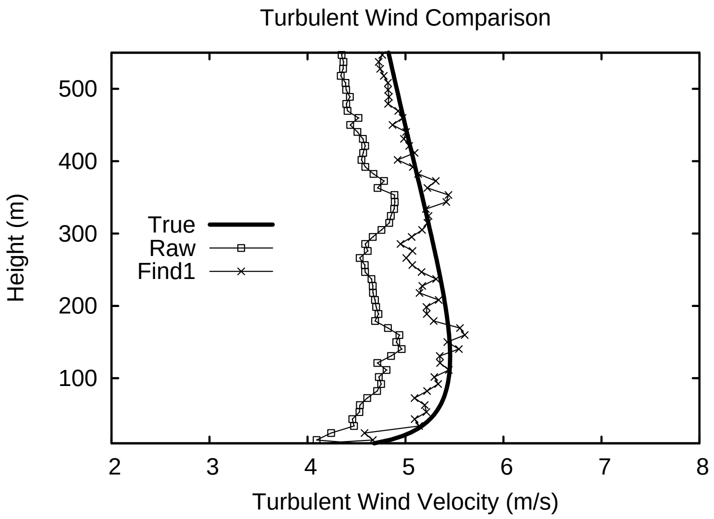

(a) Simple Model

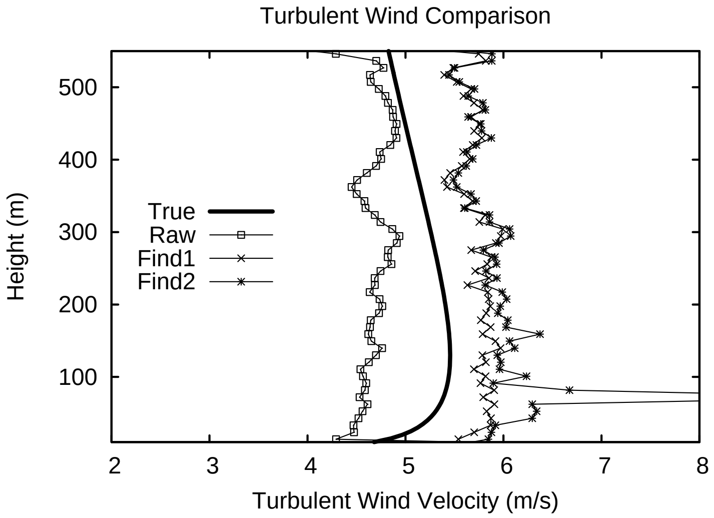

(b) Alternative Model

Figure 3.27: Comparison of the turbulent wind velocity profile, "Raw" refers to the composition results based on raw dropwindsonde measurements, "Find1" refers to the wind retrieved by the wind finding equations, "Find2" refers to the calculation results of equation (3.42) and "True" refers to the preset value of the pseudo-stochastic wind field.

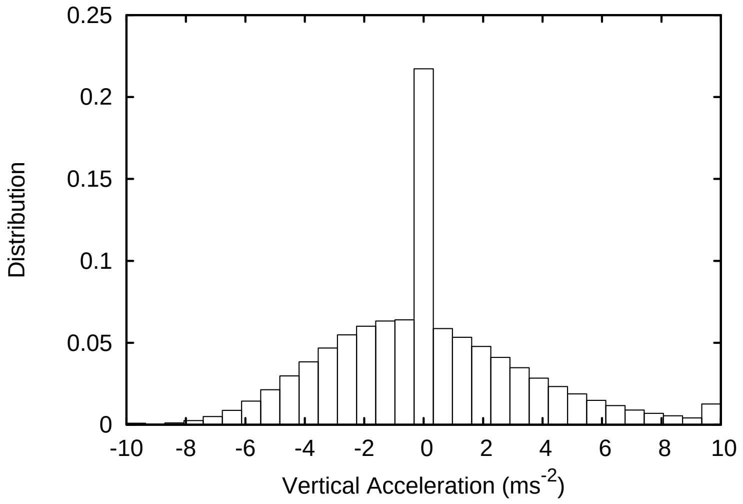

Figure 3.28: Distribution of the dropsonde vertical acceleration over a range $[-10ms^{-2}, 10ms^{-2}]$, boxes show the probability density.

intensity of the measured wind field for both the original equation introduced by Hock and Franklin (1999) and for equation (3.42) with the additional correction. This can be explained by the alternative model nature which includes the variation of the dropwindsonde aerodynamics with angle of attack. From equations (3.37) and (3.38), it can be seen that the influence of the driving wind is not only on the driving forces but also on the angle of attack, which in turn influences the dropwindsonde aerodynamic values. Thus, the dropwindsonde motion described by the alternative model is more sensitive to fluctuations of the driving wind comparing with the simple model described dropwindsonde motions. This effect is illustrated in Fig. 3.27, as the turbulent wind velocity calculated by compositing raw dropwindsonde measurements is higher in the simulations using the alternative motion model than in the simulations using the simple motion model. Moreover, the dynamic correction in the wind finding equations duplicates the influence of fluctuating winds since both the horizontal dropwindsonde velocity $\dot{x}$, $\dot{y}$ and dropwindsonde falling rate $\dot{z}$ implicitly contains this influence. As a result, the use of the wind finding equations overestimates the turbulent wind velocity if the variation of the dropwindsonde aerodynamics with angle of attack is not neglected. However, a low-pass filter is often utilized in processing actual dropwindsonde measurements which reduces fluctuations of both horizontal and vertical dropwindsonde "reported" wind velocities. As a result, the overestimation seen in Fig. 3.27 is not expected in processing dropwindsonde measurements in practise, at least not with a similar magnitude.

3.6.3 Calculation of the Vertical Wind

The vertical wind estimation is critical in calculating turbulent fluxes, since both turbulent momentum flux and heat flux calculations depend on estimates of the vertical turbulent wind. However, the vertical wind measurement taken by the dropwindsonde has not been thoroughly investigated, but only a crude estimation is available presently based on the theoretical dropwindsonde falling rate. More specifically, the vertical wind is calculated by subtracting the theoretical falling speed from the measured falling speed. Comparing with this crude calculation, equation (3.45) is expected to give a better estimate of the vertical wind.

Using equation (3.45), the vertical wind can be calculated from the pseudo dropwindsonde measurements derived in the numerical dropwindsonde motion simulations. Meanwhile, the pseudo-stochastic wind field also contains the exact vertical wind used in the numerical simulation. If the error is defined as the absolute value of the velocity difference between vertical wind calculated using equation (3.45) and interpolated from pseudo-stochastic wind field, it can be treated as one raw measurement in the composition process to produce a mean error profile. As a result, the improvement of using equation (3.45) in estimating the vertical wind can be quantified. Figure 3.29 shows the comparison of such mean error profiles. Obviously, equation (3.45) calculates a more accurate vertical wind for all heights. More specifically, equation (3.45) improves the accuracy in estimating the vertical wind by nearly 70% comparing with the crude estimation currently used. In addition, the turbulent momentum flux is calculated based on two vertical wind estimates, as shown in Fig. 3.30. As for the error comparison, this substantiates that equation (3.45) indirectly gives a more accurate estimate of the turbulent momentum flux. Since the turbulent flux calculation is crucial in predicting intensities of hurricanes (Nolan et al., 2009b,a), this improvement is important in fully utilizing dropwindsonde measurements to give a more reliable turbulence model of the

HBL.

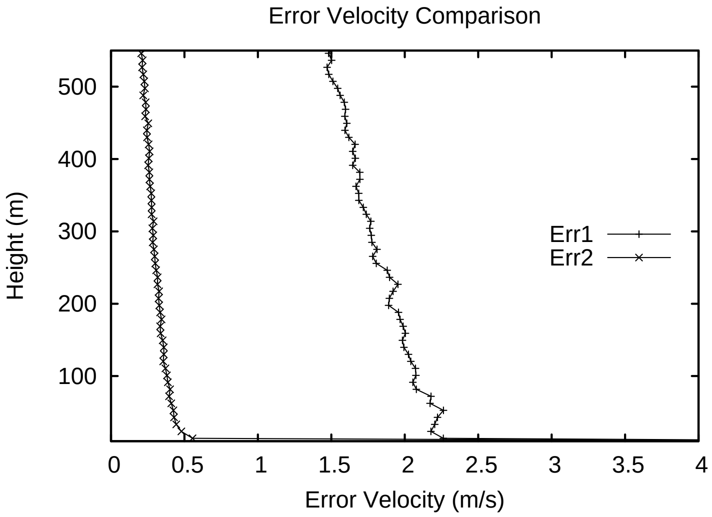

Figure 3.29: Comparison of the error in calculating vertical wind using different methods, the "Err1" refers to the error resulted from the conventional calculation, the "Err2" refers to the error resulted from the calculation using equation (3.45).

In reality, the angle of attack is not reported by the dropwindsonde instrumentation, and therefore there is no way to find out real-time drag coefficients in practise as in simulations. Besides, the vertical acceleration is not directly reported, but must be calculated by differentiating the dropwindsonde falling rate. In some cases, even the dropwindsonde falling rate itself is calculated as the differentiation result of height measurements. Thus, there are three potential error sources for the vertical wind calculation using equation (3.45): the error introduced in finding real-time aerodynamic drag coefficients and the errors introduced by finite differences, for calculating either the dropwindsonde vertical acceleration or dropwindsonde falling rate. Currently, there is no way to check the error introduced in the process of finding the real-time aerodynamic drag coefficient, and therefore only the error introduced by finite differences is quantified based on simulation results here. To do that, the dropwindsonde motion simulation results needs to be processed as if they are actual dropwindsonde measurements. Since the time step used in the numerical simulation is $0.05s$, which is substantially smaller than the sampling interval used currently, $0.5s$, simulation results need to be sampled at a frequency of $2Hz$

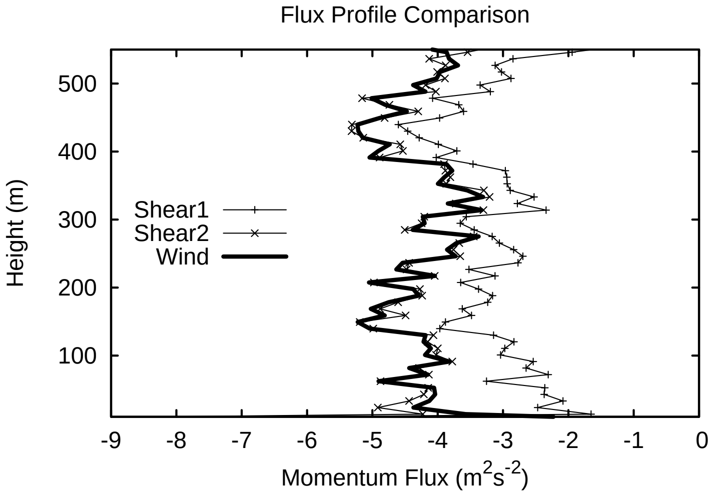

Figure 3.30: Comparison of the turbulent momentum flux calculated using different vertical winds, "Shear1" refers to the estimation based on the conventionally calculated vertical wind, "Shear2" refers to the estimation based on the vertical wind calculated using equation (3.45) and "Wind" refers to the calculation based on the "true" wind interpolated from the pseudo-stochastic wind field.

to generate the "pseudo" measurement. Then, the first-order backward finite difference, which is used widely in processing actual dropwindsonde measurements, is conducted to calculate the vertical falling rate from "pseudo" height measurements and the vertical acceleration from "pseudo" falling rate measurements. After these pseudo measurements are processed as described above, the error, which is defined exactly as in Fig. 3.29, can be calculated and composited. Shown in Fig. 3.31 is the comparison of mean error profiles. Clearly in the error comparison, the most significant improvement is introduced by using the "true" vertical dropwindsonde accelerations which are directly solved in the simulation. This trend is also seen in Fig. 3.32, which compares the turbulent momentum flux profiles as the turbulent momentum flux calculated using "true" vertical accelerations gives a profile closest to the one calculated using the "true" vertical wind interpolated from the pseudo-stochastic wind field. This suggests the significant improvement of using equation (3.45) to calculate the vertical wind seen in Fig. 3.29 depends on an accurate estimate of the vertical dropwindsonde acceleration. However, even when the vertical acceleration is only crudely calculated by differentiating the dropwindsonde falling rate, equation (3.45) still improves the vertical wind estimates noticeably. From the discussion above, the conclusion can be drawn that equation (3.45) outperforms the crude vertical wind estimation currently used, and therefore is recommended in processing actual dropwindsonde measurements.

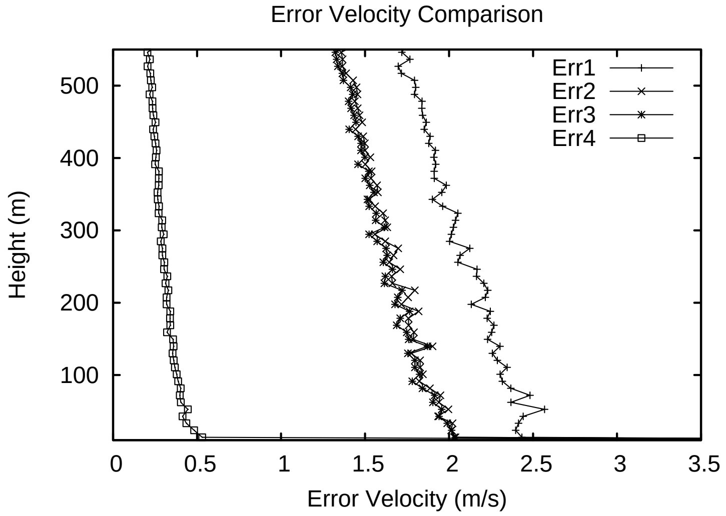

Figure 3.31: Comparison of the error in calculating vertical wind using different methods, "Err1" indicates the use of the conventional calculation while "Err2" through "Err4" all resulted from the use of equation (3.46), in which "2" uses both differentiated vertical acceleration and falling rate, "3" replaces differentiated falling rate with the "true" value in the simulation and "4" uses both the "true" falling rate and vertical acceleration.

From the discussion given above, the angle of attack is demonstrated to be important in calculating the vertical wind, and then in calculating the turbulent flux. In addition, the angle of attack is capable of identifying questionable measurements. Because a large angle between the dropwindsonde body orientation and relative motion direction may indicate the rope linking the parachute and dropwindsonde body is loose, it implies an invalid measurement, at least for the acceleration calculation. Thus, the dropwindsonde body orientation impacts not only the calculation of real-time dropwindsonde aerodynamics, but also on the validity of its measurement. For this reason, the angles of attack produced in simulations are investigated. Figure 3.33 shows the distribution of angles of attack in all simulation runs. As expected, the angle of attack in most cases is in the range of $(-30°, 30°)$. The corresponding drag coefficient, from the wind tunnel results, is in the range of $(0.51, 0.60)$, while the value implied by the terminal falling rate of the

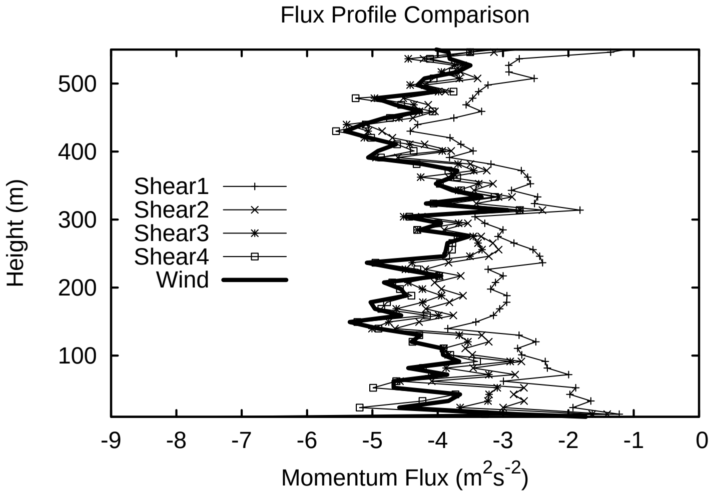

Figure 3.32: Comparison of the turbulent momentum flux calculated using different vertical winds, where the vertical wind used is in the same order as in the error comparison. "Wind" represents the result calculated using the "true" wind interpolated from the pseudo-stochastic wind field.

dropwindsonde is 0.61 (Hock and Franklin, 1999). On the other hand, shown in the figure, there is a considerable amount of simulation runs in which the angle of attack exceeds the range of $(-50°, 50°)$.

3.6.4 Conclusions

Based on the findings made in the wind tunnel tests, the assumption that the dropwindsonde drag coefficient is independent from the angle of attack is found to be invalid. Therefore, the use of the wind finding equations, which are derived based on such assumptions, in retrieving horizontal winds from dropwindsonde measurements is questionable. Since the wind finding equations had been found important in recovering both the mean and turbulent structure of the measured wind field, it is necessary to recheck its validity taken into consideration that the variation of its aerodynamics is not negligible. For that purpose, an alternative dropwindsonde motion model is employed. Since the dropwindsonde body in the alternative model has one rotation degree of freedom, the variation of the drag coefficient is explicitly modelled. In the derivation of the alternative model, it is found that the wind finding equations are still valid even if the variation of the

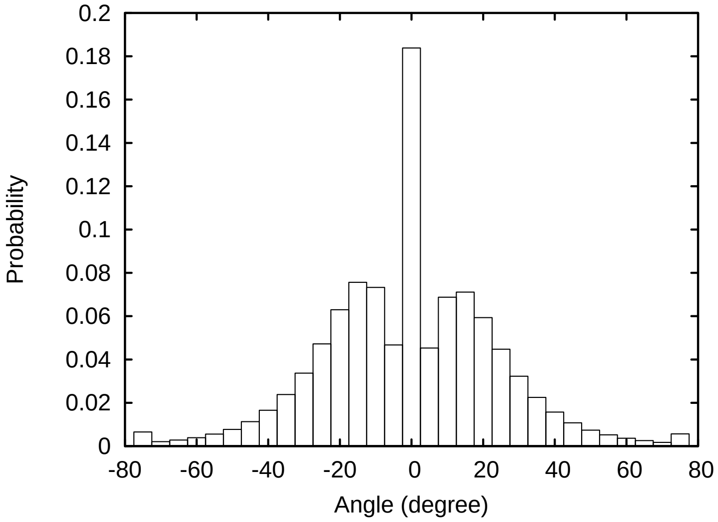

Figure 3.33: Distribution of angle of attack plot over the range $(-75°, 75°)$, boxes show the probability density.

dropwindsonde aerodynamics are not neglected. In addition to the theoretical analysis, numerical simulations of the dropwindsonde motion in the pseudo-stochastic wind field, similar to the one presented in section 3.1, are conducted, which further validated the use of the wind finding equations.

Besides, the alternative motion model also produces a new approach to calculate the vertical wind. When compared to the crude calculation currently used, the new approach takes two additional factors into account, the variation of the drag coefficient with angle of attack and the dropwindsonde vertical acceleration. It has been found that it improves the accuracy in estimating the vertical wind by 70%, and the improvement is also seen in calculating the turbulent momentum flux.

It has been found in discussing the numerical simulation results that the dropwindsonde body orientation is one important piece of information in retrieving winds from dropwindsonde measurements since it can be used to calculate the angle of attack. In addition, this information can also be used to identify questionable dropwindsonde measurements since it may imply that the connection between the dropwindsonde body and parachute is lost. Thus, it is worth adding a direct measurement of the dropwindsonde body orientation in its instrumentation as the technology equipped in the dropwindsonde develops.

Chapter 4

Wind Characteristics of the HBL

As discussed in chapter 1, the HBL plays a key role in overall hurricane dynamics (Wang and Wu, 2004). In addition, studies have indicated that correctly modelling turbulence exchanges within the HBL is one of the keys in a successful numerical simulation of hurricanes (Nolan et al., 2009a; Braun and Tao, 2000; Davis and Bostart, 2002). Besides, turbulence in the hurricane surface layer determines wind loads on structures in hurricane-prone regions (Yu et al., 2008). Therefore, turbulence characteristics in the HBL, especially its vertical structure, deserve a systematical and thorough study. However, few efforts have been made advancing our understanding of HBL turbulence (Moss, 1978; Zhang et al., 2009, 2011), and therefore the turbulence within the HBL is usually assumed similar to that in the standard ABL for engineering and meteorological applications. For example, the PBL schemes designed to describe turbulent mixing in the standard ABL have been widely used in numerically simulating hurricanes (Nolan et al., 2009b,a). In the following discussion, the standard ABL is defined as the ABL over land or over the sea in near-neutral stability, and its general wind strength (measured as mean of wind velocities under $500m$ from the surface) should be less than $20m/s$. The mean wind profile in the standard ABL can be described by a logarithmic function of height and the turbulence diffusivity in the standard ABL follows the prediction made by the mixing length theory proposed by Prandtl (1925).

According to the findings made about the wind retrieval from raw dropwindsonde measurements through numerically simulating the dropwindsonde motion in the measured wind field as detailed in chapter 3, turbulence characteristics of the HBL are derivable provided the composition data size of dropwindsonde measurements is large enough. In this chapter, the actual dropwindsonde measurements are processed and composited to produce the desired turbulence information of the measured HBL wind field, which covers the turbulence intensity, vertical spatial correlations, turbulent integral length scale and height scale of the HBL. To fully incorporate the outcomes of the dropwindsonde motion simulation, a package of the specially designed codes developed as part of this thesis work, named PostSonde, is used to do the post-processing and composition. Since this newly developed software is not thoroughly validated, the individual dropwindsonde profiles post-processed by other two widely used sounding analysis systems, namely EDITSONDE and Aspen, are compared to the results from PostSonde to validate the post-processing part of this newly developed processing system. Furthermore, the mean wind profiles are also calculated and compared to the mean wind structure of the HBL found in several previous studies to validate the composition part of PostSonde, which also produces a more comprehensive insight into the mean wind structure of the HBL.

Both a description of the processing and composition methodology and a discussion of the composition results are presented in this chapter, so it is divided into two parts. The first part is devoted to describing the data set, processing procedures and composition schemes, which are presented in section 4.1. Since the findings made based on compositing dropwindsonde wind measurements constitute the main outcomes of this thesis work, they are elaborated in four successive sections. Section 4.2 discusses the mean wind profiles calculated by the composition and their comparison to the results of several previous studies; section 4.3 presents the vertical structure of the turbulence intensity, which is validated by the reconnaissance flight observations described by Zhang et al. (2009); section 4.4 describes the way to calculate vertical correlations of turbulence, and presents the turbulent integral length scale calculated based on vertical turbulence correlations; section 4.5 discusses the HBL height found in the composition using the analysis framework provided by Zhang et al. (2011). From the wind characteristics found by compositing dropwindsonde measurements, conclusions and suggestions on modelling the HBL turbulence are summarized in section 4.6.

4.1 Dropwindsonde data and composition techniques

As described by Hock and Franklin (1999), the dropwindsonde was introduced to take measurements of winds and other meteorological variables in the HBL in the early 1990's, and it has been intensively involved in systematical hurricane observation projects since then. Its measurement database accumulated in the last decade has provided an unprecedented opportunity to reveal the vertical wind structure within the HBL. As pioneered by Powell et al. (2003), composition techniques are employed to produce the mean wind profile based on dropwindsonde measurements. Vickery et al. (2009) followed the same methodology and used a larger database to do a more comprehensive analysis of the mean wind structure in the HBL, and provided an empirical profile function describing the vertical variation of the mean wind velocity in the HBL. Details about these two studies can be found in section 2.2 of the literature review chapter.

The same composition philosophy is adopted here to process and composite dropwindsonde measurements in conjunction with a measurement database larger than that of Vickery et al. (2009). The composition utilized in previous studies only produces the mean wind profile of the measured HBL wind field. In an effort to extend these previous works, the turbulence information is derived in addition to the mean wind structure in the composition process. For such purpose, a package of specially designed codes developed as part of this thesis work, which gives users more control over the processing and composition of dropwindsonde measurements, is used here to fully incorporate the findings made by analyzing the dropwindsonde motion characteristics. As for the composition configurations, several other grouping indicators are adopted in addition to the Mean Boundary Layer (MBL) wind speed, which is a standard composition scheme employed in previous studies (Powell et al., 2003; Franklin et al., 2003; Vickery et al., 2009). Given that this section is devoted to presenting the background information about the composition results and procedures producing these results, it is divided into two parts: one, a brief description of the HBL characteristics discussed; two, a depiction of the database, post-processing procedures and composition schemes.

4.1.1 The composited HBL wind characteristics

At first, the mean wind structure is derived, as in previous studies. In the derivation, the composition framework adopted by Vickery et al. (2009) is followed, in which both the MBL wind speed, defined as the mean of the wind speeds measured below $500m$, and the relative position of the measurement are used as grouping indicators. Although Vickery et al. (2009) also used the RMW of storms as another grouping indicator in the composition, this indicator is not adopted here. However, another grouping indicator, the gradient wind velocity, is added in the composition scheme. The gradient wind velocity is calculated by averaging the wind velocity measured from $1500m$ to $2000m$ (height above the sea surface). In addition, grouping according to the relative position of the dropwindsonde measurement is refined, which leads to three, instead of two, regional categories set up in the composition scheme. More specifically, the horizontal dropwindsonde measurement position is categorized into the inner core region, the eye-wall region and the out-skirt region. Comparing to two regional categories scheme adopted in the study of Vickery et al. (2009), one near the RMW and one away from the RMW, this grouping scheme shows the composition results in a more organized and comprehensive way.

Secondly, the vertical structure of the turbulence intensity is calculated after the mean wind profile is taken away. This calculation relies on finding the turbulent component of the measured wind velocity, which requires some additional processing. Since the additional processing is innovative and unvalidated, the turbulent wind velocity calculated is compared to similar results from the CBLAST experiment in the lowest $500m$ (J. Zhang 2011, personal communication). As will be seen in this comparison, the compositional approach to find the turbulent component of the measured wind is consist with the HBL turbulent wind vertical structure found based on other observations. From this validation, the discussion of the turbulent wind vertical structure in the HBL is carried out, which covers the entire HBL up to $3000m$.

Thirdly, the turbulent integral length scale is calculated based on turbulence vertical spatial correlation coefficients found beforehand. Unlike the turbulence intensity, the turbulent integral length scale influences the turbulence diffusivity directly, which is one important parameter in the boundary layer turbulence models used for atmospheric flow numerical simulations. As currently utilized in WRF, the Yonsei University Scheme (YSU) scheme prescribes the turbulence diffusivity profile as a cubic function of height (Hong and Pan, 1996; Hong et al., 2006). This formulation is widely used in hurricane numerical simulations despite the fact that it is designed to describe turbulent mixing in the standard ABL (Troen and Mahrt, 1986; Noh et al., 2003). Considering that the turbulence diffusivity is closely related to the turbulence length scale in the ABL according to the ”mixing length” theory (Pena et al., 2010), an accurate and reliable description of the turbulence length scale varying with height can help correctly model the turbulence diffusivity behaviour in the ABL as explored by Gryning et al. (2007) and Pena et al. (2010). Therefore, the turbulent component of the measured wind found in the previous step is used to calculate the vertical spatial correlation coefficient, which then produce the vertical turbulent integral length scale through a integration approach. The calculated length scale, combining with an assumed variation of the turbulent momentum flux, produces the turbulence diffusivity profile. The profile calculated from observations is then compared to the profile prescribed in the YSU scheme to check the applicability of the scheme in simulating turbulent mixing in the HBL.

Finally, the height of the HBL, another important factor in the boundary layer turbulence modelling (Zhang et al., 2011), is investigated. This parameter is important because, first, it determines up to where the PBL scheme applies; second, many ”non-local” PBL schemes, including the YSU scheme, use the boundary layer height as a parameter to prescribe the turbulence diffusivity vertical profile (Hong and Pan, 1996;

Hong et al., 2006). From previous studies (Zhang et al., 2009, 2011), there is no consensus among the hurricane research community on what should define the top of HBL due to the poor understanding of HBL turbulence processes. Therefore, the composition of dropwindsonde measurements is used to calculate the HBL heights according to various definitions following the methodology given by Zhang et al. (2011). The major issue associated with the HBL height calculation is the discrepancy of the height value calculated based on different definitions. In extending the study of Zhang et al. (2011), the height found based on the turbulent integral length scale given in the previous step is included in the discussion. Given that the current understanding relates the HBL height to turbulence processes in the HBL, this height definition should provide insights into this important length scale of the HBL.

4.1.2 Data and Processing Technique

As described by Hock and Franklin (1999), the dropwindsonde is released by reconnaissance flights penetrating through tropical cyclones, and it is able to report the wind velocity, air temperature, humidity, etc. every $0.5s$. The accuracy of its measurement for the wind speed is about $1m/s$, for the temperature is about 0.2°C, and for the relative humidity is about 5%. Its falling speed decreases as it moves downwards due to the increase of the air density and eventually researches its terminal velocity, which is about $12m/s$.

As maintained by the HRD of NOAA, a considerable dropwindsonde measurement database has been built up which allows a derivation of turbulence characteristic within the HBL. To get statistically meaningful results, a database much larger than that used in previous studies is adopted here. More specifically, dropwindsonde measurements gathered from the earliest publicly available time, the year 1997 to the year 2010, constitute the measurement database utilized here. The total number of dropwindsonde profiles processed is more than 10000. However, many profiles are eliminated from the database due to the failure in calculating the reliable storm center and RMW for those particular profiles. As a result, the total number of the profiles composited is around 4000, and is different for different composition strategies. The necessity and details of calculating the storm track and RMW are given in the following paragraphs.

Before compositing dropwindsonde measurements to produce the desired statistics of the measured wind field, dropwindsonde measured profiles need to be post-processed, which includes a quality control process, dynamic corrections of the wind and other thermodynamic variables and low-pass filtering of dropwindsonde profiles. The quality control process is either an automatic or a human-intervention process to eliminate erroneous and questionable measurements from an individual dropwindsonde profile. Dropwindsonde wind measurements are then dynamically corrected using the wind finding equations, which have been found important in deriving not only the mean but also turbulent wind structure of the measured wind field. Finally, dropwindsonde profiles are low-pass filtered to eliminate high-frequency measurement noise. As mentioned above, a package of specially designed code, named PostSonde, is employed to complete the post-processing described above. Following the functions provided and procedures utilized by EDITSONDE (J. L. Franklin 2010, personal communication), PostSonde is able to conduct a fairly comprehensive quality control, and PostSonde gives users the control over the selection of the differentiation scheme to calculate the dropwindsonde acceleration, which is required in the wind finding equations. In addition, the design of the low-pass filter is also adjustable in PostSonde. To justify the use of PostSonde, several selected post-processed dropwindsonde profiles, produced by PostSonde and other popular dropwindsonde measurements processing systems, namely EDITSONDE and Aspen, are compared. One of the comparisons is shown in Fig. 4.1. Although the comparison indicates processed profiles from three different programs are not identical for all the heights, they are nearly indistinguishable for a large portion of the comparison, and those noticeable differences can be explained by the different criteria used in the quality control process. It should be noted that the post-processing scheme is not fully retrievable for EDITSONDE and Aspen, since EDITSONDE processing results are taken directly from the database maintained by the HRD, and Aspen is a total "black-box" software from which no internal processing scheme can be uncovered. Thus, the quality control criteria and dynamic correction procedures are inevitably different for three different processing systems. Nevertheless, the obvious agreement shown in the figure supports the use of PostSonde in post-processing dropwindsonde measurements. As for the configuration of the post-processing, the second-order central difference is used to calculate the dropwindsonde accelerations, and a moving average filer with a cut-off time scale of 3s is used to smooth the curve.

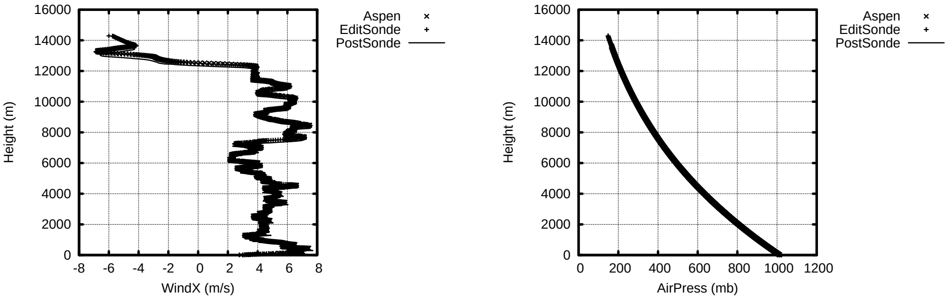

(a) Longitudinal Wind Comparison (b) Air Pressure Comparison

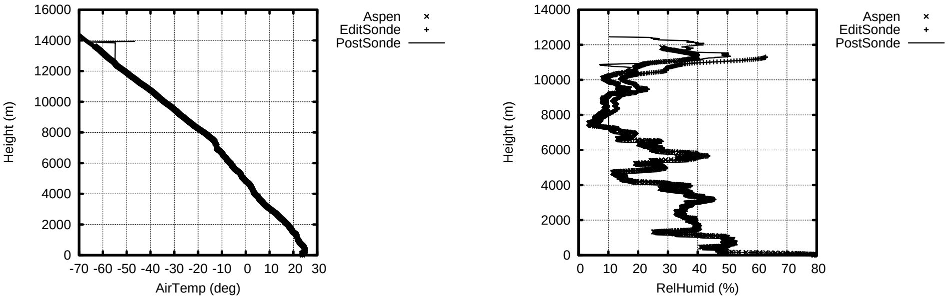

(c) Air Temperature Comparison (d) Relative Humidity Comparison

Figure 4.1: Comparison between dropwindsonde profiles processed by PostSonde, EDITSONDE and Aspen, the wind velocity shown is decomposed from the total wind velocity according to its orientation relative to the longitude circle.

After the post-processing procedures articulated above, dropwindsonde profiles are composited to produces desired statistics of the measured wind field. Following the same methodology proposed by Powell et al. (2003), dropwindsonde profiles are composited according the mean wind velocity measured in lowest 500m, or the MBL wind velocity. Given that the current database is much larger than that used in previous studies, the resolution of the MBL wind speed based composition can be increased. In detail, dropwindsonde profiles are divided into 18 groups, corresponding to the MBL wind velocity from $20m/s$ to $74m/s$ increasing at a $3m/s$ step. Since the gradient wind velocity is also an important velocity scale in the HBL (Kepert, 2001; Foster, 2009), the mean of the wind velocities measured from $1500m$ to $2000m$ is also used as a grouping indicator. In addition, considering that the wind field measured by dropwindsondes obviously varies horizontally, the combination of the MBL wind velocity and dropwindsonde splash down location, defined as where the dropwindsonde hits the sea surface, is also used to group processed dropwindsonde profiles. In order to keep the composition size large enough to produce statistically meaningful results for each group in the combined composition, the MBL wind velocity step is increased to $10m/s$. As mentioned above, the dropwindsonde splash down location is categorized into three regions, the inner core region, the eye-wall region and the out-skirt region based on its normalized radius to the storm center, which is defined as the actual radius divided by the storm RMW. Moreover, to validate the composition part of PostSonde, the exactly same composition strategy, as in the study of Vickery et al. (2009), is adopted. Then, the composition results are compared to the calculations results of their empirical profile function.

Since the grouping scheme combining the MBL wind speed and dropwindsonde splash down location requires the center location and RMW of storms to be found before the composition, the track and size of tropical cyclones are calculated first. Following the technique proposed by Kepert (2005), the track and RMW of a storm are determined by fitting the sea level pressure observed by the dropwindsonde, and sometimes the geopotential height observed by concurrent reconnaissance flights, to an idealized pressure, or geopotential, horizontal profile. The fitting results are then subjectively reviewed and compared to the BestTrack data from HRD. Those results giving unrealistic tracks, motions, or RMWs of storms are thrown away, which leads to eliminating the corresponding dropwindsonde profiles from the composition database. In addition to the combined grouping scheme, the storm track is also required to decompose measured wind velocities into tangential and radial components, and the storm motion is required in dividing the reconstructed wind field into four quadrants since the north direction of the storm relative coordinate system used in setting up quadrants is the direction of the storm motion.

As dropwindsonde profiles are appropriately grouped according to various schemes, the composition is applied to every groups to calculate desired statistics of the measured wind field. The calculation is done in three steps. First, the processed dropwindsonde profile is segmented into several bins according to the measurement height in a profile. Each of bins contains measurement points with height differences less than $30m$. In this case, the height of the measured wind field, which is assumed to be $3000m$ as in the study of Powell et al. (2003), is divided into 100 bins. Second, measurement points within one height bin from numerous different processed profiles constitute the sampling database to calculate the desired statistics. The calculation process is essentially a weighted-averaging process. This process can be applied to raw dropwindsonde measurements, which produces a mean wind profile, or remains left by eliminating the mean wind profile, which produces the turbulence statistics. In the weighted-averaging, the weight is assigned to each measurement point according to the distance from the measurement height to the height bin center. A weight of 1 is assigned if the measurement is coincidently located at the height bin center while a weight of 0 is assigned if the measurement is taken at the boundary of the height bin. Any measurements taken in the region between the height bin center and boundary has a weight linearly interpolated between 1 and 0. Therefore, the calculated value represents the desired statistic at the height bin center. Third, values for all height bins are assembled to produce the profile of the desired statistics. The actual number of measurement points used in the composition is presented in Fig. 4.2, which illustrates the number of measurements within each group in the MBL wind based composition. The number for a single group is calculated as the mean of all height bin sampling databases.

4.2 Mean Profiles

Since both the post-processing and composition of dropwindsonde measurements are performed by an unvalidated automatic software system, namely PostSonde, it is nec-

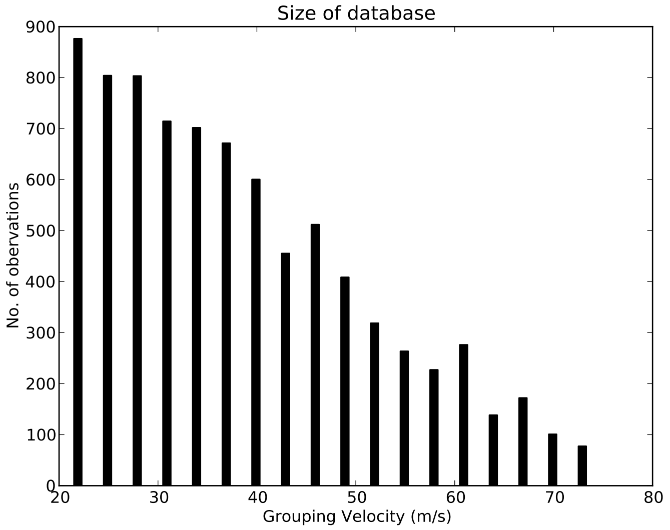

Figure 4.2: Number of measurements averaged across all height bins for each group when grouping dropwindsonde profiles according to the MBL wind speed.

essary to conduct a through validation of its use. In addition to comparing individual processed dropwindsonde profiles to processed results from other commonly used systems, the composited mean wind profile, calculated following the same composition strategy given in the study of Vickery et al. (2009), is compared to their empirical profile function. After the validation, different composition strategies are employed to reveal different aspects of the mean wind structure of the HBL. This section is structured into two parts in the order described above.

4.2.1 Validation of the Empirical Profile Function

In compositing dropwindsonde measurements to find a wind field model for engineering applications, Vickery et al. (2009) derived an empirical profile function to describe the mean wind speed vertical variation in the HBL over water. The function is of the form,

$$U(z) = \frac{u_*}{k}\left[\ln\left(\frac{z}{z_0}\right) - a\left(\frac{z}{H^*}\right)^n\right] \tag{4.1}$$

in which U gives the mean wind velocity, z represents the height from the sea surface, u_* is the surface friction velocity, k represents the Von-Karman constant, z_0 is the aerodynamic roughness length, and H^* denotes the HBL height scale. a and p are function shape parameters which take the values of 0.4 and 2 respectively according to Vickery et al. (2009). Based on dropwindsonde measurements gathered from 1998 to 2003 for more than 30 hurricanes, they found that the empirical profile function is valid to represent the mean HBL wind profile in the HBL with the MBL wind speed up to $70m/s$. However, their database of dropwindsonde measurements was still relatively small, and therefore it is of interest to validate this empirical profile function more strictly using a larger dropwindsonde measurement database.

In addition to validating the empirical profile function, or equation (4.1), the mean wind profile calculated following the composition strategy provided by Vickery et al. (2009) also gives an opportunity to check the composition part of the specially designed software, PostSonde. More specifically about this scheme, the composition is based mainly on the MBL wind speed, increasing from $20m/s$ to $70m/s$ at a step of $10m/s$. In addition to the MBL wind speed, the storm RMW and dropwindsonde splash down location are also taken into consideration. While the dropwindsonde splash down location is categorized into two groups, one near the RMW and one outside the RMW, the storm RMW is divided into three groups, ranging from $10km$ to $30km$, from $30km$ to $60km$ and above $60km$. Using the composition schemes described above, dropwindsonde measurements gathered in this study are post-processed and composited using PostSonde, which yields results comparable to the calculation according to equation (4.1). It can be noticed that there are two parameters controlling the profile shape, the surface friction velocity u_*, and height of the HBL, H^*. Their values are calculated through a fit approach minimizing the squared difference between the observed and calculated mean wind profile in the linear-logarithmic space, as detailed in the study of Vickery et al. (2009) (see their table 6). In this validation comparison, their values are taken directly. Figure 4.3 shows the comparison of the mean wind profile from the eye-wall region, or the group corresponding to the dropwindsonde splash down location near the RMW. It should be noted that the comparison shown in Fig.4.3 is for the RMW in the range $30km - 60km$. Comparisons for the other two RMW groups, the RMW in the range $10km - 30km$ and above $60km$, show a similar trend, and therefore are not presented here. On one hand, it is obvious that the mean wind profile composited from dropwindsonde measurements gathered in this study is in reasonable agreement with the calculation based on the empirical profile function, which validates the composition part of PostSonde since the composition of dropwindsonde measurement is performed using this newly developed software. On the other hand, there still is noticeable differences in the lower portion of the measured wind field under high wind speed conditions. These differences can be explained by a combination of the sparseness of measurements and the influence of the unresolved wave effect. When the high wind speed near the sea surface introduces significant waves, the wind strongly interacts with waves which drives the mean wind speed deviating from that predicted by the logarithmic profile. As for the difference in the high wind speed region, it is attributed to the unavoidable fluctuation of the measured wind speed since the last group in the composition corresponds to a MBL wind ranging from $70m/s$ to the maximum observed MBL wind, which is about $100m/s$.

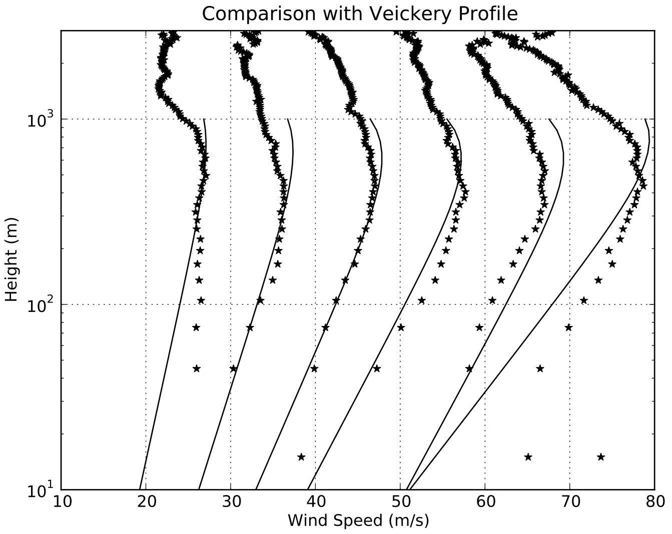

Figure 4.3: Comparison between composition results and the profile function provided by Vickery et al. (2009), where the stars represents composition results and the line depicts the profile function.

In summary, the comparison of the mean wind profile between composited from dropwindsonde measurements and calculated according to the empirical function not only validates the applicability of the empirical profile function in describing the mean wind structure in the HBL based on a larger dropwindsonde measurement database, but also validate the composition part of PostSonde. Thus, the composition scheme is adjusted in the configuration of PostSonde to investigate various aspects of the mean wind structure in the HBL.

4.2.2 The Mean Wind Profiles

As validated in the discussion above, PostSonde is adequate to produce reliable mean wind structures of the HBL, which provided the basis for further investigations of the mean wind structure based on dropwindsonde measurements composited using PostSonde. To extend the analysis in the studies of Powell et al. (2003) and Vickery et al. (2009), the composition scheme is adapted to produce a more comprehensive mean wind structure of the HBL. First, the composition resolution is increased. In previous studies, dropwindsonde profiles were grouped together if they reported the MBL wind speed with a difference no larger than $10m/s$. This resolution step is significantly reduced to $3m/s$ in the composition here. Second, the gradient wind speed, calculated by averaging the wind velocities measured from $1500m$ to $2000m$ above the sea surface, is employed as another grouping indicator since the modelling studies indicated that the gradient wind velocity is one important velocity scale in determining the mean wind profile in the HBL (Sharpiro, 1980; Kepert, 2001). Third, the radius of the dropwindsonde splash down location from the storm center is normalized by the storm RMW to indicate the storm region where the measurement is taken. Since only grouping dropwindsonde profiles based on the measurement region mixes up the wind structures from hurricanes with different intensities, the MBL wind speed is combined with the dropwindsonde splash down location to serve as one grouping indicator in the composition. Details of calculating the information required by different composition schemes are present in section 4.1.

In producing the mean wind profile, the composited mean wind profile is fitted to the empirical profile function by minimizing their squared differences between profile composited from dropwindsonde measurements and calculated according to the empirical profile function, which produces the parameters describing wind characteristics of the HBL, i.e. the surface friction velocity u_* and HBL height scale H^*. More specifically in this fitting process, only the composition results from $60m$ to $3000m$ are utilized since the low portion of the profile is strongly influenced by waves, which leads to the composition result deviating from the logarithmic profile as discussed above. Figure 4.4 shows the comparison of the mean wind profile composited based on the MBL wind speed and calculated by the empirical function, in which it is evident that the empirical function provided by Vickery et al. (2009) yields a description of the vertical variation of the mean wind in the HBL with a satisfactory accuracy. Considering that the composited profile shown in the comparison is calculated by a higher resolution composition, this agreement further substantiates the validity of the empirical profile function. The surface friction velocity u_* derived in the fitting process is presented in Fig. 4.5. In the figure, it is found that the surface friction velocity first increases with the MBL wind speed, and then starts showing large amplitude fluctuations. In the study of Powell et al. (2003) and Vickery et al. (2009), they concluded that the sea surface drag coefficient levels off when the $10-m$ wind velocity exceeds some critical value. Since the sea surface drag coefficient C_D related to the sea surface friction velocity u_* as,

$$\rho u_*^2 = C_D U_{10}^2 \tag{4.2}$$

in which ρ is the air density and U_{10} is the mean wind velocity at $10m$ height, it is expected to see the friction velocity u_* increases monotonously with the MBL wind speed considering U_{10} increases with the MBL wind. This feature is not shown in Fig. 4.5. The conflict indicates the complicity of the sea surface drag behaviour under high wind speed conditions, and implies that the sea surface drag coefficient may decrease with the increasing MBL wind in extremely high wind speed region. It should be noted that the variation shown in Fig. 4.5 is with the MBL wind speed rather than $10m$ the wind speed used predominately in previous studies (Powell et al., 2003; Vickery et al., 2009) due to the unavoidable error generated in estimating the $10m$ wind speed from fitted mean wind profile.

As mentioned above, the composition is also carried out based on the gradient wind velocity measured by dropwindsonde profiles. Figure 4.6 shows the comparison of the mean wind profiles, similar to that shown in Fig. 4.4, produced by the gradient wind velocity based composition. Again, the reasonable agreement verifies the validity of the empirical profile function in describing the mean wind profile of the HBL even when the gradient wind is the controlling velocity scale. In addition, the fact that both compositions, based on the MBL wind speed and on the gradient wind speed, show the same inherent mean wind structure in the HBL reveals that the gradient wind is also an influencing velocity scale in the HBL, as indicated by the modelling studies (Kepert, 2001; Foster, 2009). As a result, the gradient wind velocity should also be considered as a grouping indicator in using wind measurements taken by a vertical moving sensor, such as the dropwindsonde. Similarly to the MBL wind based composition, the surface friction velocity can be derived in fitting the composited mean wind profile to the empirical profile function. Figure 4.7 gives the variation of the surface friction velocity with the gradient wind. In the figure, the similar trend, as in Fig.4.5, is seen, but the fluctuations begin at a lower wind speed. This is understandable since in terms of boundary conditions the wind field of the HBL is determined by both the upper and lower boundary conditions. According to the modelling study of Sharpiro (1980) and Kepert (2001), the lower boundary condition, or the drag of the sea surface, is influenced not only by the upper level wind strength but also hurricane translations. Thus, the gradient wind velocity is not entirely reflected the boundary conditions determining the wind structure in the HBL. Furthermore, the surface friction velocity, u_*, is more influenced by the lower boundary conditions of the HBL. As a result, the surface friction velocity u_* indicated by the dropwindsonde profiles within one group in the gradient wind based composition can be substantially different, and therefore generates the fluctuations seen in Fig. 4.7.

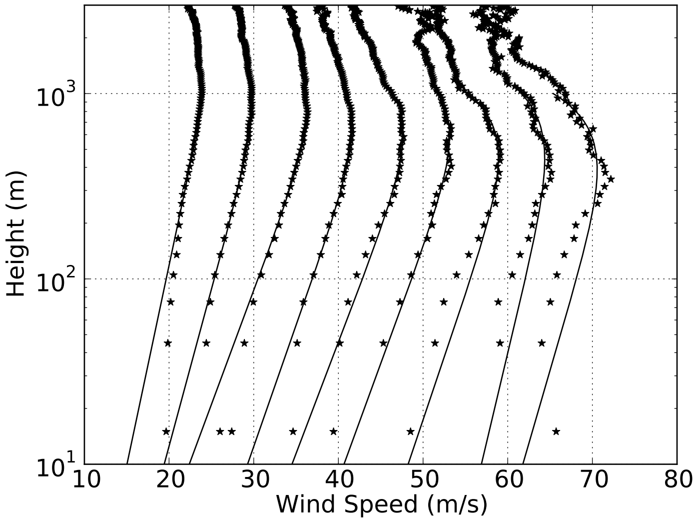

(a) Part I

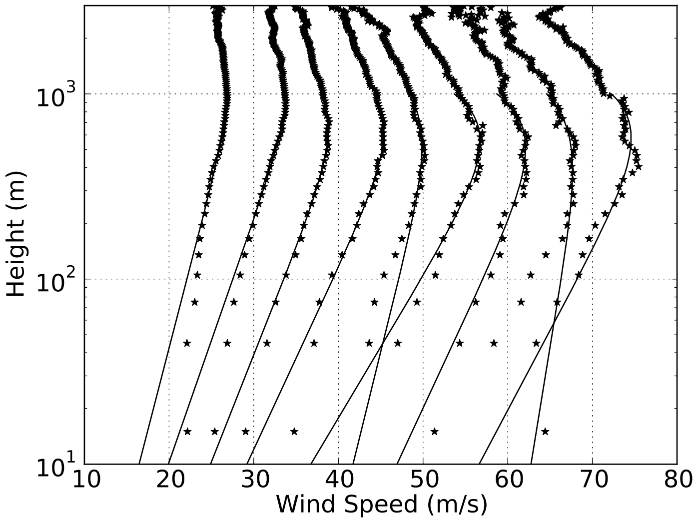

(b) Part II

Figure 4.4: Composition resulting profile and its best fitting result based on the profile function of Vickery et al. (2009), where stars represent the composition result and lines represent the best fitting profile function. Part I gives comparisons of group $1, 3, 5, 7, 9, 11, 13, 15, 17$, and part II gives comparisons of group $2, 4, 6, 8, 10, 12, 14, 16$. The grouping is based on the MBL wind speed.

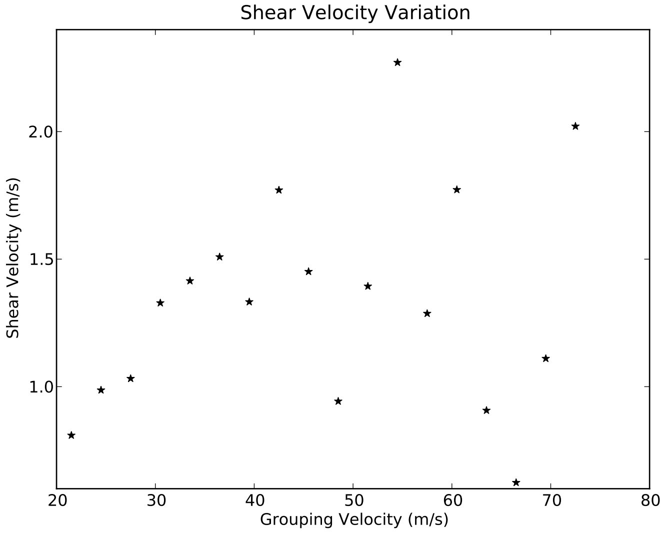

Figure 4.5: Friction velocity variation with the MBL wind speed.

Besides compositing dropwindsonde measurements purely based on the wind speed, the relative horizontal measurement position should be included in the composition, considering that the wind field of the HBL obviously varies horizontally. For that reason, dropwindsonde profiles are grouped according to the combination of the MBL wind speed and dropwindsonde splash down location. Figure 4.8 shows the resulting mean wind profiles produced by the combined composition. It is obvious that there is a systematical difference among profiles from different regions of a storm for all the wind speeds. The inner core profiles give the lowest wind velocities at the height of $500m$ and above where the profiles from the eye-wall region and the out-skirt region show a similar wind strength. In contrast, below $500m$, the profiles from the eye-wall region and the inner core region give a stronger wind estimate than the profiles from the out-skirt region. This is expected since hurricane inflows bring wind momentum from the out-skirt region inwards to enforce the wind strength in the eye-wall region and inner core region. The fact that the profiles from the inner-core region and eye-wall regions gives stronger wind estimates comparing with the profiles from out-skirt region substantiates that the inflow is confined to the lower portion of the HBL. In addition, if the wind field is rotated horizontally to let the storm motion vector pointing the north in compositional coordinate system, the measurement

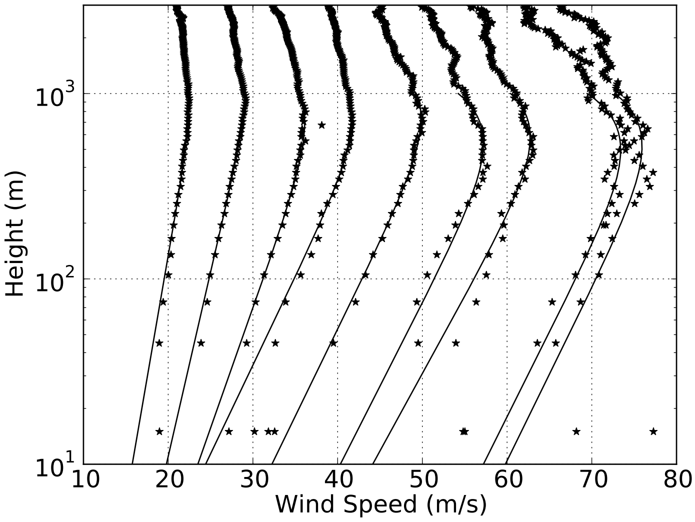

(a) Part I

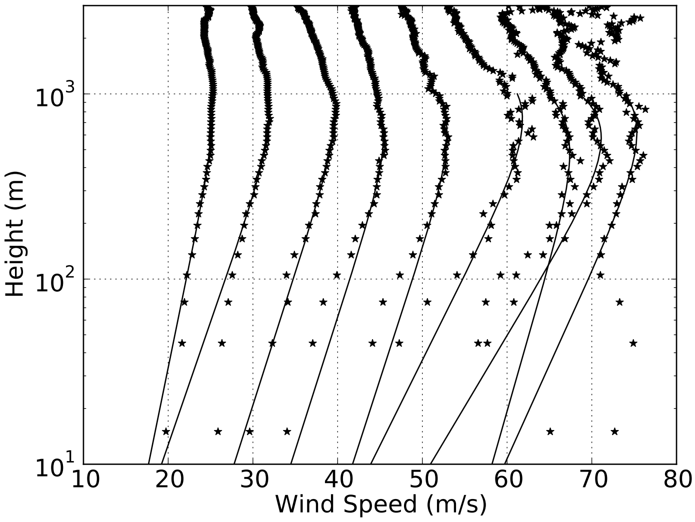

(b) Part II

Figure 4.6: Composition resulting profiles and its best fitting profile function according to Vickery et al. (2009), where stars represents the composition results and lines represents the best fitting profile function. Part I gives comparisons of group $1, 3, 5, 7, 9, 11, 13, 15, 17$, and part II gives comparisons of group $2, 4, 6, 8, 10, 12, 14, 16$. The grouping is based on the gradient wind speed.

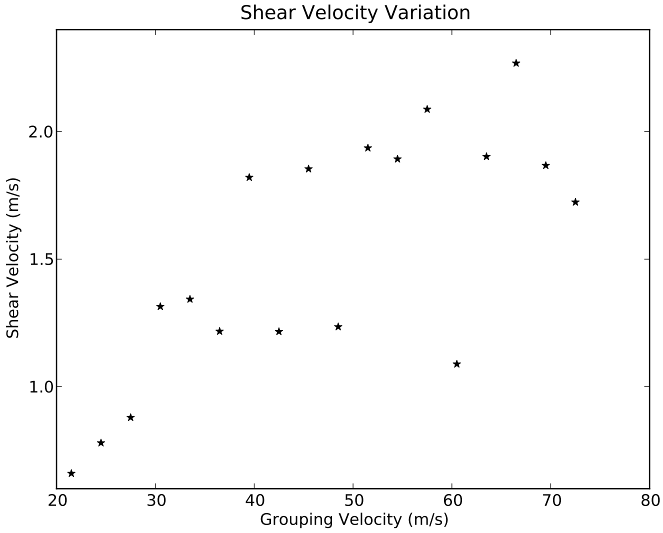

Figure 4.7: Friction velocity variation with the gradient wind speed.

regions can be further separated into four quadrants. Figure 4.9 shows the comparison of the profiles from four quadrants in the eye-wall region for all investigated wind speeds. Only small differences are shown in Fig. 4.9, and they do not keep the same trend for all the wind speeds. This indicates that the expected systematical asymmetry of the hurricane wind field is not found here. The asymmetry evolution may be the cause of this phenomenon. As indicated by Rogers and Uhlhorn (2008), the theoretical asymmetry of the tropical cyclone wind field is evolving with the tropical cyclone development. Since this composition did not take the development stage of hurricanes into consideration, the systematical asymmetry predicted by several modelling studies, such as those of Sharpiro (1980) and Kepert (2001), is swallowed by fluctuations of the measured wind velocity in the composition process.

4.3 Turbulence Intensity

As mentioned in section 4.1, dropwindsonde measurements gathered from 1997 to 2010, which contains more than 4000 dropwindsonde profiles, are believed to be able to produce statistically meaningful results of turbulence characteristics in the HBL. However, the

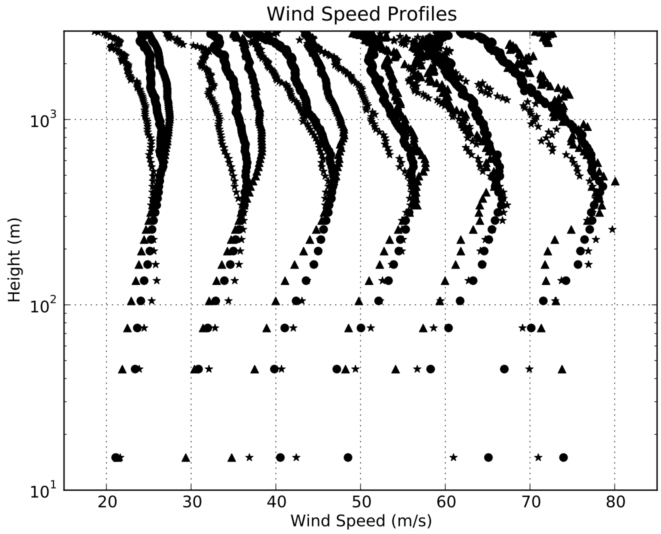

Figure 4.8: Composited profile of wind velocity. Stars represent profile from the inner core region, circles represent profile from eye-wall region and triangles represents profile from the out-skirt region.

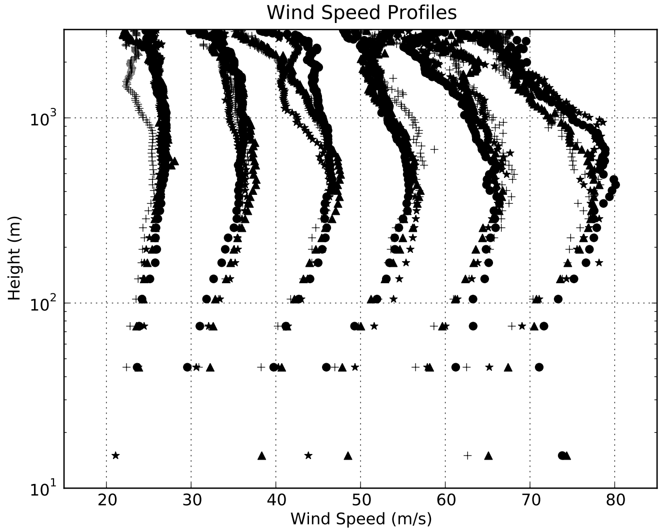

Figure 4.9: Composited profile of wind velocity. All profiles from the eye-wall region where stars represent profile from the first quadrant, circles represent profile from the second quadrant, triangles represents profile from the third quadrant and pluses represent profile from the last quadrant.

dropwindsonde measurement has not been used for such a purpose yet. Due to the difficulties of taking direct measurements, studies on turbulence characteristics in the HBL based on the direct observations are relatively rare, and their data sources are limited. Therefore, to completely understand the potential impact of the turbulence characteristics composited from dropwindsonde measurements, it is necessary to review studies focusing the HBL turbulence and using direct observations. In addition, since the HBL measurement is used to calculate the turbulence for the first time, additional processing procedures should be further discussed and the validity of the procedures needs to be investigated. Provided the calculation is validated, the turbulent wind velocity profile composited from dropwindsonde measurements can be analyzed and discussed. In brief, this section focuses on the turbulent wind velocity composited from dropwindsonde measurements, and therefore is divided into a review of studies concerning the HBL turbulence, a description of the additional processing procedures to find the turbulent component of the measured wind speed and a discussion on the turbulence intensity of the HBL found through compositing dropwindsonde measurements.

4.3.1 Background of the HBL Turbulence Calculation

Since reconnaissance flights have only very recently been able to take direct measurements of winds and other thermodynamical variables at an altitude low enough to calculate turbulence characteristics of the HBL (Zhang et al., 2009; Zhang, 2010), most studies concerning the HBL turbulence use either remote sensing techniques (Lorsolo et al., 2010), or in-situ observations over land (Yu et al., 2008). When using the remote sensing techniques to measure turbulence in the HBL, the measurements taken within a predefined spatial grid cell are used to calculated a spatially averaged mean to represent the mean wind velocity at the center of the grid cell. In the calculation of turbulence information, the spatial resolution is limited by the size of these predefined spatial grid cell which is usually crude from the perspective of resolving turbulence in the HBL. As indicated by Lorsolo et al. (2010), the resolvable turbulence scale, calculated based on Doppler radar observations, is only $\sim 1km$. For that reason, the detailed vertical turbulence structure of the HBL is presently not derivable based on airborne Doppler radar observations. As for in-situ observations over land, the measurement is generally taken by towers or portable observational masts. While the tower observation data are extremely scarce due to the slim chance that a hurricane wind field would sweep a particular observation tower, portable mast measurements give only the wind velocity at a few vertical discrete points below $30m$ due to the instrument limitation. Therefore, the detailed vertical turbulence structure of the HBL is neither calculable based on in-situ observations over land. In contrast, the CBLAST experiment (Black et al., 2007), provides the best opportunity so far to determine the vertical turbulence structure in the HBL using reconnaissance flight observations (Zhang et al., 2009; Zhang, 2010).

On the other hand, although many studies has been conducted to get the mean wind field within the HBL based on dropwindsonde observations, there are no published studiesthat have been conducted to derive the HBL turbulence structure based on these observations. The advantages of using dropwindsonde measurements, when compared to using remote sensing techniques and in-situ observations over land, are obvious. First, the dropwindsonde produces the wind profile of the entire HBL, from the sea surface up to $\sim 5000m$. Second, the resolution provided by the dropwindsonde, $\sim 6m$, is significantly higher than that provided by current remote sensing techniques, e.g. $\sim 1km$ in the case of airborne Doppler radar observations in hurricanes (Lorsolo et al., 2010). The major obstacles of using dropwindsonde measurements in investigating the HBL turbulence may be the horizontal scarcity of dropwindsonde measurements and inherent deficiency of the composition methodology, which introduces unpredictable variations of the measured wind velocity other than that introduced by the turbulence. Given that the dropwindsonde measurement database has accumulated appreciably in the last decade, which allows a derivation of the turbulence structure in the HBL, it is worth trying to preliminarily investigate turbulence characteristics of the HBL based on dropwindsonde measurements.

4.3.2 Additional Processing and Validation

To calculate wind characteristics of the HBL based on dropwindsonde measurements, the use of the composition methodology is unavoidable since an individual dropwindsonde profile provides only a little information about the entire measured wind field. Because one individual dropwindsonde drop only provides a profile reflecting the instantaneous wind velocity variation with height in a small region of the whole hurricane wind field, the calculation of the turbulence information from dropwindsonde measurements should be based on a compositional approach taking numerous dropwindsonde profiles together. For that reason, the same composition strategy, as in the analysis of the mean wind profile detailed in section 4.2, is followed to calculate the HBL turbulence in this section. In addition, since the turbulence is commonly recognized as a local phenomenon, which indicates the horizontal measurement position is not important in the calculation, only the MBL wind speed and gradient wind are used as grouping indicators. Naturally, the residuals of raw measurements, left by eliminating the mean wind profile, should be adequate to represent the turbulent component of the measured wind velocity, and therefore the calculation should be based on the composition of these remains. However, as discussed in section 4.2 about the mean wind profile from different regions in a hurricane, there is a systematical difference of the mean wind profile from different hurricane regions. Thus, direct compositing the residuals includes the variations beyond that introduced by the turbulence.

To reduce this inherent deficiency of the composition methodology, a high-pass filter is applied to the remains left over by eliminating the mean wind profile calculated as detailed in section 4.2. The high-pass filtering process is employed because it is obvious that the variations introduced by the systematical difference shown in Fig. 4.8 have a spatial scale much larger than turbulence length scale. The simple moving average filter is revised and applied to do the high-pass filtering. Since the moving average procedure filters out high frequency fluctuations of signals to smooth curves, the part of the measured wind velocity filtered out by the moving average filter is taken as the turbulent component of the wind measurement. This process is illustrated in Fig. 4.10. When using the revised moving average filter, the only parameter that needs to be determined for the filter design is the length scale within which fluctuations are taken as turbulence. With no other references, a subjectively decided scale of $800m$ is used, because it is a reasonable assumption of the turbulence influencing scale. It should be noted that the analysis of reasons introducing the fluctuations of the dropwindsonde measured wind velocity does not exhaust all possibilities, and therefore variations introduced by other methodology deficiencies may have a spatial scale similar to that introduced by turbulence. As a result, the composition methodology and the use of the high-pass filter should be validated by the turbulence calculated based on other observations. More importantly, the arbitrarily chosen cut-off scale, $800m$, lacks a sound theoretical base. Although a sensitivity analysis shows that the turbulence intensity composition results are not that sensitive to the filter scale given the scale varies within the order of magnitude of $\sim 100m$, the error brought by this arbitrarily chosen cut-off scale can only be detected by comparing the composition turbulence results to that calculated based on other observations.

The turbulent wind velocity profile calculated based on the CBLAST observational data are suitable for validating the additional processing procedures used to find turbulent component of dropwindsonde wind measurement articulated above. The profile of the turbulent wind velocity, defined as the square root of the measured wind velocity variations, composited from dropwindsonde measurements is compared to the turbulent wind velocity found in the CBLAST experiment (J. Zhang 2011, personal communication). The comparison is shown in Fig. 4.11. It should be noted that the turbulent wind velocity is calculated based on the tangential wind, decomposed from the total wind measurement using storm tracks found earlier, because it is close to its counterpart in the CBLAST data, the along-wind turbulent wind velocity. Furthermore, only two groups, corresponding to the MBL wind velocity ranging from $20m/s$ to $23m/s$ and from $23m/s$ to $26m/s$, are shown in the comparison because their measured wind field has a strength comparable to that observed in the CBLAST experiment. The qualitative agreement shown in the comparison indicates the validity of the composition methodology and the use of the high-pass filter, including the subjectively chosen cut-off scale.

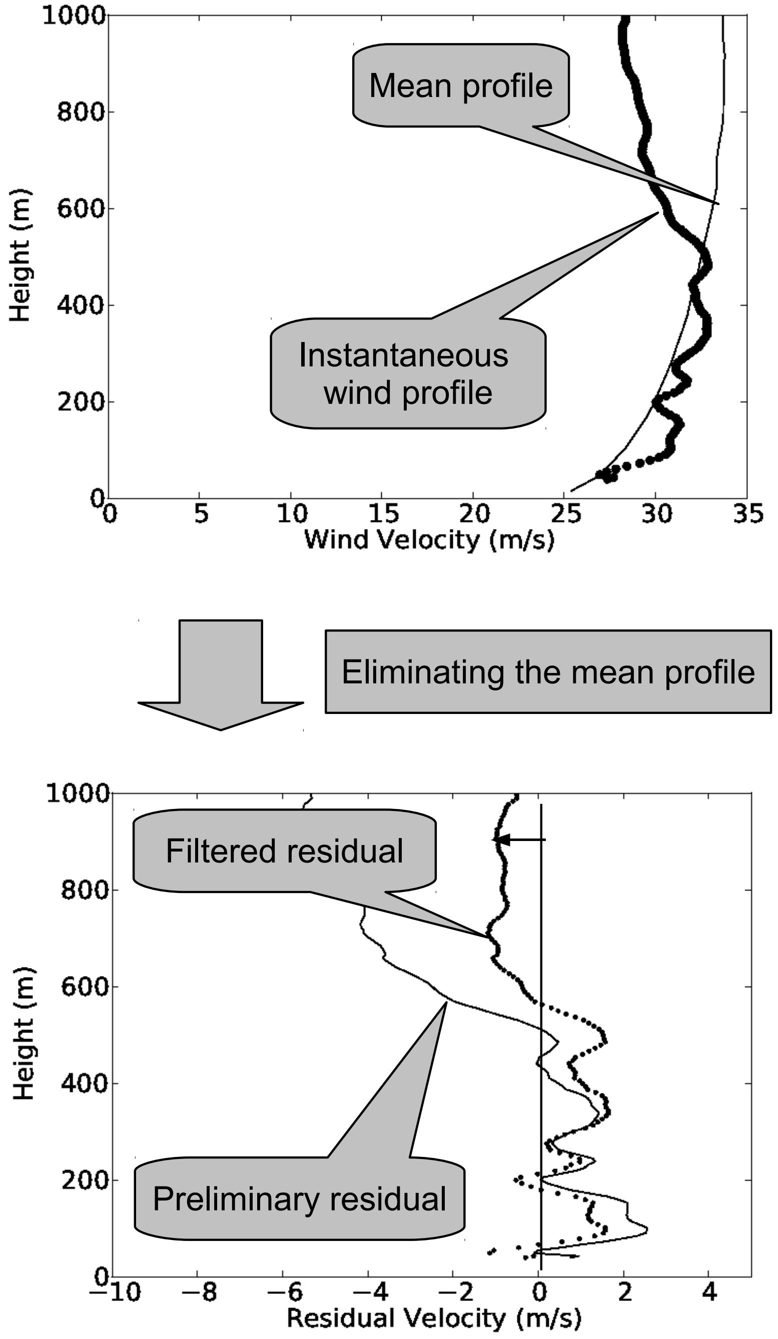

Figure 4.10: Sketch illustrating the process to calculate the turbulent wind from instantaneous dropwindsonde wind measurements. The arrow in the lower figure indicates the turbulent component produced by the high-pass filter. Profiles shown in the figure are calculated based on a real dropwindsonde profile.

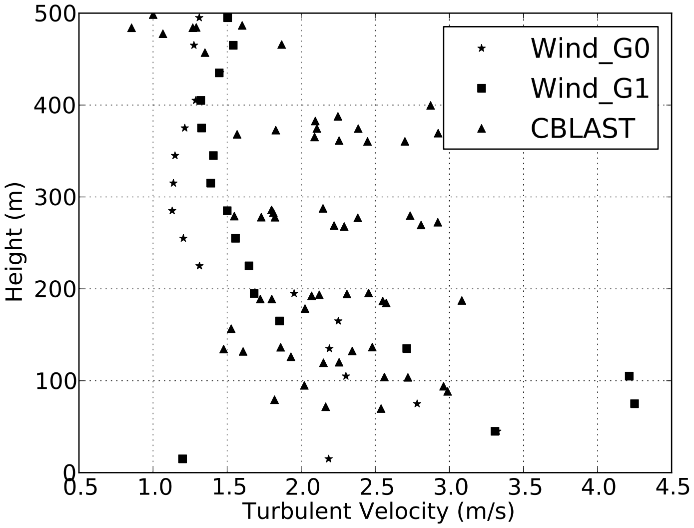

Figure 4.11: Comparison of the turbulent velocity for the tangential wind with the results from CBLAST experiment, only first two groups corresponding to MBL wind speed $20m/s - 23m/s$ and $23m/s - 26m/s$ are shown.

4.3.3 Turbulent Wind Velocity and Turbulence Intensity

As indicated by the title of this section, only the turbulent wind velocity, defined as in the validation shown in Fig. 4.11, and the turbulence intensity, defined as the turbulent wind velocity normalized by the mean wind velocity composited at the same height, are presented and discussed here. In addition to calculating the turbulence structure in the HBL based on the absolute wind velocity, the total wind measured is decomposed into tangential and radial components to generate the turbulence structure for decomposed winds. In compositing the mean wind profile, as detailed in section 4.2 and conducted in previous studies (Powell et al., 2003; Vickery et al., 2009), the absolute wind velocity measured by the dropwindsonde is taken as the longitudinal wind component, u. This is only an approximation considering that the wind directions measured by a single dropwindsonde profile change substantially in the fall of the dropwindsonde. However, this approximation is acceptable in calculating the mean wind profile since the inaccuracy of the wind direction associated with this approximation only introduces limited errors in calculating the longitudinal wind velocity, and the error is decreased in the averaging process calculating the mean wind profile. The turbulence composition, on the other hand, is more sensitive to the inaccuracy of wind direction measurements since the error will be accumulated as measured ”turbulence” variations in the composition process. For that reason, the wind decomposition is necessary in calculating turbulent wind by a composition approach. Naturally, the total wind is decomposed into tangential and radial components based on storm tracks found beforehand as detailed in section 4.1. The following discussions are mainly based on the turbulence structure found for decomposed wind components.

In addition to validating the composition methodology and the use of the high-pass filter, one finding of Zhang et al. (2009) is substantiated by the comparison shown in Fig. 4.11, which shows the turbulence intensity in the HBL decreases with height in the lower portion of the HBL. It is obvious that the CBLAST data shown in the figure gives a less clear trend than the dropwindsonde composition results. This is due to the fact that the general wind strength of each of the turbulent wind velocity points calculated based on the CBLAST data, shown in Fig. 4.11, is different. However, the structure shown in the study of Zhang et al. (2009) (see their Fig. 7), which is derived based on a more systematical investigation, confirms the decreasing trend of the turbulent wind velocity revealed by the dropwindsonde composition results shown here.

Figure 4.12 gives the profiles of the turbulence intensity of the tangential wind in the HBL, from the sea surface up to $3000m$. It shows that all the profiles, corresponding to different MBL wind speeds, collapse to a single curve which first decreases with height and then levels off above $800m$. This reveals that the vertical structure of the turbulence intensity in the HBL is independent from the general strength of the wind field. Although it is shown that there are a few large amplitude variations (larger than 10%) in the profiles from the groups with higher MBL wind speeds at heights above $1000m$, this does not disprove the general trend summarized above since these spikes can be explained by the inaccuracy of calculating the storm center for some dropwindsonde profiles. One evidence of the explanation is that these spikes are not seen in the turbulence intensity profiles calculated based on the absolute wind velocity, which is shown in Fig.4.13. Furthermore on the turbulence structure of the absolute wind, it shows a similar trend, as seen in Fig. 4.12, but the turbulence intensity values are significantly reduced. This substantiates the need to decompose the wind and calculate the turbulence in each direction since the "turbulence" shown in Fig. 4.13 is only the variation of the measured wind speed magnitude rather than the turbulence. As for the radial wind, the turbulence intensity is defined as the radial turbulent wind normalized by the mean tangential wind due to the fact that the mean radial wind is close to 0. Using this definition, the profiles of the turbulence intensity are calculated and shown in Fig.4.14. As in Fig. 4.12, the same decreasing trend is seen in Fig. 4.14. Moreover, the independence of the vertical turbulence variation from the boundary layer wind strength (measured as the MBL wind) is substantiated since all profiles collapse to a single curve.

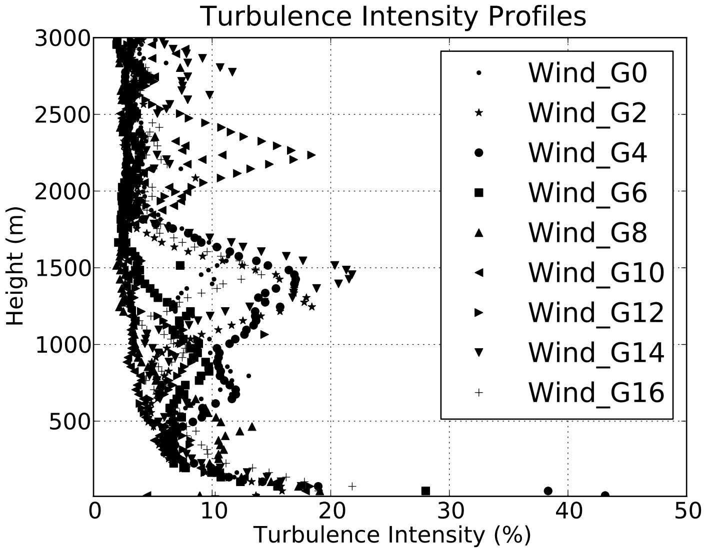

Figure 4.12: Variation of the composited turbulence intensity, calculated from tangential winds, with heights, the composition is based on the MBL wind speed.

In addition to compositing dropwindsonde measurements based on the MBL wind speed, the composition is also conducted based on the gradient wind speed. The comparison of the tangential turbulent wind velocity profiles, composited using the gradient wind speed in the range as the MBL wind speed shown in Fig. 4.11, and the results

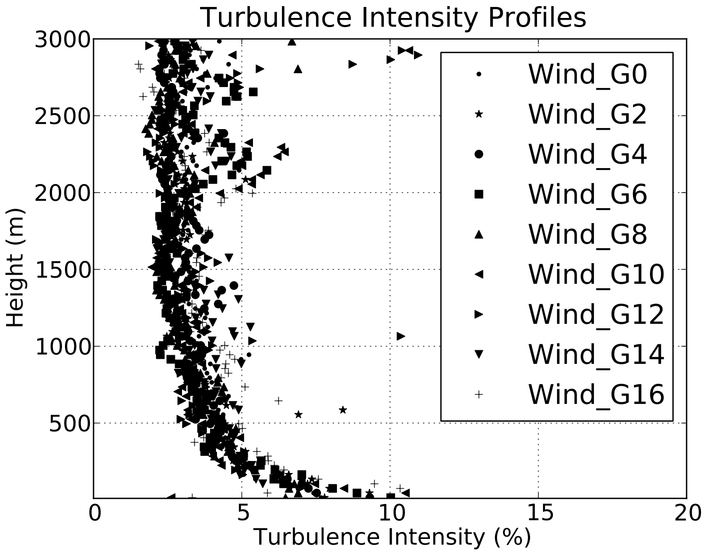

Figure 4.13: Variation of the composited turbulence intensity, calculated from absolute wind speeds, with heights. The composition is based on the MBL wind speed.

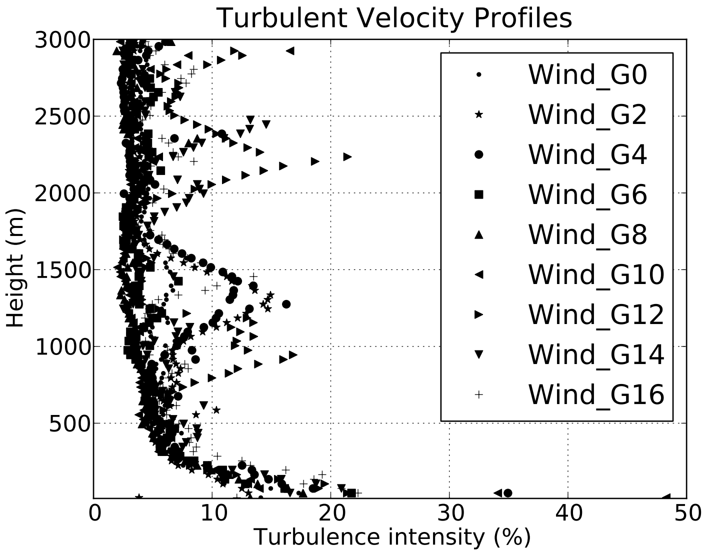

Figure 4.14: Variation of the composited turbulence intensity, calculated from radial winds, with heights. The composition is based on the MBL wind speed.

from CBLAST experiment are shown in Fig. 4.15. It is obvious that the turbulent wind velocity calculated in the gradient wind based composition is larger than that calculated in the MBL wind based composition and CBLAST results. Moreover, its vertical structure is not as clear as in the MBL wind based composition. The same explanation, as in the discussion of the mean wind profile, can be employed. As analyzed in section 4.2, comparing with the MBL wind speed, the gradient wind is less affected by surface characteristics. Considering that the turbulent wind velocity analyzed in Fig. 4.15 is limited to the lowest $500m$, which is strongly influenced by surface air-sea exchanges, the variance of the dropwindsonde wind measurements grouped together according to the gradient wind contains that induced by different air-sea exchange characteristics. This explains the larger value of the turbulent wind velocity. Moreover, these additional variations are multi-sourced and without an inherent structure, which explains the feature of less organized vertical turbulence structure.

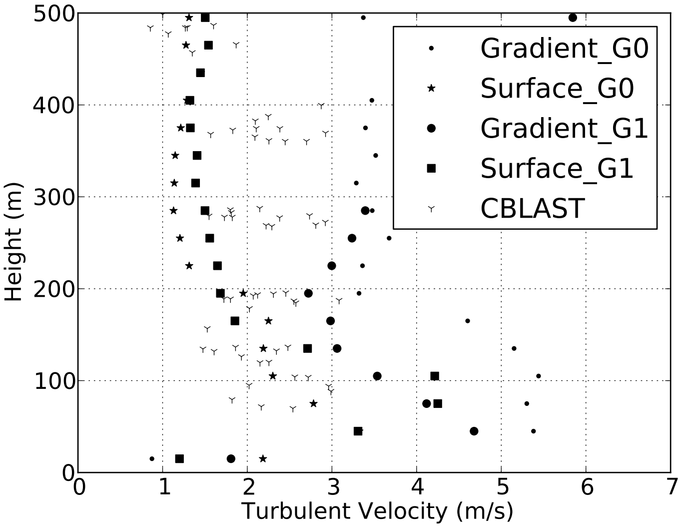

Figure 4.15: Comparison of the turbulent velocity for the tangential wind from composition based on the MBL wind speed and gradient wind speed with the results from CBLAST experiment, only first two groups corresponding to MBL wind speed $20m/s - 23m/s$ and $23m/s - 26m/s$ are shown.

4.4 Turbulence Length Scale

According to the "mixing length" theory, the turbulence length scale is closely related to turbulent mixing (Prandtl, 1925). Following the physical interpretations provided in the theory, the "mixing length" can be interpreted as the vertical integral length scale of a turbulence field. Although Bradshaw (1974) argued that there is no evidence supported the connection between the "mixing length" and any measurable turbulence length scales, from flow dimensions to micro-scales, studies suggested that there is a similar variation between the turbulent integral length scale, calculated from spatial correlation coefficients, and the "mixing length" (Chen and Sofia, 1987; Davis, 1994). Thus, it is worth exploring the possibility of deriving the turbulence diffusivity, one key parameter in modelling turbulent mixing in the ABL, from vertical correlation coefficients of a turbulence field. Using the unprecedented opportunity provided by the dropwindsonde, which measures the wind in a way such that the vertical spatial correlation of the measured wind field can be directly derived and the vertical turbulent integral length scale can be calculated. On the other hand, the YSU scheme, which prescribes the turbulence diffusivity as a cubic function of height, implies a turbulence length scale model. Comparing the turbulent integral length scale calculated based on dropwindsonde measurements and the model implied by the YSU scheme yields insights into turbulent mixing in the HBL and sheds some lights on improving the YSU scheme in simulating the HBL turbulence. This section is divided into two parts, the first part articulates theoretically the relationship between the turbulence diffusivity and turbulence length scale while the second part discusses the turbulent integral length scale calculated based on dropwindsonde observations and its impact on the turbulence diffusivity formulation adopted in the YSU scheme.

4.4.1 Theoretical Background

Since the "mixing length" theory has been widely used to analyze turbulence in geophysical and atmospheric flows, many models has been proposed to give the variation of the "mixing length" with height in the ABL (Prandtl, 1932; Blackadar, 1962; Panofsky, 1973; Lettau, 1962; Gryning et al., 2007), which leads to our current understanding of turbulent mixing in the ABL. Many of these models are derived based on the observed mean wind profile and the turbulent mixing equation which relates the mixing length to the mean wind profile, since the mixing length itself is hard, if not impossible, to be measured directly. As the dropwindsonde gives an unprecedented opportunity to calculate vertical turbulence correlation coefficients in hurricanes, the turbulence integral length scale can be directly integrated from these correlation coefficients and compared to the mixing length inferred from the mean profile following the methodology given by Panofsky (1973) and Pena et al. (2010). Such a comparison may not only advance our understanding of turbulent mixing in the HBL but amy also provide additional evidence supporting the relationship between the turbulent integral length scale and mixing length.

Meanwhile, the PBL scheme has been widely employed in current numerical simulation packages concerning atmospheric flows (Nolan et al., 2009b,a). Non-local PBL schemes, such as the YSU scheme used in WRF, prescribe and parametrize the turbulence diffusivity profile, which is critical in the overall atmospheric flow simulation since it reflects the influence of the surface boundary condition and modifies the fields predicted in the lower portion of the atmosphere. These PBL schemes are, however, mainly designed to describe turbulent mixing in the standard ABL (Hong and Pan, 1996; Hong et al., 2006). Thus, its validity in simulating turbulent mixing in the HBL is questionable despite the fact that they are already widely adopted in researches and the numerical forecasts of hurricanes. It is worth comparing the turbulence length scale derived from these PBL schemes to the turbulent integral length scale calculated based on dropwindsonde measurements, which not only checks the validity of such PBL schemes in simulating the HBL turbulence but also provides opportunities to make suggestions on possible improvements upon its original formulation.

Following and extending the study of Pena et al. (2010), the turbulence diffusivity can be expressed as the product of a turbulent velocity scale and a length scale following the Prandlt's mixing length theory. As in the first-order closure, the momentum flux

$\tau = \rho\overline{u'w'}$ for the longitudinal and vertical components of the wind can be related to the derivative of the mean wind velocity as,

$$\tau = \rho K_m \frac{dU}{dz} \tag{4.3}$$

where ρ gives the density of the air, U is the longitudinal wind component and the turbulence diffusivity for the momentum, K_m, can be expressed as

$$K_m = l^2 \left| \frac{dU}{dz} \right| \tag{4.4}$$

In equation (4.4), l represents the mixing length. Once the momentum flux τ is modelled based on the shear velocity u_* as,

$$\tau = \rho u_*^2 \tag{4.5}$$

the turbulence diffusivity of momentum, K_m, can be derived, combining expressions (4.4) and (4.5), as a function of the shear velocity u_* and mixing length l as,

$$K_m = u_*(z)l(z) \tag{4.6}$$

It should be noted that this shear velocity u_* does not only reflect the shear stress at surface, but is a function of height, $u_*(z)$, giving the shear stress for the entire boundary layer. Following Panofsky (1973); Gryning et al. (2007); Pena et al. (2010), the vertical variation of the shear stress in the entire boundary layer can be expressed in terms of the shear velocity as,

$$u_*(z) = u_{*0}(1 - \frac{z}{z_i}) \tag{4.7}$$

where z_i gives the boundary layer height and u_{*0} gives the u_* value at surface. Combing expressions (4.7) and (4.6), the turbulence diffusivity for the momentum can be rewritten as,

$$K_m = u_{*0}(1 - \frac{z}{z_i})l(z) \tag{4.8}$$

where the mixing length l should also be a function of height, and therefore rewritten as $l(z)$.

Although many models using a mixing length profile $l(z)$ have been proposed, as summarized by Pena et al. (2010), only the length model implicitly used by the turbulence diffusivity formulation of the YSU scheme is investigated here. As described by Hong and Pan (1996) and Hong et al. (2006), the turbulence diffusivity profile of the YSU scheme, based on the study of Brost and Wyngaard (1978) and Troen and Mahrt (1986), is prescribed as a function of height as,

$$K_m = kw_s z(1 - \frac{z}{z_i})^p \tag{4.9}$$

where k is the von-Karman constant, $w_s = u_{*0}\phi^{-1}$ is the mixed layer velocity, and p is the model parameter that currently takes the value of 2.0 in the operational WRF. Rewriting it in the same format as in equation (4.8), K_m used by the YSU scheme is,

$$K_m = u_{*0}\phi^{-1}(1 - \frac{z}{z_i}) \cdot kz(1 - \frac{z}{z_i})^{p-1} \tag{4.10}$$

In comparing equation (4.10) to equation (4.8), it can be seen that the turbulent velocity scale used in YSU scheme has one more parameter ϕ^{-1}, which is the Monin-Obukhov function evaluated at the top of the surface layer, and the mixing length, implied by the YSU scheme, is modelled as,

$$l(z) = kz(1 - \frac{z}{z_i})^{p-1} \tag{4.11}$$

Given that the model parameter p takes the value of 2.0, equation (4.11) shows that the YSU scheme requires the turbulence length scale, or the mixing length, to be a parabolic function of height.

4.4.2 Composition Procedures and Its Result

Just as in the calculation of the turbulence intensity structure, the turbulent component of the measured wind speed needs to be found first in deriving the turbulence vertical correlation coefficient. Procedures used to post-process raw dropwindsonde measurements in order to calculate the turbulent component of the measured wind can be found in sections 4.1 and 4.3. Unlike the calculation of the turbulence intensity, the turbulent integral length scale calculation is based on vertical spatial correlation coefficients of the turbulence component of the dropwindsonde wind measurement which involves the product of two wind measurements. As a result, the composition process needs to be adapted to cope with this complexity. The adapted calculation is presented in complementing the composition methodology presented in the previous sections. In brief, vertical turbulence correlation coefficients are calculated in four steps. First, the turbulent component of the measured wind velocity are multiplied for every combination of the measurement points in an individual dropwindsonde profile, and then the products are binned according to the vertical distance from the first to the second turbulent wind measurement. Second, a matrix is set up based on these turbulent wind products for all dropwindsonde profiles from one composition group, each element of the matrix contains various turbulent velocity products whose first factor has similar height and second factor has similar distances from the first factor. In this matrix, each row contains elements in the same height bin but showing different vertical distances of their factors, while each column contains elements giving the same vertical distance in all the height bins. The setup of this matrix and the meaning of its elements are illustrated in Fig. 4.16. Third, all products from one height bin are weighted-averaged to get the covariance. In other words, every element, which contains many turbulent wind products, in the above described matrix are used as the sampling database to calculate the covariance. In the calculation, the weight is given based on the distance from the first measurement to the center of the height bin. Finally, the covariance is normalized by the square root of the turbulence variance derived in calculating the turbulent wind velocity profile presented section 4.3.

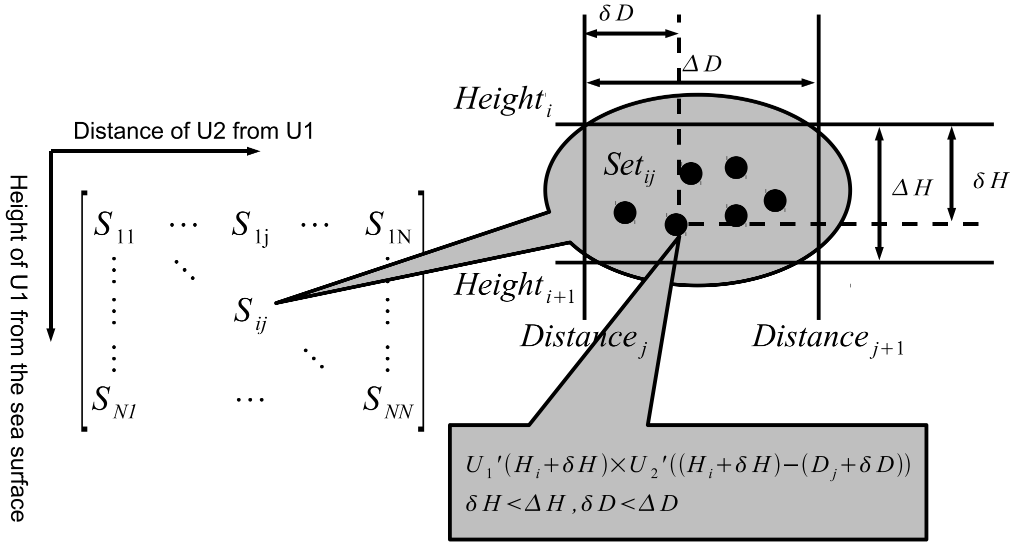

Figure 4.16: Sketch illustrating the matrix used in calculating the turbulence sptial correlation coefficient. In the figure, U' is the turbulent component of dropwindsonde wind measurements which is assumed to be only a function of height H, and the distance D is assumed in the vertical direction.

Since the turbulence is expected to be a local phenomenon, i.e. independent from the relative horizontal measurement location, only compositions based on the wind speed are investigated. More specifically, both the MBL wind and gradient wind are used as grouping indicators while the dropwindsonde splash down location is abandoned in this calculation. Due to the computational capacity limitation, $900m$ is used as the longest distance in the vertical correlation coefficient calculation which implies the correlation of turbulent winds beyond that distance is assumed to be negligible. From the analysis shown below, it can be seen that it is a reasonable assumption.

Although correlation coefficients calculated as articulated above are assumed to reflect spatial correlation coefficients of the turbulence in the vertical direction, it actually produces correlation coefficients following the trajectory of the dropwindsonde, which is obviously not in a perfectly vertical direction. However, Taylor's hypothesis assumes the mean wind convecting the dropwindsonde also convects the turbulent wind along with the dropwindsonde. Under this assumption, to calculate the turbulence spatial correlation coefficient in the right vertical direction, the horizontal displacement of the turbulent wind should be removed before the calculation which leads to the calculation along the trajectory of the dropwindsonde is in fact in the right vertical direction given that the displacements of the turbulent wind and dropwindsonde are similar. This assumption is reliable when the vertical distance of two measurements used in correlation coefficient calculation is small and the wind shear within them is small.

Figure 4.17 shows a set of typical correlation coefficients. As expected, the correlation coefficient decays as the distance grows, and the correlation coefficient at a higher altitude decays more slowly than that at a lower altitude. This indicates that the correlation of the turbulence at a higher attitude is stronger due to the existence of larger eddies. Moreover, it can be seen that the fluctuation of correlation coefficient beyond the point where it reaches zero, which is far less than $900m$, is somewhat random and with a smaller amplitude. This feature substantiates the subjective choice of $900m$ as the cut-off distance in calculating correlation coefficients. In addition, this feature shows that the turbulence correlation calculated as articulated above is not reliable to be used to calculate the integral length scale beyond the point where it cross zero for the first time. To ensure the integral length scale calculation to be positive, the integration is performed before the point where the correlation coefficient crosses zero for the first time.

Following the method described above, the turbulent integral length scale can be calculated by integrating the correlation coefficients of one height bin. In other words, the turbulent integral length scale is calculated by adding elements in same row in the matrix described above to a point before the first negative value appears, after elements are weighted-averaged to calculate correlation coefficients. The variation of the turbulent integral length scale is formulated based on a series calculated results at different heights. Figure 4.18 gives the profile of the turbulent integral length scale when the composition is conducted based on the MBL wind speed. It is shown that there is a general trend in the turbulent integral length scale below $300m$ altitude, which is increasing with height first. More specifically, the calculated turbulent integral length scale increase with

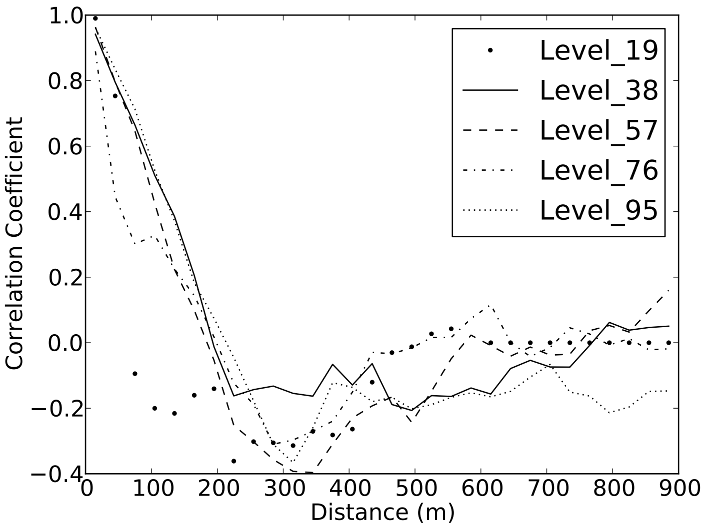

Figure 4.17: Correlation coefficient of turbulence where the number of level indicates the height of the correlation; the larger the level number, the higher altitude at which the correlation coefficient is calculated. Level 1 was 15m from the sea surface and Level 100 was 2985m from the sea surface.

height up to 150m. For some low MBL wind speed groups, the turbulent integral length scale keep increasing with height above 150m, while some groups with high MBL wind speeds, the turbulent integral length sale start to decrease with height. Above 300m, the calculated turbulent integral length randomly fluctuates around a constant value. This can be explained as follows. Turbulent mixing in the HBL depends on sizes of eddies buried in turbulent flow. In the lower portion of the HBL, the eddy size increase with height since the vertical distance is the main boundary for an eddy to grow. Beyond the point at which turbulent integral length scale starts decreasing with height, eddies reaches their maximum size and starts breaking down to generate eddies with various scales. Similarly, Fig. 4.19 shows the turbulent integral length scale profiles when the composition is based on the gradient wind. The same trend is seen in the lower portion of the figure, but the fluctuations showing in the upper portion of the figure are reduced comparing to the MBL wind speed based composition. This indicates when compositing dropwindsonde measurements according to the gradient wind, turbulent characteristics found in the upper level of the hurricane atmosphere are more clear and systematical since the gradient wind is an indicator of the wind strength at the upper level of the hurricane atmosphere.

It should be noted that there is a methodology drawback that makes the turbulent integral length scale calculated as described above not reliable in the higher portion of the hurricane atmosphere. As described above, the turbulent component of the dropwindsonde measured wind is found by first eliminating the mean wind profile composited and then having the remains pass through a high-pass filter. This step assumes that any trends in the large scale variation of the HBL wind is eliminated. While this assumption is reasonable for measurements near the surface, as indicated by the analysis of the mean wind profile and previous studies (Powell et al., 2003; Vickery et al., 2009), it is not the case for the measurements taken in the upper portion of the HBL. Given that the high-pass filter used is inclined to transfer a linear large scale trend into a series of negatively correlated measurements by producing positives at one end while negatives at the other. The vertical correlation coefficient calculated then mixes up the turbulence correlation with the large scale mean flow trend. This indicates that the turbulent integral length scale found previously should be used with caution, especially for the part at the upper level of the hurricane atmosphere.

Since the YSU scheme, which requires the turbulent length scale in the HBL is a parabolic function of height, is widely used in simulating hurricane winds, the test is conducted to check if the turbulence diffusivity profile used by the YSU scheme is a good approximation of turbulent mixing behaviour found by compositing dropwindsonde measurements. The test consists of two parts: firstly, the test is carried out theoretically based on the mean wind profile of the HBL; secondly, the turbulence length scale implied by the YSU scheme is compared to the turbulent integral length scale found by dropwindsonde observations. In the test based on the mean wind profile, the empirical profile function, introduced by Vickery et al. (2009) and confirmed by the mean wind structure analysis found in section 4.2, rather than the actual dropwindsonde composited mean wind profile, is used. Here, the profile function is repeated,

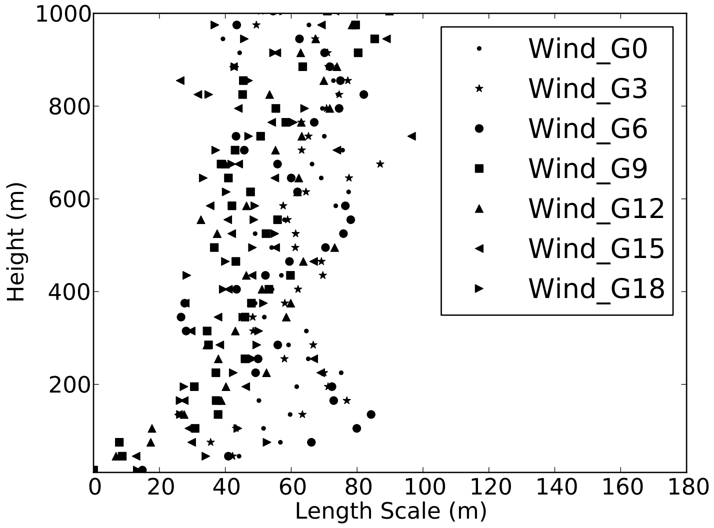

Figure 4.18: The integral length scale profile, the composition is based on the MBL wind speeds.

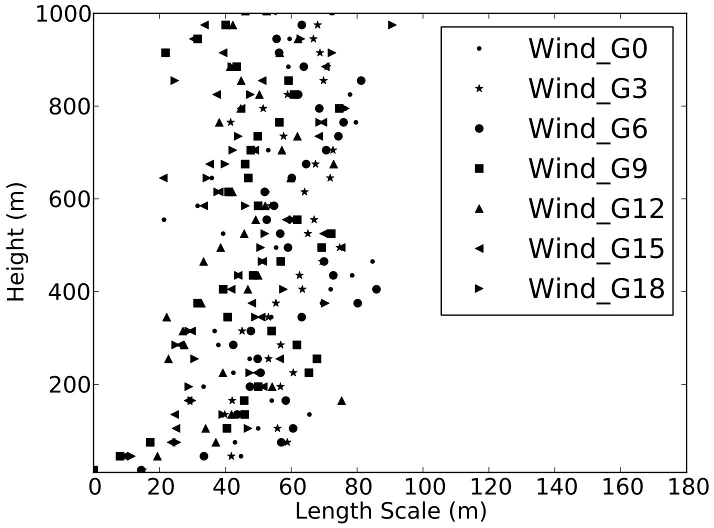

Figure 4.19: The integral length scale profile, the composition is based on the gradient wind speeds.

$$u(z) = \frac{u_{*0}}{k}\left[\ln\left(\frac{z}{z_0}\right) - a\left(\frac{z}{H^*}\right)^p\right] \tag{4.12}$$

where z_0 is the aerodynamic roughness length and a, p are the model parameters. Following Pena et al. (2010) (see their equation 9), the derivative of the mean wind profile is related to the shear velocity and turbulence length scale as,

$$\frac{dU}{dz} = \frac{u_*}{l} \tag{4.13}$$

Combing equations (4.12) and (4.13), the turbulence length scale profile can be derived as,

$$\frac{1}{l} = \frac{1}{kz} + \frac{1}{-k(H^*)^2/(2az)} \tag{4.14}$$

under the assumption that a constant u_* is maintained throughout the entire boundary layer. In equation (4.14), the second term in the right hand side hardly influences the shape of the l profile. In detail, the first term in the right hand side of equation (4.14) is in the order of $1/z$ while the second term is in the order of $z/(H^*)^2$, and therefore the ratio of the first term to the second term is $(H^*)^2/z^2$. In a large portion of the HBL, this ratio is large enough to neglect the second term in equation (4.14). For example, when $z/H^* < 0.5$, this ratio is larger than 4.0. In summary, the constant shear velocity, u_*, gives the original length scale model proposed by Prandtl (1932) based on the empirical profile function of the mean HBL wind,

$$l = kz \tag{4.15}$$

If the shear velocity is assumed to decrease linearly in the boundary layer, as indicated in equation (4.7), the length scale profile is given as,

$$\frac{1}{l} = \frac{1}{kz(1 - \frac{z}{H^*})} + \frac{1}{\frac{-k(H^*)^2(1-z/H^*)}{2az}} \tag{4.16}$$

Similar as in equation (4.14), the second term in the right hand side is not important.

In detail, the ratio of the first term to the second term in the right hand side of equation (4.16) is in the order of $(H^*)^2(1-z/H)^2$. Even when $z/H^* \approx 0.9$, this ratio is larger than 2000 under the assumption that $H^* \approx 500m$. Thus, the length scale profile described by equation (4.16) is a parabolic function of height,

$$l = kz(1 - \frac{z}{H^*}) \tag{4.17}$$

The fact that turbulent length scale is a parabolic function of height is exactly one derivation of the turbulence diffusivity formulation used by the YSU scheme, as shown in equation (4.11).

Based on the analysis presented above, the empirical mean wind profile function, which is derived based on direct dropwindsonde observations, implies two possible turbulence length scale profile models in the HBL, and one of them is a parabolic function of height as implied by the YSU scheme. To validate this finding more directly, the turbulent integral length scale profiles calculated previously are compared to the profiles given by equations (4.15) and (4.17). The only parameter needed in the calculation is the boundary layer height scale H^*, and even H^* is not important in equation (4.15) as it only appears in the unimportant term. Naturally, the H^* value found by fitting the composited mean wind profile to the empirical profile function, which is detailed in section 4.2, is used. Figure 4.20 gives the comparison of the turbulent integral length scale and profiles calculated using equations (4.15) and (4.17) when the composition is for the MBL wind speed ranging from $32m/s$ to $35m/s$. It is shown that both equations (4.15) and (4.17) yields estimates of the turbulent integral length scale in the surface layer of the hurricane atmosphere, i.e. the lowest $50m$ in the HBL. Above the height of $50m$, equation (4.15) starts to overestimate the turbulent integral length scale, while equation (4.17) still yields a reasonable estimates of the turbulent integral length scale up to a height of $150m$. From the height of $150m$ upwards, the turbulent integral length scale calculated through compositing dropwindsonde measurements fluctuates around a constant. In contrast, both equations (4.15) and (4.17) indicates that there still are functional variations. Similarly, Fig. 4.21 shows the comparison between the turbulent integral length scale calculated by compositing dropwindsonde measurements according to the gradient wind and estimated by equations (4.15) and (4.17). As in the discussion on the comparison shown in Fig. 4.20, the comparison shown in Fig. 4.21 also indicates that equation (4.15) only yields reasonable estimates of turbulent integral length scale below the height of $100m$ while equation (4.17) yields reasonable estimates up to a height of $200m$. In summary, both equations (4.15) and (4.17) produce reasonable estimates of turbulent integral length scale in the lower portion of the HBL (in the order of $10m$). Equation (4.17) produces reasonable turbulent integral length scale to an altitude higher than the altitude below which both equations (4.15) and (4.17) are valid.

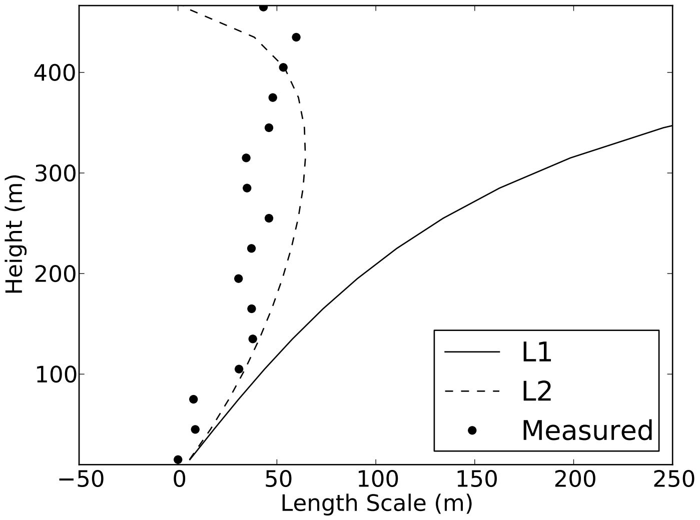

Figure 4.20: Comparison of integral length scale and modelled turbulence length scale. $L1$ represents length scale calculated based on equation (4.15), $L2$ represents length scale calculated based on equation (4.17) with fitting H^*.

From the discussion presented above, the theoretical analysis based on the mean wind profile function which is introduced by Vickery et al. (2009) indicates that the turbulence diffusivity formulation used by the YSU scheme is adequate to describe turbulent mixing in the HBL. This conclusion is drawn under two conditions: First, the shear velocity in the HBL can be modelled as linearly decreasing with height; Second, the height scale used in the empirical profile function, i.e. equation (4.12), and the surface shear velocity

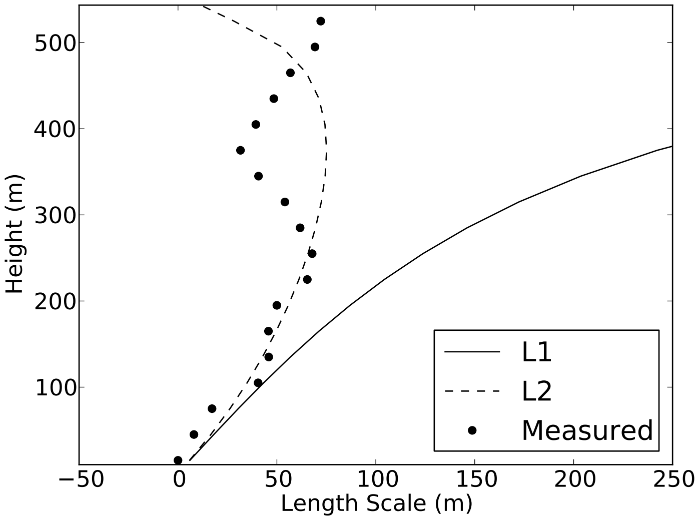

Figure 4.21: Comparison of integral length scale and modelled turbulence length scale. $L1$ represents length scale calculated based on equation (4.15), $L2$ represents length scale calculated based on equation (4.17) with fitting H^*.

u_* should be used as height scale and velocity scale in the YSU scheme turbulence diffusivity formulation. Comparing the theoretical model with the turbulent integral length scale calculated through compositing dropwindsonde measurements, however, indicates that a further investigation of the turbulence length scale in the HBL is necessary since there is appreciable difference between the model estimates and dropwindsonde observations. There are two parameters should be adjusted in the YSU scheme according to the theoretical analysis. The adjustment concerning the velocity scale is expected since the stability of the HBL has been found near neutral (French et al., 2007), and therefore $\phi^{-1}(0.1h/L)$, the Monin-Obukhov function evaluated at the top of the surface layer, is approaching 1.0 since the Monin-Obukhov length scale L is approaching infinity. In other words, under the near-neutral condition the Monin-Obkhov length scale stops being an important length scale and therefore should not be included in the HBL turbulence model. The adjustment concerning the height scale of the HBL is more complicated and will be discussed in detail in the next section.

4.5 The Height of the Boundary Layer

In section 4.4, it is shown that the HBL height scale is one important parameter in non-local PBL schemes, and it can be adjusted to make the YSU scheme more suitable to simulate turbulent mixing in the HBL according to theoretical analysis based on the mean wind profile function introduced by Vickery et al. (2009). As seen in equation (4.8) and (4.9), the height of boundary layer determines the formulation of the turbulence diffusivity in the boundary layer, and therefore determines the overall performance of the PBL scheme. Besides as a key parameter in the turbulence diffusivity formulation in "non-local" schemes, the boundary layer height also determines whether the PBL scheme is applied to solve the turbulent mixing equation at a certain height. Thus, an investigation on the HBL height is necessary by investigating turbulent characteristics revealed by compositing dropwindsonde measurements.

The HBL height is also one of the keys to understand the turbulence structure within the HBL. As discussed by French et al. (2007), the stability of the HBL is near-neutral due to the fact that both productions and dissipations of the turbulent kinetic energy are dominated by dynamic processes in the HBL which implies the Monin-Obukhov length scale is no longer an appropriate choice for scaling purpose. As shown by Zhang (2007, Chapter5), the HBL height is an appealing candidate for the length scaling parameter in such an environment. An accurate estimate of the HBL height would not only help improve the numerical simulation of hurricanes but also reproduce the generality of the turbulence structure within the HBL.

Due to the importance of the HBL height stated above, it is necessary to investigate the HBL in a more systematical and thorough way. To do that, the HBL heights are calculated, according to various definitions, based on dropwindsonde measurements. As argued by Zhang et al. (2011), the major issue associated with the HBL height calculation is that there are many definitions available and they usually produce different estimates of the HBL. Definitions adopted to calculate the HBL height are reviewed before the discussion of the dropwindsonde measurement composition results.

4.5.1 Theoretical Background

As introduced above, different definitions of the PBL height show a discrepancy in directing the HBL height calculation, which then leads to the difference of the calculation results. In fact, the study of Zhang et al. (2009) indicates the height defined thermodynamically is just half of that defined dynamically. Thus, following the philosophy used in the study of Zhang et al. (2011), the comparison of the HBL heights calculated differently would advance our understanding of this important HBL length scale and also improve the boundary layer turbulence model. To assist the discussion of the comparison, all definitions used are summarized as follows.

First, the height scale, H^*, used in the empirical profile function provided by Vickery et al. (2009), or equation (4.12), is adopted. Within the same framework detailed in section 4.2, the dropwindsonde data are composited to produce the mean wind profile of the HBL. Then, the value of H^* is found by fitting the composited mean wind profile to the empirical profile function. Details of calculating the mean wind profile by compositing dropwindsonde measurements and the best fitting approach can be found in section 4.2.

Second, the inflow layer depth is calculated when the measured wind velocity is decomposed into tangential and radial components. Following the method used by Zhang et al. (2011), the inflow layer depth is defined as the height at which the radial velocity reaches 10% of the strongest inflow beneath.

Third, the mean virtual potential temperature profile is calculated and investigated. As introduced by Anthes and Chang (1978) and followed by Zhang et al. (2011), the top of the mixed layer, which is also the top of the ABL thermodynamically, is the place where the virtual potential temperature deviates from the mean of virtual potential temperatures measured in the lowest $150m$ by $0.5K$.

Fourth, a critical Richardson number is used. As currently adopted in the YSU scheme (Hong and Pan, 1996; Hong et al., 2006), the height of the boundary layer is calculated as the height where the bulk Richardson number exceeds some critical value. The formula provided by Zhang et al. (2011), rather than the original one used in the YSU scheme, is adopted here due to the difficulties in estimating the surface thermal variables required by the original formulation. The formula, from the summary of Zhang et al. (2011), is repeated,

$$Ri = \frac{(g/\theta_{vs})(\theta_z - \theta_{vs})(z - z_s)}{(U_z - U)^2} \tag{4.18}$$

where Ri is the bulk Richardson number, θ_v gives the virtual potential temperature, z gives the height and U gives the wind velocity. Subscripts z and s separate values at the top of the boundary layer from those at surface. In the calculation based on dropwindsonde measurements, the critical Richardson number is taken as 0.25, and the surface value at a height of $0m$ is calculated as the mean of the measurements taken below $50m$ to get rid of the measurement fluctuations close to the sea surface.

4.5.2 The Composition Result and Comparisons

Based on the definitions articulated above, the HBL height is calculated through compositing dropwindsonde measurements. Figure 4.22 gives the comparison of the HBL heights calculated according to different definitions when the composition is based on the MBL wind. While the inflow layer depth is found close to H^*, which is also a dynamic HBL height indicator, the height calculated based on the virtual potential temperature and the critical Richardson number is far lower than those defined dynamically. This substantiates the finding made by Zhang et al. (2011). Moreover, the two dynamically defined HBL heights decrease with the increasing MBL wind speed. In contrast, the height calculated according to thermodynamic definitions, i.e. the virtual potential temperature definition and the critical Richardson number approach, keeps a constant regardless of MBL winds. When investigating the HBL height calculated according to thermodynamic boundary layer characteristics more closely, the height calculated based on the virtual potential temperature is constant in relative low wind speed region while the height calculated through a critical Richardson number approach slightly increase with MBL wind speeds in low wind speed region (lower than $25m/s$).

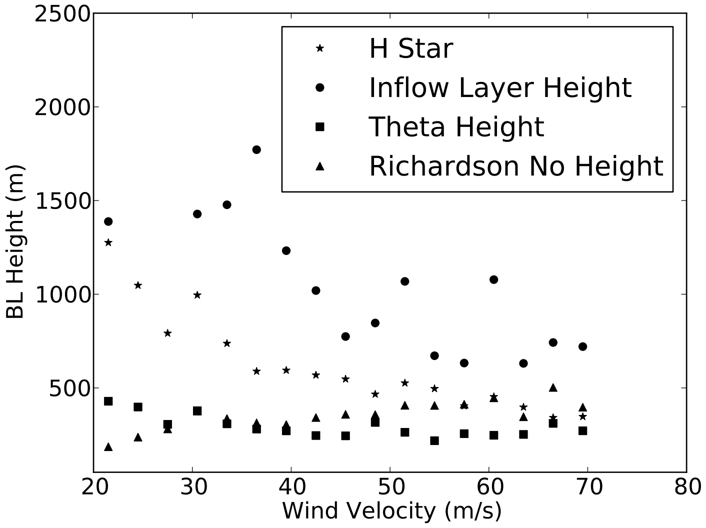

Figure 4.22: Boundary layer height comparison where Theta represents height calculated based on the virtual potential temperature, others are self explained. The composition is based on the MBL wind speeds.

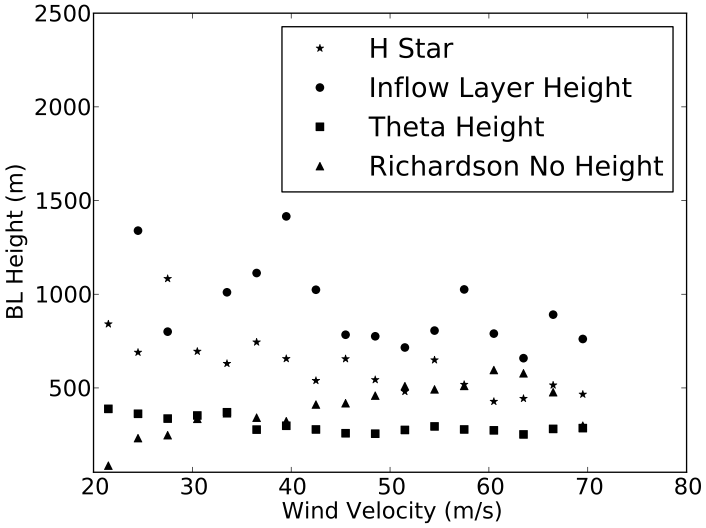

Figure 4.23: Boundary layer height comparison where Theta represents height calculated based on the virtual potential temperature, others are self explained. The composition is based on the gradient wind speeds.

The difference between the HBL height calculated according to thermodynamic definitions and dynamic definitions may be able to be explained by the assumption adopted by Zhang et al. (2008) and Zhu (2008), i.e. the existence of large eddies in the HBL. Considering the HBL height calculated according to the virtual potential temperature profile is indicate the top of a relatively vertically flat virtual potential temperature profile, this HBL height shows the upper boundary of a well mixed layer. Meanwhile, large eddies are more effective in transporting and mixing, the well mixed layer may indicate that large eddies dominates turbulent mixing in this layer. The fact that the thermodynamically defined HBL height is lower than dynamically defined HBL height actually substantiates the existence of large eddies in the lower portion of the HBL.

4.6 Conclusion

Although it has been shown that turbulent exchanges are important in overall tropical cyclone dynamics, few studies have been conducted to reveal turbulence structures and characteristics within the HBL. To fill this gap in our knowledge, the HBL turbulence is investigated using dropwindsonde measurements accumulated in the last decade. More specifically, more than 4000 dropwindsonde profiles gathered from 1997 to 2010 are processed and composited to produce not only the mean but also the turbulent wind structure of the HBL, including the turbulence intensity and turbulence length scale. Based on the dropwindsonde motion simulation study, as detailed in chapter 3, this composition data size is large enough to give statistically meaningful turbulence results.

The mean wind profile composited, validating the empirical profile function from the study of Vickery et al. (2009) more strictly in terms of the composition resolution, shows that the sea surface drag coefficient behaves more complicated than several previous studies has been revealed. The composited dropwindsonde measurements showed that the sea surface drag coefficient may decrease under extreme high wind speed conditions (higher than $50m/s$), while previous studies indicates the sea surface drag coefficient levels-off when the MBL wind exceeds some critical value. In addition to grouping dropwindsonde profiles according to the MBL wind speed, composition based on the gradient wind is conducted and shows that it is also a reasonable grouping indicator. However, the results calculated based on the gradient wind lack the capacity of reflecting wind characteristics in the lower portion of the HBL. In addition, mean wind profiles composited according to the combination of the dropwindsonde splash down location and MBL wind show that there is a systematical difference among the mean wind vertical structure from different regions of a tropical cyclone.

Thanks to the large database of the dropwindsonde measurement, the turbulence intensity can be calculated in addition to the mean wind profile. Validating the finding of the CBLAST experiment, the turbulence intensity of the tangential wind shows a clear trend of decreasing with height and then levelling off above $400m$. The collapse of turbulence intensity profiles, corresponding to different MBL wind speeds, shows the independence of the vertical turbulence intensity structure from the hurricane wind strength. The composition according to the gradient wind, on the other hand, does not give results as good as the composition according to the MBL wind, since the gradient wind speed preserves only a weak connection with wind characteristics in the lower portion of the HBL. This suggests although the gradient wind speed is a reasonable grouping indicator to study the mean wind profile in the HBL, it is not recommended in studying wind structures strongly influenced by surface characteristics.

Based on the same database, the vertical structure of the turbulent integral length scale is calculated. Since the turbulence diffusivity, which is critical in the PBL scheme used in various numerical simulation packages, can be modelled as the product of a turbulent velocity scale and a turbulent length scale, the profile of the turbulent integral length scale can be used to investigate the turbulence diffusivity formulation used in the YSU scheme. While a theoretical analysis, which is based on the mean wind profile function introduced by Vickery et al. (2009), substantiates the use of the YSU scheme to simulate turbulent mixing in the HBL, the turbulent integral length scale calculated through compositing dropwindsonde measurements shows the necessity of a further investigation. According to the theoretical analysis, there are two parameters adjustable in the YSU scheme to make it more suitable to simulate turbulent mixing in the HBL. First, the velocity scale used in the turbulence diffusivity formulation should be purely dynamical. Second, the HBL height should be carefully calculated.

Since the boundary layer height critically influences modelling turbulent mixing in the HBL, the HBL height calculated based on various HBL characteristics are compared to provide some insights into turbulence processes in the HBL and to make suggestions on improving the HBL height calculation used in PBL schemes. In an agreement with Zhang et al. (2011), it has been found that the thermodynamically defined height is much lower than the dynamically defined HBL height. It is argued that large eddies, or roll vortices, retained in the low portion of the HBL are the reason for such a phenomenon.

In conclusion, dropwindsonde measurements, which describes the entire HBL wind with an unprecedented accuracy and resolution, provide an opportunity to derive turbulence characteristics in the HBL, and the composited dropwindsonde measurements reveals the vertical structure of the mean wind, turbulence intensity, turbulent integral length scale and height scale in the HBL. Among turbulent characteristics investigated, the turbulent integral length scale provided an opportunity to analyze the turbulence diffusivity formulation adopted by the YSU scheme.

Chapter 5

Numerical Simulation

As discussed by many previous studies (Braun and Tao, 2000; Davis and Bostart, 2002; Nolan et al., 2009b,a), turbulent mixing within the HBL plays a key role in determining the output wind or thermodynamical variable fields of numerical simulations of hurricanes. The PBL scheme, which is one software component in numerical simulation packages, governs turbulent mixing within the ABL by formulating the turbulence diffusivity coefficient used in the vertical diffusion term in the flow governing equations. Although numerical simulation is one major technique used in studying tropical cyclones, the PBL schemes widely adopted by main stream numerical simulation codes are designed to describe turbulence characteristics in the standard ABL rather than in the HBL. The standard ABL can be defined as the ABL with a general wind strength (measured as mean of wind velocities in the lowest $500m$ in the ABL) lower than $20m/s$. This deficiency is crucial since the NWP is the most advanced technique based on which real-time hurricane predictions are made. Thus, it is reasonable to expect numerical simulations to give a more realistic prediction when the special turbulence characteristics found by compositing dropwindsonde measurements are incorporated into the turbulence diffusivity formulation in the PBL scheme used in numerical simulations of hurricanes.

As in the discussion on the turbulent integral length scale found by the composited dropwindsonde measurements, the YSU scheme is found to be valid to describe turbulent mixing in the HBL through a theoretical analysis using the mean wind profile function introduced by Vickery et al. (2009). While the turbulent integral length scale calculated through compositing dropwindsonde measurements indicates that the vertical variation of the turbulence length scale implied by the YSU is not in an agreement with dropwindsonde observations, it is worthwhile to check the validity of the YSU scheme in simulating turbulent mixing in the HBL more directly through numerical simulations. In the theoretical discussion presented in section 4.4, it has been found that there are two revisions necessary to make the YSU scheme more suitable under hurricane wind conditions. First, the surface friction velocity u_* should replace the mixed layer velocity $u_*\phi^{-1}(0.1h/L)$ in the turbulence diffusivity formulation as the turbulence velocity scale. Second, the HBL height calculated through the critical Richardson number approach should be revised. Since the first revision is expected to be taken care of by the formulation itself as the stability of the HBL approaches near-neutral condition as revealed by French et al. (2007), we focus on the HBL height calculation in this chapter. In investigating the HBL height calculation used in PBL schemes, high resolution numerical simulations of an idealized tropical cyclone are conducted. The simulation results are then compared to the composited dropwindsonde measurements, which is able to not only validate the use of the YSU scheme in simulating the hurricane wind field but also shed some lights on improving the HBL height calculations.

After the first section discusses the background information on the numerical simulation of hurricanes and HBL calculations from the theoretical perspective, the numerical simulation configuration of the high resolution numerical simulation is described in section 5.2. The comparison of the simulation results to the composited dropwindsonde measurement is presented in section 5.3, which forms the base for validating of the use of the YSU scheme and investigation of the HBL height calculations. Conclusions are given in section 5.4

5.1 Introduction

In analyzing the turbulent integral length scale calculated through compositing dropwindsonde measurements, the validity of the YSU scheme to simulate turbulent mixing in the HBL has been discussed. To extend this discussion and to investigate the use of the YSU scheme to simulate the HBL turbulent mixing more directly, a numerical simulation of hurricanes using the YSU is conducted in a comparison with the composition results of dropwindsonde measurements. In the discussion of turbulent integral length scale, a theoretical analysis based on the mean wind profile function introduced by Vickery et al. (2009) suggests revising the HBL calculation (see section 4.4). Zhang et al. (2011) studied the HBL height scale using dropwindsonde measurements which showed that the critical Richardson number approach currently utilized by the YSU scheme gives a HBL height radial variation different from the calculations based on other boundary layer characteristics. Therefore, a thorough investigation on the YSU scheme, including possible improvements through revising the HBL height calculation, should include a analysis of the numerical simulation results produced by different HBL calculations. Before analyzing the numerical simulation results, it is necessary to first discuss the HBL height from a theoretical perspective. As a result, this section is divided into two parts, a description of the background information concerning numerical simulations and a theoretical analysis of the HBL height.

5.1.1 Background of the Numerical Simulation

As indicated by several previous studies (Braun and Tao, 2000; Davis and Bostart, 2002; Nolan et al., 2009b,a), the numerical simulation results of tropical cyclones are sensitive to the formulation of the PBL scheme, which is responsible for modelling vertical turbulent mixing in the boundary layer. The PBL schemes currently used by various numerical packages are, however, designed to describe turbulent mixing in the standard ABL since direct observations of the turbulence characteristics within the HBL is relatively rare until very recently. To advance hurricane intensity numerical predictions, it is necessary to revise the currently utilized PBL scheme to take special turbulence characteristics of the HBL into account.

Among PBL schemes currently adopted, the YSU scheme used in WRF is widely used in numerical simulations of tropical cyclones, and therefore have been investigated by Nolan et al. (2009b) and Nolan et al. (2009a), who conducted high resolution numerical simulations of Hurricane Isabel (2003) using WRF with different PBL schemes. It has been found that the YSU model, which was originally developed based on the MRF model (Hong and Pan, 1996; Hong et al., 2006), provided results most consistent with observations given that it is revised to take into consideration the sea surface drag coefficient behaviour under high wind speed conditions. In addition, in the analysis of the turbulent integral length scale and in the discussion of the HBL height calculation (presented in sections 4.4 and 4.5), it is argued that the PBL height calculation currently employed in the YSU scheme may be inadequate to correctly estimate the HBL height. This issue was also discovered by Zhang et al. (2011), who used dropwindsonde measurements to directly calculate the HBL height according to different HBL height definitions. In the study of Zhang et al. (2011), it has been found that the HBL height calculated through the critical Richardson number approach, which is currently used in the YSU scheme, gives a radial variation different from those calculated differently. To investigate possible revisions up the original YSU scheme, the numerical simulations conducted in this study employ different boundary layer characteristics to estimate the HBL, which include the deviation of the virtual potential temperature, the height of the maximum simulated wind and a critical Richardson number approach.

As pointed out by Hill and Lackmann (2009), the horizontal grid spacing of numerical simulations, i.e. the averaged horizontal grid size, in tropical cyclones significantly influences the results. According to their study, which analyzed the wind and other thermodynamic variable fields of an idealized tropical cyclone simulated using WRF, the difference among simulated hurricane's intensities produced by different grid resolutions can be up to 30%. Thus, a high resolution numerical simulation is needed to ensure the reliability of outcomes of hurricane numerical simulations. However, it should be noted that the numerical simulation of atmospheric flows, unlike the simulation of other small scale engineering flows, keeps producing more detailed structure of simulated fields as the grid resolution increases, and therefore the grid independence required in usual computational fluid dynamics can not be achieved here. Therefore, the grid resolution independence check is not performed in this simulation. Details of the simulation configuration is presented in section 5.2.

5.1.2 Theoretical Analysis on the Height of the HBL

As discussed above, the YSU scheme can be made more suitable to describe turbulent mixing in the HBL by revising the velocity scale used in the turbulence diffusivity formulation and HBL height calculation. In the turbulence diffusivity formulation of the original YSU scheme, the velocity scale used is the mixed layer velocity, which can be expressed as $u_*\phi^{-1}(0.1h/L)$ while the composited dropwindsonde measurements suggests the surface friction velocity u_* is a better velocity scale in the turbulence diffusivity formulation describing turbulent mixing in the HBL. (see equation 4.10 for the meanings of the symbols). It can be easily seen that the mixed layer velocity approximates the surface friction velocity as the Monin-Obukhov length scale L increases since $\phi^{-1}(0.1/L) \approx 1$ as L increases. Under the condition that L approaches the infinite, the atmospheric stability approaches near-neutral condition and the Monin-Obukhov length scale stops being an important length scale. As found by French et al. (2007) and Drennan et al. (2007), this actually is the case for the HBL. As a result, the revision concerning the velocity scale is taken care of by the formulation itself. The revision concerning the HBL height calculation, however, is more complicated as indicated by Zhang et al. (2011). The discussion concerning the HBL height calculation, which is presented in section 4.5, is extended in this section to include some additional theoretical considerations.

From the model provided by Kepert (2001), the height scale of the HBL can be expressed as,

$$\delta = \sqrt{\frac{2K_m}{I}} \tag{5.1}$$

where δ gives the height scale, and the inertial stability I can be expressed as

$$I = \sqrt{\left(f + 2\frac{V}{r}\right)\left(f + \frac{V}{r} + \frac{\partial V}{\partial r}\right)} \tag{5.2}$$

while the classic Ekman equation gives the height scale of the ABL as,

$$\delta = \sqrt{\frac{2K_m}{f}} \tag{5.3}$$

In expressions (5.1) and (5.3), K_m is the turbulence diffusivity for the momentum, V denotes the gradient wind velocity, r gives the radius from the center of the storm and f is the Coriolis parameter. The height scale given by equation (5.1) shows a clear decreasing trend towards the storm center (Kepert, 2001), which is substantiated by reconnaissance flight observations (Frank, 1984), and dropwindsonde composition results (Vickery et al., 2009). In contrast, the classic Ekman equation gives a constant boundary layer depth everywhere in the atmosphere. Furthermore, provided by Kepert (2001), the height scale of the HBL can also be approximated by its relationship with the gradient wind as,

$$\delta \sim \frac{V}{I} \tag{5.4}$$

Meanwhile, based on the turbulence diffusivity formulation of the YSU scheme, the height scale given by the classic Ekman equation can be approximated by the relationship,

$$\delta \sim \frac{u_{*0}}{f} \tag{5.5}$$

Equations (5.4) and (5.5) show two different variations of the boundary layer height with wind speeds. Since I increases faster than V approaching the storm center as indicated by the decrease of the HBL height, as shown in the studies of Frank (1984), Kepert (2001) and Vickery et al. (2009), δ decreases with the increasing V in equation (5.4) whereas δ increases with the increasing u_{*0} in equation (5.5). Taken into consideration that the surface drag is generally increasing with the overall wind strength, equation (5.5) shows the height scale of the boundary layer increases with the wind speed. The conflict articulated above indicate that two different HBL turbulent mixing modelling approaches provided that the turbulence diffusivity is formulated based on the PBL height as in "non-local" PBL schemes. In detail, while equation (5.1) indicates turbulence processes in the HBL do not only depend on surface characteristics and the distance from the surface but also the relative position in storms, equation (5.3) shows that turbulence processes in the PBL is a "horizontally local" phenomenon in which horizontal large scale flows should be absent in the model. Although both the modelling and observational studies support the use of equation (5.1) in calculating the HBL height, its implication that turbulence processes depend on large scale flow characteristics is not throughly validated, and therefore should be further investigated.

On the other hand, the study of Zhang et al. (2009) revealed that the thermodynamically defined HBL height is significantly less than the dynamically defined HBL height in analyzing the turbulence characteristics in the HBL in outer rainbands observed by reconnaissance flights. This finding inspired Zhang et al. (2011) to investigate the HBL height scale more comprehensively through compositing dropwindsonde measurements. In this follow-up study, it is found that the HBL heights calculated based on the virtual potential temperature profile and the critical Richardson number are nearly half of that calculated based on the inflow layer depth and the maximum wind velocity. In addition, Zhang et al. (2011) also discovered that the HBL height calculated based on the critical Richardson number, which is currently employed in the YSU scheme, produces a questionable radial variation when compared to the HBL height calculated otherwise. This finding poses a requirement to revise the HBL height calculation adopted currently by the YSU scheme.

Since a virtual potential temperature profile showing the virtual potential temperature is a constant regardless of height, which is the indicator of the "mixed layer", implicitly reflects turbulent mixing, it is often used to define the PBL height. As a result, it is reasonable to assume that the discrepancy described above implies there may be two separate boundary layer heights existing in the HBL. In other words, in addition to the surface layer, there may be two layers, with different turbulence characteristics, existing in the HBL since both dynamical and thermodynamical boundary layer height definitions reflect important boundary layer turbulence characteristics. In detail, the top of the first layer is given by the thermodynamically defined HBL height while the dynamically defined HBL height gives the top of the second layer which is also the height of the entire HBL. The first layer, which can be labelled as the "mixed layer", is dominated by "horizontally local" turbulence processes, and therefore turbulence characteristics of this layer are similar to those found in the standard ABL. Furthermore, it is reasonable to assume large eddies, or roll vortices using the term discussed by Zhu (2008) and Zhang et al. (2008), are responsible for turbulent mixing within this layer. This explains the shape of the virtual potential temperature profile found within the thermodynamically defined HBL, since the large eddies are more effective in mixing to produce a vertically homogeneous virtual potential temperature field. Since the large eddy size should be determined by the distance from the surface rather than any horizontal length scales, turbulence processes in the first layer should depend only on surface characteristics and the distance from the surface, which made it a "horizontally local" phenomenon. The second layer, which is unique in the HBL, is influenced by large scale flows of tropical cyclones, the main vortices. Its depth, and therefore the height of the entire HBL, is governed by the inertial stability I, which is determined by the main vortex gradient wind field. Although it is only a preliminary attempt, the three-layer hypothesis articulated above successfully explains the conflict of the HBL estimated using equations (5.4) and (5.5) and the finding that the thermodynamically defined HBL height is significantly lower than the dynamically defined HBL height.

5.2 Simulation Configuration

One of the most important issues concerning, and a key factor in the configuration of, the numerical simulation is the grid spacing. As stated by Nolan et al. (2009b), the high resolution numerical simulation has been actively involved in researches on tropical cyclones as the computation capacity available keeps increasing in the past decade. Hill and Lackmann (2009) discussed the sensitivity of the simulation results to the grid spacing in the configuration. In these previous studies, the numerical simulation with a grid resolution as high as possible is always suggested since less processes need to be modelled in the high resolution simulation and the increase of the grid resolution has not questioned the numerical simulation base yet. Thus, a resolution even higher than the highest one used by Hill and Lackmann (2009) is adopted here. The finest horizontal grid spacing is $1km$, and 49 layers are formulated in the vertical direction whereas the simulation conducted by Hill and Lackmann (2009) used the finest horizontal grid spacing $4km$ and 31 vertical layers.

Considering the ultimate validation of the simulation result is the composited dropwindsonde measurements gathered in numerous hurricanes, it represents a "general picture" of wind, virtual potential temperature and relative humidity fields in hurricanes, an idealized, rather than any specific, tropical cyclone should be simulated and a compositional averaging post-processing approach should be employed to give general, representative features of tropical cyclones which are comparable to the composition result. Following Hill and Lackmann (2009), an environment which is favourable in generating and developing a tropical cyclone is assumed in formulating the initial and boundary conditions. Dunion and Marron (2008) reviewed the Jordan mean tropical atmosphere sounding (Jordan, 1958), and revised it by taking into account the influence of the Saharan Air Layer. The summary of their revised sounding (see their table 2) is adopted to provide the boundary conditions for the simulation. In addition, to ensure the simulated tropical cyclone has enough potential energy to achieve a steady-state intensity, a constant value of $29°C$ for the sea surface temperature is used in the simulation.

Taking elements mentioned above into consideration, the version 3.3 of WRF Advanced Research WRF (WRF-ARW) is used to simulate the idealized tropical cyclone. Four different domains, with horizontal grid spacings of $27km, 9km, 3km$ and $1km$ are utilized to give the "telescope nest" effect of the simulation. The most inner domain has 244 grid points in both horizontal directions which covers an area approximately a area of $245km \times 245km$. For the coarse domains with the grid spacing $27km$ and $9km$, the Kain-Fritsch cumulus scheme (Kain and Fritsch, 1993; Kain, 2004) is invoked to simulate convective processes while it is not activated for the domains with the grid spacing $3km$ and $1km$, since their high resolution is able to solve convective processes explicitly (Hill and Lackmann, 2009). The top of all domains is $50hPa$ and a Rayleigh damping layer is employed at the model top for the sake of numerical stability. As for microphysics, the Lin scheme is used (Lin and Farley, 1983) while the Rapid Radiative Transfer Model (RRTM) scheme (Mlawer et al., 1997) and the Dudhia scheme (Duhia, 1989) are used to simulate long-wave and the short-wave radiations respectively. The summary of the key information of the simulation configuration can be found in table 5.1.

Table 5.1: The key configuration of the numerical simulation

Domain Index	Cumulus Scheme	Grid Spacing (km)	Horizontal Dimension
Domain 1	Kain-Fritsch	27	90×90
Domain 2	Kain-Fritsch	9	91×91
Domain 3	None	3	148×148
Domain 4	None	1	244×244

For simulating turbulent mixing within the boundary layer, the YSU scheme is employed for all four domains. Since the surface layer scheme, which is responsible for calculating surface layer characteristics, is bundled with the PBL scheme in the current version of WRF-ARW, the Monin-Obukhov scheme, whose version is compatible with the YSU scheme, is selected. In the discussion about the HBL height calculation presented in section 5.1, it is shown that there are various definitions available to calculate the HBL height. According to the study of Zhang et al. (2011), they often disagree with each other. The numerical simulation provides an opportunity to investigate the influence of the HBL height calculation on the simulation results. In addition, as discovered by Zhang et al. (2011), the dynamically defined HBL height share the same radial variation which is confirmed by the height defined based solely on the virtual potential temperature profile. The height calculated through the critical Richardson number approach, however, gives a different trend. To investigate issues stated above, in addition to the critical Richardson number criteria which is currently used in the YSU scheme, one dynamic indicator, the maximum of the wind velocity in a vertical profile, and one thermodynamical indicator, the deviation of the virtual potential temperature are used to adapt the YSU scheme in the numerical simulation. Following Anthes and Chang (1978) and Zhang et al. (2011), the HBL height calculated based on the deviation of the virtual potential temperature is as the height at which the virtual potential temperature is deviated from its mean within the lowest $150m$ by $0.5K$. The adaption leads to three separate simulations, and comparing their results shows the influence of the PBL height calculation on the overall numerical simulation of hurricanes.

To facilitate the simulation, a well structured bogus vortex is inserted into the initial field described by the revised Jordan mean tropical sounding (Dunion and Marron, 2008). As discussed by Hill and Lackmann (2009), the influence of this bogus vortex is mainly on the time needed for the simulated tropical cyclone to reach a quasi-steady state. Thus, an arbitrarily chosen weak bogus vortex, with the maximum $10m$ wind speed of $30m/s$ and the RMW of $60km$, is used in the initialization. To ensure the simulated hurricane reaches the required quasi-steady state, a relatively long simulation period (10 days) is adopted. As argued by Hill and Lackmann (2009), this duration is long enough considering the inserted bogus vortex of their study is in fact weaker then the one currently used. Figure 5.1(b) shows a 240 hours time history of the minimum sea level pressure from the simulations. It can be seen that the quasi-steady state for all three simulations is simultaneously achieved between 150 to 180 hours from the start of the simulation. Thus, the outputs at the simultaneously steady-state moment, 180 hours from the start of the simulation, are compositional averaged and compared. At this moment, the simulated hurricanes intensities, measured as the maximum $10m$ wind speed, are $113.4m/s$, $91.1m/s$ and $100.4m/s$ for simulations based on the original YSU scheme, the revision using the virtual potential temperature and the maximum wind to calculate the PBL height respectively.

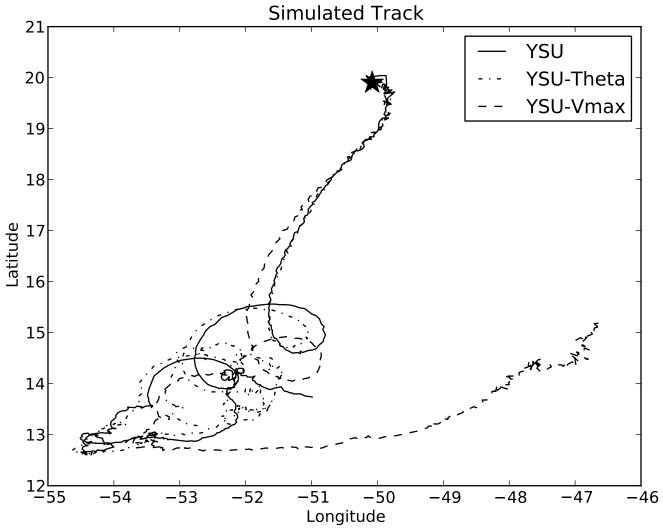

(a) Track

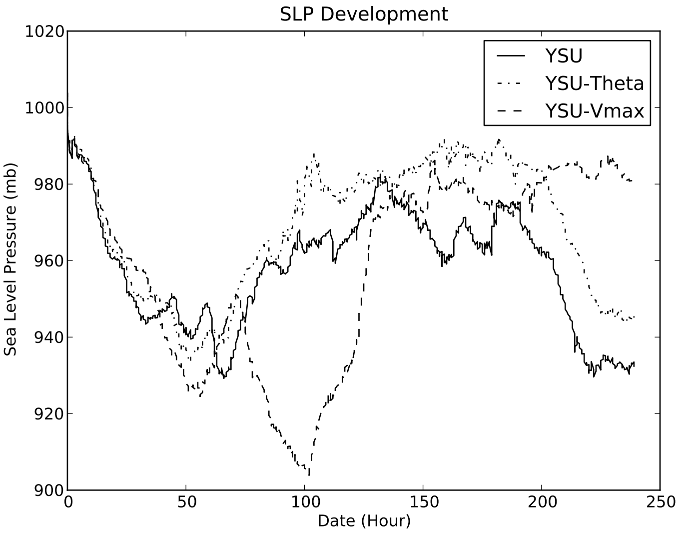

(b) Sea Level Pressure

Figure 5.1: Track and the intensity development of the hurricane in the 10 days simulation, the "YSU" denotes the output from original YSU scheme while the "YSU-Vmax" and "YSU-Theta" denote simulations using different calculations of the HBL height. Details can be found in the text. The star in the track plot denotes the start of simulations.

5.3 Simulation Results and Discussion

To more directly investigate the YSU scheme in simulating HBL turbulent mixing, numerical simulation results are compared to the composited dropwindsonde measurements. The comparison is not limited to the wind structure to provide a broader base for the investigation. In addition to investigating the YSU scheme, the composition can also be used to examine the three-layer hypothesis proposed in section 5.1. The investigation is conducted indirectly by comparing the results from the numerical simulations to the theoretical prediction concerning the variation of the boundary layer height with wind speeds, which is detailed in section 5.1. Hereafter, the simulation using the original YSU scheme is denoted as YSU simulation, the simulation calculating the PBL height based solely on the virtual potential temperature is denoted as YSU-Theta simulation and the simulation calculating the PBL height based on the maximum wind velocity is denoted as YSU-Vmax simulation. In order to reliably conduct the investigation of both the YSU scheme and the three-layer hypothesis, the output fields from the numerical simulations are compositional averaged just as in calculating the desired statistics using dropwindsonde measurements. Three parts are presented in this section, which are a description of the numerical simulation results post-processing procedures, the investigation of the YSU scheme and a discussion on the HBL height calculation.

Comparison Strategy

All the processing and composition procedures used to obtain the observational statistical profiles from dropwindsonde measurements are presented in chapter 4. As a result, the statistics of the HBL used in the following discussion are the same as in the analysis of dropwindsonde observations. Since the current numerical simulation is inadequate to produce any explicitly solved turbulence information in the HBL, only mean profiles of the wind velocity, virtual potential temperature and relative humidity are extracted from the composition of dropwindsonde measurements. Since the variation of the HBL height with wind speeds needs to be checked, the composition results based on both the MBL wind speed and gradient wind are extracted. An assumption underlying the composition according to wind speeds is that the wind structure of the HBL is only determined by the overall wind strength indicated by either the MBL wind or gradient wind. In addition, the composition results calculated based on the combination of the MBL wind and the relative horizontal measurement position are also included in the following discussion.

In order to be comparable to the composited dropwindsonde measurements, the outputs of numerical simulations are also compositionally averaged to produce the vertical profile of the desired mean profiles. More specifically, the simulated fields produced by the finest domain are taken, and the vertical profiles of meteorological variables at each horizontal computational grid are treated as an individual dropwindsonde profile. As a result, the composition database of the numerical simulation results contains 244×244 profiles. Following the same composition methodology used for the dropwindsonde measurements, both the MBL wind speed and the gradient wind speed are calculated to serve as grouping indicators in the compositional averaging process. Besides, the center and RMW of the simulated storm are calculated by fitting the sea level pressure output from the simulations to the simple Holland pressure profile model (Holland, 1980). This information is used to divide the considered domain into the inner core, eye-wall, and out-skirt regions as in the analysis of the composition of dropwindsonde measurements. The composition is then constructed combining the region division and the MBL wind speed in addition to based purely on wind speeds. The main difference between the two compositions, i.e. based on dropwindsonde measurements and based on simulated wind fields, is that the second is actually a spatial averaging since the simulation only provides a "snapshot" of the tropical cyclone structure.

Given both the dropwindsonde measurements and the simulation outputs are utilized to calculate the desire mean profiles in the same compositional way, their results of the wind velocity, virtual potential temperature and relative humidity are compared. It should be noted that both the dropwindsonde and numerical simulation, using WRF-ARW, do not directly report the virtual potential temperature. Thus, the air temperature, air pressure and relative humidity are used to calculated the virtual potential temperature before the composition.

5.3.1 Validation of the YSU scheme

Comparisons shown in Figs. 5.2 and 5.3, especially the comparison of the wind profile calculated for the composition according to the gradient shown in Fig. 5.3(b), indicate the boundary layer structure produced by the YSU simulation is close to that found by the dropwindsonde, especially in the lower portion of the HBL. It should be noted that although only the group with the MBL wind or the gradient wind in the region $(23m/s, 26m/s)$ is shown in Figs. 5.2 and 5.3, profiles from groups with other wind speeds show a similar trend. It is seen that the wind estimated by the YSU simulation is slightly larger than that observed by the dropwindsonde below $200m$. Moreover, the composited dropwindsonde measurements and the numerical simulation compositional means are in reasonable agreement in the range $(200m, 1000m)$ for both the MBL wind based and the gradient wind based compositions. However, the wind profile produced by the numerical simulation starts to overestimate the wind velocity from $1000m$ upwards for the MBL wind based composition and from $2000m$ for the gradient wind based composition. This implies the YSU simulation is inadequate to reproduce the mean wind structure of the entire HBL. In other words, the wind speed prediction produced by the YSU simulation is only close to the observed wind speed in the grouping height region, which is $0m - 500m$ for the MBL wind based composition and is $1500m - 2000m$ for the gradient wind based composition. This feature questions the the validity of the YSU scheme in describing turbulent mixing in the entire HBL. Recalling the analysis on the turbulent integral length scale calculated through compositing dropwindsonde measurements (see section 4.4 for detail), this feature substantiates the finding that the turbulent integral length scale estimated using the YSU scheme turbulence diffusivity formulation is close to the observation within $200m$ from the sea surface and shows a different trend from observation above $200m$. Furthermore, the comparison of the virtual potential temperature shows that dropwindsonde observations and numerical simulation outputs share the same trend. However, it can be seen that the numerical simulation result keeps deviating from the observed profile as the height increases. Although the "shift" effect seen in Fig. 5.2 can be explained by the unavoidable inaccuracy of setting the sea surface temperature to a constant value of $29°C$, which is different from the "averaged" sea surface temperature buried in a composition group, it reveals the inadequacy of the YSU scheme in reproducing the boundary layer thermodynamic structure. Unlike the comparison of the wind and virtual potential temperature, the relative humidity comparison (shown in Fig. 5.4) gives a larger discrepancy between the simulation results and dropwindsonde composition results. However, this does not suggest the performance of the YSU simulation is poorer in reproducing the humidity structure in the HBL since the "shift" effect is also seen in Fig. 5.4. Moreover, the horizontal scale is relatively small ($60\% - 100\%$ in Fig. 5.4), which exaggerates the difference. As for the "shift" effect seen in the relative humidity comparison, the same explanation can be applied. Since the surface scheme of the WRF-ARW relies on the sea surface temperature to calculate the surface layer humidity structure, which in turn is a boundary value for the relative humidity profiles seen in Fig. 5.4, the inaccuracy of setting the sea surface temperature to an arbitrarily chosen constant eventually leads to an unrealistic boundary value for the relative humidity profile.

As shown in the figures comparing the vertical structure found by the dropwindsonde and output from the numerical simulations, the difference gradually increases with height. Even in the gradient wind based composition, the observed and simulated vertical structure in the lower potion of the HBL are in reasonable agreement if the "shift" is removed. This is surprising since it is expected, from the comparison of the wind and other thermodynamic variables calculated for the MBL wind based composition, that the difference should be pronounced outside the grouping height, which is $(500m, 3000m)$ for the MBL wind based composition and $(0m, 1500m), (2000m, 3000m)$ for the gradient wind based composition. The reasonable agreement shown in the lower portion of the comparisons, therefore, requires an explanation beyond the consequence of the grouping scheme in the composition configuration. One reasonable explanation is that the YSU scheme is adequate to reproduce reliable structure of the wind and other thermodynamic variables in the lower portion of the HBL despite the fact that turbulent mixing at higher altitudes

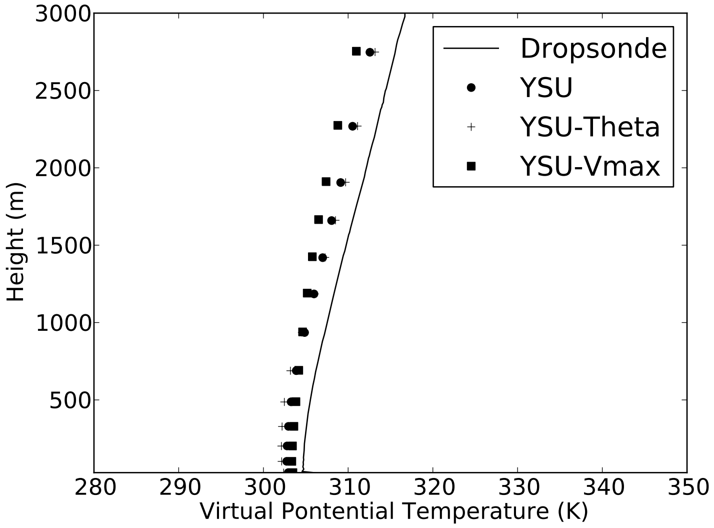

(a) MBL Wind Grouping

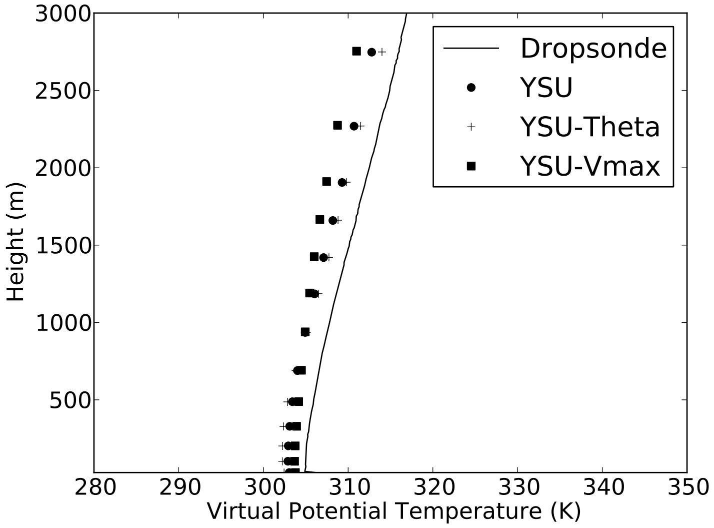

(b) Gradient Wind Grouping

Figure 5.2: The comparison of the profile of the virtual potential temperature, the wind velocity is $23m/s - 26m/s$ (for both the MBL winds and gradient winds), the "YSU" denotes the output from original YSU scheme while the "YSU-Vmax" and "YSU-Theta" denote simulations using different calculations of the HBL height. Details can be found in the text. the "Dropsonde" denotes the observation result from the dropwindsonde measurement.

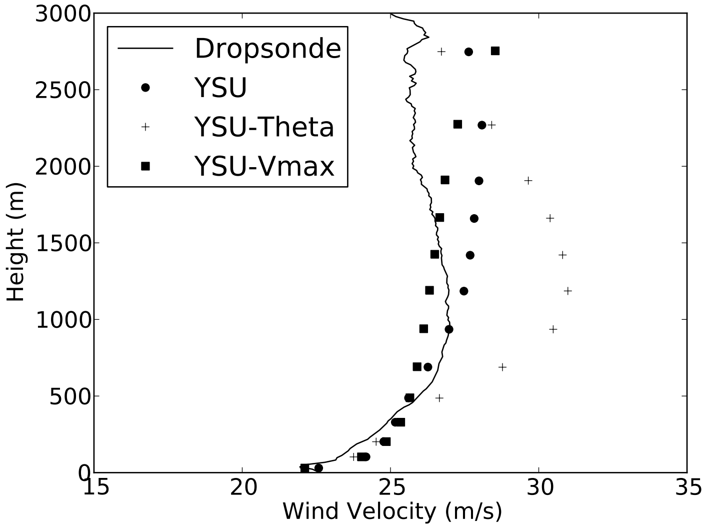

(a) MBL Wind Grouping

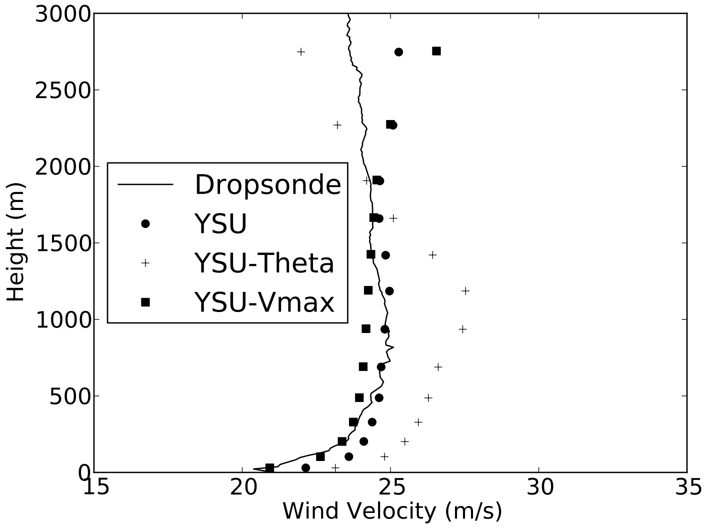

(b) Gradient Wind Grouping

Figure 5.3: The comparison of the profile of the wind velocity, the wind velocity is $23m/s - 26m/s$ (for both MBL winds and gradient winds), the "YSU" denotes the output from original YSU scheme while the "YSU-Vmax" and "YSU-Theta" denote simulations using different calculations of the HBL height. Details can be found in the text. the "Dropsonde" denotes the observation result from the dropwindsonde measurement.

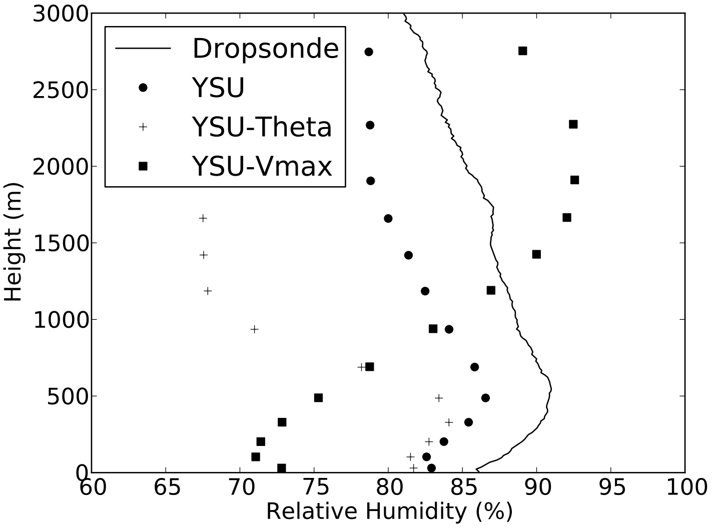

(a) MBL Wind Grouping

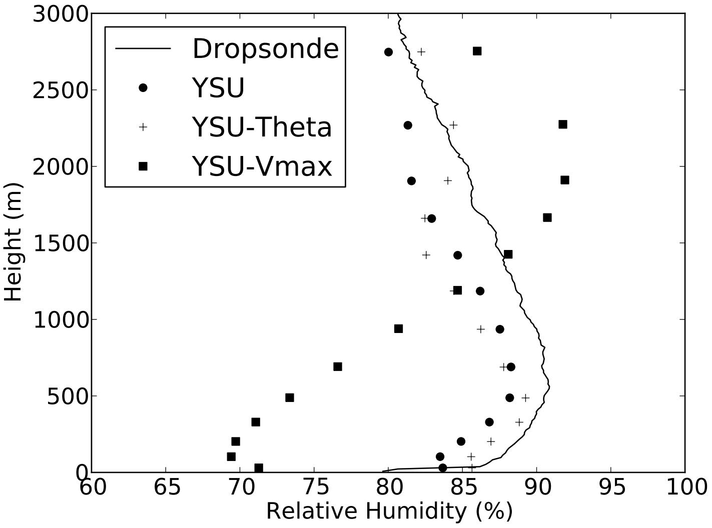

(b) Gradient Wind Grouping

Figure 5.4: The comparison of the profile of the relative humidity, the wind velocity is $23m/s - 26m/s$ (for both MBL winds and gradient winds), the "YSU" denotes the output from original YSU scheme while the "YSU-Vmax" and "YSU-Theta" denote simulations using different calculations of the HBL height. Details can be found in the text. the "Dropsonde" denotes the observation result from the dropwindsonde measurement.

deviates from the formulation used in the YSU scheme.

In short, based on the discussion presented above, the numerical simulations using the YSU scheme are able to reproduce the general shape of the vertical structures of the wind and other thermodynamic variables in the lower portion of the HBL and the fields output from the numerical simulations deviate from the observed values in the upper portion of the HBL. The deviation implies that, although the YSU scheme reliably represents turbulent mixing in the lower portion of the HBL (below $200m$), it does not describe turbulence processes in the upper portion of the HBL correctly.

5.3.2 Investigation on the PBL Height Calculation

As discussed in section 5.1, the HBL height calculation critically influences the reliability of the overall outputs from numerical simulations, and the critical Richardson number approach used by the original YSU scheme is questionable (Zhang et al., 2011), which is confirmed in the validation of the YSU scheme. Thus, the numerical simulations using other HBL height calculations, in addition to the critical Richardson number approach, are conducted to investigate the influence of the HBL height calculation on the simulation results. Details of HBL height calculations evaluated can be found in section 5.2.

First, the influence of the HBL height calculation on the long-term and large scale outputs from the numerical simulations is investigated. Shown in Fig. 5.1 is the track and intensity development of the simulated hurricanes from the YSU, the YSU-Theta and the YSU-Vmax simulations. Shown in Fig. 5.1(a), tracks of the simulated hurricanes are indistinguishable at the beginning, and the YSU-Vmax simulation starts to deviate from the YSU simulation far earlier than the YSU-Theta simulation. In addition, the YSU-Vmax simulation shows a significantly different intensity development history when compared to the YSU and the YSU-Theta simulations by giving an obvious intensification around 100 hours from the start of the simulation when the YSU and the YSU-Theta simulations keep a relatively constant intensity and is relatively stable at the end of the simulation when the YSU and the YSU-Theta simulations show a clear intensification.

This is expected since the YSU simulation, which uses the critical Richardson number to determine the HBL height, and YSU-Theta simulation, which determines the HBL height based on the virtual potential temperature, calculate the HBL height thermodynamically. In contrast, the YSU-Vmax simulation calculates the HBL height based on the maximum wind found in a vertical profile. Thus, the difference between the YSU and the YSU-Vmax simulations should be more pronounced than the difference between the YSU and the YSU-Theta simulations.

Second, detailed structures of meteorological variable fields output from the three simulations are compared to show the influence of the HBL height calculation on the detailed, short-term outputs of the numerical simulations. The comparison of the virtual potential temperature profile from the three simulations and composited dropwindsonde measurements is shown in Fig. 5.2. In the figure, it is obvious that the output from the YSU-Vmax simulation deviates from the YSU simulation above 1200m while the output from the YSU and YSU-Theta simulations are in reasonable agreement for nearly all heights. The difference between the output from the YSU-Vmax simulation and the composited dropwindsonde measurements is more obvious than the difference between the YSU simulation and the composited dropwindsonde measurements. This trend is also seen in the relative humidity comparison (shown in Fig. 5.4). In the figure, the output from the YSU-Vmax simulation gives a different vertical trend while the output from the YSU and the YSU-Theta simulations follows the trend shown by the composited dropwindsonde measurements. This reveals that calculating the HBL height according to the height of the maximum wind is inadequate to produce a reliable thermodynamic structure of the HBL since it only concerns kinetic characteristics in the HBL. Unlike the comparisons discussed above, Fig. 5.3 shows the wind velocity profile produced by the YSU and the YSU-Vmax simulations are in reasonable agreement, which are close to the profile observed by the dropwindsonde, while the YSU-Theta simulation significantly overestimates the wind speed for nearly all heights. The explanation of this feature relies on the difference of boundary layer characteristics, on which different HBL height calculations are based. Although the critical Richardson number is often taken as a thermodynamical definition of the boundary layer height, it involves the vertical wind profile. Thus, when compared to the YSU-Theta simulation, the YSU simulation reflects, to a limited extent, kinetic characteristics of the HBL, and therefore it should be expected to see the HBL height calculation based on the height of the maximum wind and the critical Richardson number are somewhat equally good at reproducing kinetic structures of the HBL.

It should be noted that there is a fundamental difference between two composition methodologies, used for dropwindsonde measurements and used for simulation outputs. As discussed above, the second is indeed a spatial averaging rather than an ensemble composition. To gain a more direct understanding of this difference, the distribution of the MBL wind and gradient wind, calculated as detailed in the composition of dropwindsonde measurements, from the output fields of the numerical simulations are shown in Fig. 5.5. It is obvious that both the MBL wind and gradient wind show a similar horizontal distribution, which is that high wind speeds are often seen in the eye-wall region of simulated hurricanes while the low wind speeds are found in either the inner core or the out-skirt region. Since the relative horizontal position is strongly related to both MBL winds and gradient winds in the numerical simulation output fields, as shown in Fig. 5.5, compositions based only on the wind speed introduce methodological differences in the comparisons. To more thoroughly investigate findings presented above, it is necessary to compare the numerical simulations and composited dropwindsonde measurements based on a composition combing the MBL wind speed and the horizontal measurement position. Such comparisons of the virtual potential temperature, relative humidity and wind velocity are shown in Fig. 5.6 which reflects wind characteristics of the HBL with the MBL wind in the range of $(40m/s, 50m/s)$ in the eye-wall region. In the lower portion of the HBL, the simulated and the observed structures are in reasonable agreement, including both the kinetic and thermodynamic structures. However, the simulated profile deviates from the observed profile from the middle of the HBL upwards. Moreover, the YSU and the YSU-Vmax simulations outperform the YSU-Theta simulation in predicting the wind profile while the relative humidity profile produced by the YSU-Theta simulation is in best agreement with in general, the observed value. Two conclusions can be drawn from these observed features. First, the original YSU scheme is adequate in describing turbulent mixing in the lower portion of the HBL (below $200m$ from the sea surface). Second, while the YSU and the YSU-Thata simulations produce similar HBL thermodynamic structure, which is in a general agreement with that observed by the dropwindsonde, both the YSU and YSU-Vmax simulations are capable of reproducing correct kinetic structures of the HBL.

To more directly investigate the influence of HBL height calculation on detailed structures of wind fields output from numerical simulations, the horizontal cross sections of the output wind fields are shown in Fig. 5.7. It is obvious that the HBL height calculation introduces significant differences in numerical simulation results. The horizontal wind field output from the YSU-Vmax simulation shows the most organized structures and those produced by the YSU simulation is the second. The wind field, including the vertical wind field, from the YSU-Theta simulation is highly asymmetric, and the main vortex core is hardly seen in Figs. 5.7(c) and 5.7(d). Similar as the comparisons shown in Fig. 5.7, the vertical cross sections of air temperature and wind fields output from numerical simulations are compared in Fig. 5.8. The comparison confirms the organized vortex structure and clearly defined warm core are not obvious in the outputs of the YSU-Theta simulation. Since the simulated hurricane intensity in the YSU-Theta simulation is high, $91.1m/s$ (the $10m$ maximum wind speed), it should produce a well organized main vortex according to our current understanding of tropical cyclone wind fields. The unorganized feature shown in the outputs of the YSU-Theta simulation may imply that calculating the HBL height according solely to the virtual potential temperature is inadequate to describe turbulence characteristics within the HBL. However, the horizontal sea level pressure profile comparison, shown in Fig. 5.9, illustrates the profile output by the YSU simulation is close to the YSU-Theta simulation while the profile produced by the YSU-Vmax simulation is significantly different from this ”consensus” variation. In the comparison, the radial profile of the sea level pressure is calculated by azimuthally averaging the output sea level pressure fields, which represents the general variation of

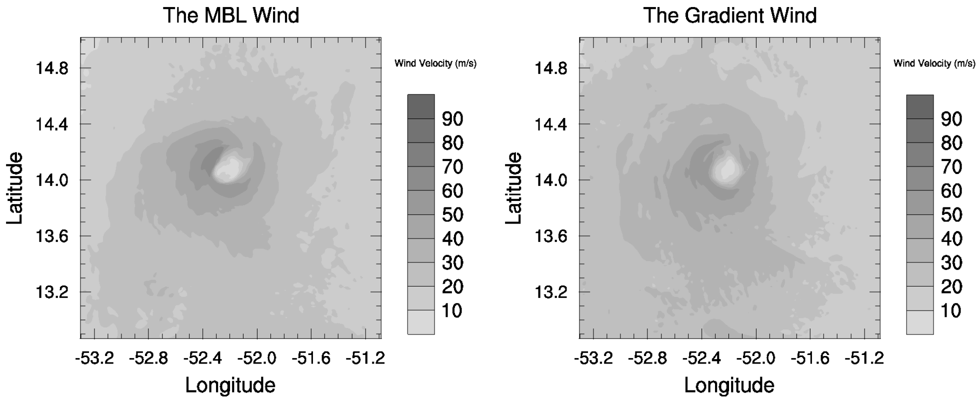

(a) MBL Wind from YSU (b) Gradient Wind from YSU

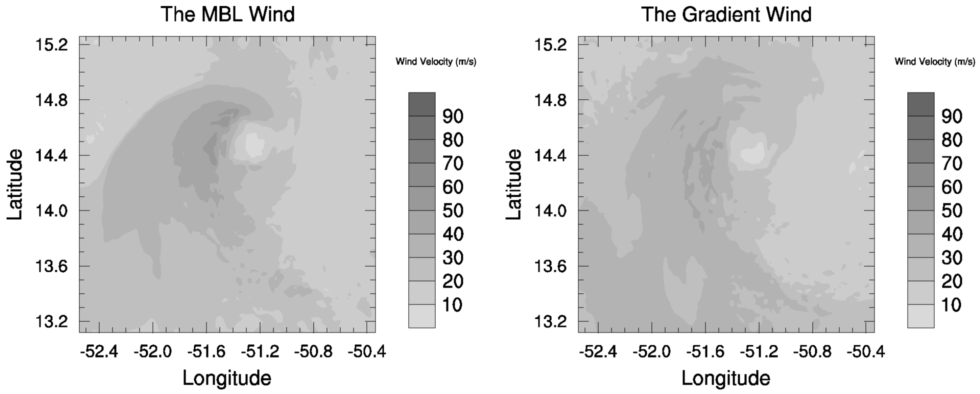

(c) MBL Wind from YSU-Theta (d) Gradient Wind from YSU-Theta

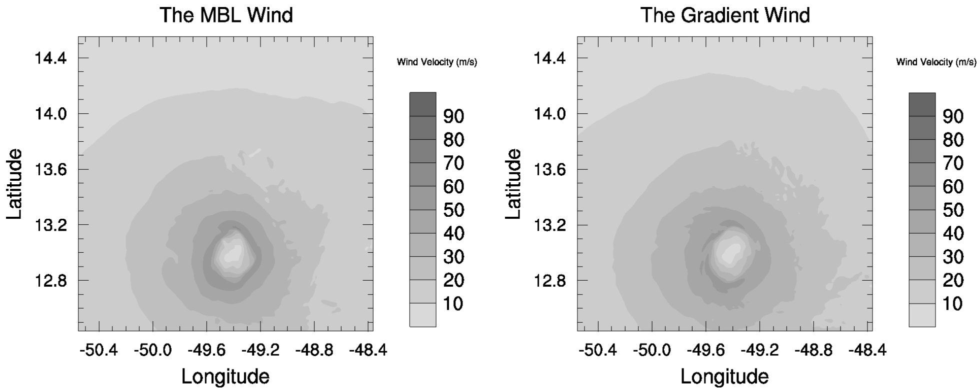

(e) MBL Wind from YSU-Vmax (f) Gradient Wind from YSU-Vmax

Figure 5.5: Horizontal contour of the MBL wind and the gradient wind of simulated hurricanes.

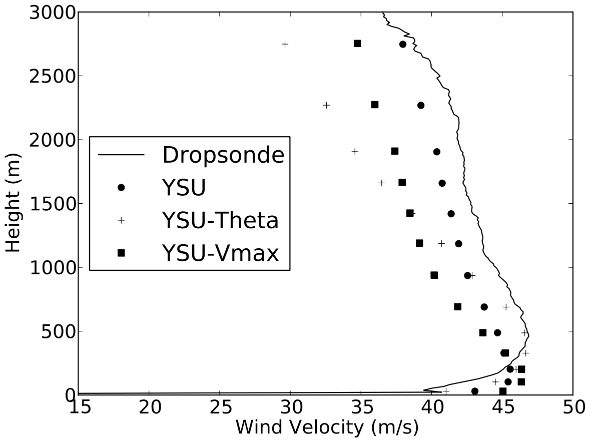

(a) Wind Profile

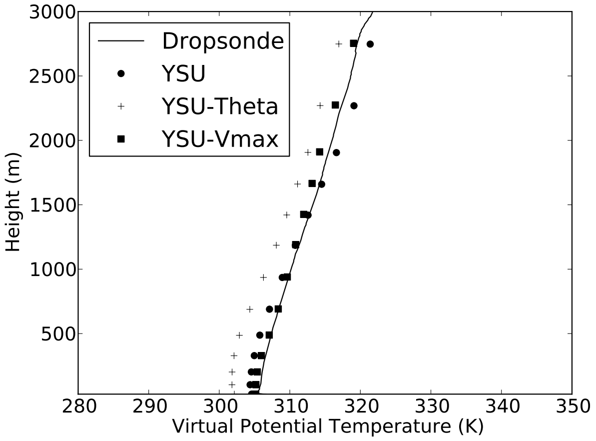

(b) Virtual Potential Temperature Profile

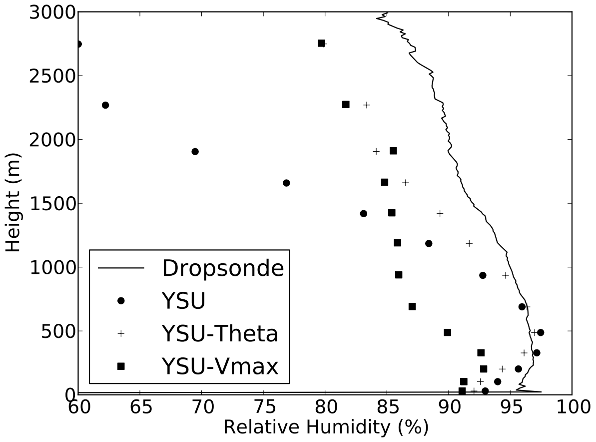

(c) Relative Humidity Profile

Figure 5.6: Comparison of the vertical structure found in the eye-wall region, the wind velocity is $40m/s - 50m/s$ (for both MBL winds and gradient winds), the "YSU" denotes the output from original YSU scheme while the "YSU-Vmax" and "YSU-Theta" denote simulations using different calculations of the HBL height. Details can be found in the text. the "Dropsonde" denotes the observation result from the dropwindsonde measurement.

the simulated sea level pressure field. As a result, the comparison shown in Fig. 5.9 indicates, although the detailed horizontal and vertical structures of air temperature and wind fields output from the YSU-Theta simulation are different from those output from the YSU simulation, their azimuthally averaged profiles are similar since they both are based on a HBL height calculated thermodynamically.

According to the discussion presented above, the HBL height calculation influences significantly outputs of numerical simulations, and the influence is not only on the detailed structure of output fields but also on the overall features of simulated hurricanes. Thus, it is necessary to investigate the HBL height itself more directly by comparing the PBL height output by the numerical simulations to the value calculated based on dropwindsonde observations. As in analyzing the numerical simulation outputs, different definitions are utilized to estimate the HBL height based on dropwindsonde measurements. Using the HBL height calculated in discussing dropwindsonde observations, as detailed in section 4.5, the HBL heights calculated based on dropwindsonde measurements provide a comparable criteria in evaluating the PBL height output from the numerical simulations.

Shown in Fig. 5.10 is the comparison of the HBL height calculated based on the simulation results and on the composited dropwindsonde measurements according to different PBL height definitions. It is obvious that the dynamically defined HBL heights, including the inflow layer depth, H^* and PBL height output by the YSU-Vmax simulation, are different from the thermodynamically defined HBL heights, including the height calculated according to the critical Richardson number and virtual potential temperature profile and the PBL height output from the YSU-Theta simulation, in two aspects. First, the value of the HBL height calculated according to a dynamic definition is significantly larger than the value calculated according to a thermodynamic definition. Second, the HBL height variation with the wind speed is different for the height defined dynamically and height defined thermodynamically. While the thermodynamically defined HBL height, either based on the numerical simulation results or based on dropwindsonde observations, shows that it is independent from the wind speeds (expect for the height

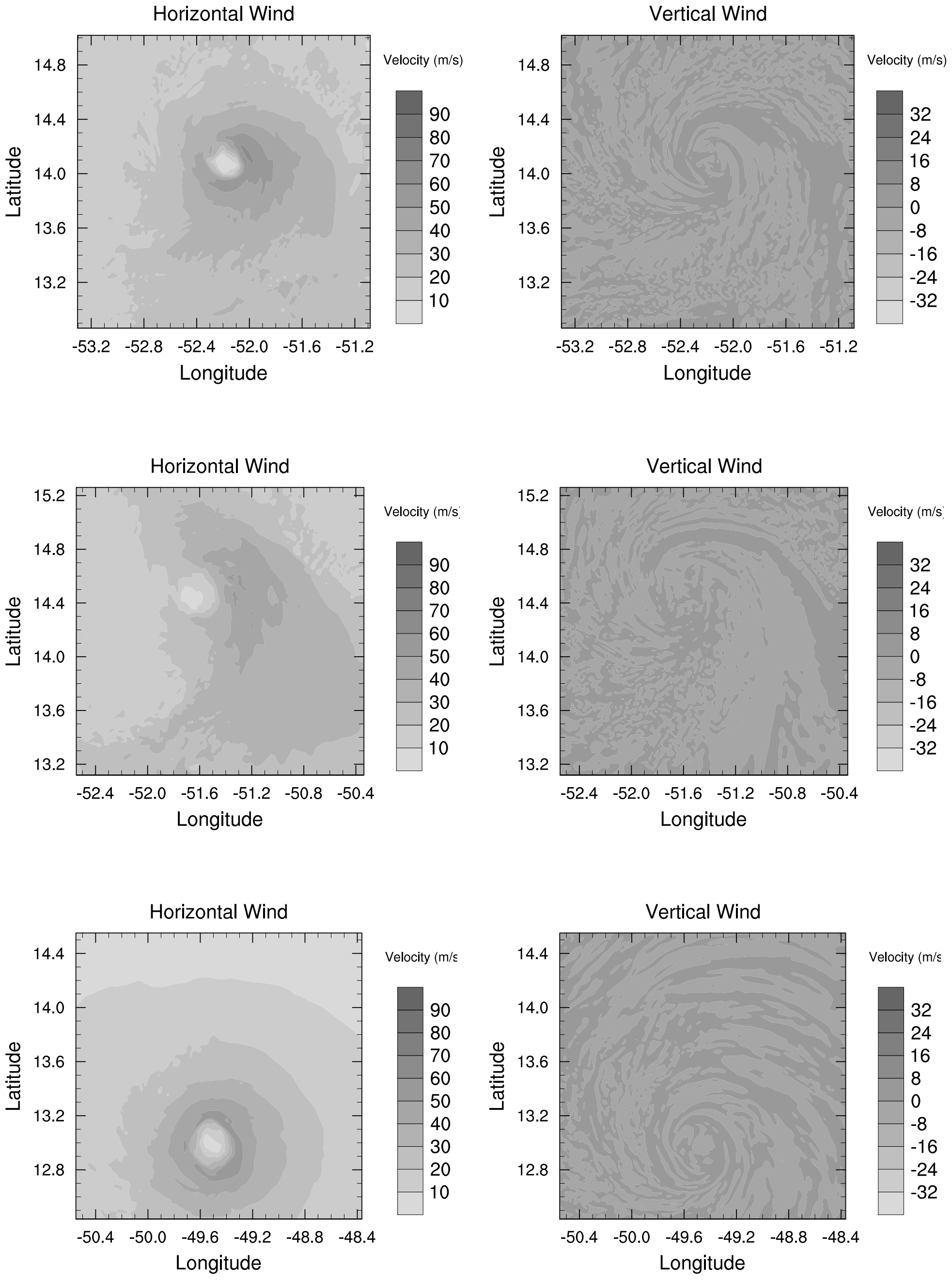

(e) Horizontal Wind from YSU-Vmax (f) Vertical Wind from YSU-Vmax

Figure 5.7: The comparison of the horizontal cross section, at $1000m$ above the sea surface, of simulated hurricanes. The velocity in legend indicates the magnitude of absolute winds.

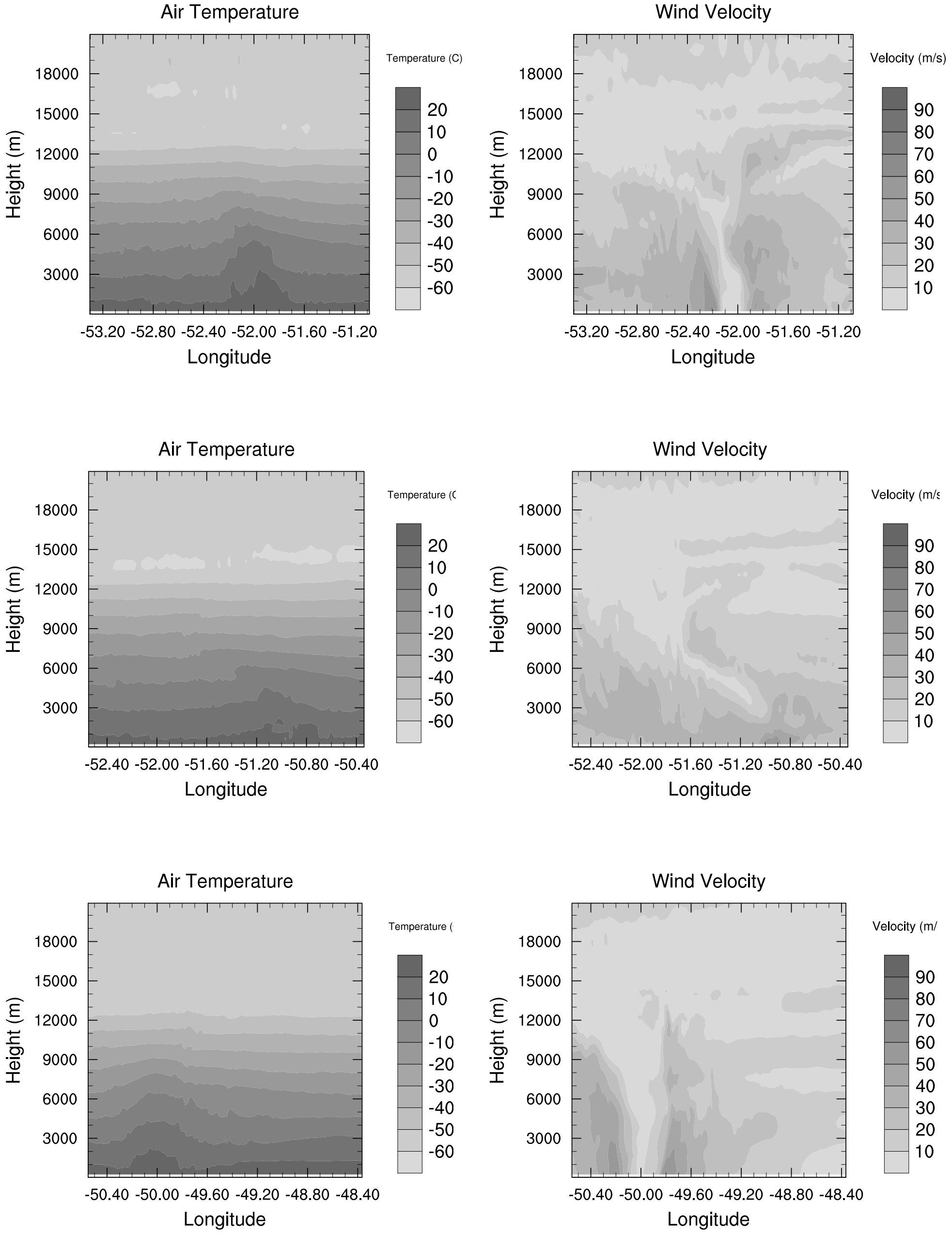

(e) Temperature from YSU-Vmax

(f) Horizontal Wind from YSU-Vmax

Figure 5.8: The comparison of the vertical cross section, through the center of the storm, of simulated hurricanes. The velocity in legend indicates the magnitude of absolute winds.

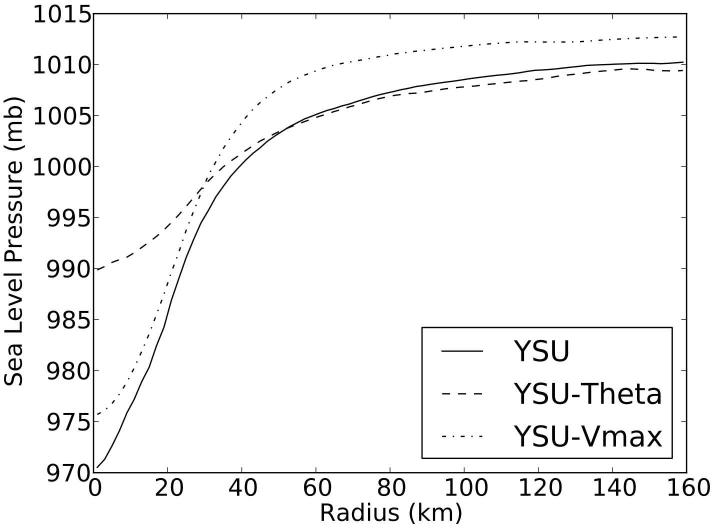

Figure 5.9: The radial profile of the sea level pressure.

calculated based on the critical Richardson number which increases with the wind speed in the lower wind speed region), the dynamically defined HBL height clearly decreases with the increasing wind speed. In the theoretical analysis on the HBL height as detailed in section 5.1, the depth of the layer influenced by large scale flows in tropical cyclones is expected to decrease with the increasing gradient wind while the depth of the "horizontally local" layer should increase with the surface friction velocity. As a result, the variation of the HBL height shown in Fig. 5.10 substantiates the hypothesis that the HBL should be considered as two layers in addition to the surface layer. In Fig. 5.10, the dynamically defined HBL heights, which are the sum of the depths of these two layers according to the three-layer hypothesis, shows the trend of decreasing with the increasing wind speed, which is actually a feature of the second layer given that the depth of the first layer, which is reflected by the thermodynamically calculated HBL height, is constant. The constant thermodynamically defined HBL regardless of wind speeds seems to conflict with the theoretical analysis if the thermodynamically defined HBL height gives the depth of the "horizontally local" layer, since it should increase with the surface friction velocity. However, it does not disprove the hypothesis since it can be explained by the finding made by Powell et al. (2003), which is confirmed by Vickery et al. (2009), that the sea surface drag coefficient levels off, or even decreases, when the

$10m$ wind speed exceeds some critical value, which indicates the surface friction has lost its conventional connection to the overall wind strength of boundary layer. As a result, the thermodynamically defined HBL height, or the depth of the second layer on the top of the surface layer, which is assumed to rely on the surface friction, maintains only a weak link to the overall wind strength measured as the mean of wind velocities in the lowest $500m$ above the sea surface.

In conclusion, the three-layer hypothesis is preliminarily validated which states that the HBL can be divided into three layers. The first layer is the surface layer in which meteorological structures are governed by Monin-Obukhov similarity theory. The second layer has the top found by the thermodynamically defined HBL height. Turbulence processes in this layer are mainly determined by horizontally local variables, such as the surface friction velocity u_* and distance from the surface. In this case, large scale flows of tropical cyclones, such as the gradient wind field of main vorteces, should not be included in a turbulence model of this layer, and therefore the turbulence diffusivity formulation designed to describe turbulent mixing in the standard ABL is still applicable. The third layer is the remaining part of the HBL. It is strongly influenced by large scale flows, and therefore its depth is determined by gradient wind flow characteristics of tropical cyclones, such as the inertial stability I.

To thoroughly investigate the PBL height output from the simulations and to check their radial trend following the methodology given by Zhang et al. (2011), horizontal contours and radial variations of the PBL heights output by the simulations are shown in Figs. 5.11 and 5.12. As discussed by Zhang et al. (2011), the HBL height calculated according to the critical Richardson number based on dropwindsonde measurements decreases outwards from the storm center while the height calculated otherwise shows an opposite trend. As illustrated in Fig. 5.11, although the PBL height output by the YSU-Vmax simulation is significantly larger than that output by the YSU and YSU-Theta simulations, they show a similar pattern of horizontal variations. Furthermore, the radial trend of the PBL height output by the YSU and YSU-Theta simulations, as shown

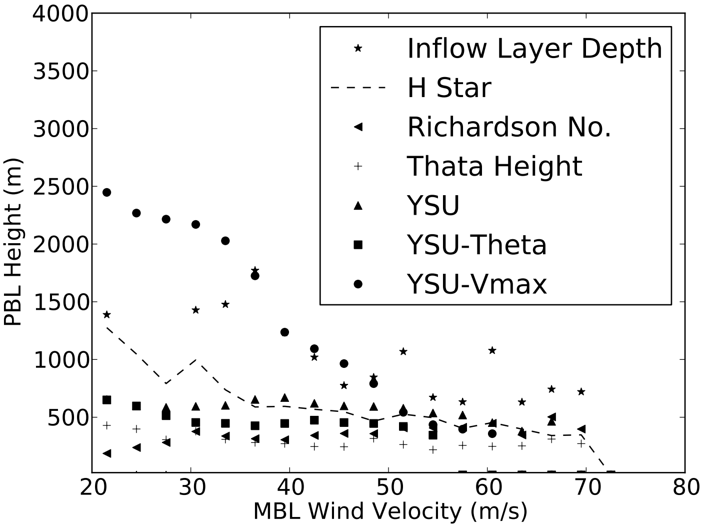

(a) MBL Wind Grouping

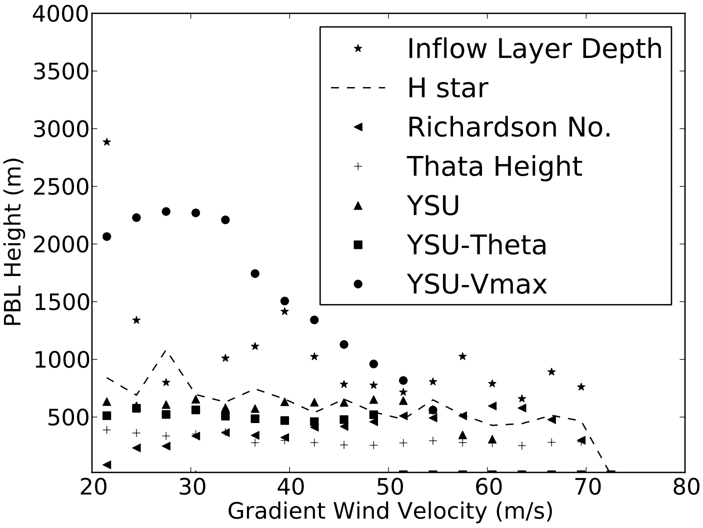

(b) Gradient Wind Grouping

Figure 5.10: The comparison of the variation of the PBL Height with the wind velocity, the definition used in calculation can be found in the text, the "Theta Height" denotes the height calculated based on the deviation of the virtual potential temperature, the "YSU" denotes the output from original YSU scheme while the "YSU-Vmax" and "YSU-Theta" denote simulations using different calculations of the HBL height.

in Fig. 5.12, follow the "consensus" trend found in the study of Zhang et al. (2011). This conflicts with the conclusion presented in the study of Zhang et al. (2011). Noticing that the radius shown in Fig. 5.12 is normalized by the RMW of the simulated hurricane, the PBL height output by the YSU-Vmax simulation decreases first to the minimum outside the eye-wall region, and then increases with radius. This reveals, combining the finding made based on the comparison shown in Figs. 5.2, 5.4 and 5.3, that simply changing the HBL height calculation is inadequate to correctly simulate the HBL wind field, and estimate the HBL height itself. Therefore, a deeper revision of the YSU scheme turbulence diffusivity formulation is required in numerically simulating hurricanes.

5.4 Conclusion

As pointed out by many previous studies, the PBL scheme used by numerical simulation packages has a great influence on their simulation results of tropical cyclones. Despite its importance, the widely used PBL schemes are designed to describe turbulent mixing in the standard ABL rather than in the HBL due to the lack of direct measurements. Thanks to the large database of the dropwindsonde measurement accumulated in the past decade, it is now possible to investigate the applicability of widely adopted PBL schemes in simulating turbulence processes within the HBL directly.

In theoretically analyzing the wind mean profile function introduced by Vickery et al. (2009), it has been found that the turbulent mixing length scale implied by the YSU scheme is in a reasonable agreement with that derived from the profile function used to describe mean wind velocity variation with height in the HBL. However, the turbulent integral length scale calculated by compositing dropwindsonde measurements shows that the turbulence length scale estimated by the YSU scheme does not agree with observations in the entire HBL (see section 4.4). To investigate this issue more directly, it is necessary to conduct numerical simulations of hurricanes using the YSU scheme and comparing the numerical simulation results with dropwindsonde observations.

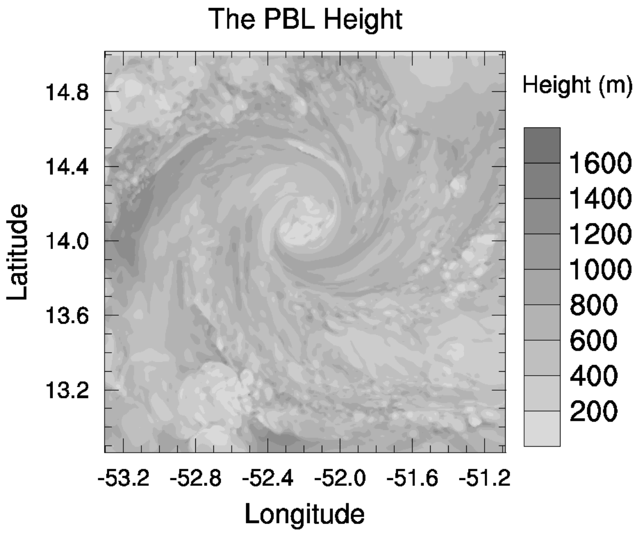

(a) PBL Height from YSU

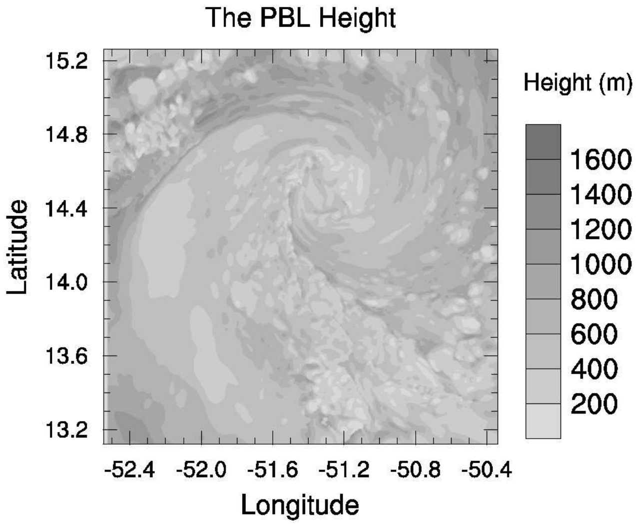

(b) PBL Height from YSU-Theta

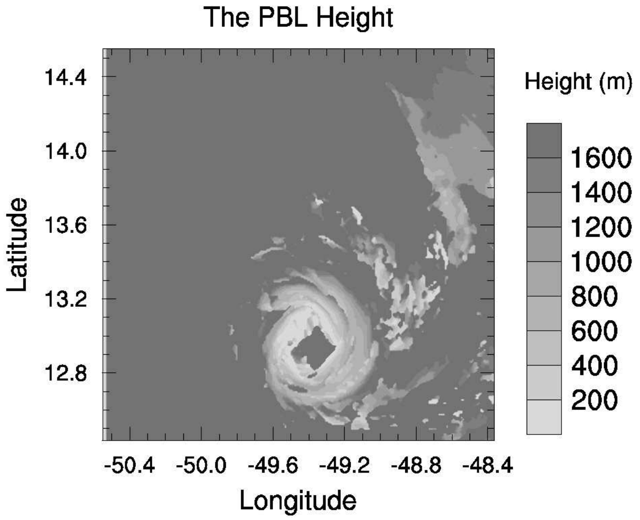

(c) PBL Height from YSU-Vmax

Figure 5.11: The comparison of the horizontal structure of the PBL Height.

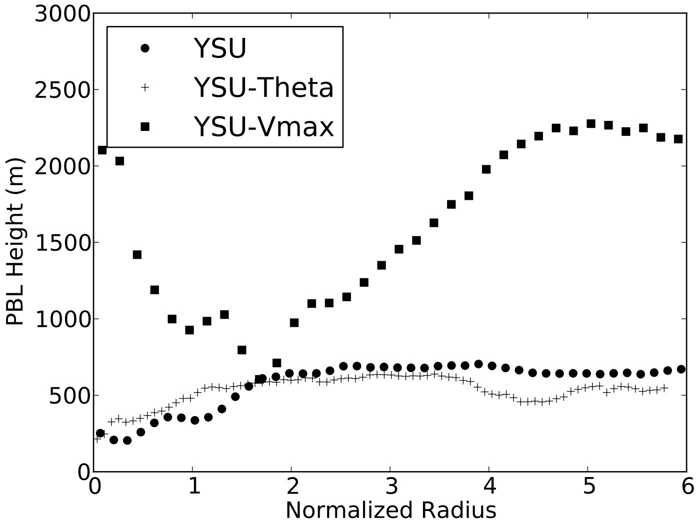

Figure 5.12: The radial variation of the PBL Height, the radius is normalized by the Radius of Maximum Wind,the ”YSU” denotes the output from original YSU scheme while the ”YSU-Vmax” and ”YSU-Theta” denote simulations using different calculations of the HBL height. Details can be found in the text.

In addition, there are two revisions needed to make the YSU scheme more suitable to simulate turbulent mixing in the HBL as indicated by the theoretical analysis detailed in section 4.4. One, the surface friction velocity should replace the mixed layer velocity to serve as the velocity scale in the turbulence diffusivity formulation. Two, the HBL height calculation should be revised to take special turbulence characteristics in the HBL into consideration. Given that the mixed layer velocity scale automatically approximates the surface friction velocity in the simulated hurricane since the stability of the HBL is found approaching neutral condition (French et al., 2007), we focus on the HBL calculation in this chapter. Kepert (2001) proposed a model to describe the boundary layer wind structure of tropical cyclones in which the HBL height scale depends on the inertial stability I of hurricanes. This leads to a decreasing trend of the HBL height with wind velocities. This feature conflicts with the understanding of the behaviour of the ABL height derived from the classic Ekman equation, which predicts a increasing trend of the ABL height with the wind speed. On the other hand, the dynamically defined HBL height is significantly larger than that defined thermodynamically (Zhang et al., 2011),. Synthesizing the findings articulated above , it is reasonable to hypothesize that there are three layers in the HBL. The first is the surface layer. The second layer has the depth found by the thermodynamically defined HBL height. The third layer, whose depth determines the height of the entire HBL, is strongly influenced by the large scale flow, and therefore its depth is determined by large scale features of hurricanes, such as I.

To more directly investigate the YSU scheme, and evaluate the three-layer hypothesis, high resolution numerical simulations of an idealized tropical cyclone are conducted. The compositional averaged numerical simulation results are then compared to the composited dropwindsonde measurements. The comparison indicates that the YSU scheme is inadequate to correctly models turbulence processes in the entire HBL although it produces a reasonable dynamic and thermodynamic structure in the lower portion of the HBL (around $200m$ from the sea surface). As illustrated in the theoretical analysis, the HBL height calculation is critical in the turbulence diffusivity formulation in a "non-local" PBL scheme. Therefore, the simulations include revisions of the HBL height calculations. The comparison of the simulation results to the composited dropwindsonde measurements shows:

- the calculation of the HBL height has a significantly impact on outputs of simulations, including overall features, such as the track of simulated hurricanes, and detailed simulated variable fields;
- changing the HBL height calculation alone is inadequate to make a "non-local" scheme, such as the YSU scheme, to correctly model turbulent mixing within the HBL;
- the three-layer hypothesis produced in the theoretical analysis part is indirectly validated since the prediction made based on the hypothesis agrees with the numerical simulation results.

Thus, findings made based on the numerical simulations and the analysis of dropwindsonde observations call for a further validation of the three-layer hypothesis. Since this validation requires more detailed direct measurements of turbulence characteristics in the upper portion of the HBL, it is beneficial to involve other observations in the investigation.

Chapter 6

Conclusions and Future Work

Reviewing the work that has been done in this thesis, it is clear that the theme is to reveal turbulence characteristics of the HBL by compositing direct measurements taken by dropwindsondes. The findings on turbulence within the HBL are useful because they are important in overall numerical models of tropical cyclones, and therefore are important in determining the reliability and accuracy of NWP model outputs used for real-time forecasts of tropical cyclones. Besides, HBL turbulent characteristics also influence dynamic responses of structures in hurricane-prone regions, and therefore code specifications concerning the wind-resistance structural design. Despite its importance, turbulence within the HBL has not been thoroughly investigated due to the scarcity of direct measurements. Thanks to the dropwindsonde measurement database accumulated for the past decade, a composition study of dropwindsonde measurements is able to give some useful features of HBL turbulence. To help readers review the essence of this work, a brief summary of the steps taken, together with the key findings made in each step, are given in section 6.1. Based on that, a discussion on possible future extensions is given in section 6.2.

6.1 Summary

Since the dropwindsonde takes direct measurements of the wind and other meteorological variables in neither a conventional Eulerian framework nor a perfect Lagrangian framework, the validity of deriving conventional Eulerian turbulence statistics from compositing dropwindsonde measurements is questionable. To fully understand the dropwindsonde motion in the measured wind field, and then to better interpret its wind measurements, an analysis of dropwindsonde motion characteristics is conducted as the first step in this thesis work. The analysis is built upon two bases. One, the analytical solution to the linearized dropwindsonde motion governing equations. Two, simulations of the dropwindsonde motion in a numerically generated pseudo-stochastic wind field with statistics close to those found in natural winds using the full nonlinear dropwindsonde motion governing equations. From the simulated dropwindsonde motions, the pseudo dropwindsonde measurements are sampled and processed to produce statistics of the measured wind field. Various aspects of post-processing and compositing dropwindsonde measurements are then investigated, which covers the validity of wind finding equations introduced by Hock and Franklin (1999), the finite difference scheme used to calculated the dropwindsonde acceleration required in the wind finding equations, the filter design used to smooth individual dropwindsonde profile, the influence of the composition data size, the gust time scale of the dropwindsonde wind measurement and the spectral information derived from dropwindsonde documented wind velocities.

From the discussion based on the analytical solution, it is found that the dropwindsonde can only pick up low frequency turbulence information. As a result, wind measurements taken by the dropwindsonde are required to be dynamically corrected to include high frequency turbulence information. Introduced by Hock and Franklin (1999), the wind finding equations, which are originally used to reduce the deficiency of the dropwindsonde in reproducing the mean wind velocity profile in a strongly shear flow, is actually adequate to return the high frequency turbulence information missed by the dropwindsonde by adding its acceleration as a dynamic correction. In addition, the numerical simulation provides a chance to investigate the finite difference scheme and the low-pass filter. It is found that although these post-processing schemes have little influence on the mean profile composition, they impact the turbulence information derived from dropwindsonde measurements appreciably and therefore should be chosen carefully when compositing dropwindsonde measurements if the turbulence information is of interest. Supported by the numerical simulation, dropwindsonde measurements accumulated in the last decade are sufficient to derive a reliable HBL turbulence structure. It should be noted that the simulation conducted at this stage is based on a relatively simple motion model which treats the dropwindsonde as a point object with a constant drag coefficient.

Since it is found that the wind finding equations are essential in reproducing not only the mean wind profile but also the vertical turbulence structure of the measured wind field, one assumption providing the foundations to derive the wind finding equations is that the dropwindsonde drag coefficient is constant, independent from angles of attack. Through the wind tunnel tests of a dropwindsonde model with a parachute, the dropwindsonde drag coefficient is found to vary appreciably with angles of attack. To investigate the influence of this finding on the use of the wind finding equations to retrieve winds from raw dropwindsonde measurements, the dropwindsonde motion is simulated based on an alternative model which includes an explicit expression for the dropwindsonde body orientation and therefore the angle of attack. Following the same approach as in the dropwindsonde motion simulation using the simple motion model, wind statistics derived from pseudo dropwindsonde measurements are compared to the ”true” statistics calculated through a statistical analysis of the known pseudo-stochastic wind field. The comparison evaluates the influence of the dropwindsonde drag coefficient variation with angle of attack on the wind retrieval using the wind finding equations and validates a new approach to calculate the vertical wind.

Since the alternative motion model described above is more sophisticated and realistic when compared with the simple model which treats the dropwindsonde as a point object, the wind finding equations are validated more strictly in the dropwindsonde motion simulation using the alternative motion model. In a comparison of the statistics derived from pseudo dropwindsonde measurements with the ”true” values calculated through a statistical analysis of the known pseudo-stochastic wind field, it has been found that the improvement of using the wind finding equations to estimate both the mean and turbulent wind profile found in the simulation using the alternative motion model is similar to that found the simulation using the simple motion model. This indicates that although the dropwindsonde drag coefficient varies with angle of attack appreciably, the wind finding equations are still valid since the dropwindsonde drag coefficient variation is implicitly reflected by the measured dropwindsonde falling rate. In addition, the comparison of statistics shows that a new approach to calculate the vertical wind, derived based on the alternative dropwindsonde motion model and including a correction using the angle of attack, improves the accuracy by 70%, and therefore is recommended in processing actual dropwindsonde measurements provided that the dropwindsonde angle of attack can be reliably measured.

To fully utilize the findings made by analyzing its motions to process dropwindsonde wind measurements, a package of specially designed codes, named PostSonde, are implemented to post-process and to composite dropwindsonde measurements gathered from the year 1997 to the year 2010. The composition methodology proposed by Powell et al. (2003) and Vickery et al. (2009) is followed and extended. dropwindsonde profiles, after a quality control and dynamic correction process, are composited in bins constructed vertically to formulate the desired statistical profiles of the measured wind field. To investigate the HBL wind field more comprehensively, the gradient wind, calculated by averaging the wind measurements taken from the height of $1500m$ to the height $2000m$, and the dropwindsonde splash down position are also used as grouping indicators in addition to the MBL wind speed, calculated by averaging the wind measurements taken from the sea surface to the height of $500m$. The significant contribution of this work is the post-processing and composition of dropwindsonde measurements produces not only the mean wind profile, but also the profiles of the turbulence intensity, profiles of the vertical turbulent integral length scale and height scale of the HBL. Since the turbulent wind velocity profile composited is consistent with the turbulent wind velocity profile found in the CBLAST experiment (Zhang et al., 2009), the turbulent wind calculation adopted here is validated. Due to the importance of the HBL height, the dropwindsonde measurements are used to investigate the HBL height calculation by comparing different estimates made based on different HBL height definitions.

In analyzing the dropwindsonde composition results, the mean wind structure in the HBL is found to be quite similar to that described by Powell et al. (2003) and Vickery et al. (2009). The empirical profile function introduced by Vickery et al. (2009) is validated based on a higher resolution composition conducted. The composition taking the dropwindsonde splash down location into account shows that there is a systematic difference among the mean wind profiles measured in different radial regions of a tropical cyclone. Supported by the turbulent wind velocity results derived from the CBLAST experiment, the dropwindsonde measurement composition reveals some reliable features of the turbulence within the HBL. For example, the turbulence intensity profile found by compositing dropwindsonde measurements shows that the vertical turbulence structure in the HBL is independent from the HBL wind strength and an universal scaling law can be applied. In addition, the vertical structure of the turbulence integral length scale shows that the turbulence diffusivity formulation used in the YSU scheme in WRF is applicable, in general, to describe turbulent mixing in the lower portion of the HBL (below $200m$). From a theoretical analysis of the turbulence length scale based on the empirical profile function validated before, there are two revisions necessary to make the YSU scheme more suitable to simulate turbulent mixing in the HBL. The two revisions are : one, the surface friction velocity, replacing the mixed layer velocity scale, should be used as the turbulent velocity scale in the turbulence diffusivity formulation; two, the PBL height calculation used by the original YSU scheme should be modified. In analyzing the HBL height found through analyzing dropwindsonde dynamical and thermodynamical measurements, one conclusion from Zhang et al. (2011) is substantiated that the thermodynamically defined HBL height is much lower than the dynamically defined HBL height.

To further investigate the YSU scheme and HBL height calculation, high resolution numerical simulations of an idealized tropical cyclone are conducted. Between the two revisions upon the YSU scheme found previously, the replacement of the turbulent velocity scale is expected to be taken care of by the YSU scheme formulation itself since the mixed layer velocity scale approximates the surface friction velocity in the near-neutral stability found in the HBL. Thus, we focus on investigating the HBL height calculation in numerical simulations. To investigate the use of the YSU scheme to simulate the HBL turbulence structure and the influence of the HBL height calculation on overall and detailed outputs from numerical simulations, the YSU scheme is adapted to include different HBL height calculations. The simulation results are then compared to each other and to the dropwindsonde observations to show the direction of possible improvements of the HBL turbulence modelling.

First, the comparison of the boundary layer profiles obtained in the simulations and calculated by composting dropwindsonde measurements substantiates the general use of the YSU scheme to describe the boundary layer structure in the lower portion of the HBL (up to around $200m$). Second, it is found that the YSU scheme is not valid for the entire HBL and simply changing the HBL height calculation does not ultimately solve the problem. Instead, a three-layer hypothesis is proposed to synthesize the turbulence characteristics observed by this work and previous studies (Zhang et al., 2009, 2011). This hypothesis is preliminarily validated by the high resolution numerical simulation results since they are indirectly consistent with the theoretical predictions made based on the three-layer hypothesis. The hypothesis states that the HBL should be considered as three layers: the surface layer, which is governed by Monin-Obukhov similarity theory; the mixed layer, which has the top found by the thermodynamically defined HBL height and is no significantly different, in terms of turbulence modelling, from the standard ABL; and the remain of the HBL, which is unique in the HBL and is strongly influenced by large scale flows of a tropical cyclone. Although this hypothesis needs to be further validated by involving more detailed observations of the turbulence characteristics in the upper portion of the HBL, it successfully explained the discrepancy of the HBL height calculated differently and the different trend of the HBL height varying with wind velocities indicated by Kepert's model Kepert (2001) and classic Ekman equation.

6.2 Future Work

As one important factor in overall tropical cyclone dynamics, the turbulence within the HBL plays a key role in determining the intensity and structure of the whole tropical cyclone. However, it has not been thoroughly investigated due to the lack of direct observations. This thesis work should be taken as only the first step contributing to a clear understanding of turbulence characteristics within the HBL, as many features of the HBL turbulence are still unclear. To extend this work, further researches can be conducted in three areas: to further validate the YSU scheme by conducting numerical simulations of a specific hurricane, to conduct a deeper investigation on the three-layer hypothesis based on other observational data and to develop a engineering model describing the turbulence structure of the HBL wind field over land.

6.2.1 Further Validation of the YSU scheme

Although high resolution numerical simulations are already conducted in this thesis work to validate that the YSU scheme is, in general, adequate to describe turbulent mixing in the HBL, at least for the lower portion of the HBL (below $200m$), it is performed for an idealized tropical cyclone. In order to compare the simulation results to the statistics derived from dropwindsonde observations, which are composited from numerous individual dropwindsonde profiles taken in different tropical cyclones, the simulation of an idealized tropical cyclone is inevitable in the scope of this thesis work. However, numerical simulations of a specific tropical cyclone are necessary to further validate the YSU scheme, and such simulations can be conducted for a sufficiently observed tropical cyclone. In this case, the wind fields reconstructed based on observations cane be used as the validation criteria in evaluating the YSU scheme. Unlike simulations of an idealized tropical cyclone, simulations of a specific tropical cyclone would take the real observed environment as the initial and boundary conditions. This realistic approach gives an opportunity to test the performance of the YSU scheme in an environment similar to that used for real-time NWP, and might enlighten further revisions upon the original YSU scheme.

6.2.2 Further Investigation on the Three-layer Hypothesis

As demonstrated in this work, the three-layer hypothesis is currently the best candidate for describing turbulence characteristics found in the HBL. As partially validated by the composition of dropwindsonde measurements and the numerical simulations, turbulent mixing in the lower portion of the HBL is found following the formulation of the YSU scheme. The investigation on the three-layer hypothesis should focus on its predictions of the turbulence characteristics in the upper portion of the HBL. Since the dropwindsonde measurement is not suitable to reveal the turbulence information in the upper portion of the HBL, at least based on the commonly used composition methodology, other observations need to be involved in the further investigation on the three-layer hypothesis. According to the three-layer hypothesis presented, the turbulence characteristics in the upper portion of the HBL is different from those observed in the standard ABL and are strongly influenced by large scale flow structures of a tropical cyclone. Thus, the investigation of the three-layer hypothesis, focusing on the its prediction of turbulence characteristics in the upper portion of the HBL, should take the large scale tropical cyclone flow characteristics into consideration.

6.2.3 Modelling the Turbulence Structure of the HBL for Engineering Applications

Dynamic responses of structures are calculated based on the turbulence in winds in current engineering practise. Since one major damage associated with tropical cyclones is the structure failure in hurricane-prone regions, it is necessary to set up a model describing the turbulence in hurricane winds up to a height below which the majority of man-made structures are found. Although this thesis, and the study of Zhang et al. (2009) and Zhang (2010), provide some preliminary descriptions of the vertical turbulence structure in the HBL over water, no study, as far to my knowledge, has been done to reveal general descriptions of the vertical turbulence structure in the HBL over land to a sufficient height. Obviously, one way to solve this problem is to establish more observations over land with a more powerful equipment to take measurements up to a couple hundred meters. This approach is currently unrealistic due to the limitation of the measuring technology. The other solution is to transit the vertical turbulence structure found over water to over land. As an extension to this thesis, it is possible to conduct a research on the transition of the turbulence within the HBL. With help of such a transition model, the turbulence within the HBL over water, which has more observational data sources, can be used to produce a model describing the turbulence in hurricane winds over land. Such a model, together with the mean wind profile in the HBL over land, would help improve the wind-resistance design of structures built in hurricane-prone regions.

Appendix A

Analytical Solution

Equation (3.13) and (3.14) are typical linear ordinary differential equation and therefore the analytical solution exists if the falling rate $\dot{z}$ is assumed to be constant. The general form of the solution can be expressed as

$$\dot{x} = \left(\int_0^t u(\tau)\frac{g}{\dot{z}}e^{\frac{g}{\dot{z}}}\,d\tau + A_x\right)e^{-\frac{g}{\dot{z}}} \tag{A.1}$$

$$\dot{y} = \left(\int_0^t v(\tau)\frac{g}{\dot{z}}e^{\frac{g}{\dot{z}}}\,d\tau + A_y\right)e^{-\frac{g}{\dot{z}}} \tag{A.2}$$

where A_x and A_y are constants determined by the initial condition and $u(\tau), v(\tau)$ denote the external excitation, which are primarily horizontal wind perturbations. When the falling rate of the dropwindsonde is assumed to be constant, these external excitation can be linearly transfered from the wind profile. For instance, $u(\tau)$ can take the logarithmic form if the measuring wind field is log-law governed.

Equation(A.1) and (A.2) depict the dynamic response of the dropwindsonde system under external excitation. In other words, these equations give the explicit analytical expression of the velocity of the dropwindsonde if the horizontal wind perturbations, $u(\tau)$ and $v(\tau)$, are known. For example, if $u(\tau)$ and $v(\tau)$ take the sinusoidal form, $u(\tau) = u_0 \sin(\omega\tau)$ and $v(\tau) = v_0 \sin(\omega\tau)$, the spectral analysis of the dropwindsonde response can be directly conducted which made it is easy to investigate the dropwindsonde response varying with the external excitation frequency. Under such condition, the explicit expression of the solution are

$$\dot{x}(t) = U \sin(\omega t + \phi) + A_x e^{-\frac{g}{\dot{z}}t} \tag{A.3}$$

$$\dot{y}(t) = V \sin(\omega t + \phi) + A_y e^{-\frac{g}{\dot{z}}t} \tag{A.4}$$

where U and V are

$$U = (\frac{g}{\dot{z}})\frac{1}{\sqrt{(\frac{g}{\dot{z}})^2 + \omega^2}}u_0 \tag{A.5}$$

$$V = (\frac{g}{\dot{z}})\frac{1}{\sqrt{(\frac{g}{\dot{z}})^2 + \omega^2}}v_0 \tag{A.6}$$

and the phase angle ϕ has the expression as

$$\phi = \tan^{-1}\left[-\omega\left(\frac{\dot{z}}{g}\right)\right] \tag{A.7}$$

Obviously in equation (A.5),(A.6) and (A.7), the response of the dropwindsonde system depends on the quantity $g/\dot{z}$ and the frequency, ω, of the external excitation. Under the normal condition, as indicated by Hock and Franklin (1999), the falling rate of the dropwindsonde is $-12m/s$ and the gravity can take the value $-9.8m/s^2$. Based on that, the magnitude of the dropwindsonde response can be calculated as shown in the Fig.A.1(a) while the calculated phase angle is shown in the Fig.A.1(b). Since the dropwindsonde response magnitude drops dramatically when the excitation frequency exceed $0.2Hz$ (see Fig. A.1(a)), the dropwindsonde hardly response to high frequency excitations (higher than $1Hz$). Moreover, its response lag increases with external excitation frequency. This feature of the dropwindsonde illustrates that the high frequency turbulent information buried in wind perturbations may be missed if only the dropwindsonde horizontal motion is report as the horizontal wind and corrections are necessary to return high frequency turbulent energy.

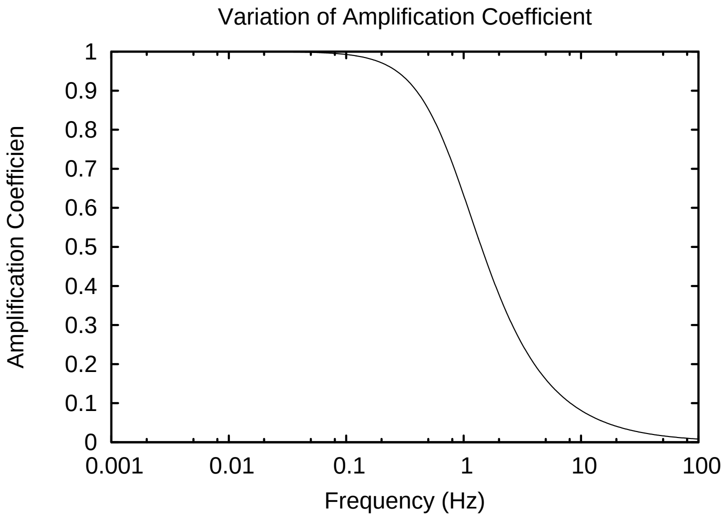

(a) Magnitude

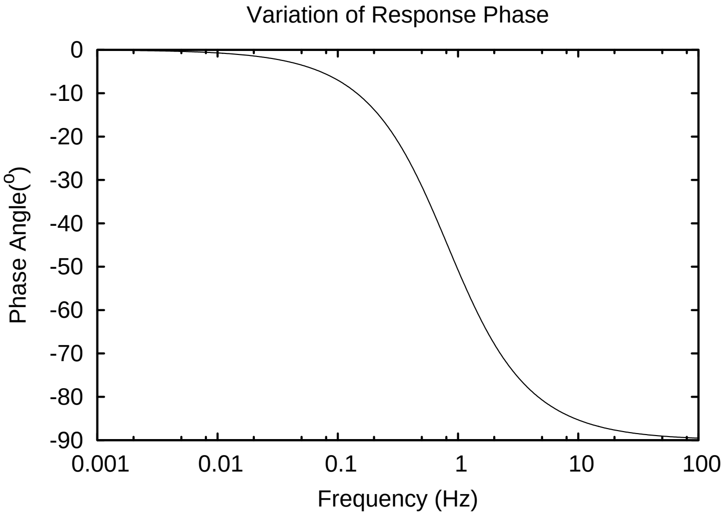

(b) Phase

Figure A.1: Magnitude and phase variation of the response of the dropwindsonde, varied with the frequency of excitation with the gravity $g = -9.8m/s^2$ and the falling rate $\dot{z} = -12m/s$

Appendix B

Detailed Result from the Wind Tunnel Test

Tables summarizing the details of testing results are given in this appendix. The aerodynamic parameters are indicated by the caption and shown by the capital letter in the table, i.e. D represents the drag coefficient, L represents the lift coefficient and T represents the torque coefficient. The number after this capital letter indicates the wind speed under which the measurement is taken, 1 represents $6.1m/s$, 2 represents $9.1m/s$, 3 represents $12.2m/s$, 4 represents $15.2m/s$, 5 represents $18.3m/s$, and 6 represents $21.3m/s$. The last column of the table gives the mean value of the parameter calculated from averaging parameters measured under different wind speed. The unit of the angle of attack is degree.

Table B.1: Drag coefficient with parachute in a smooth flow

Angle of Attack	D1	D2	D3	D4	D5	D6	Dmean
-75	0.7416	0.7656	0.7812	0.8033	0.8112	0.8142	0.7862
-70	0.7448	0.7783	0.7977	0.8143	0.8242	0.8266	0.7976
-65	0.7539	0.7725	0.7978	0.8139	0.8197	0.8232	0.7969
-60	0.7324	0.7526	0.7832	0.8010	0.8029	0.8083	0.7801
-55	0.7180	0.7413	0.7638	0.7797	0.7803	0.7802	0.7605
-50	0.7151	0.7184	0.7481	0.7477	0.7402	0.7393	0.7348
-45	0.6841	0.6881	0.7163	0.7158	0.7089	0.7082	0.7036
-45	0.6653	0.6727	0.7057	0.7077	0.6975	0.6992	0.6913
-40	0.6560	0.6372	0.6734	0.6663	0.6631	0.6609	0.6595
-35	0.6406	0.6084	0.6374	0.6396	0.6317	0.6250	0.6304
-30	0.6203	0.5903	0.6077	0.6157	0.5926	0.5994	0.6043
-25	0.5912	0.5653	0.5832	0.5827	0.5615	0.5682	0.5754
-20	0.5734	0.5547	0.5727	0.5661	0.5533	0.5481	0.5614
-15	0.5637	0.5386	0.5614	0.5475	0.5368	0.5197	0.5446
-15	0.5390	0.5256	0.5490	0.5422	0.5421	0.5187	0.5361
-10	0.5465	0.5266	0.5545	0.5412	0.5496	0.5243	0.5405
-5	0.5370	0.5169	0.5179	0.5148	0.5331	0.5501	0.5283
0	0.5367	0.5165	0.5233	0.5108	0.5068	0.4882	0.5137
5	0.5311	0.5266	0.5394	0.5384	0.5311	0.5262	0.5322
10	0.5465	0.5242	0.5422	0.5266	0.5066	0.4929	0.5232
15	0.5458	0.5414	0.5372	0.5369	0.5038	0.5020	0.5279
15	0.5242	0.5256	0.5412	0.5349	0.5138	0.5048	0.5241
20	0.5570	0.5458	0.5633	0.5591	0.5390	0.5403	0.5508
25	0.5665	0.5554	0.5846	0.5809	0.5609	0.5621	0.5684
30	0.5865	0.5762	0.5962	0.6054	0.5875	0.5857	0.5896
35	0.6093	0.6040	0.6270	0.6299	0.6202	0.6185	0.6181
40	0.6428	0.6339	0.6521	0.6590	0.6504	0.6532	0.6485
45	0.6581	0.6592	0.6891	0.7004	0.6907	0.6934	0.6818
45	0.6769	0.6650	0.6805	0.6959	0.6947	0.6912	0.6840
50	0.6741	0.6971	0.7155	0.7310	0.7262	0.7253	0.7115
55	0.6963	0.7030	0.7369	0.7543	0.7619	0.7606	0.7355
60	0.7216	0.7294	0.7531	0.7732	0.7794	0.7832	0.7567
65	0.7259	0.7392	0.7609	0.7900	0.7898	0.7933	0.7665
70	0.7371	0.7423	0.7574	0.7881	0.7949	0.7929	0.7688
75	0.7344	0.7351	0.7537	0.7759	0.7808	0.7830	0.7605

Table B.2: Lift coefficient with parachute in a smooth flow

Angle of Attack	L1	L2	L3	L4	L5	L6	Lmean
-75	-0.0609	-0.0713	-0.0754	-0.0724	-0.0692	-0.0652	-0.0691
-70	-0.0939	-0.0962	-0.0974	-0.0912	-0.0902	-0.0901	-0.0932
-65	-0.1147	-0.1156	-0.1141	-0.1097	-0.1071	-0.1017	-0.1105
-60	-0.1216	-0.1205	-0.1229	-0.1222	-0.1216	-0.1172	-0.1210
-55	-0.1514	-0.1413	-0.1387	-0.1348	-0.1315	-0.1289	-0.1378
-50	-0.1822	-0.1546	-0.1450	-0.1397	-0.1348	-0.1301	-0.1477
-45	-0.1944	-0.1768	-0.1714	-0.1656	-0.1627	-0.1588	-0.1716
-45	-0.1869	-0.1692	-0.1645	-0.1601	-0.1556	-0.1511	-0.1646
-40	-0.1833	-0.1544	-0.1521	-0.1466	-0.1428	-0.1398	-0.1532
-35	-0.1859	-0.1543	-0.1508	-0.1444	-0.1415	-0.1383	-0.1525
-30	-0.1692	-0.1374	-0.1320	-0.1275	-0.1252	-0.1215	-0.1355
-25	-0.1376	-0.1194	-0.1124	-0.1099	-0.1076	-0.1027	-0.1149
-20	-0.1165	-0.0987	-0.0948	-0.0934	-0.0900	-0.0879	-0.0969
-15	-0.0955	-0.0717	-0.0678	-0.0629	-0.0627	-0.0588	-0.0699
-15	-0.0838	-0.0663	-0.0648	-0.0596	-0.0587	-0.0529	-0.0643
-10	-0.0820	-0.0543	-0.0528	-0.0474	-0.0453	-0.0434	-0.0542
-5	-0.0443	-0.0158	-0.0169	-0.0188	-0.0200	-0.0185	-0.0224
0	-0.0180	-0.0013	0.0019	0.0008	-0.0005	0.0013	-0.0026
5	0.0086	0.0187	0.0232	0.0235	0.0247	0.0254	0.0207
10	0.0092	0.0384	0.0407	0.0471	0.0502	0.0481	0.0389
15	0.0206	0.0614	0.0580	0.0616	0.0611	0.0602	0.0538
15	0.0421	0.0589	0.0610	0.0651	0.0649	0.0645	0.0594
20	0.0694	0.0897	0.0881	0.0913	0.0907	0.0884	0.0863
25	0.1070	0.1012	0.1018	0.1043	0.1023	0.1014	0.1030
30	0.1224	0.1233	0.1220	0.1234	0.1207	0.1191	0.1218
35	0.1356	0.1417	0.1399	0.1367	0.1329	0.1345	0.1369
40	0.1476	0.1515	0.1499	0.1476	0.1419	0.1393	0.1463
45	0.1484	0.1636	0.1621	0.1609	0.1537	0.1510	0.1566
45	0.1463	0.1477	0.1570	0.1596	0.1564	0.1535	0.1534
50	0.1660	0.1701	0.1742	0.1711	0.1664	0.1635	0.1685
55	0.1636	0.1648	0.1637	0.1679	0.1640	0.1625	0.1644
60	0.1524	0.1516	0.1582	0.1520	0.1525	0.1511	0.1530
65	0.1402	0.1424	0.1392	0.1366	0.1399	0.1391	0.1396
70	0.1068	0.1231	0.1267	0.1171	0.1212	0.1213	0.1194
75	0.0831	0.1049	0.1048	0.0966	0.0996	0.1009	0.0983

Table B.3: Torque coefficient with parachute in a smooth flow

Angle of Attack	T1	T2	T3	T4	T5	T6	TMean
-75	0.2752	0.3123	0.3270	0.3389	0.3416	0.3435	0.3231
-70	0.2522	0.2911	0.3054	0.3118	0.3175	0.3200	0.2997
-65	0.2363	0.2632	0.2790	0.2875	0.2900	0.2908	0.2745
-60	0.2048	0.2253	0.2453	0.2575	0.2589	0.2623	0.2423
-55	0.1927	0.2058	0.2182	0.2275	0.2295	0.2318	0.2176
-50	0.1914	0.1833	0.1975	0.1987	0.1981	0.2014	0.1951
-45	0.1839	0.1806	0.1953	0.1961	0.1954	0.1972	0.1914
-45	0.1424	0.1465	0.1654	0.1701	0.1678	0.1705	0.1605
-40	0.1419	0.1239	0.1381	0.1371	0.1357	0.1349	0.1353
-35	0.1186	0.0986	0.1057	0.1058	0.1026	0.0999	0.1052
-30	0.1059	0.0878	0.0897	0.0905	0.0821	0.0831	0.0898
-25	0.0858	0.0739	0.0733	0.0710	0.0646	0.0648	0.0722
-20	0.0756	0.0631	0.0614	0.0584	0.0536	0.0509	0.0605
-15	0.0592	0.0468	0.0487	0.0436	0.0405	0.0365	0.0459
-15	0.0504	0.0436	0.0464	0.0417	0.0406	0.0356	0.0430
-10	0.0431	0.0307	0.0322	0.0268	0.0253	0.0215	0.0299
-5	0.0337	0.0123	0.0109	0.0121	0.0129	0.0132	0.0159
0	0.0036	-0.0053	-0.0079	-0.0068	-0.0056	-0.0058	-0.0046
5	-0.0252	-0.0257	-0.0264	-0.0262	-0.0253	-0.0240	-0.0255
10	-0.0106	-0.0320	-0.0371	-0.0361	-0.0328	-0.0278	-0.0294
15	-0.0325	-0.0560	-0.0525	-0.0523	-0.0473	-0.0460	-0.0478
15	-0.0514	-0.0556	-0.0566	-0.0547	-0.0498	-0.0472	-0.0526
20	-0.0489	-0.0624	-0.0680	-0.0683	-0.0631	-0.0618	-0.0621
25	-0.0743	-0.0746	-0.0833	-0.0841	-0.0776	-0.0771	-0.0785
30	-0.0858	-0.0891	-0.0967	-0.1020	-0.0955	-0.0938	-0.0938
35	-0.1087	-0.1127	-0.1193	-0.1209	-0.1149	-0.1151	-0.1153
40	-0.1287	-0.1366	-0.1474	-0.1520	-0.1490	-0.1514	-0.1442
45	-0.1484	-0.1567	-0.1738	-0.1824	-0.1799	-0.1842	-0.1709
45	-0.1599	-0.1594	-0.1723	-0.1831	-0.1856	-0.1860	-0.1744
50	-0.1652	-0.1848	-0.2039	-0.2132	-0.2163	-0.2187	-0.2003
55	-0.1874	-0.2092	-0.2295	-0.2425	-0.2451	-0.2449	-0.2264
60	-0.2126	-0.2384	-0.2584	-0.2684	-0.2731	-0.2743	-0.2542
65	-0.2449	-0.2700	-0.2860	-0.3028	-0.3036	-0.3060	-0.2856
70	-0.2759	-0.2966	-0.3139	-0.3276	-0.3321	-0.3320	-0.3130
75	-0.3039	-0.3251	-0.3425	-0.3523	-0.3557	-0.3581	-0.3396

Table B.4: Drag coefficient without parachute in a smooth flow

Angle of Attack	D1	D2	D3	D4	D5	D6	DMean
-75	0.3078	0.2959	0.2958	0.3033	0.3064	0.3059	0.3025
-70	0.3208	0.3093	0.3110	0.3158	0.3164	0.3152	0.3147
-65	0.3163	0.3024	0.3094	0.3117	0.3128	0.3121	0.3108
-60	0.3017	0.2945	0.3015	0.3034	0.3037	0.3025	0.3012
-55	0.2943	0.2833	0.2879	0.2895	0.2886	0.2853	0.2882
-50	0.2696	0.2664	0.2636	0.2623	0.2569	0.2534	0.2620
-45	0.2358	0.2300	0.2282	0.2265	0.2226	0.2165	0.2266
-45	0.2159	0.2139	0.2143	0.2133	0.2107	0.2064	0.2124
-40	0.2014	0.1841	0.1809	0.1751	0.1724	0.1709	0.1808
-35	0.1574	0.1431	0.1461	0.1432	0.1428	0.1418	0.1457
-30	0.1385	0.1149	0.1183	0.1170	0.1169	0.1165	0.1204
-25	0.0986	0.0818	0.0887	0.0919	0.0931	0.0936	0.0913
-20	0.0756	0.0648	0.0694	0.0728	0.0742	0.0742	0.0718
-15	0.0562	0.0437	0.0416	0.0454	0.0474	0.0465	0.0468
-15	0.0468	0.0398	0.0437	0.0506	0.0513	0.0499	0.0470
-10	0.0442	0.0281	0.0256	0.0316	0.0358	0.0363	0.0336
-5	0.0362	0.0207	0.0189	0.0237	0.0286	0.0291	0.0262
0	0.0374	0.0163	0.0133	0.0172	0.0203	0.0205	0.0208
5	0.0378	0.0202	0.0166	0.0214	0.0256	0.0266	0.0247
10	0.0521	0.0307	0.0237	0.0277	0.0300	0.0306	0.0325
15	0.0586	0.0440	0.0447	0.0501	0.0513	0.0506	0.0499
15	0.0494	0.0401	0.0444	0.0504	0.0514	0.0500	0.0476
20	0.0741	0.0663	0.0745	0.0783	0.0801	0.0796	0.0755
25	0.1009	0.0856	0.0945	0.0972	0.0977	0.0979	0.0956
30	0.1347	0.1151	0.1223	0.1224	0.1211	0.1204	0.1227
35	0.1649	0.1488	0.1505	0.1499	0.1493	0.1476	0.1518
40	0.1962	0.1863	0.1867	0.1826	0.1783	0.1762	0.1844
45	0.2295	0.2254	0.2237	0.2199	0.2171	0.2120	0.2213
45	0.2337	0.2296	0.2281	0.2263	0.2243	0.2199	0.2270
50	0.2702	0.2640	0.2644	0.2640	0.2635	0.2579	0.2640
55	0.2915	0.2816	0.2850	0.2862	0.2873	0.2871	0.2864
60	0.3027	0.2912	0.2972	0.2982	0.3009	0.3003	0.2984
65	0.3156	0.3006	0.3051	0.3086	0.3084	0.3079	0.3077
70	0.3178	0.3026	0.3002	0.3060	0.3078	0.3064	0.3068
75	0.3098	0.2969	0.2904	0.2935	0.2964	0.2959	0.2971

Table B.5: Lift coefficient without parachute in a smooth flow

Angle of Attack	L1	L2	L3	L4	L5	L6	LMean
-75	-0.0875	-0.0936	-0.0920	-0.0914	-0.0922	-0.0921	-0.0915
-70	-0.1043	-0.1165	-0.1197	-0.1202	-0.1211	-0.1205	-0.1171
-65	-0.1431	-0.1465	-0.1481	-0.1465	-0.1478	-0.1472	-0.1466
-60	-0.1643	-0.1687	-0.1699	-0.1673	-0.1675	-0.1659	-0.1672
-55	-0.1766	-0.1796	-0.1855	-0.1815	-0.1818	-0.1782	-0.1805
-50	-0.1838	-0.1913	-0.1929	-0.1880	-0.1802	-0.1739	-0.1850
-45	-0.1871	-0.1868	-0.1879	-0.1845	-0.1777	-0.1725	-0.1828
-45	-0.1874	-0.1877	-0.1832	-0.1770	-0.1731	-0.1684	-0.1795
-40	-0.1795	-0.1749	-0.1713	-0.1636	-0.1585	-0.1555	-0.1672
-35	-0.1654	-0.1653	-0.1594	-0.1535	-0.1520	-0.1482	-0.1573
-30	-0.1497	-0.1489	-0.1422	-0.1334	-0.1324	-0.1309	-0.1396
-25	-0.1182	-0.1226	-0.1152	-0.1115	-0.1118	-0.1109	-0.1150
-20	-0.1169	-0.1042	-0.0995	-0.0966	-0.0953	-0.0947	-0.1012
-15	-0.0744	-0.0698	-0.0641	-0.0636	-0.0651	-0.0642	-0.0669
-15	-0.0699	-0.0676	-0.0645	-0.0641	-0.0646	-0.0638	-0.0657
-10	-0.0507	-0.0528	-0.0487	-0.0505	-0.0525	-0.0525	-0.0513
-5	-0.0134	-0.0188	-0.0207	-0.0198	-0.0213	-0.0218	-0.0193
0	0.0067	0.0017	0.0027	0.0008	0.0008	0.0016	0.0024
5	0.0227	0.0220	0.0234	0.0244	0.0236	0.0238	0.0233
10	0.0468	0.0496	0.0504	0.0502	0.0515	0.0533	0.0503
15	0.0719	0.0681	0.0683	0.0671	0.0668	0.0679	0.0683
15	0.0739	0.0665	0.0639	0.0653	0.0658	0.0677	0.0672
20	0.1235	0.1019	0.0993	0.0993	0.0972	0.0979	0.1032
25	0.1326	0.1223	0.1182	0.1170	0.1151	0.1141	0.1199
30	0.1713	0.1525	0.1477	0.1414	0.1380	0.1363	0.1479
35	0.1810	0.1726	0.1684	0.1615	0.1574	0.1555	0.1661
40	0.1899	0.1827	0.1775	0.1704	0.1618	0.1598	0.1737
45	0.1931	0.1898	0.1864	0.1790	0.1737	0.1711	0.1822
45	0.1914	0.1878	0.1857	0.1830	0.1760	0.1723	0.1827
50	0.1850	0.1875	0.1893	0.1885	0.1845	0.1785	0.1856
55	0.1578	0.1682	0.1723	0.1734	0.1748	0.1744	0.1701
60	0.1617	0.1557	0.1578	0.1613	0.1591	0.1598	0.1592
65	0.1264	0.1333	0.1334	0.1378	0.1379	0.1372	0.1343
70	0.0962	0.0967	0.0974	0.0998	0.0987	0.1000	0.0981
75	0.0721	0.0811	0.0763	0.0752	0.0731	0.0722	0.0750

Table B.6: Torque coefficient without parachute in a smooth flow

Angle of Attack	T1	T2	T3	T4	T5	T6	TMean
-75	-0.0456	-0.0426	-0.0416	-0.0399	-0.0401	-0.0401	-0.0416
-70	-0.0500	-0.0477	-0.0484	-0.0492	-0.0486	-0.0485	-0.0487
-65	-0.0595	-0.0571	-0.0555	-0.0552	-0.0548	-0.0544	-0.0561
-60	-0.0637	-0.0593	-0.0584	-0.0582	-0.0573	-0.0569	-0.0590
-55	-0.0616	-0.0606	-0.0590	-0.0572	-0.0569	-0.0561	-0.0586
-50	-0.0570	-0.0547	-0.0556	-0.0555	-0.0543	-0.0540	-0.0552
-45	-0.0611	-0.0577	-0.0551	-0.0548	-0.0550	-0.0561	-0.0566
-45	-0.0538	-0.0543	-0.0539	-0.0528	-0.0540	-0.0553	-0.0540
-40	-0.0473	-0.0526	-0.0554	-0.0577	-0.0593	-0.0602	-0.0554
-35	-0.0618	-0.0617	-0.0646	-0.0651	-0.0661	-0.0668	-0.0643
-30	-0.0476	-0.0544	-0.0574	-0.0597	-0.0605	-0.0605	-0.0567
-25	-0.0470	-0.0502	-0.0517	-0.0513	-0.0523	-0.0526	-0.0508
-20	-0.0336	-0.0396	-0.0407	-0.0414	-0.0422	-0.0420	-0.0399
-15	-0.0324	-0.0318	-0.0326	-0.0319	-0.0317	-0.0316	-0.0320
-15	-0.0286	-0.0305	-0.0317	-0.0322	-0.0315	-0.0318	-0.0310
-10	-0.0216	-0.0238	-0.0239	-0.0245	-0.0251	-0.0255	-0.0241
-5	-0.0070	-0.0085	-0.0095	-0.0098	-0.0095	-0.0097	-0.0090
0	0.0016	-0.0010	-0.0012	-0.0009	-0.0010	-0.0011	-0.0006
5	0.0043	0.0070	0.0067	0.0069	0.0076	0.0076	0.0067
10	0.0257	0.0238	0.0226	0.0228	0.0229	0.0235	0.0235
15	0.0281	0.0295	0.0294	0.0300	0.0305	0.0308	0.0297
15	0.0319	0.0310	0.0305	0.0309	0.0311	0.0313	0.0311
20	0.0442	0.0418	0.0412	0.0414	0.0413	0.0412	0.0419
25	0.0459	0.0465	0.0480	0.0491	0.0498	0.0506	0.0483
30	0.0541	0.0557	0.0570	0.0569	0.0573	0.0583	0.0566
35	0.0561	0.0573	0.0604	0.0623	0.0633	0.0635	0.0605
40	0.0510	0.0500	0.0526	0.0531	0.0547	0.0558	0.0528
45	0.0532	0.0486	0.0495	0.0495	0.0504	0.0514	0.0504
45	0.0570	0.0493	0.0497	0.0493	0.0502	0.0507	0.0510
50	0.0552	0.0510	0.0515	0.0505	0.0496	0.0490	0.0511
55	0.0563	0.0529	0.0525	0.0514	0.0508	0.0505	0.0524
60	0.0514	0.0511	0.0515	0.0510	0.0512	0.0513	0.0513
65	0.0508	0.0478	0.0485	0.0487	0.0473	0.0475	0.0484
70	0.0450	0.0448	0.0430	0.0421	0.0420	0.0421	0.0432
75	0.0408	0.0346	0.0346	0.0346	0.0341	0.0335	0.0354

Table B.7: Drag coefficient with parachute in a turbulent flow

Angle of Attack	D1	D2	D3	D4	D5	DMean
-15	0.4620	0.4729	0.4967	0.5064	0.5035	0.4883
-10	0.4840	0.4814	0.5024	0.4971	0.5051	0.4940
-5	0.4754	0.4719	0.5076	0.4838	0.5033	0.4884
0	0.4692	0.4713	0.5042	0.4872	0.4809	0.4826
5	0.4713	0.4786	0.4899	0.4923	0.4907	0.4846
10	0.4865	0.4826	0.4910	0.4894	0.4816	0.4862
15	0.4981	0.4943	0.5057	0.5006	0.4891	0.4976
15	0.4741	0.4918	0.5097	0.5165	0.5082	0.5000
20	0.5159	0.5237	0.5264	0.5277	0.5228	0.5233
25	0.5392	0.5378	0.5453	0.5555	0.5384	0.5432
30	0.5373	0.5378	0.5499	0.5571	0.5427	0.5449
35	0.5607	0.5564	0.5710	0.5753	0.5676	0.5662
40	0.5743	0.5701	0.5766	0.5904	0.5838	0.5791
45	0.6006	0.5944	0.6129	0.6141	0.6038	0.6052
45	0.6311	0.6230	0.6302	0.6391	0.6383	0.6323
50	0.6366	0.6443	0.6566	0.6671	0.6590	0.6527
55	0.6557	0.6673	0.6852	0.6864	0.6795	0.6748
60	0.6947	0.6917	0.7025	0.7064	0.7009	0.6992
65	0.7014	0.6967	0.7076	0.7181	0.7107	0.7069
70	0.7191	0.7028	0.7066	0.7212	0.7158	0.7131
75	0.7217	0.7017	0.7137	0.7182	0.7014	0.7113

Table B.8: Lift coefficient with parachute in a turbulent flow

Angle of Attack	L1	L2	L3	L4	L5	LMean
-15	-0.1081	-0.0797	-0.0705	-0.0632	-0.0599	-0.0763
-10	-0.0896	-0.0522	-0.0429	-0.0448	-0.0441	-0.0547
-5	-0.0746	-0.0300	-0.0249	-0.0215	-0.0222	-0.0347
0	-0.0617	-0.0053	0.0005	0.0031	0.0040	-0.0119
5	-0.0065	0.0060	0.0143	0.0238	0.0276	0.0130
10	0.0144	0.0293	0.0332	0.0375	0.0469	0.0323
15	0.0191	0.0500	0.0610	0.0649	0.0665	0.0523
15	-0.0183	0.0044	-0.0027	-0.0054	-0.0020	-0.0048
20	-0.0395	-0.0254	-0.0103	-0.0045	0.0023	-0.0155
25	-0.0637	-0.0446	-0.0147	-0.0193	-0.0097	-0.0304
30	0.0422	0.0135	0.0344	0.0351	0.0298	0.0310
35	0.0707	0.0693	0.0528	0.0430	0.0415	0.0555
40	0.0039	0.0159	0.0144	0.0206	0.0270	0.0163
45	0.1058	0.0345	0.0576	0.0506	0.0487	0.0594
45	0.1081	0.1383	0.1505	0.1515	0.1495	0.1396
50	0.1503	0.1642	0.1611	0.1579	0.1584	0.1584
55	0.1330	0.1509	0.1563	0.1608	0.1586	0.1519
60	0.1277	0.1459	0.1524	0.1518	0.1492	0.1454
65	0.1102	0.1306	0.1397	0.1414	0.1363	0.1316
70	0.0860	0.1167	0.1213	0.1202	0.1214	0.1131
75	0.0539	0.0883	0.0957	0.0970	0.0944	0.0859

Table B.9: Torque coefficient with parachute in a turbulent flow

Angle of Attack	T1	T2	T3	T4	T5	TMean
-15	0.0708	0.0637	0.0656	0.0646	0.0621	0.0654
-10	0.0727	0.0485	0.0424	0.0434	0.0447	0.0503
-5	0.0500	0.0194	0.0178	0.0164	0.0185	0.0244
0	0.0314	-0.0068	-0.0099	-0.0104	-0.0096	-0.0011
5	-0.0158	-0.0219	-0.0279	-0.0346	-0.0360	-0.0272
10	-0.0331	-0.0439	-0.0495	-0.0508	-0.0551	-0.0465
15	-0.0517	-0.0693	-0.0774	-0.0752	-0.0733	-0.0694
15	-0.0568	-0.0717	-0.0683	-0.0676	-0.0704	-0.0670
20	-0.0779	-0.0814	-0.0883	-0.0892	-0.0871	-0.0848
25	-0.1012	-0.1024	-0.1035	-0.1067	-0.1064	-0.1040
30	-0.1193	-0.1265	-0.1304	-0.1316	-0.1226	-0.1261
35	-0.1380	-0.1436	-0.1483	-0.1500	-0.1459	-0.1452
40	-0.1650	-0.1673	-0.1723	-0.1783	-0.1740	-0.1714
45	-0.1978	-0.1986	-0.2051	-0.2080	-0.2059	-0.2031
45	-0.2064	-0.1993	-0.2080	-0.2120	-0.2108	-0.2073
50	-0.2185	-0.2181	-0.2274	-0.2359	-0.2337	-0.2267
55	-0.2385	-0.2413	-0.2516	-0.2578	-0.2554	-0.2489
60	-0.2670	-0.2621	-0.2704	-0.2758	-0.2759	-0.2702
65	-0.2870	-0.2800	-0.2875	-0.2947	-0.2919	-0.2882
70	-0.3152	-0.3000	-0.3078	-0.3143	-0.3126	-0.3100
75	-0.3514	-0.3293	-0.3354	-0.3370	-0.3300	-0.3366

Table B.10: Drag coefficient without parachute in a turbulent flow

Angle of Attack	D1	D2	D3	D4	D5	DMean
-15	0.0443	0.0537	0.0554	0.0590	0.0599	0.0545
-10	0.0377	0.0430	0.0434	0.0446	0.0455	0.0428
-5	0.0312	0.0357	0.0347	0.0369	0.0369	0.0351
0	0.0233	0.0293	0.0294	0.0316	0.0301	0.0287
5	0.0279	0.0324	0.0317	0.0353	0.0355	0.0326
10	0.0392	0.0439	0.0414	0.0432	0.0414	0.0418
15	0.0576	0.0597	0.0578	0.0590	0.0588	0.0586
15	0.0428	0.0535	0.0560	0.0582	0.0590	0.0539
20	0.0742	0.0858	0.0857	0.0910	0.0896	0.0853
25	0.0990	0.1020	0.1034	0.1063	0.1081	0.1038
30	0.1243	0.1233	0.1231	0.1234	0.1256	0.1240
35	0.1486	0.1494	0.1459	0.1476	0.1476	0.1478
40	0.1751	0.1756	0.1709	0.1702	0.1685	0.1721
45	0.1986	0.1995	0.1973	0.1941	0.1929	0.1965
45	0.2277	0.2238	0.2200	0.2185	0.2176	0.2215
50	0.2503	0.2511	0.2486	0.2461	0.2420	0.2476
55	0.2708	0.2713	0.2701	0.2660	0.2630	0.2683
60	0.2858	0.2885	0.2853	0.2829	0.2777	0.2840
65	0.3039	0.2988	0.2995	0.2962	0.2883	0.2973
70	0.2951	0.2934	0.2935	0.2908	0.2862	0.2918
75	0.2623	0.2731	0.2735	0.2786	0.2726	0.2720

Table B.11: Lift coefficient without parachute in a turbulent flow

Angle of Attack	L1	L2	L3	L4	L5	LMean
-15	-0.0885	-0.0748	-0.0694	-0.0669	-0.0655	-0.0730
-10	-0.0546	-0.0509	-0.0465	-0.0445	-0.0442	-0.0481
-5	-0.0282	-0.0289	-0.0274	-0.0251	-0.0239	-0.0267
0	-0.0132	-0.0059	-0.0038	-0.0024	-0.0011	-0.0053
5	0.0074	0.0168	0.0196	0.0202	0.0224	0.0173
10	0.0343	0.0428	0.0419	0.0427	0.0437	0.0411
15	0.0575	0.0619	0.0639	0.0638	0.0648	0.0624
15	0.0679	0.0502	0.0537	0.0623	0.0601	0.0588
20	0.0864	0.0423	0.0512	0.0494	0.0527	0.0564
25	0.0620	0.0737	0.0598	0.0633	0.0682	0.0654
30	0.1178	0.1168	0.1008	0.0887	0.0817	0.1012
35	0.1306	0.1461	0.1286	0.1203	0.1163	0.1284
40	0.1256	0.1358	0.1294	0.1195	0.1166	0.1254
45	0.1056	0.1242	0.1246	0.1173	0.1141	0.1172
45	0.0486	0.0999	0.1017	0.1061	0.1071	0.0927
50	0.1216	0.1453	0.1316	0.1219	0.1179	0.1277
55	0.1798	0.1651	0.1485	0.1359	0.1276	0.1514
60	0.1117	0.1069	0.0934	0.0972	0.0961	0.1010
65	0.1765	0.1371	0.1248	0.1107	0.0980	0.1294
70	0.0811	0.0631	0.0561	0.0536	0.0485	0.0605
75	-0.0380	0.0026	0.0029	0.0056	0.0043	-0.0045

Table B.12: Torque coefficient without parachute in a turbulent flow

Angle of Attack	T1	T2	T3	T4	T5	TMean
-15	-0.0299	-0.0297	-0.0296	-0.0292	-0.0294	-0.0296
-10	-0.0216	-0.0216	-0.0200	-0.0204	-0.0207	-0.0209
-5	-0.0092	-0.0103	-0.0106	-0.0103	-0.0104	-0.0102
0	-0.0031	-0.0022	-0.0012	-0.0015	-0.0014	-0.0019
5	0.0054	0.0066	0.0068	0.0077	0.0081	0.0069
10	0.0140	0.0181	0.0185	0.0185	0.0181	0.0174
15	0.0255	0.0258	0.0269	0.0278	0.0283	0.0269
15	0.0302	0.0281	0.0282	0.0290	0.0291	0.0289
20	0.0356	0.0372	0.0380	0.0378	0.0376	0.0372
25	0.0450	0.0464	0.0466	0.0475	0.0482	0.0467
30	0.0483	0.0538	0.0545	0.0549	0.0559	0.0535
35	0.0563	0.0583	0.0593	0.0614	0.0624	0.0595
40	0.0566	0.0587	0.0593	0.0612	0.0623	0.0596
45	0.0559	0.0533	0.0551	0.0564	0.0580	0.0557
45	0.0507	0.0539	0.0547	0.0563	0.0578	0.0547
50	0.0532	0.0548	0.0548	0.0543	0.0551	0.0545
55	0.0549	0.0529	0.0534	0.0525	0.0528	0.0533
60	0.0551	0.0536	0.0531	0.0518	0.0515	0.0530
65	0.0550	0.0509	0.0516	0.0512	0.0498	0.0517
70	0.0452	0.0446	0.0436	0.0426	0.0427	0.0437
75	0.0379	0.0336	0.0330	0.0327	0.0311	0.0337

Bibliography

Aberson, S. D., M. T. Montgomery, M. Bell, and M. Black, 2006: Hurricane Isabel (2003): New insights into the physics of intense storms. Part II: Extreme localized wind. *Bull. Amer. Meteor. Soc.*, **87**, 1349–1354.

Anthes, R. A. and S. W. Chang, 1978: Response of the hurricane boundary layer to changes of sea surface temperature in a numerical model. *J. Atmos. Sci.*, **35**, 1240–1255.

Black, P. G., et al., 2007: Airsea exchange in hurricanes, synthesis of observations from the coupled boundary layer airsea transfer experiment. *Bull. Amer. Meteor. Soc.*, **88**, 357–374.

Blackadar, A. K., 1962: The vertical distribution of wind and turbulent exchange in a neutral atmosphere. *J. Geophys. Res.*, **67**, 3095–3102.

Bradshaw, P., 1974: Possible origin of Prandtl's mixing length theory. *Nature*, **249**, 135–136.

Braun, S. A. and W. Tao, 2000: Sensitivity of high resolution simulation of Hurricane Bob (1991) to planetary boundary parameterizations. *Mon. Wea. Rev.*, **128**, 3941–3961.

Brost, R. A. and J. C. Wyngaard, 1978: A model study of the stably stratified planetary boundary layer. *J. Atmos. Sci.*, **35**, 1427–1440.

Bryan, G. H. and R. Rotunno, 2009: The maximum intensity of tropical cyclones in axisymmetric numerical model simulations. *Mon. Wea. Rev.*, **137**, 1770–1789.

Carassale, L., G. Solari, and F. Tubino, 2007: Proper orthogonal decomposition in wind engineering. Part II: Theoretical aspects and some applications. *Wind and Structure*, **10**, 177–208.

Chen, K. L. and S. Sofia, 1987: Validity test of the mixing-length theory of deep convection. *Science*, **235**, 465–467.

Cockrell, D. J., 1987: The aerodynamics of parachutes. Tech. rep., The University of Leicester, U.K.

Croll, R. H., P. C. Klimas, R. E. Tate, and D. F. Wolf, 1981: Summary of parachute wind tunnel testing methods at sandia national laboratory. *7th Aerodynamic Decelerator*

Systems Technology Conference, San Diego, CA, American Institute of Aeronautics and Astronautics.

Davenport, A. G., 1967: The dependence of wind loads on meteorological parameters. *International Research Seminar on Wind Effects on Buildings and Structures*, Ottawa,ON,Canada, National Research Council of Canada, 19–82.

Davis, C. and L. Bostart, 2002: Numerical simulations of the genesis of Hurricane Diana (1984). Part II: sensitivity of track and intensity prediction. *Mon. Wea. Rev.*, **130**, 1100–1124.

Davis, M. R., 1994: Integral scales and mixing lengths in turbulent mixing and combustion. *Experimental Thermal and Fluid Science*, **8**, 239–244.

Dorst, N. M., 2007: The National Hurricane Research Project : 50 years of research, rough rides, and name changes. *Bull. Amer. Meteor. Soc.*, **88**, 1566–1588.

Drennan, W. M., J. Zhang, J. R. French, C. McCormick, and P. G. Black, 2007: Turbulent fluxes in the hurricane boundary layer. Part II: latent heat flux. *J. Atmos. Sci.*, **64**, 1103–1115.

Duhia, J., 1989: Numerical study of convection observed during the winter monsoon experiment using a mesoscale two-dimensional model. *J. Atmos. Sci.*, **46**, 3077–3107.

Dunion, J. P. and C. S. Marron, 2008: A reexamination of the Jordan mean tropical sounding based on awareness of the saharan air layer: results from 2002. *J. Climate*, **21**, 5142–5253.

Fichtl, G. H., 1971: The responses of rising or falling spherical wind sensor to atmospheric wind perturbations. *J. Appl. Meteor.*, **10**, 1275–1284.

Foster, R. C., 2009: Boundary-layer similarity under an axisymmetric, gradient wind vortex. *Boundary-Layer Meteorol.*, **131**, 321–344.

Frank, W. M., 1984: A composite analysis of the core of a mature hurricane. *Mon. Wea. Rev.*, **112**, 2401–2420.

Franklin, J. L., M. L. Black, and V. Krystal, 2003: GPS Dropwindsonde wind profiles in hurricanes and their operational implications. *Wea. Forecasting*, **18**, 32–44.

Franklin, J. L., S. E. Feuer, J. Kaplan, and S. D. Aberson, 1996: Tropical cyclone motion and surrounding flow relationships : Searching for beta gyres in Omega Dropwindsonde datasets. *Mon. Wea. Rev.*, **124**, 64–84.

French, J. R., W. M. Drennan, J. Zhang, and P. G. Black, 2007: Turbulent fluxes in the hurricane boundary layer. Part I: momentum flux. *J. Atmos. Sci.*, **64**, 1089–1102.

Gryning, S., E. Batchvarova, B. Brmmer, H. Jrgensen, and S. Larsen, 2007: On the extension of the wind profile over homogeneous terrain beyond the surface boundary layer. *Boundary-Layer Meteorol.*, **124**, 251–268.

Hill, K. A. and G. M. Lackmann, 2009: Analysis of idealized tropical cyclone simulations using the weather research and forecasting model: sensitivity to turbulence parameterization and grid spacing. *Mon. Wea. Rev.*, **137**, 745–765.

Hock, T. F. and J. L. Franklin, 1999: The NCAR GSP Dropwindsonde. *Bull. Amer. Meteor. Soc.*, **80**, 407–420.

Holland, G. J., 1980: An analytical model of the wind and pressure profiles in hurricanes. *Mon. Wea. Rev.*, **108**, 1212–1218.

Hong, S., Y. Noh, and J. Dudhia, 2006: A new vertical diffusion package with an explicit treatment of entrainment processes. *Mon. Wea. Rev.*, **134**, 2318–2341.

Hong, S. and H. Pan, 1996: Nonlocal boundary layer vertical diffusion in a medium range forecast model. *Mon. Wea. Rev.*, **124**, 2322–2339.

Jordan, C. L., 1958: Mean soundings for the West Indies area. *J. Atmos. Sci.*, **15**, 91–97.

Kain, J. S., 2004: The Kain-Fritsch convective parameterization: An update. *J. Appl. Meteor.*, **43**, 170–181.

Kain, J. S. and J. M. Fritsch, 1993: Convective parameterization for mesoscale models: The Kain-Fritsch scheme. *The Representation of Cumulus Convection in Numerical Models, Meteor. Monogr.*, **46**, 165–170.

Kepert, J., 2001: The dynamic of boundary layer jet with in tropical cyclone, Part I: linear theory. *J. Atmos. Sci.*, **58**, 2469–2484.

Kepert, J. and Y. Wang, 2001: The dynamic of boundary layer jet with in tropical cyclone, Part II: nonlinear enhancement. *J. Atmos. Sci.*, **58**, 2485–2501.

Kepert, J. D., 2005: Objective analysis of tropical cyclone location and motion from high-density observations. *Mon. Wea. Rev.*, **133**, 2406–2421.

Kepert, J. D., 2006a: Observed boundary layer wind structure and balance in the hurricane core. Part I: Hurricane Georges. *J. Atmos. Sci.*, **63**, 2169–2193.

Kepert, J. D., 2006b: Observed boundary layer wind structure and balance in the hurricane core. Part II: Hurricane Mitch. *J. Atmos. Sci.*, **63**, 2194–2211.

Khain, A. P. and M. B. Pinsky, 1995: Drop inertia and its contribution to turbulent coalescence in convective clouds. Part I : Drop fall in the flow with random horizontal velocity. *J. Atmos. Sci.*, **55**, 196–206.

Lettau, H., 1962: Theoretical wind spirals in the boundary layer of a barotropic atmosphere. *Beitr. Phys. Atmos.*, **35**, 195–212.

Lin, Y. L. and H. D. Farley, R. D.and Orville, 1983: Bulk parameterization of the snow field in a cloud model. *J. Climate Appl. Meteor.*, **22**, 1065–1092.

Lorsolo, S., J. Zhang, F. Marks Jr., and J. Gamache, 2010: Estimation and mapping of hurricane turbulent energy using airborne doppler measurements. *Mon. Wea. Rev.*, **138**, 3656–3670.

Mann, J., 1994: The spatial structure of neutral atmospheric surface-layer turbulence. *J. Fluid Mech.*, **273**, 141–168.

Mann, J., 1998: Wind field simulation. *Prob. Eng. Mech.*, **13**, 269–282.

Masters, F. J., H. W. Tieleman, and J. A. Balderrama, 2010: Surface wind measurements in three Gulf Coast hurricanes of 2005. *J. Wind Eng. Ind. Aerodyn.*, **98**, 533–547.

Mlawer, E. J., S. J. Taubman, P. D. Brown, M. J. Iacono, and S. A. Clough, 1997: Radiative transfer for inhomogeneous atmosphere: Rrtm, a validated correlated-k model for the long wave. *J. Geophys. Res.*, **102**, 16 66316 682.

Moss, M. S., 1978: Low-level turbulence structure in the vicinity of a hurricane. *Mon. Wea. Rev.*, **106**, 841–849.

Nastrom, G. D. and T. E. Vanzandt, 1982: An analytical study of nonlinear response of rising balloons to horizontal wind. *J. Appl. Meteor.*, **21**, 413–419.

Noh, Y., W. G. Choen, Y. Hong, and S. Raasch, 2003: Improvement of the k-profile model for the planetary boundary layer based on large eddy simulation data. *Boundary-Layer Meteorol.*, **107**, 401–427.

Nolan, D. S., D. P. Stern, and J. Zhang, 2009a: Evaluation of planetary boundary layer parameterizations in tropical cyclones by comparison of in situ observations and high-resolution simulations of Hurricane Isabel (2003). Part II: inner-core boundary layer and eyewall structure. *Mon. Wea. Rev.*, **137**, 3675–3698.

Nolan, D. S., J. Zhang, and D. P. Stern, 2009b: Evaluation of planetary boundary layer parameterizations in tropical cyclones by comparison of in situ observations and high-resolution simulations of Hurricane Isabel (2003). Part I: initialization, maximum winds, and the outer-core boundary layer. *Mon. Wea. Rev.*, **137**, 3651–3674.

Panofsky, H. A., 1973: Tower micrometeorology. *Workshop on Micrometeorology*, Amer. Meteor. Soc., 151–176.

Pena, A., S. Gryning, J. Mann, and C. B. Hasager, 2010: Length scales of the neutral wind profile over homogeneous terrain. *J. Appl. Meteor. Climatol.*, **49**, 792–806.

Pinsky, M. B. and A. P. Khain, 1996: Simulations of drop fall in a homogeneous isotropic turbulent flow. *Atmos. Res.*, **40**, 223–259.

Powell, M. D., 1982: The transition of Hurricane Frederic boundary-layer wind field of the open Gulf of Mexico to landfall. *Mon. Wea. Rev.*, **110**, 1912–1932.

Powell, M. D., P. J. Vickery, and T. A. Reinhold, 2003: Reduced drag coefficient for high wind speed in tropical cyclone. *Nature*, **422**, 279–283.

Prandtl, L., 1925: Bericht uber untersuchungen zur ausgebildeten turbulenz (report on the investigations of developed turbulence). *Z. Angew. Math. Mech.*, **5**, 136–139.

Prandtl, L., 1932: Meteorologische anwendung der stromungslehre (meteorological application of fluid mechanics). *Beitr. Phys. Atmos.*, **19**, 188–202.

Rogers, R. and E. Uhlhorn, 2008: Observations of the structure and evolution of surface and flight-level wind asymmetries in Hurricane Rita (2005). *Geophys. Res. Lett. (USA)*, **35**, L22 811 (6 pp.) –.

Rotunno, R., Y. Chen, C. Wang, D. J. Dudhia, and G. J. Holland, 2009: Large eddy simulation of tropical cyclone. *Bull. Amer. Meteor. Soc.*, 1783–1788.

Schroeder, J. L., B. P. Edwards, and I. M. Giammanco, 2009: Observed tropical cyclone wind flow characteristics. *Wind and Structures*, **12**, 349–381.

Schroeder, J. L. and D. A. Smith, 2003: Hurricane Bonnie wind flow characteristics as determined from wemite. *J. Wind Eng. Ind. Aerodyn.*, **91**, 767–789.

Schroeder, J. L., D. A. Smith, and R. E. Peterson, 1998: Variation of turbulence intensities and integral scales during the passage of a hurricane. *J. Wind Eng. Ind. Aerodyn.*, **77&78**, 65–72.

Scoggins, J. R., 1965: Spherical balloon wind sensor behaviour. *J. Appl. Meteor.*, **4**, 139–145.

Sethraman, S., 1979: Atmospheric turbulence and storm surge due to Hurricane Belle. *Mon. Wea. Rev.*, **107**, 314–321.

Sharpiro, L. J., 1980: The asymmetry boundary layer flow under a translating hurricane. *J. Atmos. Sci.*, **40**, 1984–1998.

Shea, D. J. and W. M. Gray, 1973: The hurricane's inner core region. I. symmetric and asymmetric structure. *J. Atmos. Sci.*, **30**, 1544–1563.

Solari, G., L. Carassale, and F. Tubino, 2007: Proper orthogonal decomposition in wind engineering. Part I: A state-of-the-art and some prospects. *Wind and Structure*, **10**, 153–176.

Solari, G. and G. Piccardo, 2001: 3-d turbulence modeling for gust buffeting of structures. *Prob. Eng. Mech.*, **16**, 73–86.

Stern, D. P. and D. S. Nolan, 2009: Reexamining the vertical structure of tangential winds in tropical cyclones: Observations and theory. *J. Atmos. Sci.*, **66**, 3579–3600.

Troen, I. and L. Mahrt, 1986: A simple model of the atmospheric boundary layer; sensitivity to surface evaporation. *Boundary-Layer Meteorol.*, **37**, 129–148.

Vickery, P. J., D. Wadhera, M. D. Powell, and Y. Chen, 2009: A hurricane boundary layer and wind field model for use in engineering application. *J. Appl. Meteor. Climatol.*, **48**, 381–405.

Von Karman, T., 1948: Progress in the statistical theory of turbulence. *Proceedings of the National Academy of Sciences of USA*, **34**, 530–539.

Wang, Y. and C. Wu, 2004: Current understanding of tropical cyclone structure and intensity changes a review. *Meteorol. Atmos. Phys.*, **87**, 257–278.

Yu, B. and A. G. Chowdhury, 2009: Gust factors and turbulence intensities for the tropical cyclone environment. *J. Appl. Meteor. Climatol.*, **48**, 534–552.

Yu, B., A. G. Chowdhury, and F. J. Masters, 2008: Hurricane wind power spectra, cospectra, and integral length scales. *Boundary-Layer Meteorol.*, **129**, 411–430.

Zhang, J., 2007: An airborne investigation of the atmospheric boundary layer structure in the hurricane force wind regime. Ph.D. thesis, University of Miami, USA, 164 pp.

Zhang, J., 2010: Spectral characteristics of turbulence in the hurricane boundary layer over the ocean between the outer rain bands. *Quart. J. Roy. Meteor. Soc.*, **136**, 918–926.

Zhang, J., W. M. Drennan, P. G. Black, and J. R. French, 2009: Turbulence structure of the hurricane boundary layer between the outer rainbands. *J. Atmos. Sci.*, **66**, 2455–2467.

Zhang, J., K. B. Katsaros, P. G. Black, S. Lehner, J. R. French, and W. M. Drennan, 2008: Effect of roll vortices on turbulent fluxes in the hurricane boundary layer. *Boundary-Layer Meteorol.*, **128**, 173–189.

Zhang, J., R. F. Rogers, D. S. Nolan, and F. D. Marks Jr, 2011: On the characteristic height scales of the hurricane boundary layer. *Mon. Wea. Rev.*, **139**, 2523–2535.

Zhu, P., 2008: Simulation and parameterization of the turbulent transport in the hurricane boundary layer by large eddies. *J. Geophys. Res.*, **113**, D17104.

Curriculum Vitae

Name:	Sunwei Li	
Post-Secondary Education and Degrees:	Bachelor of Engineering Tsinghua University Beijing, China	2001-2005
	Master of Engineering Tongji University Shanghai, China	2005-2008
	Ph.D. University of Western Ontario London, ON, Canada	2008-2012
Honours and Awards:	Second-class Academic Excellence Scholarship	2003-2004
	Aboard Study Scholarship for Chinese Citizen	2008-2012
	Thesis Research Award	2010
	A. G. Davenport Memorial Award	2011
Related Work Experience:	Teaching Assistant The University of Western Ontario	2008-2012

Publications

- M. Gu, S. Li and Y. Zhou (2009). Numerical and Experimental Studies on Self-sustaining Equilibrium Atmosphere Boundary Layer, *Journal of Tongji University (Natural Science)*, **37(3) , 2–7.**
- S. Li and C. Miller (2012) A Study of the Motion Characteristics and Their Impact on the Wind Measurement Post-processing of the GPS Dropwindsonde, *Theoretical and Applied Climatology*, **submitted**
- S. Li and C. Miller (2012) The Variation of the GPS Dropwindsonde Drag Coefficient and Its Impact on the Wind Retrieval from Dropwindsonde Measurements,

Theoretical and Applied Climatology, **submitted**

- S. Li and C. Miller (2012) Wind Characteristics of the Hurricane Boundary Layer Observed by the GPS Dropwindsonde. Part I : Mean and Turbulent Wind Velocity Profiles, *Quarterly Journal of the Royal Meteorology Society*, **submitted**
- S. Li and C. Miller (2012) Wind Characteristics of the Hurricane Boundary Layer Observed by the GPS Dropwindsonde. Part II : Turbulent Length Scale and Boundary Layer Height, *Quarterly Journal of the Royal Meteorology Society*, **submitted**
- S. Li and C. Miller (2012) The High Resolution Numerical Simulation of an Idealized Tropical Cyclone : An Investigation of the Planetary Boundary Layer Scheme Based on the Dropwindsonde Observation, *Boundary-Layer Meteorology*, **submitted**